

A SEARCH FOR SUPERSYMMETRY IN EVENTS WITH A Z BOSON,  
JETS, AND MISSING TRANSVERSE ENERGY IN  $p - p$  COLLISIONS  
WITH  $\sqrt{s}=13$  TEV WITH THE ATLAS DETECTOR

TOVA RAY HOLMES



Physics Department  
University of California, Berkeley

August 2016 – version 1.0

Tova Ray Holmes: *A Search for Supersymmetry in Events with a Z Boson, Jets, and Missing Transverse Energy in  $p - p$  Collisions with  $\sqrt{s}=13$  TeV with the ATLAS Detector*, © August 2016





## ABSTRACT

---

A search for new phenomena in final states containing a Z boson decaying to electrons or muons, jets, and large missing transverse momentum is presented. This search uses proton–proton collision data collected during 2015 and 2016 at a center of mass energy  $\sqrt{s} = 13$  TeV by the ATLAS detector at the Large Hadron Collider, which correspond to an integrated luminosity of  $3.3 \text{ fb}^{-1}$ . The search targets the pair production of supersymmetric particles, squarks or gluinos, which decay via jets and a Z boson to the lightest Supersymmetric particle, which does not interact with the ATLAS detector. Results are interpreted in simplified models of gluino-pair (squark-pair) production, and provide sensitivity to gluinos (squarks) with masses as large as 1.3 (1.0) TeV.



## PUBLICATIONS

---

Some results and ideas presented have previously appeared in the following publications:

[this\_paper]



## ACKNOWLEDGEMENTS

---

Put your acknowledgements here.



## CONTENTS

---

<b>I INTRODUCTION</b>	<b>1</b>
<b>1 INTRODUCTION</b>	<b>3</b>
<b>II THEORY AND MOTIVATION</b>	<b>7</b>
<b>2 THEORY AND MOTIVATION</b>	<b>9</b>
<b>2.1 The Standard Model</b>	<b>9</b>
<b>2.1.1 Matter</b>	<b>9</b>
<b>2.1.2 Forces</b>	<b>11</b>
<b>2.1.3 Phenomenology of Proton-Proton Collisions</b>	<b>20</b>
<b>2.1.4 Problems in the Standard Model</b>	<b>23</b>
<b>2.2 Supersymmetry</b>	<b>25</b>
<b>2.2.1 The Minimal Supersymmetric Standard Model</b>	<b>25</b>
<b>2.2.2 Solutions to Standard Model Problems</b>	<b>27</b>
<b>2.2.3 Simplified Models of Supersymmetry</b>	<b>29</b>
<b>III THE EXPERIMENT</b>	<b>35</b>
<b>3 THE LARGE HADRON COLLIDER</b>	<b>37</b>
<b>3.1 The Injector Complex</b>	<b>38</b>
<b>3.2 Operation of the Large Hadron Collider</b>	<b>39</b>
<b>3.3 Luminosity</b>	<b>40</b>
<b>3.4 Pile-up in proton-proton Collisions</b>	<b>41</b>
<b>4 THE ATLAS DETECTOR</b>	<b>45</b>
<b>4.1 Coordinate System Used in the A Toroidal LHC Apparatus (ATLAS) Detector</b>	<b>45</b>
<b>4.2 The Inner Detector</b>	<b>46</b>
<b>4.2.1 The Pixel Detector</b>	<b>46</b>
<b>4.2.2 The Silicon Microstrip Tracker</b>	<b>48</b>
<b>4.2.3 The Transition Radiation Tracker</b>	<b>49</b>
<b>4.3 The Calorimeters</b>	<b>50</b>
<b>4.4 The Muon Spectrometer</b>	<b>51</b>
<b>4.5 The Magnet System</b>	<b>54</b>
<b>4.6 The Trigger System and Data Acquisition</b>	<b>55</b>
<b>4.7 Monte Carlo Event Generation</b>	<b>59</b>
<b>5 INNER DETECTOR TRACKING AND PIXEL CLUSTERING</b>	<b>63</b>
<b>5.1 Overview of Tracking in the ATLAS Detector</b>	<b>63</b>
<b>5.2 Clustering in the Pixel Detector</b>	<b>64</b>
<b>5.2.1 Charge Interpolation Method</b>	<b>65</b>
<b>5.2.2 Improving Measurement with Neural Networks</b>	<b>66</b>
<b>5.3 Impact of the Neural Network</b>	<b>67</b>
<b>5.3.1 The Neural Network in 13 TeV Data</b>	<b>67</b>
<b>6 OBJECT RECONSTRUCTION IN THE ATLAS DETECTOR</b>	<b>73</b>
<b>6.1 Electrons</b>	<b>73</b>

6.2	Photons . . . . .	76
6.3	Muons . . . . .	78
6.4	Jets . . . . .	80
6.5	Overlap Removal . . . . .	84
6.6	Missing Transverse Momentum . . . . .	85
<b>IV</b>	<b>SEARCHING FOR SUPERSYMMETRY</b>	<b>89</b>
<b>7</b>	<b>BACKGROUND PROCESSES</b>	<b>91</b>
7.1	Data and Monte Carlo Samples . . . . .	93
<b>8</b>	<b>OBJECT IDENTIFICATION AND SELECTION</b>	<b>95</b>
8.1	Electrons . . . . .	95
8.2	Muons . . . . .	96
8.3	Jets . . . . .	96
8.4	Photons . . . . .	97
<b>9</b>	<b>EVENT SELECTION</b>	<b>99</b>
9.1	Trigger Strategy . . . . .	100
9.2	Signal Efficiency and Contamination . . . . .	102
<b>10</b>	<b>BACKGROUND ESTIMATION</b>	<b>105</b>
10.1	Flavor Symmetric Processes . . . . .	105
10.1.1	Flavor Symmetry Method . . . . .	105
10.1.2	Sideband Fit Method . . . . .	108
10.2	$Z/\gamma^*$ + jets Background . . . . .	110
10.2.1	Photon and $Z$ Event Selection . . . . .	113
10.2.2	Smearing of Photon Events . . . . .	113
10.2.3	$p_T$ Reweighting of Photon Events . . . . .	115
10.2.4	Determining $H_T$ and $m_{\ell\ell}$ . . . . .	117
10.2.5	Subtraction of $V\gamma$ Events . . . . .	119
10.2.6	Validation in Data . . . . .	120
10.3	Fake and Non-Prompt Leptons . . . . .	120
10.4	Diboson and Rare Top Processes . . . . .	124
<b>11</b>	<b>SYSTEMATIC UNCERTAINTIES</b>	<b>129</b>
11.1	Uncertainties on Data-Driven Backgrounds . . . . .	129
11.1.1	Uncertainties on the Flavor Symmetry Method . . . . .	129
11.1.2	Uncertainties on the $\gamma$ + jets Method . . . . .	133
11.1.3	Uncertainties on the Fakes Background . . . . .	136
11.2	Theoretical and Experimental Uncertainties . . . . .	136
11.3	Impact of Uncertainties on the Signal Region . . . . .	139
<b>12</b>	<b>RESULTS</b>	<b>141</b>
<b>13</b>	<b>INTERPRETATIONS</b>	<b>147</b>
<b>V</b>	<b>CONCLUSIONS</b>	<b>151</b>
<b>14</b>	<b>CONCLUSIONS AND OUTLOOK</b>	<b>153</b>
	<b>BIBLIOGRAPHY</b>	<b>155</b>

## LIST OF FIGURES

---

Figure 1	The Standard Model of particle physics, containing all known bosons and fermions, with the addition of the hypothetical graviton. [7] . . . . .	10
Figure 2	Gluon self coupling Feynman diagrams involving 3- and 4-gluon interactions. . . . .	14
Figure 3	Quark couplings to the different types of gauge bosons. The $q_{u,d}$ labels represent any up- or down-type quarks.	15
Figure 4	The running of the strong coupling constant, $\alpha_s$ . [14]	16
Figure 5	Feynman diagrams of trilinear gauge couplings in the Standard Model (SM). . . . .	17
Figure 6	Feynman diagrams of weak couplings to leptons in the SM. . . . .	18
Figure 7	Feynman diagrams demonstrating Higgs couplings to the weak gauge bosons in the SM. . . . .	20
Figure 8	Feynman diagrams showing Higgs couplings to fermions in the SM. . . . .	20
Figure 9	2008 MSTW Parton Distribution Functions (PDFs) for various particle types given as a function of $x$ and $Q^2$ , the square of the parton-parton momentum transfer. [15] . . . . .	21
Figure 10	Cross-sections for many SM processes as a function of $\sqrt{s}$ [16]. . . . .	22
Figure 11	Galactic rotation curve of velocity as a function of radius in NGC 3198. Included is the observed data, as well as the expected velocity distribution from a disk-shaped galaxy corresponding to the expected density from electromagnetic observations. Another curve corresponding to a halo-shaped matter distribution is superimposed, and the halo and disk are summed and fit to the data. [20] . . . . .	24
Figure 12	Two example vertices allowed by the Minimal Supersymmetric Standard Model (MSSM). . . . .	27
Figure 13	Running of the strong, weak, and electromagnetic coupling constants for the SM (left) and MSSM (right). [27] . . . . .	28
Figure 14	Feynman diagram of the decay considered in the simplified models used in the analysis presented in Part iv. . . . .	30
Figure 15	13 TeV production cross-sections for sparticles, as a function of sparticle mass [32]. . . . .	30

Figure 16	Results of an 8 TeV search performed by the <a href="#">ATLAS</a> collaboration in a signal region targeting events like those in <a href="#">Figure 14</a> . The events in the signal region are displayed as a function of $m_{\ell\ell}$ , the invariant mass of the event's leading leptons. The <a href="#">SM</a> backgrounds are shown with their full uncertainties based on data-driven background estimations, and two signals are superimposed on the distribution. The observed datapoints are higher than the expected background, with a total excess of $3.0\sigma$ [1]. . . . .	31
Figure 17	Results of an 8 TeV search performed by the Compact Muon Solenoid ( <a href="#">CMS</a> ) collaboration in a signal region including a broad range of $m_{\ell\ell}$ . A $2.4\sigma$ local excess is seen in the low $m_{\ell\ell}$ region, and no excess of events is seen in the region with $m_{\ell\ell}$ consistent with an on-shell Z boson. The data is fit based on a data driven estimate of the flavor symmetric background (FS) and the Drell-Yan background (DY), with an additional component for the signal [34]. . . . .	32
Figure 18	Preliminary results from a 13 TeV search targeting the same signal region as <a href="#">Figure 16</a> , performed on $3.2 \text{ fb}^{-1}$ of 2015 data. The events in the signal region are displayed as a function of $m_{\ell\ell}$ , the invariant mass of the event's leading leptons. Flavor symmetric and $Z/\gamma^* + \text{jets}$ backgrounds are taken from data-driven methods, while the other backgrounds are taken from Monte Carlo simulation ( <a href="#">MC</a> ). They are compared to the data, which shows a $2.2\sigma$ excess of events. Distributions from two signal points are superimposed [2]. . . . .	33
Figure 19	The Large Hadron Collider ( <a href="#">LHC</a> ) main collider ring and pre-accelerator Super Proton Synchrotron ( <a href="#">SPS</a> ) overlaid on a map of Switzerland and France, with the four main <a href="#">LHC</a> experiments identified. . . . .	37
Figure 20	The pre-accelerators of the <a href="#">LHC</a> . . . . .	38
Figure 21	Cross-section of a cryodipole magnet in the <a href="#">LHC</a> . . . . .	40
Figure 22	Beam spot in the <a href="#">ATLAS</a> detector for one run in 2015. Distributions show only the highest $p_T$ vertex per event. Left is the $x - y$ distribution of vertices, while the right plot shows the $x - z$ distribution. . . . .	40
Figure 23	Instantaneous luminosity of one fill of 7 TeV data in 2011. . . . .	42
Figure 24	<a href="#">ATLAS</a> luminosity for Run 1 and Run 2, as of September 2016. . . . .	42
Figure 25	Average number of interactions per crossing shown for 2015 and 2016 separately, as well as the sum of the two years. . . . .	43

Figure 26	Diagram of the <b>ATLAS</b> detector, with subsystems and magnets identified. . . . .	45
Figure 27	Diagram of the <b>ATLAS</b> Inner Detector, containing the Pixel, SCT, and TRT subsystems. . . . .	47
Figure 28	Diagram of one-quarter of the <b>ATLAS</b> Inner Detector in the $R - z$ plane, with lines drawn to indicate various $\eta$ locations. . . . .	48
Figure 29	Diagram in the $x - y$ plane of the Insertable B-Layer ( <b>IBL</b> ) and the innermost layer of the pixel detector, Lo [42]. . . . .	49
Figure 30	The calorimeter system of the <b>ATLAS</b> detector. . . . .	50
Figure 31	Layout of the LAr calorimeter module at central $\eta$ [38]. . . . .	51
Figure 32	An $x-y$ view of the Muon Spectrometer ( <b>MS</b> ). The three barrel layers are visible, as well as the overlapping, differently sized chambers. The outer layer of the <b>MS</b> is about 20m in diameter. . . . .	52
Figure 33	An $r-z$ view of the <b>MS</b> . The three layers of the barrel and endcap <b>MS</b> are visible. . . . .	53
Figure 34	The magnet system of the <b>ATLAS</b> detector. The inner cylinder shows the solenoid which gives a uniform magnetic field in the Inner Detector ( <b>ID</b> ). Outside of that are the barrel and endcap toroids, which provide a non-uniform magnetic field for the <b>MS</b> . . . . .	54
Figure 35	Plots of the magnetic field within the <b>ATLAS</b> detector. Top is the field (broken into its $R$ and $z$ components) as a function of $z$ for several different values of $R$ . Bottom is the field integral through the Monitored Drift Tubes ( <b>MDTs</b> ) as a function of $ \eta $ for two different $\phi$ values. . . . .	56
Figure 36	Level One ( <b>L1</b> ) trigger rates for for a run in July 2016 as a function of luminosity block, an approximately 60-second long period of data-taking. The total rate is lower than the combined stack because of overlapping triggers. . . . .	57
Figure 37	High Level Trigger ( <b>HLT</b> ) trigger rates for for a run in July 2016 as a function of luminosity block, an approximately 60-second long period of data-taking. The total rate is lower than the combined stack because of overlapping triggers. . . . .	58
Figure 38	Photon trigger efficiency as a function of $E_T$ for four different <b>HLT</b> triggers with photon $p_T$ requirements of 25, 35, 120, and 140 GeV [44]. . . . .	58
Figure 39	Number of secondary vertices in a module in the first layer of the pixel detector in data (top) and <b>MC</b> (bottom). There are more events in the data than the <b>MC</b> [54]. . . . .	61

Figure 40	Event display from June 2015, with particle tracks in light blue. The main image displays a view of the $x - y$ plane of the <b>ID</b> . The <b>IBL</b> and <b>Lo</b> of the Pixel Detector are shown in red, with the remaining two layers of the Pixel Detector in green and blue. Outside those are the four double layers of the Silicon Microstrip Tracker ( <b>SCT</b> ). The smaller image on the right shows an $r - z$ view, zoomed in to only show hits in the <b>IBL</b> [55]. . . . .	63
Figure 41	A few possible types of clusters in the Pixel Detector. (a) shows a single particle passing through a layer of the detector, (b) shows two particles passing through the detector, creating a single merged cluster, and (c) shows a single particle emitting a $\delta$ -ray as it passes through the detector [57]. . . . .	65
Figure 42	One example of a two-particle cluster and its truth information compared with the output of the Neural Networks ( <b>NNs</b> ). The boxes represent pixels, with a color scale indicating charge. At top, the $p(N = i)$ values give the output of the Number <b>NN</b> , the probabilities that the cluster contains 1, 2, and 3 particles. Given the highest probability is for $N = 2$ , the other <b>NNs</b> predict the position and errors of the two particles (in white). The black arrows and squares represent the truth information from the cluster, and the black dot and dotted line show the position measurement for the un-split cluster [57]. . . . .	67
Figure 43	$x$ resolutions for clusters with 3 (top) and 4 (bottom) pixels in the $x$ direction in 7 TeV data for Connected Component Analysis ( <b>CCA</b> ) (using only charge interpolation to determine position) and <b>NN</b> clustering taken from <b>MC</b> [57]. . . . .	68
Figure 44	Performance of the pixel neural network used to identify clusters created by multiple charged particles, as a function of constant coherent scaling of the charge in each pixel in the cluster. The top figure shows the rate at which the neural network wrongly identifies clusters with one generated particle as clusters with multiple particles. The bottom figure shows the rate at which the neural network correctly identifies clusters generated by multiple particles as such. . . . .	70
Figure 45	Fraction of cluster classes as a function of the distance between tracks for IBL (top) and 2nd pixel layer (bottom). . . . .	71

Figure 46	Identification efficiencies from MC samples for Loose, Medium, and Tight working points. Left is the efficiency for identification of true electrons taken from $Z \rightarrow ee$ MC, and right is the efficiency for misidentification of jets as electrons taken from dijet MC [62]. . . . .	74
Figure 47	Combined electron reconstruction and identification efficiencies measured as a function of $\eta$ for data (using the tag-and-probe method on $Z \rightarrow ee$ events) and $Z \rightarrow ee$ MC. Distributions include electrons with $E_T > 15$ GeV. [62]. . . . .	75
Figure 48	Comparison of Tight identification efficiency measurements from data and $Z \rightarrow \ell\ell\gamma$ MC for unconverted (left) and converted (right) photons, with an inclusive $\eta$ selection. The bottom of each figure shows the ratio of data and MC efficiencies. [65]. . . . .	77
Figure 49	Muon reconstruction efficiency for the Medium and Loose working points measured with $Z \rightarrow \mu\mu$ events in data and in MC as a function of $\eta$ . The ratio between the two is shown at the bottom. The Loose working point efficiency is shown only at small $ \eta $ , where the loosened requirements cause the largest difference from the Medium working point [67]. . . . .	79
Figure 50	Muon reconstruction efficiency for the High- $p_T$ working point measured with $Z \rightarrow \mu\mu$ events in data and in MC as a function of $\eta$ . The ratio between the two is shown at the bottom. [67] . . . . .	80
Figure 51	Distribution of event $p_T$ density, $\rho$ , taken from MC dijets for different numbers of primary vertices. [69]	82
Figure 52	Energy response as a function of energy and $\eta$ for Electromagnetic (EM) jets in dijet MC. [69] . . . . .	82
Figure 53	Dijet MC distributions of the number of pile-up jets passing the Jet Vertex Tagger (JVT) and Jet Vertex Fraction (JVF) cuts (left) and the efficiency for jets from the primary vertex (right) as a function of number of primary vertices in the event [70]. . . . .	84
Figure 54	Distribution of MV2c20 output for $b$ -jets, $c$ -jets, and light-flavor jets in $t\bar{t}$ MC [71]. . . . .	84
Figure 55	Distributions of the resolution of the $x$ and $y$ components of Track Soft Term (TST) $E_T^{\text{miss}}$ in $Z \rightarrow \mu\mu$ events in data and MC. . . . .	86
Figure 56	Distributions of the jet term (top left), muon term (top right), and TST (bottom) $E_T^{\text{miss}}$ in $Z \rightarrow \mu\mu$ events in data and MC. In the jet term distribution, the feature at zero is due to events with no jets, and the spike at 20 GeV corresponds to the minimum jet $p_T$ considered for the analysis [73]. . . . .	87

Figure 57	An example Feynman diagram of $t\bar{t}$ production and decay. . . . .	91
Figure 58	An example Feynman diagram of the production and decay of a WZ event. . . . .	92
Figure 59	An example Feynman diagram of the production and decay of a $Z/\gamma^* + \text{jets}$ event. . . . .	93
Figure 60	Schematic diagrams of the control, validation and signal regions for the on-shell Z (top) and edge (bottom) searches. For the on-shell Z search the various regions are shown in the $m_{\ell\ell} - E_T^{\text{miss}}$ plane, whereas in the case of the edge search the signal and validation regions are depicted in the $H_T - E_T^{\text{miss}}$ plane. . . . .	100
Figure 61	Signal region acceptance (left) and efficiency (right) in SRZ for the simplified model with gluino pair production with $\tilde{\chi}_2^0$ decays to $\tilde{\chi}_1^0$ and an on-shell Z boson with 1 GeV neutralino LSP. Acceptance is calculated by applying the signal-region kinematic requirements to truth objects in MC, which do not suffer from identification inefficiencies or measurement resolutions. . . . .	103
Figure 62	Expected signal contamination in CRT (left) and CRFS (right) for the signal model with gluino pair production, where the gluinos decay to quarks and a neutralino, with the neutralino subsequently decaying to a Z boson and a 1 GeV neutralino LSP. . . . .	103
Figure 63	Expected signal contamination in VRS (left) and VRT (right) for the signal model with gluino pair production, where the gluinos decay to quarks and a neutralino, with the neutralino subsequently decaying to a Z boson and a 1 GeV neutralino LSP. . . . .	104
Figure 64	Measurements of $k_e$ , the ratio of electron to muon events, in bins of $p_T$ and $\eta$ . On the top is the measurements indexed by the leading lepton, while the measurements indexed by the subleading lepton are on the bottom. These efficiencies are for the 2016 dataset. . . . .	107
Figure 65	Lepton $p_T$ distribution in data and MC, demonstrating the overestimate of the high- $p_T$ tail in MC [91]. .	110
Figure 66	MC comparison of boson $p_T$ in a selection of photon and $Z \rightarrow \ell\ell$ events with $H_T > 600$ GeV. The feature at 1000 GeV is not physical, but a reflection of the change in bin size. . . . .	112
Figure 67	$E_{T,\parallel}^{\text{miss}}$ distributions in MC for $Z + \text{jets}$ $ee$ (left) and $\mu\mu$ (right) channels compared to $\gamma + \text{jets}$ in an inclusive region with $H_T > 600$ GeV. . . . .	115

Figure 68	$E_{T,\parallel}^{\text{miss}}$ distributions in MC for Z+jets ee (left) and $\mu\mu$ (right) channels compared to $\gamma + \text{jets}$ in an inclusive region with $H_T > 600$ GeV after the smearing procedure has been performed. These distributions have also been $p_T$ reweighted, as described in Section 10.2.3. . . . .	116
Figure 69	Photon reweighting factors for the ee (left) and $\mu\mu$ (right) channels derived from data and MC. . . . .	116
Figure 70	$E_T^{\text{miss}}$ distribution comparing MC distributions of photon and Z events before any smearing is applied (top), with only $p_T$ reweighting applied (bottom left), and after $p_T$ reweighting and smearing have both been applied (bottom right) in the ee channel of 2016 data. . . . .	117
Figure 71	$E_T^{\text{miss}}$ distribution comparing MC distributions of photon and Z events before any smearing is applied (top), with only $p_T$ reweighting applied (bottom left), and after $p_T$ reweighting and smearing have both been applied (bottom right) in the $\mu\mu$ channel of 2016 data. . . . .	118
Figure 72	$Z/\gamma^* + \text{jets}$ MC $m_{\ell\ell}$ distribution compared to the prediction from $\gamma + \text{jets}$ method performed on MC (left) and the prediction from $\gamma + \text{jets}$ method performed on data (right). . . . .	119
Figure 73	Comparison of data and MC in CR- $\gamma$ without any $H_T$ cut, including the contributions from various $V\gamma$ processes. . . . .	120
Figure 74	Total $\gamma + \text{jets}$ data prediction in SRZ (excluding the $E_T^{\text{miss}}$ cut) and the prediction after the $V\gamma$ subtraction. . . . .	121
Figure 75	$E_T^{\text{miss}}$ distribution in VRZ ee (left) and $\mu\mu$ (right) with total data yield compared to the sum of the prediction from the $\gamma + \text{jets}$ method, the prediction from the flavor symmetry method, the prediction from the fake background estimation (included under “other”), and the remaining backgrounds taken from MC. . . . .	122
Figure 76	$\Delta\phi(\text{jet}, p_T^{\text{miss}})$ distribution in for the leading jet (left) and the subleading jet (right). The comparison is performed in VRZ with the cut on $\Delta\phi(\text{jet}_{12}, p_T^{\text{miss}})$ removed. The total data yield is compared to the sum of the prediction from the $\gamma + \text{jets}$ method, the prediction from the flavor symmetry method, the prediction from the fake background estimation (included under “other”), and the remaining backgrounds taken from MC. . . . .	122

Figure 77	Sub-leading lepton $p_T$ for $ee$ (left) and $\mu\mu$ (right) events in the tight-tight region used to measure the real-lepton efficiency for 2016. . . . .	124
Figure 78	Sub-leading lepton $p_T$ for $\mu e$ (left) and $\mu\mu$ (right) events in the tight-tight region used to measure the fake-lepton efficiency for 2016. . . . .	124
Figure 79	Same sign validation regions in the $ee$ (top left), $\mu\mu$ (top right), $e\mu$ (bottom left) and $\mu e$ (bottom right) channels combining 2015+2016 data. Uncertainty bands include both statistical and systematic uncertainties. . . . .	125
Figure 80	Distribtuions of data and MC in VR-WZ. Reconstructed transverse mass of the $W$ (top) and mass of the $Z$ (bottom). . . . .	126
Figure 81	Distribtuions of data and MC in VR-WZ. $p_T$ of the $W$ (top) and $Z$ (bottom). . . . .	127
Figure 82	Distribtuions in VR-WZ. On the top, mass of the $Z$ bosons in the event, and on the bottom, $p_T$ of the $Z$ bosons. . . . .	128
Figure 83	MC closure plots of VRS (top) and SRZ (bottom). The number of events from MC (black points) is compared to the number of events predicted from the flavor symmetry method (yellow histogram). The comparison is performed before the expanded $m_{\ell\ell}$ window is used to predict the on- $Z$ bin, but because the shape is taken from the same MC, the result is identical. . . . .	130
Figure 84	$\alpha$ , the trigger efficiency ratio, calculated as a function of $E_T^{\text{miss}}$ from three different sources: data (blue), the usual skimmed $t\bar{t}$ MC (red), and an unskimmed $t\bar{t}$ MC (green). . . . .	132
Figure 85	Plots of the fraction of on- $Z$ events with a VR-FS-like selection as a function of $H_T$ . The top figure shows 2015 data and MC while the bottom figure shows the same for 2016. . . . .	133
Figure 86	$E_T^{\text{miss}}$ distributions for $\gamma + \text{jets}$ predictions using different reweighting variables, as well as distributions with the nominal reweighting but with smearing functions taken from data and from MC in a $\geq 2$ -jet region. . . . .	134
Figure 87	MC closure of the $\gamma + \text{jets}$ method as a function of $E_T^{\text{miss}}$ comparing the MC prediction of the $Z$ background with the $\gamma + \text{jets}$ method performed on $\gamma + \text{jets}$ MC. The uncertainty band includes both statistical and reweighting uncertainties. . . . .	135

Figure 88	Distributions of $m_T(\ell, E_T^{\text{miss}})$ , the transverse mass of the lepton and the $E_T^{\text{miss}}$ in a Validation Region ( <a href="#">VR</a> ) designed to target $W\gamma$ processes. Top is the distribution with a $E_T^{\text{miss}}$ cut at 100 GeV, and bottom is the same distribution with a $E_T^{\text{miss}}$ cut of 200 GeV. . . . . <a href="#">140</a>
Figure 89	Comparison of background predictions and data yields in four validation regions, as well as the signal region. Definitions of all regions can be found in <a href="#">Table 7</a> , with both rare top and fake backgrounds grouped together under the “other” label. The uncertainty band includes all statistical and systematic uncertainties. Below is a panel of the one-sided statistical significances of the deviations between the predicted and observed quantities for each region. . . . . <a href="#">141</a>
Figure 90	Comparisons as a function of $m_{\ell\ell}$ of background predictions with observed data in an SRZ-like region, with the $m_{\ell\ell}$ cut removed. Left is the same-flavor channel, where all background shapes are taken from <a href="#">MC</a> and scaled to their SRZ predictions, except for the $Z/\gamma^* + \text{jets}$ background, which is taken entirely from the data-driven background. Right is the different-flavor channel, in which the backgrounds are taken directly from <a href="#">MC</a> , except for $t\bar{t}$ , which is scaled to match the total data yield. . . . . <a href="#">143</a>
Figure 91	Distributions of observed data, background predictions, and simulated signals are shown in SRZ as a function of $m_{\ell\ell}$ , $p_T^{\ell\ell}$ , $E_T^{\text{miss}}$ , $H_T$ , number of jets, and number of $b$ -jets. The two example signals have $(m(\tilde{g}), m(\tilde{\chi}_2^0)) = (1095, 205)$ GeV. All background shapes are taken from <a href="#">MC</a> , and in the case of flavor symmetric and $Z/\gamma^* + \text{jets}$ backgrounds, their yields are scaled to match the data-driven predictions. Uncertainties include statistical and systematic components. . . . . <a href="#">144</a>
Figure 92	Comparisons as a function of $\Delta\phi(\text{jet}_{12}, p_T^{\text{miss}})$ of background predictions with observed data in an SRZ-like (left) and VRS-like (right) region, with the $\Delta\phi(\text{jet}_{12}, p_T^{\text{miss}})$ cut removed. All background shapes are taken from <a href="#">MC</a> and scaled to their SRZ predictions, except for the $Z/\gamma^* + \text{jets}$ background, which is taken entirely from the data-driven background. . . . . <a href="#">146</a>

Figure 93	Expected and observed exclusion contours derived from the results in SRZ for the (top) $\tilde{g}-\tilde{\chi}_2^0$ on-shell grid and (bottom) $\tilde{q}-\tilde{\chi}_2^0$ on-shell grid. The dashed blue line indicates the expected limits at 95% CL and the yellow band shows the $1\sigma$ variation of the expected limit as a consequence of the uncertainties in the background prediction and the experimental uncertainties in the signal ( $\pm 1\sigma_{\text{exp}}$ ). The observed limits are shown by the solid red line, with the dotted red lines indicating the variation resulting from changing the signal cross section within its uncertainty ( $\pm 1\sigma_{\text{theory}}^{\text{SUSY}}$ ). . . . .	<a href="#">148</a>
Figure 94	Expected and observed exclusion contours derived from the results in SRZ for the $\tilde{g}-\tilde{\chi}_1^0$ on-shell grid. The dashed blue line indicates the expected limits at 95% CL and the yellow band shows the $1\sigma$ variation of the expected limit as a consequence of the uncertainties in the background prediction and the experimental uncertainties in the signal ( $\pm 1\sigma_{\text{exp}}$ ). The observed limits are shown by the solid red line, with the dotted red lines indicating the variation resulting from changing the signal cross section within its uncertainty ( $\pm 1\sigma_{\text{theory}}^{\text{SUSY}}$ ). . . . .	<a href="#">149</a>
Figure 95	Expected 95% Confidence Level (CL) exclusion contours (dashed) and $5\sigma$ discovery contours (solid) for $L_{\text{int}} = 300^{-1}$ (black) and $3000^{-1}$ (red) for gluino pair-production, with $1\sigma$ bands representing the uncertainty on the production cross-section. Superimposed is the observed 8 TeV exclusion for similar models. [109] . . . . .	<a href="#">154</a>

## LIST OF TABLES

---

Table 1	Supermultiplets of supersymmetric and SM particles. Sfermions, on the first five rows, are all spin-0. Higgsinos and gauginos are all spin-1/2. Three sets of each fermion's supermultiplet exist, one for each generation. [25] . . . . .	26
Table 2	Simulated background event samples used in this analysis with the corresponding matrix element and parton shower generators, cross-section order in $\alpha_s$ used to normalise the event yield, underlying-event tune and PDF set. . . . .	94
Table 3	Summary of the electron selection criteria. $z_0$ gives the track's distance from the hard-scatter vertex projected in the $z$ direction, while $d_0$ gives the this distance projected onto the $x - y$ plane. . . . .	95
Table 4	Summary of the muon selection criteria. The signal selection requirements are applied on top of the baseline selection. . . . .	96
Table 5	Summary of the jet and $b$ -jet selection criteria. The signal selection requirements are applied on top of the baseline requirements. . . . .	97
Table 6	Summary of the photon selection criteria. . . . .	98
Table 7	Overview of all signal, control and validation regions used in the on-shell $Z$ search. More details are given in the text. The flavour combination of the dilepton pair is denoted as either <i>SF</i> for same-flavor or <i>DF</i> for different flavor. All regions require at least two leptons, unless otherwise indicated. In the case of CR $\gamma$ , VR-WZ, VR-ZZ, and VR-3L the number of leptons, rather than a specific flavor configuration, is indicated. The main requirements that distinguish the control and validation regions from the signal region are indicated in bold. Most of the kinematic quantities used to define these regions are discussed in the text. The quantity $m_T(\ell_3, E_T^{\text{miss}})$ indicates the transverse mass formed by the $E_T^{\text{miss}}$ and the lepton which is not assigned to either of the $Z$ -decay leptons. . . . .	101
Table 8	Lepton trigger requirements used for the analysis in different regions of lepton- $p_T$ phase space. . . . .	102

Table 9	Yields in signal and validation regions for the flavor symmetric background. Errors include statistical and systematic uncertainties, discussed in Chapter 11. . . . .	108
Table 10	Background fit results from the sideband fit method. The $t\bar{t}$ MC's normalization is taken as a free parameter in the fit to data in CRT, then that normalization factor is applied in SRZ. The results are shown here both divided between the $ee$ and $\mu\mu$ channels and summed together. All other backgrounds are taken from MC in CRT, while in SRZ, the $Z/\gamma^* + \text{jets}$ contribution is taken from the $\gamma + \text{jets}$ method. The uncertainties quoted include both statistical and systematic components. . . . .	109
Table 11	Summary of the $t\bar{t}$ normalization factors calculated by the sideband fit to CRT and VRT for the 2015+2016 data. . . . .	110
Table 12	Comparison of Flavor Symmetric (FS) background predictions from the nominal method, the flavor symmetry method, and the cross-check, the sideband fit method. Uncertainties include statistical and systematic uncertainties in both cases. . . . .	111
Table 13	List of triggers used to collect photon events in 2015 and 2016 data-taking. . . . .	114
Table 14	Control regions used to measure efficiencies of real and fake leptons. The flavour combination of the dilepton pair is denoted as either "SF" for same-flavour or "DF" for different flavour. The charge combination of the leading lepton pairs are given as "SS" for same-sign or "OS" for opposite-sign. . . . .	123
Table 15	Yields in validation regions. In VRS, data-driven background estimates are used for $Z/\gamma^* + \text{jets}$ , fakes, and FS processes. All other backgrounds are taken from MC, including all backgrounds in the multi-lepton VRS. Uncertainties include statistical and systematic components. . . . .	125
Table 16	Uncertainties in the on-Z signal and validation regions. Nominal predictions are given with statistical uncertainty (including uncertainty from subtracted backgrounds), MC Closure uncertainty, uncertainty on the prediction from varying $k$ and $\alpha$ by their statistical uncertainties, comparing the efficiencies from AODs to that of DAODs, and on the $m_{\ell\ell}$ widening, which includes MC statistics and a data/MC comparison in a loosened region. . . . .	129

Table 17	Uncertainty breakdown for the $\gamma + \text{jets}$ method in SRZ. Uncertainties considered are the impact of MC uncertainty on $V\gamma$ backgrounds, MC closure, uncertainty on $m_{\ell\ell}\text{shape}$ (also determined via MC closure), reweighting uncertainties, smearing uncertainties, and statistical uncertainty on the $\gamma + \text{jets}$ events used in the method. . . . .	136
Table 18	Systematic uncertainties on the fake-lepton background for on-Z regions for 2015+2016 yields. The nominal yield includes statistical uncertainty from the baseline selection in a given region. The following rows indicate the results of varying the real and fake lepton efficiencies up and down by their statistical uncertainty. Real cont. gives an uncertainty on the contamination of real leptons in the fake lepton efficiency. $b$ -jet and no $b$ -jet indicate the impact of requiring or vetoing $b$ -tagged jets in the regions used to measure the fake efficiency. . . . .	137
Table 19	Fractional uncertainties of dibosons in signal and validation regions from Sherpa scale variations. . .	138
Table 20	Comparison of yields in on-Z and off-Z regions in Sherpa and Powheg diboson MC at $14.7 \text{ fb}^{-1}$ . . .	138
Table 21	Overview of the dominant sources of systematic uncertainty on the total background estimate in the signal regions. The values shown are relative to the total background estimate, shown in %. . . . .	139
Table 22	Number of events expected and observed in the $ee$ , $\mu\mu$ , and combined channels. Expected predictions include all systematic and statistical uncertainties discussed in Chapter 11. Also shown is the discovery $p$ -value for zero signal strength ( $p(s = 0)$ ) [103], Gaussian significance, 95% CL observed and expected upper limits on the number of signal events ( $S^{95}$ ), and the corresponding observed upper limit on the visible cross section ( $(\epsilon\sigma)^{95}_{\text{obs}}$ ). . . . .	142

## LISTINGS

---

## ACRONYMS

---

- IBL Insertable B-Layer  
MS Muon Spectrometer  
ID Inner Detector  
SCT Silicon Microstrip Tracker  
TRT Transition Radiation Tracker  
NN Neural Network  
CCA Connected Component Analysis  
ToT Time Over Threshold  
MDT Monitored Drift Tube  
CSC Cathode-Strip Chamber  
RPC Resistive Plate Chamber  
TGC Thin Gap Chamber  
L<sub>1</sub> Level One  
HLT High Level Trigger  
L<sub>1</sub>Calo L<sub>1</sub> Calorimeter Trigger  
L<sub>1</sub>Topo L<sub>1</sub> Topological Trigger  
CTP Central Trigger Processor  
TTC Trigger Timing and Control  
ROB Read Out Board  
RoI Region of Interest  
LHC Large Hadron Collider  
LEP Large Electron-Positron  
SPS Super Proton Synchrotron  
ATLAS A Toroidal LHC Apparatus  
CMS Compact Muon Solenoid  
ALICE A Large Ion Collider Experiment  
LHCb Large Hadron Collider beauty

RF	Radiofrequency
PSB	Proton Synchrotron Booster
PS	Proton Synchrotron
OR	Overlap Removal
EM	Electromagnetic
LCW	Local Cluster Weighting
JES	Jet Energy Scale
JER	Jet Energy Resolution
JVT	Jet Vertex Tagger
JVF	Jet Vertex Fraction
CST	Calorimeter Soft Term
TST	Track Soft Term
MC	Monte Carlo simulation
SM	Standard Model
BSM	Beyond the Standard Model
SUSY	Supersymmetry
QCD	Quantum Chromodynamics
PDF	Parton Distribution Function
DM	Dark Matter
LO	Leading Order
NLO	Next to Leading Order
NLO+NLL	Next-to-Leading-Logarithmic Accuracy
SUSY	Supersymmetry
MSSM	Minimal Supersymmetric Standard Model
LSP	Lightest Supersymmetric Particle
AOD	Analysis Object Data
dAOD	derived AOD
SR	Signal Region
VR	Validation Region
CR	Control Region

FS Flavor Symmetric

CL Confidence Level

HL-LHC High Luminosity Large Hadron Collider



<sup>1</sup>

## Part I

<sup>2</sup>

### INTRODUCTION

<sup>3</sup>



4

5 INTRODUCTION

---

6 In 2010, the [LHC](#) began colliding protons in its 27 km ring, taking its place  
7 as the most powerful in a long line of accelerators aimed at uncovering the  
8 fundamental rules that govern particle physics. Its primary goal was to  
9 complete the Standard Model of particle physics by discovering the Higgs  
10 boson, the last remaining particle that physicists felt sure must exist. With  
11 its presence, the Standard Model would be consistent, explaining every ob-  
12 served interaction of known particles, with a complete mathematic frame-  
13 work to describe each feature. However, even with a Higgs boson, the  
14 Standard Model contained hints that it might be incomplete, suspicious  
15 features that suggested that at a higher energy, there might be something  
16 more.

17 In 2012, the [ATLAS](#) and [CMS](#) Experiments discovered the Higgs boson,  
18 leaving the [LHC](#) physics community without a single primary goal, but  
19 rather a host of theories to explore, each extending the Standard Model  
20 in a different way. Each theory attempts to solve one of the mysteries left  
21 by the Standard Model, providing an explanation for Dark Matter, sug-  
22 gesting a mechanism that could explain Gravity's weakness, or explain-  
23 ing the Higgs boson's mass. For decades, the most popular of these has  
24 been Supersymmetry, which proposes a fermionic symmetry and requires  
25 a menagerie of new Supersymmetric particles, none of which has yet been  
26 observed.

27 Supersymmetry simultaneously solves more of the Standard Model's  
28 problems than any other, making it appealing to theorists and experimen-  
29 talists alike. But in order to do this, Supersymmetric particles must appear  
30 with masses of approximately 1 TeV, precisely the range of energies the  
31 [LHC](#) is capable of exploring. In 2015, after a three-year shutdown, the [LHC](#)  
32 nearly doubled the energy of its collisions, opening up new territory to  
33 be explored by analyzers, and providing data that could either discover or  
34 exclude many Supersymmetric models.

35 The analysis presented in this thesis searches for Supersymmetry, seek-  
36 ing to identify events in which Supersymmetric particles are produced in  
37 proton-proton collisions, then decay via a Z boson to a chargeless Super-  
38 symmetric particle which escapes ATLAS without detection. A similar AT-  
39 LAS search, performed with data from the lower-energy collisions 2012,  
40 observed a  $3\sigma$  excess of events over the expected Standard Model back-  
41 ground [1].

42 The excess generated a great deal of interest in this channel, and re-  
43 investigating it became a top priority when the upgraded [LHC](#) turned back  
44 on in 2015. A preliminary search, performed using the 2015 data only, was  
45 released at the end of that year. Again an excess was observed, this time  
46 with a significance of  $2.2\sigma$  [2].

47 This thesis describes a search for Supersymmetry performed in this  
48 channel using data taken by the ATLAS detector in 2015 and 2016, includ-  
49 ing an explanation of the theory and motivation behind the search, and a  
50 description of the LHC and the ATLAS detector. The remaining chapters  
51 are laid out as follows:

52 CHAPTER 2 outlines the Standard Model of Particle Physics and the  
53 benefits of extending it to include Supersymmetry, then continues on to  
54 introduce the specific models used in the search presented in later chapters.  
55 It also provides an overview of the process of generating MC for use in the  
56 ATLAS experiment.

57 CHAPTER 3 describes the LHC and its operation, including the magnet  
58 system, the preaccelerator complex, and some of the phenomenology of  
59 collisions at 13 TeV.

60 CHAPTER 4 contains descriptions of the many pieces of the ATLAS de-  
61 tector, and how they serve to detect particles coming from LHC collisions.  
62 ATLAS’s magnet and trigger systems are also discussed.

63 CHAPTER 5 details the process of reconstruction, the procedure by which  
64 the electric signals in the ATLAS detector are interpreted as particles to be  
65 used for analysis.

66 CHAPTER 6 presents a neural network designed to improve tracking in  
67 the ATLAS Pixel Detector, and describes the benefits of its implementation.

68 CHAPTER 7 lists the main backgrounds for the Supersymmetry search  
69 described in this thesis, and provides general ideas of how they can be  
70 reduced.

71 CHAPTER 8 outlines how objects are identified and selected for this anal-  
72 ysis, referencing many of the working points defined in Chapter 5.

73 CHAPTER 9 explains the analysis’s search strategy, defining signal, con-  
74 trol, and validation regions, and briefly describing how each contributes  
75 to the search.

76 CHAPTER 10 describes, for each of the backgrounds described in Chap-  
77 ter 7, how estimates of the Standard Model contributions to the signal  
78 region are performed.

79 CHAPTER 11 builds off of Chapter 11, and continues to detail how the  
80 uncertainties on each estimate are assessed.

81 CHAPTER 12 shows the results of the analysis, comparing expectations  
82 based on background estimates to the observed data.

<sup>83</sup> CHAPTER 13 provides interpretations of the results, and explains the  
<sup>84</sup> statistical procedure used to define exclusions on Supersymmetric models.

<sup>85</sup> CHAPTER 14 concludes with a summary of the results, and an outlook  
<sup>86</sup> for future searches.



87

## Part II

88

### THEORY AND MOTIVATION

89

This section describes the theoretical foundation for the analysis presented in [Part iv](#). It includes an overview of the Standard Model, including its phenomenology in a  $pp$  collider. The theory of Supersymmetry is explained, and the motivation for extending the Standard Model to include it is presented. In addition, this section includes an explanation of Monte Carlo generators and details about the specific form of Supersymmetry searched for in this analysis.

90

91

92

93

94

95

96



97

98 THEORY AND MOTIVATION

---

99 The Standard Model ([SM](#)) of particle physics represents all particles and in-  
100 teractions currently known. It is formulated using the principles of Quan-  
101 tum Field Theory, with the constraints of several symmetries and physical  
102 requirements to determine the rules for allowed interactions [3]. Devel-  
103 oped in the 1960s and 70s [4–6], it has been immensely successful at pre-  
104 dicting the existence of particles before their discovery, and has held up  
105 to many high-precision tests. Despite this success, it has several shortcom-  
106 ings. Though the [SM](#) is likely correct at the energies thus far probed, it  
107 may be missing key components that become more important at higher  
108 energies. Models supplementing the [SM](#) with additional particles and in-  
109 teractions are referred to as Beyond the Standard Model ([BSM](#)) theories.

110 One possible extension of the [SM](#) is Supersymmetry ([SUSY](#)), a theory  
111 which postulates an additional symmetry between bosons and fermions  
112 to the [SM](#), creating a spectrum of [SUSY](#) particles (sparticles) which interact  
113 with the particles of the [SM](#). This theory motivates the search performed  
114 in [Part iv](#) of this thesis, and its theoretical appeals are discussed in this  
115 section, along with specific models considered in the search.

## 116 2.1 THE STANDARD MODEL

117 The [SM](#) of particle physics describes the interactions of all of the particles  
118 currently known to exist, and consists of matter particles and force carriers,  
119 as well as the Higgs boson, which fits into neither category. This model has  
120 been unprecedentedly successful in predicting new particles and phenom-  
121 ena, including the prediction of the Higgs boson almost 50 years before its  
122 discovery in 2012, which completed the [SM](#).

123 The particles of the [SM](#) are divided into two categories: fermions and  
124 bosons [3]. The fermions comprise all the matter described by the [SM](#), and  
125 are spin- $\frac{1}{2}$  particles. The bosons are integer spin-particles, most of which  
126 are spin-1. These particles provide a mechanism to explain three of the four  
127 forces known to physics, with gravity still lacking a quantum formulation.  
128 The Higgs boson, the only spin-0 particle in the [SM](#), provides a mechanism  
129 for giving mass to the other particles. The full [SM](#), with the addition of the  
130 hypothetical graviton, is presented in [Figure 1](#).

131 2.1.1 *Matter*

132 The matter described by the [SM](#) is made up of fermions, spin- $\frac{1}{2}$  particles  
133 which can be broken into two groups, quarks and leptons. The leptons all  
134 interact weakly, while the quarks additionally interact strongly. Half the  
135 leptons as well as all quarks are electromagnetically charged.

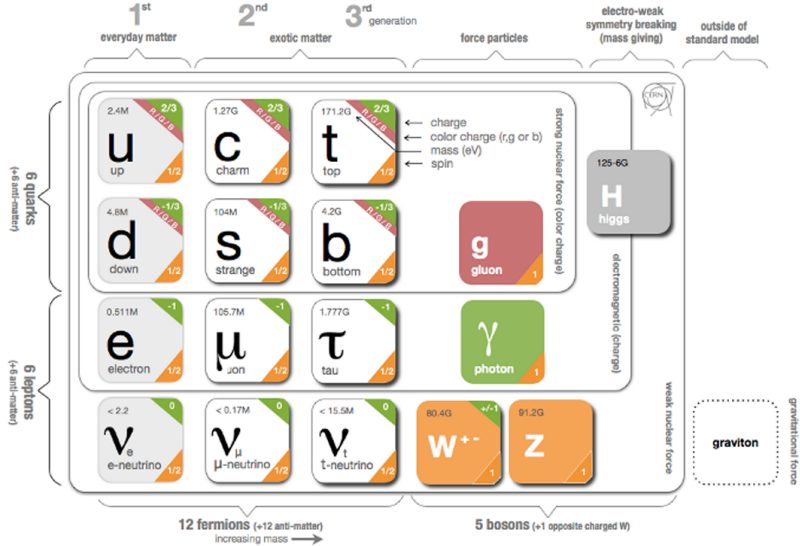


Figure 1: The Standard Model of particle physics, containing all known bosons and fermions, with the addition of the hypothetical graviton. [7]

### 136 2.1.1.1 Leptons

137 Leptons, as seen in the bottom left of Figure 1, exist in three generations,  
 138 each labeled by a flavor: electron, muon, and tau. In the case of the massive  
 139 leptons, these flavors are mass eigenstates, and the generations are placed  
 140 in an order based on increasing mass. Each massive lepton is negatively  
 141 electromagnetically charged and has a positively charged anti-particle.

142 The three neutrinos exist in the same flavors as the massive leptons, but  
 143 these flavor eigenstates do not correspond exactly to mass eigenstates [8].  
 144 As a consequence, neutrinos oscillate between flavors as they propagate  
 145 through space. These oscillations are the only evidence of neutrino mass,  
 146 which is bound from below by the mass splittings determined from the  
 147 oscillation and bound from above by cosmological limits on the universe's  
 148 mass density [9]. Though it is still uncertain if the masses of the neutrinos  
 149 follow the same hierarchy as the massive leptons, that expected ordering  
 150 is slightly experimentally preferred over the inverted hierarchy [10].

151 Unlike the massive leptons, the neutrinos are not electrically charged,  
 152 and it is not yet known whether each neutrino has a separate anti-particle,  
 153 or if it is its own antiparticle. Because they are not electromagnetically  
 154 charged, they can only interact weakly, making them extremely difficult  
 155 to detect. As a consequence of their ability to evade detection, neutrinos'  
 156 properties are nearly impossible to study with general purpose particle  
 157 detectors.

158 The SM conserves lepton number,  $L$ , which is defined as the number  
 159 of leptons minus the number of anti-leptons in a state, and can also be  
 160 defined for each lepton flavor. Though there are anomalies that appear in  
 161 second order SM interactions which could provide very small violations  
 162 of this conservation, it holds to great precision in experiment.  $\mu \rightarrow e\gamma$

163 branching ratios, for example, have been constrained to  $10^{-13}$  [11]. As a  
164 consequence of this conservation, the lightest massive lepton, the electron,  
165 is stable.

166 2.1.1.2 *Quarks*

167 Quarks, as seen in the top left of [Figure 1](#), are also electromagnetically  
168 charged particles that interact weakly, but are differentiated from the lep-  
169 tons by their strong interactions. They are also organized in three genera-  
170 tions ordered by mass, and come in pairs of *up*-type and *down*-type quarks,  
171 named after the lightest generation. Though the up quark is lighter than  
172 the down, that rule is reversed in the subsequent two generations. Up-type  
173 quarks are electromagnetically charged  $+\frac{2}{3}$ , while the down-type quarks  
174 are charged  $-\frac{1}{3}$ . Quarks are also charged under the strong interaction,  
175 whose three charges are often characterized by colors: red, green, and blue.  
176 Each quark has an anti-particle with the opposite charges.

177 These fractional charges and individual colors are never seen in nature  
178 because of the requirement (discussed further in [Section 2.1.2.2](#)) that stable  
179 particle states be color-neutral. To accomplish this, quarks can create two-  
180 particle bound states called *mesons* consisting of one quark and one anti-  
181 quark with the same color charge, or three-particle bound states of quarks  
182 or anti-quarks with the three different color charges, which are called  
183 *baryons*. The lightest color neutral state containing only quarks, the pro-  
184 ton ( $uud$ ), is stable. Extremely unstable bound states consisting of higher  
185 numbers of quarks can also exist, such as the pentaquark discovered in  
186 2015 at the [LHC](#). [12] Collectively, these multi-quark bound states are called  
187 *hadrons*.

188 Besides the proton, all hadrons are unstable, but their lifetimes have a  
189 wide range. Neutrons, for example, have a lifetime of nearly fifteen min-  
190 utes, and are stable enough to be involved in the formation of atoms.  
191 Charged pions ( $u\bar{u}$ ) and kaons ( $u\bar{s}$ ) have lifetimes on the order of 10 ns,  
192 which allows them to propagate several meters when traveling close to the  
193 speed of light. Most other hadrons decay effectively instantaneously when  
194 produced in a collision, with lifetimes much too short to be resolved by a  
195 particle detector. *B* mesons sit at the boundary between these two regimes,  
196 with lifetimes of approximately 1.5 ps, allowing them to propagate up to  
197 a few mm before decaying.

198 Like leptons, the number of quarks in a state is conserved, up to very  
199 small anomalies. However, because quarks cannot exist in an isolated state,  
200 that conservation is described in terms of baryon number (*B*) defined simi-  
201 larly to lepton number. Baryons are defined with  $B = 1$ , while anti-baryons  
202 have the quantum number  $B = -1$ . Mesons have  $B = 0$ .

203 2.1.2 *Forces*

204 The fermions in the previous section interact via the electromagnetic, weak,  
205 and strong forces. In a perturbative quantum field theory, interactions via

these forces are represented by mediating bosons. These force carriers interact only with particles charged with their force's quantum numbers. The photon, for example, interacts only with electromagnetically charged particles. Gluons, mediators of the strong force, interact only with color charged particles, quarks and gluons. All fermions are weakly charged and interact with the weak force's mediators, the  $W$  and  $Z$  bosons.

The formulation for each of these forces is developed by requiring that the SM Lagrangian be locally gauge invariant [8]. This can be accomplished by adding gauge fields to the Lagrangian, whose behavior under gauge transformations cancels out the gauge dependence of the free Lagrangian. However, adding a mass term for these fields reintroduces gauge dependence, so this mechanism only creates forces mediated by massless gauge bosons. The addition of the Higgs field provides mass terms for the weak gauge bosons (as well as other particles) without interfering with the gauge invariance.

The total gauged symmetry group for the SM is  $SU_C(3) \times SU_L(2) \times U_Y(1)$ , where  $C$  stands for color, the charge of the strong force,  $L$  stands for left, because the weak force is left-handed, and  $Y$  is the hypercharge quantum number, the charge of the unified electroweak force.

#### 2.1.2.1 The Electromagnetic Force

Electromagnetism provides the simplest example of a requirement of local gauge invariance generating a Lagrangian description of a force. Electromagnetism has one massless mediator, the photon, which interacts with all electromagnetically charged particles. What follows is a brief description of how enforcing this invariance generates a Lagrangian of the same form as the classical electromagnetic Lagrangian, which can be easily incorporated into the SM.

The particles in Section 2.1.1 are fermions, and so the Lagrangian describing their free propagation are Dirac Lagrangians and all follow the form

$$\mathcal{L} = i\bar{\psi}\gamma^\mu\partial_\mu\psi - m\bar{\psi}\psi. \quad (1)$$

Requiring that the free Lagrangians for these particles be invariant under a  $U(1)$  local gauge transformation,  $e^{iq\lambda(x)}$ , can be accomplished by adding a term to the Lagrangian which cancels the derivative term arising from  $\lambda$ 's dependence on  $x$ :

$$\mathcal{L} = i\bar{\psi}\gamma^\mu\partial_\mu\psi - m\bar{\psi}\psi - (q\bar{\psi}\gamma^\mu\psi)A_\mu \quad (2)$$

where  $A_\mu$  is a “gauge field” that transforms according to

$$A_\mu \rightarrow A_\mu + \partial_\mu\lambda. \quad (3)$$

<sup>241</sup> This vector field must also come with a free term,

$$\mathcal{L} = -\frac{1}{16\pi} F^{\mu\nu} F_{\mu\nu} + \frac{1}{8\pi} m_A^2 A^\nu A_\nu. \quad (4)$$

<sup>242</sup> The mass term for this field would not itself be invariant under the  
<sup>243</sup> transformation, but the field can simply be made massless to avoid this  
<sup>244</sup> problem. The final Lagrangian, then, is

$$\mathcal{L} = i\bar{\psi}\gamma^\mu \partial_\mu \psi - m\bar{\psi}\psi - \frac{1}{16\pi} F^{\mu\nu} F_{\mu\nu} - (q\bar{\psi}\gamma^\mu \psi) A_\mu \quad (5)$$

<sup>245</sup> which is precisely the original Lagrangian with the addition of terms  
<sup>246</sup> replicating the form of the Maxwell Lagrangian. In a quantized interpre-  
<sup>247</sup> tation, it describes a field that interacts with particles with non-zero elec-  
<sup>248</sup> tromagnetic charge  $q$  via interactions with a massless spin-1 boson, the  
<sup>249</sup> photon. In the quantum formulation, this charge is dependent on the  
<sup>250</sup> energy scale of the interaction, and the strength of the interaction is more  
<sup>251</sup> typically described by the electromagnetic coupling constant

$$\alpha_{EM}(\mu) = q(\mu)^2 / 4\pi. \quad (6)$$

<sup>252</sup> For the purpose of succinct notation, this Lagrangian is often rewritten  
<sup>253</sup> in terms of the *covariant derivative*

$$D_\mu = \partial_\mu + iq\lambda A_\mu \quad (7)$$

<sup>254</sup> which immediately cancels the gauge dependent term created by the  
<sup>255</sup> transformation. This mechanism is mathematically simple in the  $U(1)$  case,  
<sup>256</sup> but can be replicated for more complicated gauge transformations with  
<sup>257</sup> perturbative approximations.

### <sup>258</sup> 2.1.2.2 The Strong Force

<sup>259</sup> The strong force is generated by a similar process of requiring local gauge  
<sup>260</sup> invariance, but in this case, for a  $SU(3)$  transformation. The interactions of  
<sup>261</sup> the strong force are described by the theory of quantum chromodynamics,  
<sup>262</sup> which is given by the Lagrangian

$$\mathcal{L}_{strong} = -\frac{1}{4} G_{\mu\nu}^\alpha G^{\alpha\mu\nu} - \frac{1}{2} \bar{Q}_m \not{D} Q_m \quad (8)$$

<sup>263</sup> where the  $\alpha$  index runs from 1 to 8 and represents the eight force carriers  
<sup>264</sup> of the strong force, the gluons.  $m$  indexes the three quark generations, and  
<sup>265</sup>  $G_{\mu\nu}^\alpha$  is the field strength tensor, defined as

$$G_{\mu\nu}^\alpha = \partial_\mu G_\nu^\alpha - \partial_\nu G_\mu^\alpha + g_s f_{\beta\gamma}^\alpha G_\mu^\beta G_\nu^\gamma \quad (9)$$

266 where  $g_s$  is a function of the energy scale of the interaction  $\mu$ , and is  
 267 related to the strong coupling constant by

$$\alpha_s(\mu) = g_s(\mu)^2/4\pi. \quad (10)$$

268 The first term of the Lagrangian gives the gluon self-coupling interac-  
 269 tions, with terms involving 2, 3, and 4 gluon field terms. The 2-field por-  
 270 tion is simply the field strength tensor, but the other terms give gluon  
 271 self-interaction terms that can be described by the Feynman diagrams in  
 272 [Figure 2](#). Unlike photons, gluons are charged by the force they carry, mak-  
 273 ing self-interaction possible.

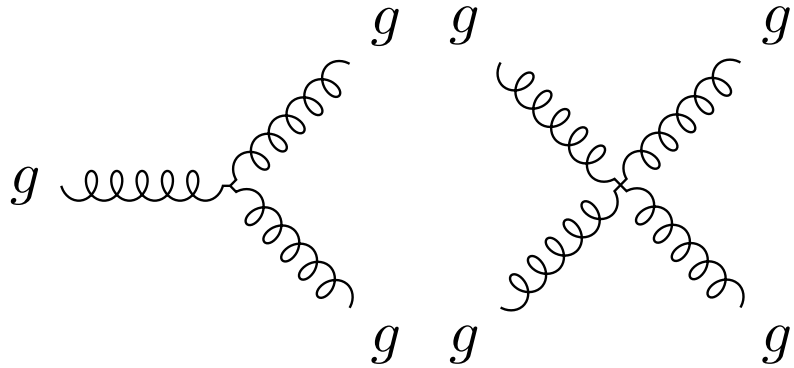


Figure 2: Gluon self coupling Feynman diagrams involving 3- and 4-gluon interactions.

274 In the second term,  $DQ_m$  is the covariant derivative acting on the quark  
 275 field. The quarks are in fact charged under all three forces, strong, electro-  
 276 magnetic, and weak, so the covariant derivative includes terms to make  
 277 each of the force's Lagrangians gauge invariant. Thus this term introduces  
 278 quark-boson interactions of four types, seen in [Figure 3](#). The quarks' cou-  
 279 pling to the gluon is the strongest, with the other couplings happening at  
 280 lower rates. The couplings to the  $W$  and  $Z$  bosons are described in [Sec-](#)  
 281 [tion 2.1.2.3](#).

282 Quantum Field Theory assumes that particles are essentially *free*, propa-  
 283 gating without interaction, and considers all interactions as perturbations  
 284 on a free theory. So long as multiple interactions are much less likely than  
 285 a single interaction, or put another way, so long as the coupling constants  
 286 for each force are much less than one, this perturbative approximation  
 287 is essentially correct. However, the strong coupling constant,  $\alpha_s$ , this as-  
 288 sumption is not always valid.  $\alpha_s$  changes as a function of the energy of an  
 289 interaction according to its renormalization group equation

$$\mu_R^2 \frac{d\alpha_s}{d\mu_R^2} = \beta(\alpha_s) = -(b_0\alpha_s^2 + b_1\alpha_s^3 + b_2\alpha_s^4 + \dots) \quad (11)$$

290 where  $\mu_R^2$  gives the renormalization scale, and each  $b_n$  gives a correction  
 291 to the  $\beta$ -function based on diagrams with  $n$  loops [[13](#)]. The overall negative

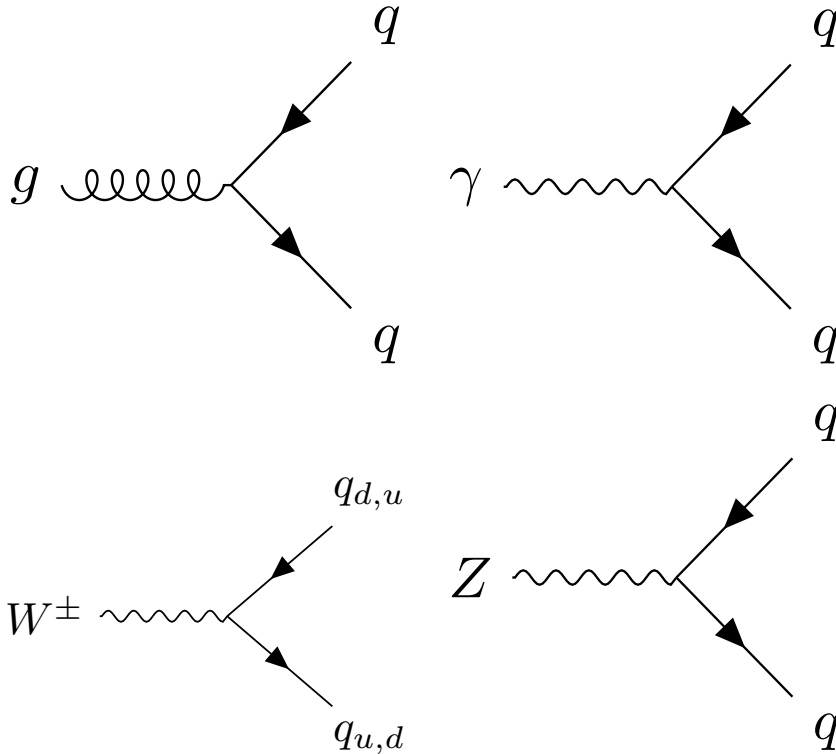


Figure 3: Quark couplings to the different types of gauge bosons. The  $q_{u,d}$  labels represent any up- or down-type quarks.

sign produces the unique energy dependence of  $\alpha_s$ , which becomes very small at high energy scales and asymptotically increases at low energies. Figure 4 shows this effect translated to distance scales, demonstrating that  $\alpha_s \ll 1$  and can be considered perturbatively at small distance scales, but at large distance scales  $\alpha_s$  approaches 1, and a perturbative approximation can no longer be used. Instead, for distances larger than  $10^{-16}$ , the colorless hadrons introduced in Section 2.1.1.2 must be used to describe strong interactions.

The boundary between these regimes is referred to as  $\Lambda_{QCD}$  and differentiates energies at which Quantum Chromodynamics (QCD) can be considered perturbatively and those at which it cannot. The LHC is capable of producing individual high-energy quarks in its hard scatterings, but they lose energy as they radiate gluons, eventually entering the energy regime below  $\Lambda_{QCD}$ . The transition between these two regimes is complex, and dictates the way that strongly charged particles appear in the ATLAS detector. This is described in more detail in Section 2.1.3.1.

### 2.1.2.3 The Electroweak Force

A similar process, using an  $SU(2)$  gauge transformation, can produce a Lagrangian that would suffice to describe the  $W$  and  $Z$  bosons of the SM, if only they were massless. However, they are not, so an alternate mechanism is needed to generate massive force carriers.

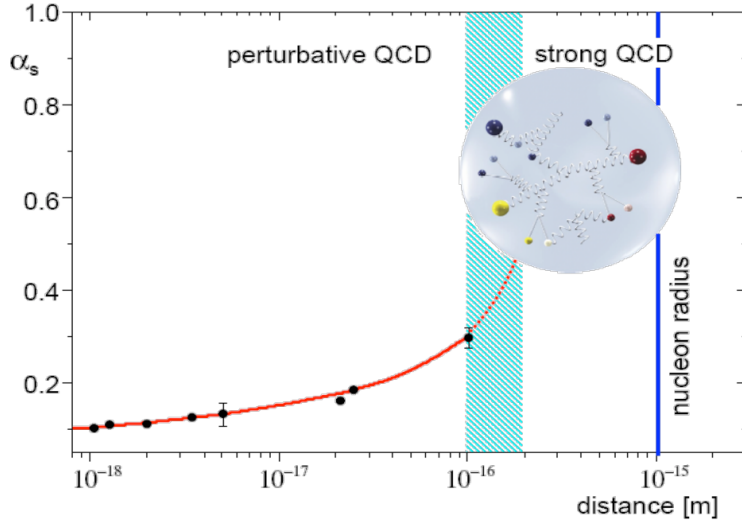


Figure 4: The running of the strong coupling constant,  $\alpha_s$ . [14]

313 Before a mechanism for their masses was understood, and before they  
 314 were discovered, the large masses of the  $W$  and  $Z$  bosons were proposed  
 315 in order to unify the electromagnetic and weak forces into the electroweak  
 316 force [8]. The large masses were crucial to explain the discrepancy in the  
 317 strength of the two forces.

318 The unified electroweak force is generated by a symmetry group written  
 319 as  $SU(2)_L \times U(1)_Y$ , where  $L$  refers to left-handed fields, and  $Y$  is the  
 320 quantum number for *hypercharge*. This new quantum number is defined as

$$Y = 2(Q - T_3) \quad (12)$$

321 where  $Q$  is the electromagnetic charge and  $T_3$  is the third component  
 322 of weak isospin  $T$ , the quantum number relating to the weak interaction.  
 323 In the unified theory, quark and lepton singlets interact according to their  
 324 hypercharge, and left-handed quarks and leptons, grouped according to  
 325 their generation, interact as doublets.

326 The gauge bosons resulting from this unified theory include a triplet,  $W$ ,  
 327 with coupling  $g_W$ , and a singlet field  $B$ , with coupling  $g'/2$ . However, the  
 328 electroweak symmetry is broken, and mixing between these states occurs.  
 329 Rewritten in their mass basis, the standard electroweak force carriers are  
 330 produced:  $W^\pm$ , two states with identical coupling resulting from the first  
 331 two states of the  $W$  triplet, the  $Z$  and the photon field  $A$  resulting from  
 332 the mixing of the last  $W$  state and  $B$ .

333 The electroweak Lagrangian is much more complicated than the strong  
 334 Lagrangian, and can be divided into several terms:

$$\mathcal{L}_{electroweak} = \mathcal{L}_{gauge} + \mathcal{L}_{fermions} + \mathcal{L}_{Higgs} + \mathcal{L}_{Yukawa}. \quad (13)$$

<sup>335</sup> The first term can be written as follows

$$\mathcal{L}_{gauge} = -\frac{1}{4}W^{a\mu\nu}W_{\mu\nu}^a - \frac{1}{4}B^{\mu\nu}B_{\mu\nu} \quad (14)$$

<sup>336</sup> where the  $a$  indices are numbered 1 through 3 and indicate the genera-  
<sup>337</sup> tors of  $SU(2)$  which are written

$$W_{\mu\nu}^a = \partial_\mu W_\nu^a - \partial_\nu W_\mu^a + g_2 \epsilon_{abc} W_\mu^b W_\nu^c \quad (15)$$

<sup>338</sup> The gauge portion of the Lagrangian then generates interaction terms  
<sup>339</sup> of between the gauge fields, which when rewritten in terms of the mass-  
<sup>340</sup> eigenstate basis, generates interactions between three gauge bosons, like  
<sup>341</sup> the ones in [Figure 5](#), as well as interactions between four gauge bosons.

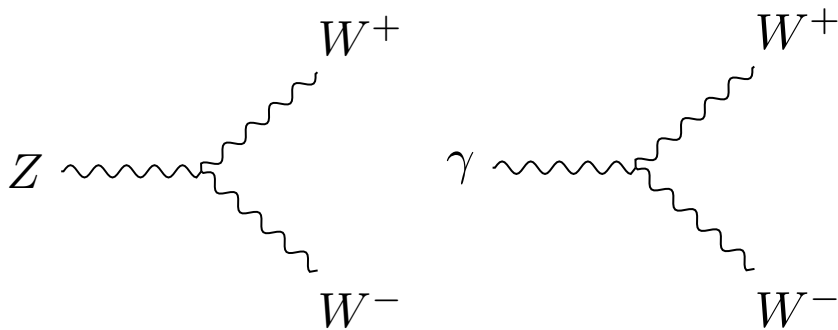


Figure 5: Feynman diagrams of trilinear gauge couplings in the [SM](#).

<sup>342</sup> The fermion portion of the Lagrangian is written as

$$\begin{aligned} \mathcal{L}_{fermion} = & -\frac{1}{2}\bar{L}_m D \not L_m - \frac{1}{2}\bar{Q}_m D \not Q_m \\ & -\frac{1}{2}\bar{U}_m D \not U_m - \frac{1}{2}\bar{D}_m D \not D_m \\ & -\frac{1}{2}\bar{E}_m D \not E_m \end{aligned} \quad (16)$$

<sup>343</sup> where  $L$  is the left-handed lepton doublet,  $Q$  is the left-handed quark  
<sup>344</sup> doublet,  $U$  is the right-handed singlet for up-type quarks,  $D$  is the same for  
<sup>345</sup> down-type quarks, and  $E$  is the right-handed singlet for electrons, muons  
<sup>346</sup> and taus. Each of these fields has an implicit index running from 1 to 3  
<sup>347</sup> to represent the three generations. The covariant derivative in each term  
<sup>348</sup> includes terms including all the gauge fields the fermion is charged un-  
<sup>349</sup>der. Unlike the other forces, the weak force treats left- and right-handed  
<sup>350</sup> fermion fields differently; it only interacts with the left-handed fields, so  
<sup>351</sup> only the first two terms' covariant derivatives include  $W$  terms. The first  
<sup>352</sup> term in this Lagrangian, for example, produces weak interactions depicted  
<sup>353</sup> in [Figure 6](#). The  $Z$  bosons, because they represent a mixing between the  
<sup>354</sup>  $W$  and  $B$  fields, can interact with right-handed leptons and quarks, but  
<sup>355</sup> do so with different strengths than left-handed particles.

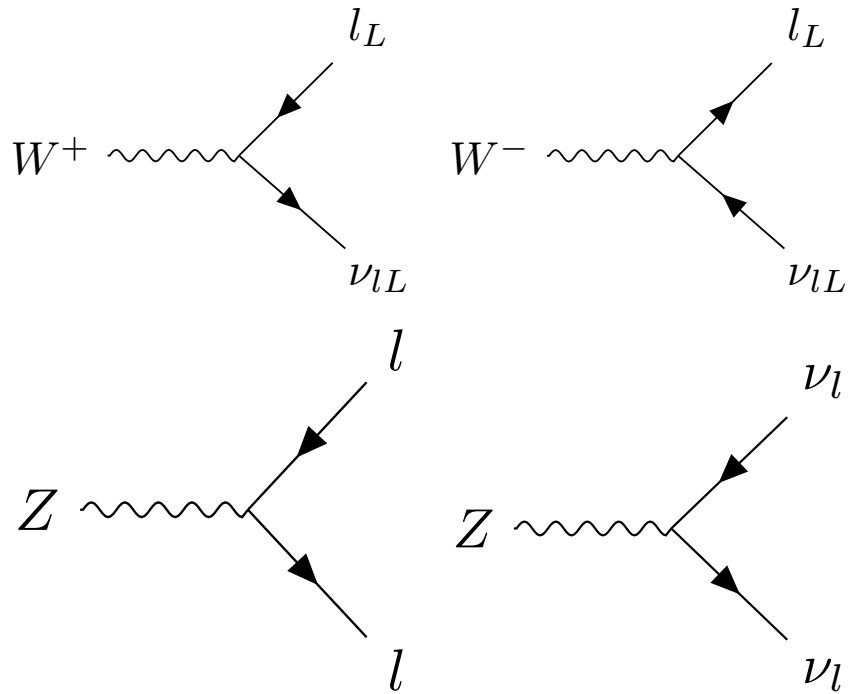


Figure 6: Feynman diagrams of weak couplings to leptons in the SM.

356     No right-handed term appears for the neutrino field, because only left-  
 357     handed neutrinos and right-handed anti-neutrinos have been observed.  
 358     However, because neutrinos have non-zero mass, their chirality can change  
 359     with frame boosts, which complicates any claim that right-handed neutrili-  
 360     nos do not exist [3]. It is possible that neutrinos are their own antiparticle,  
 361     making the right-handed anti-neutrino the solution to this problem. It's  
 362     also possible that very massive right-handed neutrinos do exist, and sim-  
 363     plly haven't been discovered yet.

364     The remaining two terms of the electroweak Lagrangian are related to  
 365     the Higgs field, which is the source of electroweak symmetry breaking.

#### 366     2.1.2.4    *The Higgs Mechanism*

367     The Higgs mechanism presents a way to generate a mass term for the  
 368     electroweak gauge bosons. It is a scalar field, with a Lagrangian

$$\mathcal{L}_{Higgs} = \frac{1}{2}(\partial_\mu \phi)^*(\partial^\mu \phi) + \frac{1}{2}\mu^2 \phi^* \phi - \frac{1}{4}\lambda^4 (\phi^* \phi)^2 \quad (17)$$

369     where  $\phi$  is a complex scalar field,  $\phi = \phi_1 + i\phi_2$ . This looks very similar to  
 370     a standard scalar field Lagrangian, but the signs on the mass and interac-  
 371     tion terms are reversed, implying an imaginary mass term. However, this  
 372     isn't a good interpretation of the Lagrangian, because it differs from all  
 373     previously considered Lagrangians in one important way: its ground state  
 374     does not occur at  $\phi = 0$ . Because quantum field theory is perturbative, its

375 validity only holds when expanded around a ground state, which, when  
376 calculated for this Higgs Lagrangian, must satisfy

$$\phi_1^2 + \phi_2^2 = \frac{\mu^2}{\lambda^4}. \quad (18)$$

377 The original Lagrangian can then be rewritten in terms of a field  $v +$   
378  $H(x)$  centered around the ground state with energy called the vacuum  
379 expectation value defined as.

$$v = \frac{\mu}{\lambda^2}. \quad (19)$$

380 This rewriting produces a Lagrangian with a non-imaginary mass. How-  
381 ever, in an effect called *spontaneous symmetry breaking*, the original  $SO(2)$   
382 rotational symmetry of the Lagrangian is lost, resulting only in a  $U(1)$   
383 rotational symmetry; the Lagrangian is invariant under a phase transfor-  
384 mation.

385 As in [Section 2.1.2.1](#), it is possible to make the Lagrangian invariant  
386 under a local  $U(1)$  transformation,  $\phi \rightarrow e^{i\theta(x)\phi}$  by adding a massless gauge  
387 field  $A^\mu$  and using the covariant derivative. Due to the many cross terms  
388 from the non-zero ground state, terms for the mass of one of the scalar  
389 bosons as well as the gauge field appear, leaving only one massless scalar  
390 boson. This massless boson, it turns out, can be completely removed from  
391 the theory via local  $U(1)$  transformations, ultimately producing a theory  
392 with one massive scalar (the Higgs) and a massive gauge field ( $W$ ).

393 The Higgs interaction with the weak gauge bosons also creates cou-  
394 plings between the particles, which can be seen in [Figure 7](#). There are also  
395 Higgs self-interaction terms included in the Lagrangian, producing vertices  
396 describing 3- and 4-Higgs interactions.

397 The remaining piece of the Lagrangian,  $\mathcal{L}_{Yukawa}$  describes the Higgs  
398 field's interactions with the fermions of the [SM](#), and can be written as

$$\mathcal{L}_{Yukawa} = -\Gamma_{mn}^e \bar{L}_m \phi E_n - \Gamma_{mn}^u \bar{Q}_m \phi U_n - \Gamma_{mn}^d \bar{Q}_m \phi D_n + h.c. \quad (20)$$

399 where *h.c.* is the hermitian conjugate term, and the  $\Gamma$  matrices are in-  
400 dexed by generation, and, when diagonalized, are proportional to the  
401 masses of the fermions. The Higgs field's vacuum expectation value pro-  
402 duces terms that look like fermion mass terms. Additionally, terms that  
403 couple the fermions to the Higgs field are produced, with each fermion's  
404 coupling proportional to its mass, according to

$$g_f = \sqrt{2} \frac{m_f}{v} \quad (21)$$

405 where  $m_f$  is the mass of the fermion. Feynman diagrams for lepton and  
406 quark terms can be seen in [Figure 8](#).

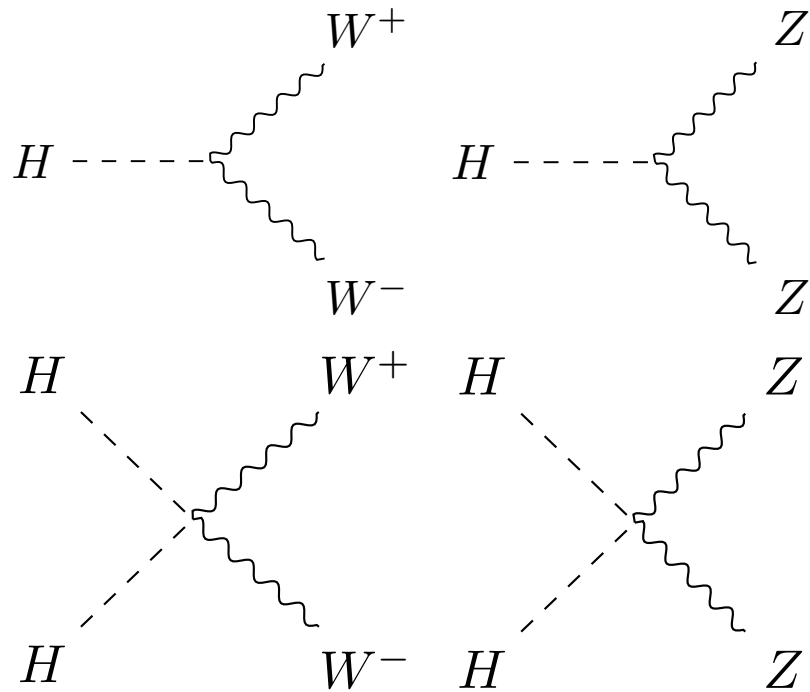


Figure 7: Feynman diagrams demonstrating Higgs couplings to the weak gauge bosons in the SM.

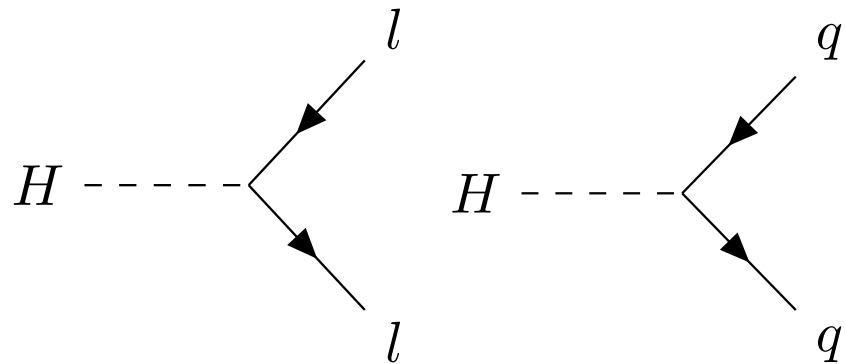


Figure 8: Feynman diagrams showing Higgs couplings to fermions in the SM.

#### 407 2.1.3 Phenomenology of Proton-Proton Collisions

408 As discussed in [Chapter 3](#), the [LHC](#) collides bunches of high-energy protons, and the interactions of these protons' constituent quarks produce the wide array of particles seen in the [ATLAS](#) detector. The [LHC](#) typically cites its energy in terms of  $\sqrt{s}$ , the center of mass energy of protons in the two colliding beams, which in Run 2 is 13 TeV. However, because the proton is not fundamental, this energy is divided among many particles that make up the proton.

415 To first order, a proton consists of three quarks: two up quarks and one down quark, held together by gluons. However, a real quantum mechanical system is much more chaotic; in addition to these three quarks, called

418 valence quarks, there are many others popping into and out of existence.  
 419 These additional quarks are called *sea* quarks and can also carry fractions  
 420 of the proton's energy.

421 The particles inside the proton can have a wide range of energies de-  
 422 pending on the internal dynamics at the moment of the collision. These  
 423 cannot be predicted exactly, but probabilistic models called Parton Dis-  
 424 tribution Functions (PDFs) describe the likelihood of any given configuration.  
 425 These functions are determined using data from hard scattering experi-  
 426 ments and give probabilistic estimates for how often a given type of parti-  
 427 cle appears with a fraction  $x$  of the total proton energy, as seen in Figure 9.

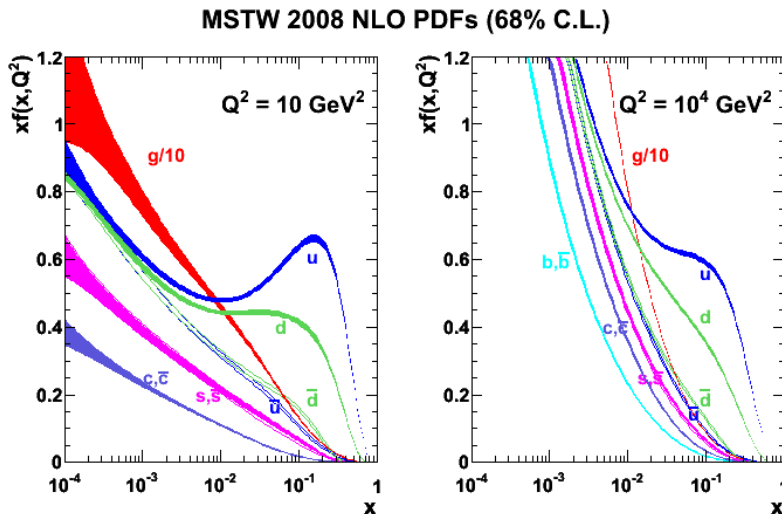


Figure 9: 2008 MSTW PDFs for various particle types given as a function of  $x$  and  $Q^2$ , the square of the parton-parton momentum transfer. [15]

428 A classical proton model would suggest that each valence quark carries  
 429 about one-third of the total proton energy. In practice, they each typically  
 430 account for less than a third of the total energy, with the remaining energy  
 431 divided among the many sea quarks and gluons. Thus, in a proton-proton  
 432 collision, the initial particles rarely have more than a third of the beam  
 433 energy, and often have a much lower energy resulting from the interaction  
 434 of sea quarks.

435 These PDFs are used at the LHC to calculate the probability for a given  
 436 process to occur, or its *cross-section*. The cross-section for a process to occur  
 437 with a two-proton initial state is given by

$$\sigma(P_1, P_2 \rightarrow X) = \sum_{i,j} \int_0^1 dx_1 dx_2 f_i(x_1, Q^2) f_j(x_2, Q^2) \hat{\sigma}(x_1 P_1, x_2 P_2, Q^2) \quad (22)$$

438 where  $i$  and  $j$  are indices representing the partons within proton 1 and  
 439 2 respectively,  $x_{i,j}$  gives these partons' momentum fraction, and  $f_{i,j}$  gives  
 440 their PDFs.  $\hat{\sigma}$  gives the cross-section for a process going from partons to  $X$ ,  
 441 also referred to as the *matrix element*, and  $Q^2$  gives the energy scale of this  
 442 hard scattering of partons.

Matrix elements, in an ideal world, would include every possible Feynman diagram that describe the initial partons producing a given final state. In practice, the calculation of these diagrams can become very complicated when more and more loops are allowed. The simplest calculations, which include diagrams without any loops, are referred to as Leading Order (**LO**), while calculations including diagrams with one loop are called Next to Leading Order (**NLO**), and additional **N**s can be added to describe more complex calculations.

**Figure 10** shows cross-sections for many **SM** processes as a function of energy, demonstrating how processes involving high-mass objects have increasingly large cross-sections as the energy of the collider increases. In the analysis discussed in **Part iv**, the most important **SM** backgrounds are from top quarks, Z bosons, and diboson processes (ZZ, WW, and WZ). Though Z boson production has the highest cross-section of those processes, it contributes the least to the background of the search because of the specific requirements made on events designed to reduce **SM** backgrounds. Details on these backgrounds and how they can appear as signal-like events are given in **Chapter 7**.

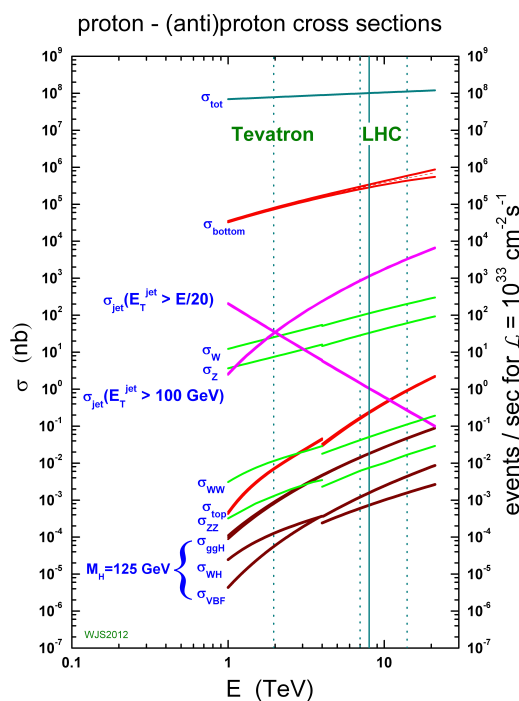


Figure 10: Cross-sections for many **SM** processes as a function of  $\sqrt{s}$  [16].

#### 2.1.3.1 Production of Jets in the **ATLAS** Detector

For most particles, the output of the hard scattering process is similar to the objects observed by a detector; electrons, photons, and muons emerging from final states are all observed as they pass through sensitive materials. There are exceptions: particles can radiate energy as they travel

466 through the detector and photons can convert into electron-positron pairs,  
 467 but in most cases, these final state particles can be directly observed. For  
 468 color-charged particles, however, this is not the case.

469 As discussed in [Section 2.1.2.2](#), quarks and gluons are strongly charged,  
 470 and the coupling constant of the strong force increases asymptotically at  
 471 large distance scales. As a consequence, colored particles undergo a pro-  
 472 cess called *fragmentation*. Rather than continuing to propagate in a colored  
 473 state, it is energetically preferable for high energy quarks and gluons pro-  
 474 duced in hard scatterings to radiate additional colored particles, which can  
 475 then be used to form colorless bound states. First, a process called *parton*  
 476 *showering* occurs, in which many new colored particles are radiated from  
 477 the original, creating a conic spray of particles along the original particle's  
 478 trajectory. This process repeats until the particles' energies reach the scale  
 479 of hadronic masses, about 1 GeV. Next, these particles *hadronize*, forming  
 480 composite particles that can propagate without interacting strongly.

481 The resulting spray of hadrons is called a *jet*, and it is jets, rather than in-  
 482 dividual quarks or gluons, that are observed by particle detectors. Group-  
 483 ing these particles into a jet is a non-trivial process, and is discussed in  
 484 [Section 6.4](#).

485 Jets don't always come directly from the hard scattering process; colli-  
 486 sions in the [LHC](#) often contain additional jets resulting from *initial and final*  
 487 *state radiation*. In these processes, either the initial partons radiate energy  
 488 (typically in the form of a gluon) or the products of the hard scattering  
 489 process radiate additional colored particles before fragmentation occurs.

#### 490 2.1.4 Problems in the Standard Model

491 Although the [SM](#) is a self-consistent theory that describes to great accuracy  
 492 all of the particles and forces it includes, it does have certain shortcomings.  
 493 The most glaring is the omission of gravity. Though the force is well un-  
 494 derstood at large scales via the theory of General Relativity, no satisfying  
 495 quantum description of gravity has been accepted, much less proven. The  
 496 Planck scale, the energy scale at which gravitational interactions become  
 497 large enough that no sound theory can ignore gravity, is at about  $10^{19}$   
 498 GeV, 16 orders of magnitude above the electroweak scale, so the exclusion  
 499 of gravity from the [SM](#) is unlikely to directly affect [LHC](#) physics.

500 Another clear omission of the [SM](#) is Dark Matter ([DM](#)), so named for its  
 501 lack of electromagnetic interactions. This type of matter was first identi-  
 502 fied in 1933 through the observation of galactic rotation curves [[17](#)]. The  
 503 speed of rotation indicated both that there was more mass in the system  
 504 than could be accounted for by observations made directly of the galaxy,  
 505 and that this additional matter was distributed in a halo, not a disk like the  
 506 typical luminous matter. This effect can be seen in [Figure 11](#), which demon-  
 507 strates that the observed galactic density as a function of radius does not  
 508 match the expected density from the luminous galactic disk. Since then, ev-  
 509 idence for [DM](#) has been observed in colliding clusters [[18](#)], measurements  
 510 of the cosmic microwave background [[19](#)], and in many more rotational

511 curves, but the particles that form DM have never been directly detected  
 512 or seen at a particle accelerator. As a consequence, very few details are  
 513 known about the nature of this matter, only its density throughout the  
 514 universe and that it does not interact strongly or electromagnetically.

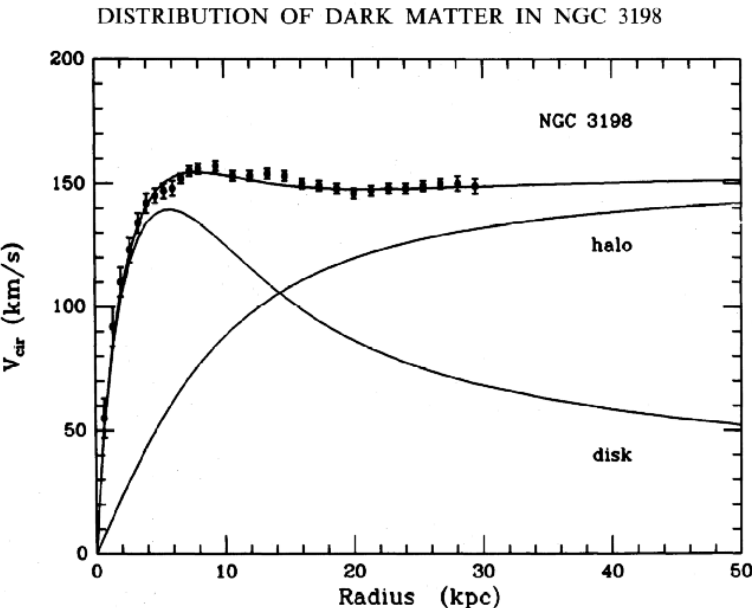


Figure 11: Galactic rotation curve of velocity as a function of radius in NGC 3198. Included is the observed data, as well as the expected velocity distribution from a disk-shaped galaxy corresponding to the expected density from electromagnetic observations. Another curve corresponding to a halo-shaped matter distribution is superimposed, and the halo and disk are summed and fit to the data. [20]

515 Beyond the omissions of gravity and DM, there are several aesthetic problems  
 516 with the SM - ones that could have no solution, but seem to suggest  
 517 that the current SM are missing some pieces. The first is the sheer number  
 518 of parameters in the SM. There are 26 independent parameters determin-  
 519 ing the mass of the particles and all the couplings between them. Besides  
 520 the rough grouping of fermions into generations, there seems to be no or-  
 521 der to masses of particles, and no way to predict many of the masses or  
 522 couplings.

523 In the past, large numbers of seemingly unrelated parameters have indi-  
 524 cated that a theory has a more fundamental form at shorter distance scales.  
 525 The large number of elements, it turned out, could be explained by differ-  
 526 ent groupings of three particles, the proton, neutron, and electron. Later,  
 527 the menagerie of hadrons became so large that a similar re-imagining of  
 528 what was fundamental took place, and the theory of quarks gave an or-  
 529 der to the many mesons and baryons [21]. This pattern leaves physicists  
 530 suspicious of any theory with too many particles and free parameters, sug-  
 531 gesting that perhaps, at a higher energy, there is a simpler model that can  
 532 unify many of the seemingly disparate elements of the SM.

533 In addition, some of these seemingly independent parameters have sus-  
 534 picious symmetry. The Higgs mass, for example, has been measured to be  
 535  $125.7 \pm 0.4$  GeV[13]. This mass is the sum of the bare mass, the one that ap-  
 536 pears in the Lagrangian, and quantum corrections from interactions with  
 537 other particles, which are proportional to the square of the particles' mass.  
 538 Since new physics must exist at the Planck scale to account for gravity,  
 539 these corrections could be up to 35 orders of magnitude larger than the  
 540 Higgs mass. Though the bare mass could theoretically cancel out this mas-  
 541 sive correction, these parameters should be independent, and the odds  
 542 that they would be precisely the same to 35 places are very, very small.  
 543 This near-exact canceling is often called *fine-tuning*, an undesirable trait in  
 544 a theory which suggests that some more fundamental symmetry has been  
 545 missed. A *natural* solution, one free of this fine-tuning, is sought to resolve  
 546 this SM problem.

## 547 2.2 SUPERSYMMETRY

548 Supersymmetry (SUSY) was proposed and developed in the 1970s to give  
 549 solutions to many of these SM shortcomings [22–24]. The theory works  
 550 by introducing a fermionic symmetry to the SM, in addition to the usual  
 551 spacetime symmetries of translations, rotations, and changes of Lorentz  
 552 frame. The combination of the usual spacetime with this fermionic dimen-  
 553 sion is called a *superspace*. Rotations in this dimension result in a particle's  
 554 spin changing by  $1/2$ , turning a spin- $1/2$  fermion into a spin- $0$  particle,  
 555 for example. As a consequence, this symmetry requires the existence of  
 556 many new particles - a bosonic *sfermion* for each fermion of the SM and a  
 557 fermionic *gaugino* for each of the gauge bosons. These superpartners of SM  
 558 particles should have identical quantum numbers to the original particle,  
 559 except for their spins. Table 1 shows the SM particles and their superpart-  
 560 ners.

561 If the theory is symmetric under these fermionic rotations, these particle-  
 562 sparticle pairs can be described by a single *superfield*, which simultane-  
 563 ously describes the behavior of both SM and SUSY particles in the super-  
 564 space. However, this completely symmetric behavior is untenable given  
 565 basic observations of matter in the universe. For example, if there were a  
 566 *selectron* (the superpartner of the electron,  $\tilde{e}$ ), with identical mass to the  
 567 electron, it would have been detected long ago. In fact, such a particle  
 568 would fundamentally change atomic structure, with the bosonic selectrons  
 569 capable of piling into the ground state of an atom, and removing all the  
 570 interesting valence-shell interactions of electrons that determine molecular  
 571 structure. Thus, if SUSY does exist, the symmetry must be broken, so that  
 572 the superpartners have much higher masses than the original SM particles.

### 573 2.2.1 The Minimal Supersymmetric Standard Model

574 The Minimal Supersymmetric Standard Model (MSSM) was designed to be  
 575 the simplest supersymmetric extension of the SM that remains self consis-

Names	sparticles	particles	$SU(3)_C, SU(2)_L, U(1)_Y$
squarks, quarks	$Q$	$(\tilde{u}_L \tilde{d}_L)$	$(u_L d_L)$
	$\tilde{u}$	$\tilde{u}_R^*$	$u_R^\dagger$
	$\tilde{d}$	$\tilde{d}_R^*$	$d_R^\dagger$
sleptons, leptons	$L$	$(\tilde{\nu} \tilde{e}_L)$	$(\nu e_L)$
	$\tilde{e}$	$\tilde{e}_R^*$	$e_R^\dagger$
Higgs, higgsinos	$H_u$	$(\tilde{H}_u^+ \tilde{H}_u^0)$	$(H_u^+ H_u^0)$
	$H_d$	$(\tilde{H}_d^0 \tilde{H}_d^-)$	$(H_d^0 H_d^-)$
gluino, gluon	$\tilde{g}$	$g$	$(8, 1, 0)$
winos, $W$ bosons	$\tilde{W}^\pm \tilde{W}^0$	$W^\pm W^0$	$(1, 3, 0)$
bino, $B$ boson	$\tilde{B}^0$	$B^0$	$(1, 1, 0)$

Table 1: Supermultiplets of supersymmetric and SM particles. Sfermions, on the first five rows, are all spin-0. Higgsinos and gauginos are all spin-1/2. Three sets of each fermion's supermultiplet exist, one for each generation. [25]

tent, and it results in the particles seen in Table 1[25]. The formulation of the MSSM begins by introducing a second Higgs doublet to account for the different masses of the sparticles. As with the SM Higgs, electroweak symmetry breaking results in the loss of degrees of freedom, and only five of the original eight states remain, the lightest of which,  $h^0$ , can be interpreted as the SM Higgs already discovered. There are two remaining neutral states,  $A^0$  and  $H^0$ , as well as two charged Higgses,  $H^\pm$ .

The neutral Higgs states mix with the neutral gauge bosons, while the charged Higgs states mix with the charged gauge bosons, producing a series of states labeled only by their charge and the order of their masses. The neutral states, collectively called the neutralinos, are identified from lightest to heaviest,  $\tilde{\chi}_1^0, \tilde{\chi}_2^0, \tilde{\chi}_3^0$ , and  $\tilde{\chi}_4^0$ . The charged states, referred to as charginos, are similarly called  $\tilde{\chi}_1^\pm$  and  $\tilde{\chi}_2^\pm$ .

The MSSM introduces many new interactions between SM particles and sparticles. Though these don't represent all possible interactions, a general rule is that any SM vertex can have two interacting particles replaced with their sparticle equivalents, and this vertex will be part of the MSSM. Figure 12 gives two examples of such vertices.

In addition to these interactions, there are several terms that appear in the MSSM Lagrangian that violate the  $B$  and  $L$  conservation observed in the SM. In fact, these terms violate  $B - L$ , which, unlike  $B$  and  $L$  conservation individually, does not have even small violations in the SM. These superpotential terms appear as follows

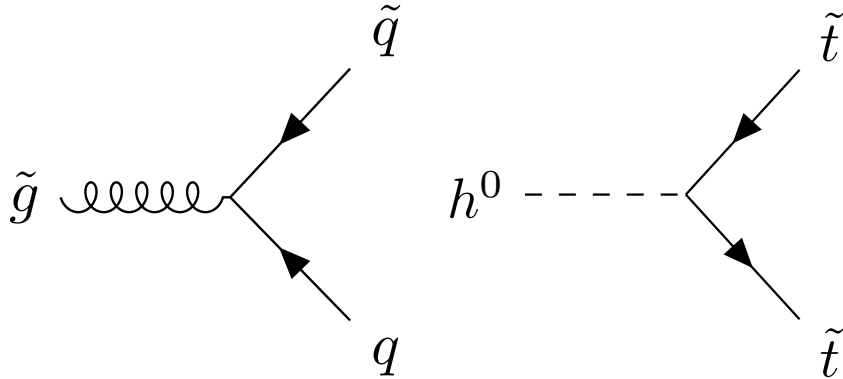


Figure 12: Two example vertices allowed by the [MSSM](#).

$$W_{\Delta L=1} = \frac{1}{2} \lambda^{ijk} L_i L_j \bar{e}_k + \lambda'^{ijk} L_i Q_j \bar{d}_k + \mu'^i L_i H_u \quad (23)$$

$$W_{\Delta B=1} = \frac{1}{2} \lambda''^{ijk} \bar{u}_i \bar{d}_j \bar{d}_k. \quad (24)$$

Because there are very strong limits on non-conservation of  $B - L$  from proton decay experiments, these terms present a challenge for the [MSSM](#). It would be possible, of course, to simply tune the  $\lambda$  parameters to be small enough to fit within experimental constraints, but these terms can also be eliminated by introducing a new conserved quantity,  $R$ -parity. It is defined by

$$P_R = -1^{3(B-L)+2s} \quad (25)$$

where  $s$  is the spin of the particle. Requiring that all terms in the Lagrangian have a multiplicative  $P_R$  of 1 excludes the terms in [Equation 24](#), removing the interactions that would lead to proton decay. All [SM](#) particles are  $R$ -parity even, while the sparticles are  $R$ -parity odd, so the conservation of  $R$ -parity can translate into a conservation of number of particles and sparticles. As a consequence, massive sparticles typically decay through a chain of lighter sparticles, emitting [SM](#) particles along the way.

### 2.2.2 Solutions to Standard Model Problems

Perhaps the most compelling consequence of [SUSY](#) comes from  $R$ -parity, which, through the formation of a new quantum number unique to sparticles, requires the Lightest Supersymmetric Particle ([LSP](#)) to be stable. This stable particle, if it is not electromagnetically charged, provides an excellent candidate [DM](#) particle. The lightest neutralino, for example, is a viable [DM](#) candidate because it does not interact electromagnetically or strongly, a constraint required due to measurements of the relic density of [DM](#) in the universe. An interaction cross-section higher than what's

expected for weak interactions would have led the DM particle and its anti-particle to annihilate at lower densities, leaving a much smaller amount of DM in the universe than what is observed today [26].

Many believe that a complete SM should include a unification of the three forces, as electromagnetism and the weak force have already been unified. This requires that at some higher energy, the coupling constants of all three forces merge. However, in the SM, the coupling constants come close to aligning, but don't perfectly cross. With the addition of MSSM particles with masses at the TeV scale, the alignment is near perfect, as shown in Figure 13. This may be a mathematical coincidence, but it's very compelling to those physicists who believe that *grand unified theory* must exist.

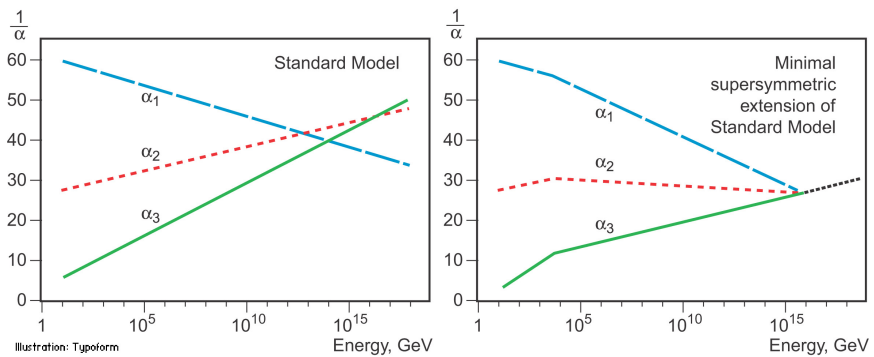


Figure 13: Running of the strong, weak, and electromagnetic coupling constants for the SM (left) and MSSM (right). [27]

SUSY also has the potential to solve the naturalness problem in the SM. In the SM, the massive amounts of fine tuning are required to cancel the quadratic corrections to the Higgs mass that result from loops involving, most importantly, the top quark. In the MSSM, a similar loop involving the stop quark (the vertex for which is depicted in Figure 12) contributes to the Higgs mass with the opposite sign, making it possible to naturally cancel the corrections without fine tuning. However, the larger the mass difference between the top quark and stop quark, the larger the remaining correction when the two terms cancel. Consequentially, to preserve a reasonable degree of naturalness (and here the definition of "reasonable" is subject to some debate), the stop quark should appear at masses not too much larger than the top's, at approximately the TeV scale.

This naturalness mass limit, as well as the unification of couplings, make the argument for searching for SUSY at the LHC particularly compelling, as the LHC is the first collider capable of producing particles at the TeV scale. As new exclusions on SUSY are set, the remaining phase space becomes slightly less natural. But there is no shortage new SUSY models with un-excluded parameters, which are continually proposed as new limits are created.

652 2.2.3 *Simplified Models of Supersymmetry*

653 There are many different theorized models of [SUSY](#), with different mechanisms  
 654 for breaking the symmetry. The [MSSM](#) has 120 free parameters, with  
 655 complex interactions that determine the mass hierarchy and interaction  
 656 rates of the sparticles. From an experimental point of view, the details of  
 657 these theories and the exact way the hierarchies are generated are less  
 658 relevant to a search than their outputs.

659 Simplified models, which are typically inspired by more complete theories,  
 660 are used to tune the observables of a model more directly. These models  
 661 each consist of one production and decay diagram, with the masses  
 662 and branching ratios of the particles free to be tuned directly. In a more  
 663 complete theory, it is instead necessary to modify more fundamental pa-  
 664 rameters like the symmetry breaking scale. A change like this impacts the  
 665 properties of all the sparticles, but the details of its impact are model de-  
 666 pendent. The simplified models allow for relatively model independent  
 667 interpretations that can be reinterpreted in the context of a more complete  
 668 [SUSY](#) theory [28].

669 In the analysis presented in [Part iv](#), a simplified model is used which  
 670 produces the decay depicted in [Figure 14](#) with a 100% branching ratio.  
 671 This decay chain begins with the pair production of gluinos, which decay  
 672 via a pair of quarks to the second lightest neutralino, which then decay via  
 673 a Z boson to the lightest neutralino. Only events in which the Z boson de-  
 674 cays to pairs of electrons or muons are considered, with all-hadronic final  
 675 states left to other searches [29]. The quarks emitted in the gluon decay are  
 676 allowed to have flavors  $u$ ,  $d$ ,  $c$ , and  $s$ , each with a 25% probability. A similar  
 677 model involving squark pair production is also considered, with the same  
 678 breakdown of flavors. In this simplified model, the lightest neutralino is  
 679 the [LSP](#), and is stable.

680 Using this simplified model, the masses of the particles can be set di-  
 681 rectly. This is very helpful for the generation of [MC](#), discussed in [Sec-](#)  
 682 [tion 4.7](#), because a grid of different mass values of the important sparticles  
 683 involved in the decay can be generated. Cross-sections calculations are  
 684 performed for each point on these grids [30]. This grid allows analyzers to  
 685 make predictions of likely signals, and to exclude the simplified models  
 686 as a function of the mass of the sparticles in the case that no discrepancies  
 687 between predictions and observations are seen.

688 2.2.3.1 *Context and Motivation*

689 This channel is well motivated from a theoretical perspective. Production  
 690 of strongly charged sparticles, shown in [Figure 15](#), is hypothesized to oc-  
 691 cur at much larger rates than the production of other particles, due to the  
 692 difference in coupling constants. The specific decay considered in these  
 693 simplified models does not have the largest branching ratio of all possi-  
 694 ble decays; even considering only changes to the [SM](#) decays involved, a  
 695  $Z \rightarrow qq$  decay is roughly seven times more likely than  $Z \rightarrow \ell\ell$ . However,  
 696 processes with higher branching ratios, like those producing an all-jet final

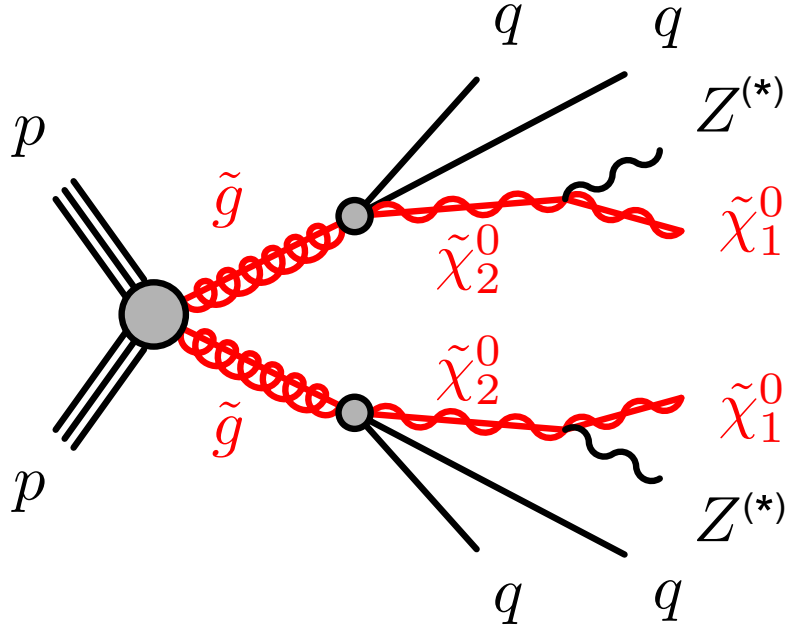


Figure 14: Feynman diagram of the decay considered in the simplified models used in the analysis presented in Part iv.

697 state, often have much higher SM backgrounds, making them difficult to  
 698 identify, even if they occur more frequently. This final state balances SM  
 699 backgrounds and branching ratios, and when compared to other searches  
 700 performed by the ATLAS collaboration, has competitive expected sensitivity  
 701 to SUSY [31].

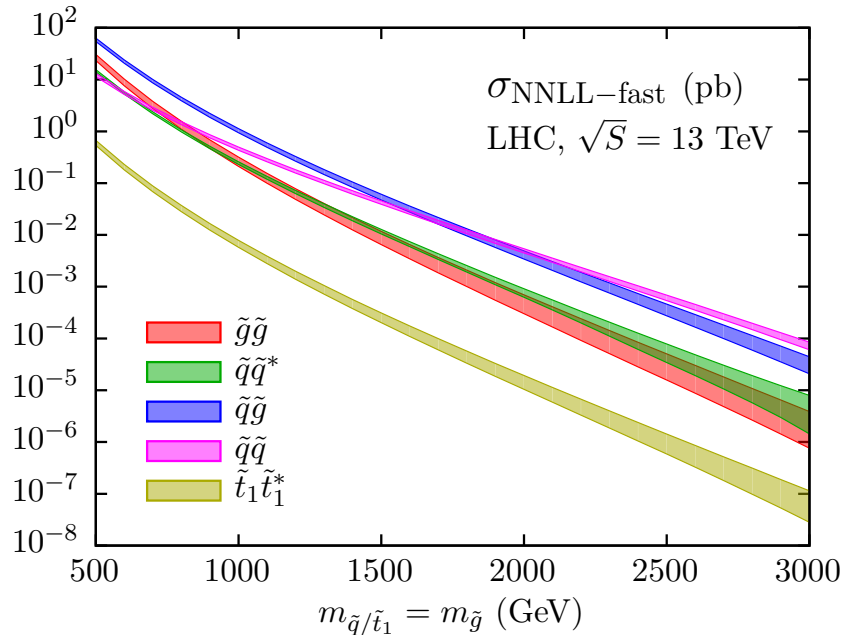


Figure 15: 13 TeV production cross-sections for sparticles, as a function of sparticle mass [32].

Processes similar to the one described by Figure 14 have been the target of previous LHC searches. Both CMS and ATLAS performed searches for SUSY in the two lepton channel with the 8 TeV data collected in 2012. The ATLAS search saw a  $3\sigma$  excess, shown in Figure 16 [1]. The CMS search saw no excess in a similarly motivated signal region, albeit with different kinematic cuts than ATLAS's, following up on a 7 TeV search that saw no excess [33, 34].

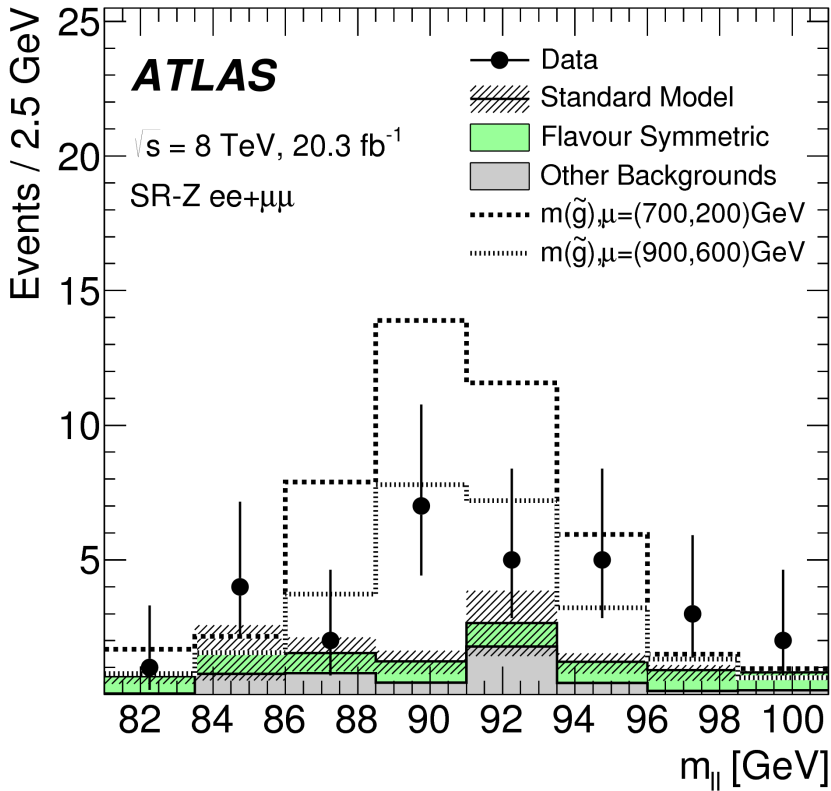


Figure 16: Results of an 8 TeV search performed by the ATLAS collaboration in a signal region targeting events like those in Figure 14. The events in the signal region are displayed as a function of  $m_{ll}$ , the invariant mass of the event's leading leptons. The SM backgrounds are shown with their full uncertainties based on data-driven background estimations, and two signals are superimposed on the distribution. The observed data-points are higher than the expected background, with a total excess of  $3.0\sigma$  [1].

Both searches also identified events with two leptons that weren't consistent with an on-shell Z decay, and in this region, an excess with a local significance of  $2.4\sigma$  was observed by CMS, shown in Figure 17. No excess was observed by the ATLAS collaboration in a signal region with identical kinematic cuts [1].

These two excesses generated significant interest in the two lepton channel, and both CMS and ATLAS produced preliminary results in December 2015 with the first  $3.2 \text{ fb}^{-1}$  of 13 TeV data. ATLAS again reported an excess on the Z mass peak [2], shown in Figure 18, while CMS saw no excesses [35].

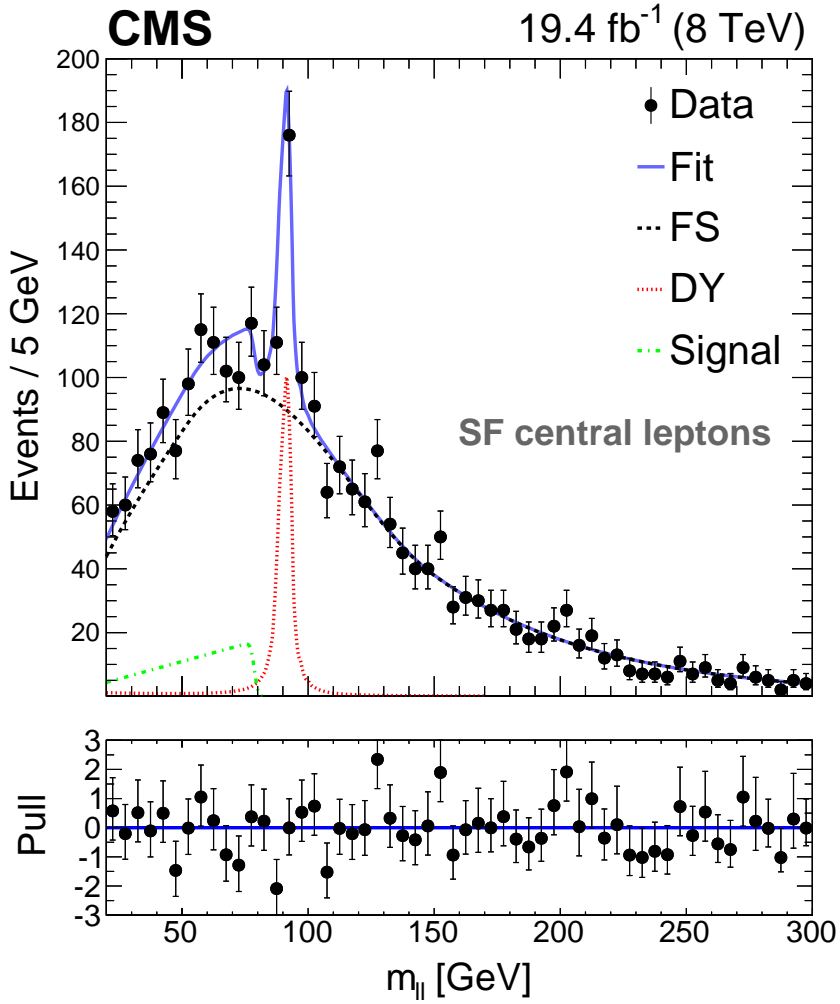


Figure 17: Results of an 8 TeV search performed by the CMS collaboration in a signal region including a broad range of  $m_{\ell\ell}$ . A  $2.4\sigma$  local excess is seen in the low  $m_{\ell\ell}$  region, and no excess of events is seen in the region with  $m_{\ell\ell}$  consistent with an on-shell Z boson. The data is fit based on a data driven estimate of the flavor symmetric background (FS) and the Drell-Yan background (DY), with an additional component for the signal [34].

<sup>718</sup> An all-hadronic ATLAS SUSY search released in 2016 which was sensitive to  
<sup>719</sup> the same models also saw no significant excess [29].

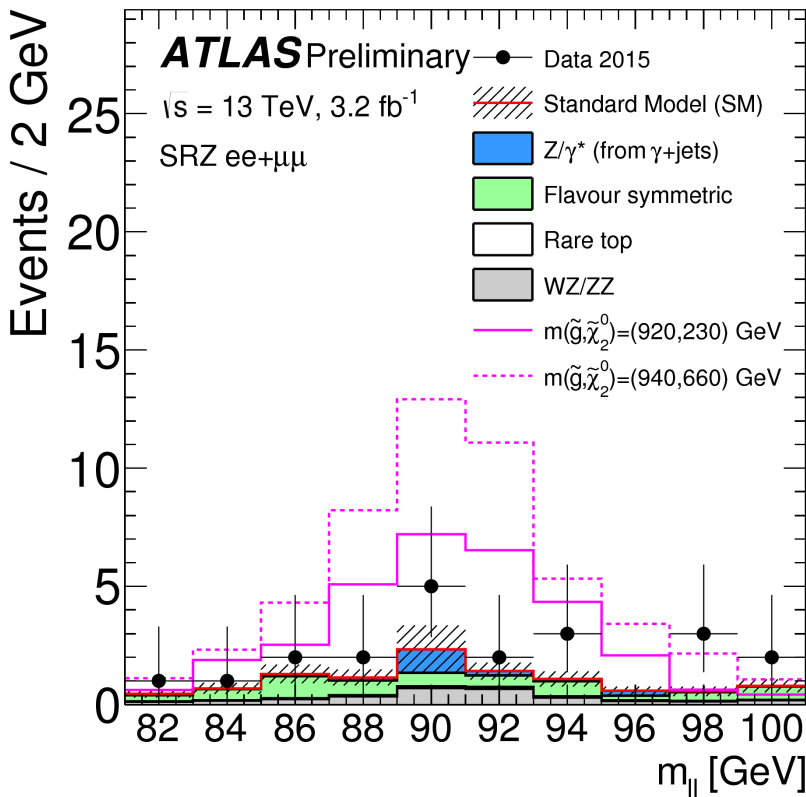


Figure 18: Preliminary results from a 13 TeV search targeting the same signal region as Figure 16, performed on  $3.2 \text{ fb}^{-1}$  of 2015 data. The events in the signal region are displayed as a function of  $m_{\ell\ell}$ , the invariant mass of the event's leading leptons. Flavor symmetric and  $Z/\gamma^* + \text{jets}$  backgrounds are taken from data-driven methods, while the other backgrounds are taken from MC. They are compared to the data, which shows a  $2.2\sigma$  excess of events. Distributions from two signal points are superimposed [2].



720

### Part III

721

## THE EXPERIMENT

722

四

123

724

725

This section describes the LHC accelerator and the ATLAS detector, which collectively provide the physical environment and the data collection for the analysis discussed in [Part iv](#). Reconstruction of events in the ATLAS detector is also explained, with an emphasis on the reconstruction of tracks in the inner-most part of the detector.



# 3

728

## 729 THE LARGE HADRON COLLIDER

730 The LHC is unique in the world, producing proton-proton collisions at  
731 energies nearly an order of magnitude higher than any accelerator before  
732 [36]. It provides unique environments at its collision points where massive,  
733 unstable particles can exist for an instant, then decay to the lighter, more  
734 stable SM particles normally observed in the universe. It is the goal of  
735 the ATLAS experiment to identify these short-lived particles, but the LHC's  
736 work of producing them is equally complex.

737 The LHC was built in a 26.7 km circular tunnel that straddles the French-  
738 Swiss border outside of Geneva, originally built in 1989 for the Large  
739 Electron-Positron (LEP) collider [37]. In the LHC, two beams of protons  
740 are accelerated to 6.5 TeV, then focused and collided at four points around  
741 the ring, which can be seen in Figure 19. These points are each encased  
742 by particle detectors, which can examine the outputs of the collisions, and  
743 have different strengths and goals. The two multipurpose detectors are  
744 ATLAS and CMS, which have very complex detectors aimed at measuring  
745 as many SM particles as possible and discovering new processes [38, 39].  
746 Large Hadron Collider beauty (LHCb) examines processes related to the  $b$   
747 quark [40]. Meanwhile, A Large Ion Collider Experiment (ALICE) focuses  
748 on special runs of the LHC which collide lead ions instead of protons, and  
749 seeks to understand the high energy densities resulting from the collisions  
750 of such massive, complex particles [41].

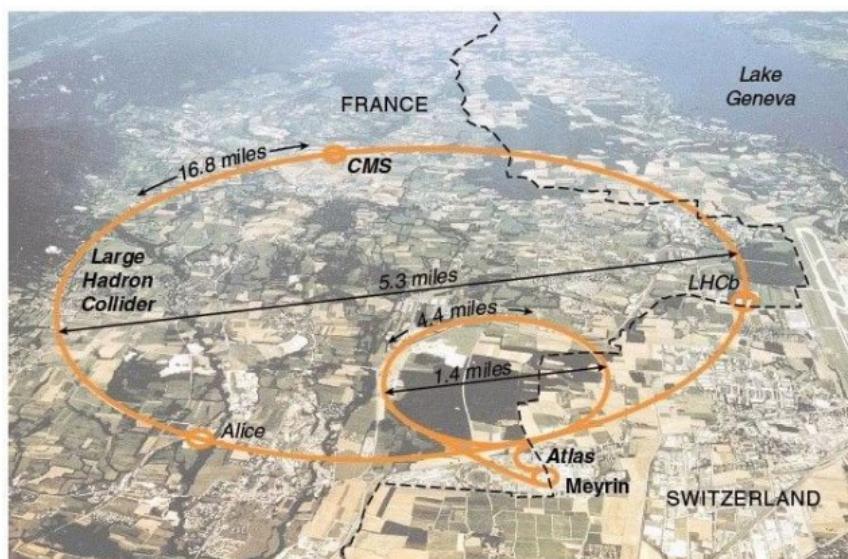


Figure 19: The LHC main collider ring and pre-accelerator SPS overlaid on a map of Switzerland and France, with the four main LHC experiments identified.

## 751 3.1 THE INJECTOR COMPLEX

752 The primary goal of the LHC is to provide high luminosity proton-proton  
 753 collisions at 13 TeV<sup>1</sup>. To achieve this, it must be capable of rapidly accel-  
 754 erating large numbers of protons and holding them at a constant energy,  
 755 and organizing them into bunches which can be focused and collided at  
 756 precise points and times. To do this, a complex system of pre-accelerators  
 757 is required, as well as a precisely engineered system of magnets within the  
 758 LHC. The full system of pre-accelerators is shown in Figure 20.

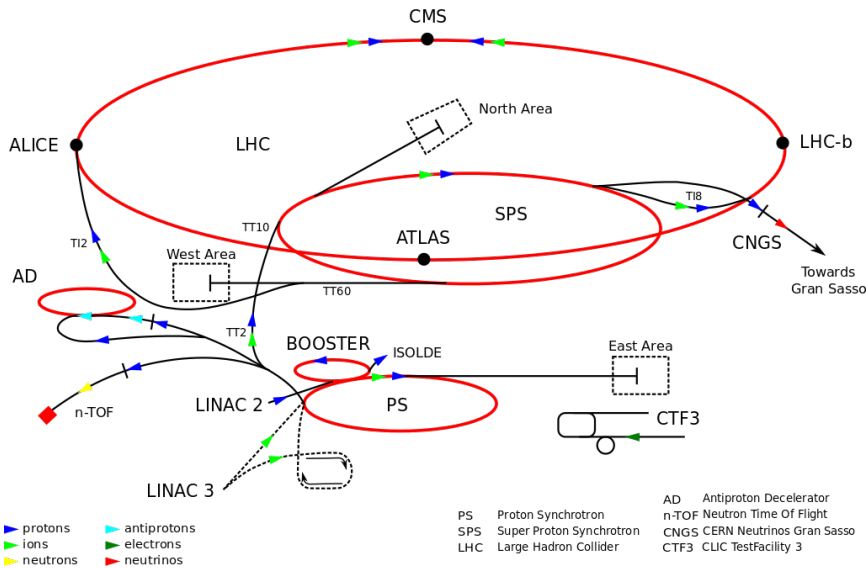


Figure 20: The pre-accelerators of the LHC.

759 The chain begins with when hydrogen gas is stripped of its electrons  
 760 and injected in short pulses into Linac2, a linear accelerator which uses  
 761 Radiofrequency (RF) cavities, which use alternating positive and negative  
 762 electric fields to simultaneously push and pull particles forward through  
 763 the accelerator. This RF behavior keeps the bunches of protons resulting  
 764 from the original pulses separated, beginning the formation of the bunch  
 765 structure used for collisions. Quadrupole magnets along the accelerator  
 766 keep the beam focused. By the end of this accelerator, protons have reached  
 767 50 MeV.

768 The proton beam is then injected into the Proton Synchrotron Booster  
 769 (PSB), the first circular accelerator in the pre-accelerator chain. It increases  
 770 its magnetic field as the protons increase in speed, ultimately accelerating  
 771 them to 1.4 GeV.

772 At this point the proton beam is injected into the Proton Synchrotron  
 773 (PS), a 600 m long circular accelerator that consists of RF cavities that accel-  
 774 erate protons up to 25 GeV, as well as room-temperature electromagnets  
 775 that bend the beam.

---

<sup>1</sup> The LHC also collides lead ions in special runs, but these instances are not discussed in this thesis.

776 The last accelerator before injection into the LHC is the SPS, a 7 km long  
777 ring which, long before the LHC tunnel was built, was used for the dis-  
778 covery of the W and Z bosons. The SPS accelerates particles up to 450  
779 GeV before they are launched into the LHC.

780 Proton bunches are structured for ease of acceleration, with distinct  
781 features resulting from each of the pre-accelerators. The PS produces 72  
782 bunches separated by 25 ns, which are injected into the SPS. However, as  
783 the magnetic field directing these protons out of the PS loop is turned on,  
784 there must be a gap in the bunch structure. Without this gap, called the  
785 injection kicker rise time, the changing magnetic field would direct parti-  
786 cles out of the accelerator and produce high amounts of unsafe radiation  
787 around the PS. A similar gap in bunch structure is required for the injec-  
788 tion from the SPS to the LHC. The injection process is repeated until the  
789 LHC is completely filled with over 2000 bunches, which takes about three  
790 minutes.

### 791 3.2 OPERATION OF THE LARGE HADRON COLLIDER

792 The LHC consists of eight straight sections each connected by an arc. In  
793 each straight section, RF cavities accelerate protons, ultimately bringing  
794 them up to 6.5 GeV. Between these straight sections, 8.4 T dipole mag-  
795 nets bend the beams to maintain the approximately circular path. How-  
796 ever, because the LHC is a proton-proton collider as opposed to a proton-  
797 antiproton collider, the two counter-rotating beams must be housed in  
798 separate rings and be accelerated separately. To achieve this, twin-bore su-  
799 perconducting magnets, one example of which can be seen in Figure 21,  
800 surround the two rings and accelerate them both. Quadrupole magnets  
801 are used at the four collision points to focus the beams, which cross at  
802 an interaction point at the center of a detector. In total there are over 6000  
803 superconducting magnets magnets, which are kept below their critical tem-  
804 perature of 1.9 K by liquid helium cooling.

805 When first injected into the LHC, the protons must be accelerated with  
806 increasing RF frequencies over many turns through the machine, with the  
807 magnetic field from the dipoles increasing with each pass to apply more  
808 force with which to bend the beam. Once the protons have reached a max-  
809 imum energy, a process called *squeezing* occurs. The quadrupole magnets  
810 are used to reduce the total transverse area of the beam and elongate the  
811 bunches slightly. The shape produced by this process determines the *beam*  
812 *spot* for the ATLAS detector, the area in which collisions occur within the  
813 detector. As shown in Figure 22, the collisions mostly occur within 0.5 mm  
814 of one another in the  $x - y$  plane, but have a spread of about 400 mm in  
815 the  $z$  direction<sup>2</sup>.

816 Once the beams are at a stable energy and have been squeezed, the  
817 LHC indicates that it is ready to provide collisions to the experiments  
818 around the ring, and, after some additional checks by each experiment,  
819 data-taking can begin. As collisions occur, the number of protons in the

<sup>2</sup> The coordinate system used here is discussed in Section 4.1.

### LHC DIPOLE : STANDARD CROSS-SECTION

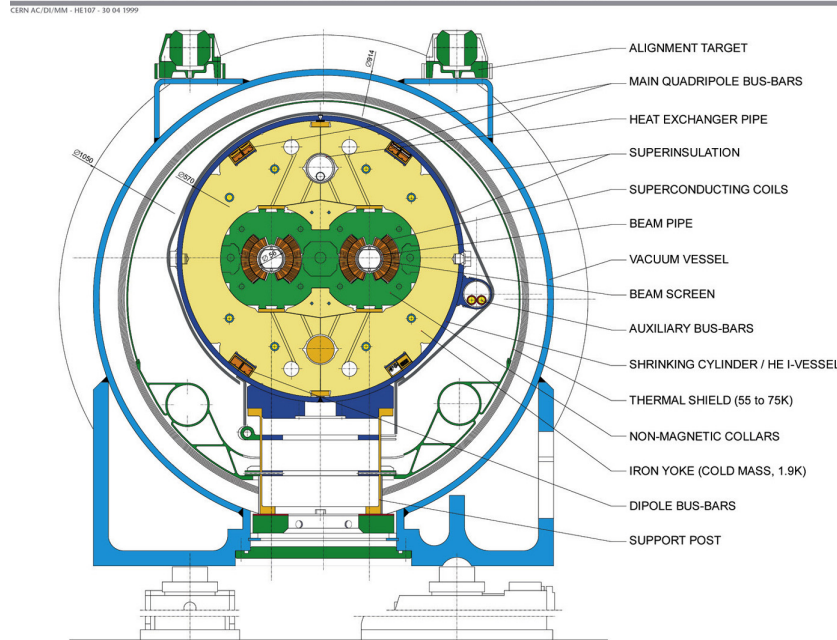


Figure 21: Cross-section of a cryodipole magnet in the LHC.

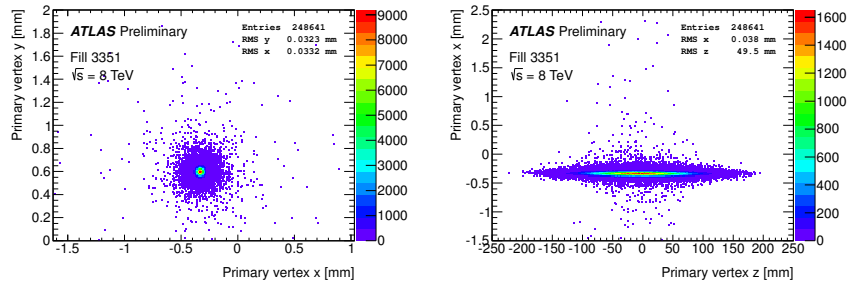


Figure 22: Beam spot in the ATLAS detector for one run in 2015. Distributions show only the highest  $p_T$  vertex per event. Left is the  $x - y$  distribution of vertices, while the right plot shows the  $x - z$  distribution.

beam decreases, and when it is sufficiently depleted to require a new fill, or if any instability occurs, the beam is dumped into a cavern filled with steel and concrete, which absorbs the energy.

### 3.3 LUMINOSITY

The goal of the collisions provided by the LHC is to produce SM and BSM particles, which can be observed by the detectors. How frequently a given process could occur was a crucial consideration in its design. The number of events of a given type is given by

$$N_{\text{event}} = \int dt L \sigma_{\text{event}} \quad (26)$$

where  $L$  is the luminosity delivered by the LHC and  $\sigma_{event}$  is the cross-section of the process in question. These cross-sections vary over many orders of magnitude for different processes, as shown in Figure 10, a plot of many different SM cross-sections. Because the higher-mass processes are so rare, a large amount of luminosity is required to produce them, and because other processes like jet production occur so much more frequently, they must be produced at high enough rates that analyzers have enough statistical power to differentiate them from more common events.

The instantaneous luminosity at the LHC is given by

$$L = \frac{N_b^2 n_b f_{rev} \gamma_r}{4\pi \epsilon_n \beta_*} F \quad (27)$$

where  $N_b$  is the number of protons per bunch ( $\sim 10^{11}$ ),  $n_b$  is the number of bunches in each beam ( $\sim 10^3$ ),  $f_{rev}$  is the number of times per second that the beam travels around the ring (1 kHz),  $\gamma_r$  is the relativistic gamma factor ( $\sim 7000$ ),  $\epsilon_n$  is the normalized transverse beam emittance ( $\sim 4$  mm  $\mu\text{m}$ ), and  $\beta_*$  is the  $\beta$ -function at the collision point, which describes the transverse displacement of particles in the beam ( $\sim 0.5\text{m}$ ).  $F$  gives the reduction factor due to the geometry of the beam crossings, and is given by

$$F = (1 + (\frac{\theta_c \sigma_z}{2\sigma_*})^2)^{-1/2} \quad (28)$$

where  $\theta_c$  is the crossing angle of the beams,  $\sigma_z$  is the RMS of the bunch length in the  $z$  direction, and  $\sigma_*$  is the same in the transverse direction.

As the proton beams circulate and collide,  $N_b$  decreases, producing a falling instantaneous luminosity, as seen in a Run 1 example in Figure 23. In Run 2, peak instantaneous luminosity was brought up to  $1.39 \times 10^{34}$   $\text{cm}^{-2}\text{s}^{-1}$ . This high instantaneous luminosity and consistent running resulted in much faster data collection than in Run 1, which is depicted in Figure 24.

### 3.4 PILE-UP IN PROTON-PROTON COLLISIONS

One consequence of the high instantaneous luminosity is *pile-up*, or multiple simultaneously interactions. Because the instantaneous luminosity is much larger than the total proton inelastic cross-section, it is very likely that multiple protons will collide in the same bunch crossing. In fact, the average number of simultaneous interactions in 13 TeV data, shown in Figure 25, is about twenty. For detectors with read-out windows larger than the bunch spacing of the LHC, *out-of-time* pile-up can also occur. In these cases, an event mistakenly includes measurements of objects resulting from other events' collisions.

Pile-up can be a difficult challenge for the ATLAS analyses because it typically results in additional jets in an event, and can increase SM backgrounds for analyses seeking to identify events with jets. It can also add

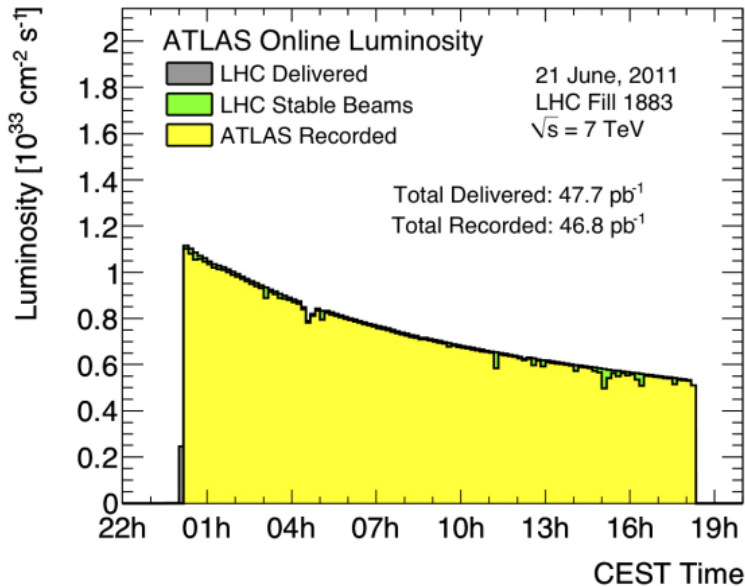


Figure 23: Instantaneous luminosity of one fill of 7 TeV data in 2011.

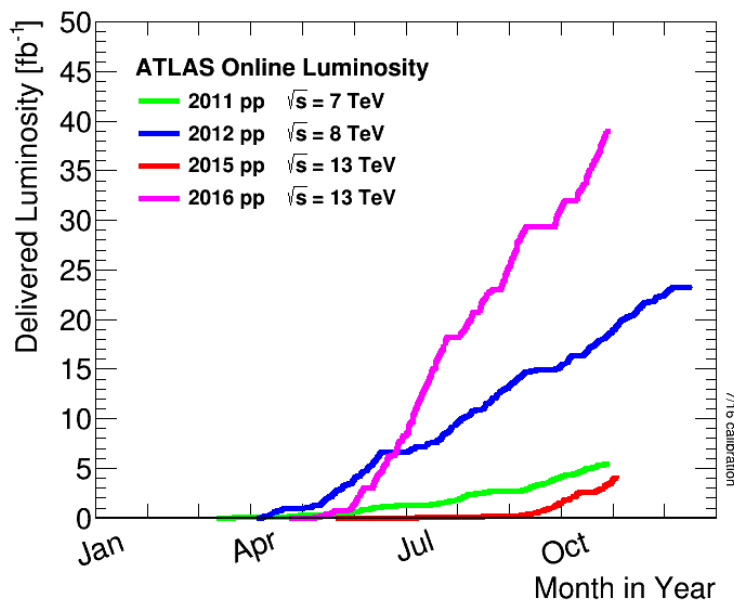


Figure 24: ATLAS luminosity for Run 1 and Run 2, as of September 2016.

866 to the overall hadronic energy of an event, and that energy can be mis-  
 867 assigned to other objects. Fortunately, the multiple interactions occur at  
 868 different points along the beam line, and the particles emerging from each  
 869 can be traced back to create *vertices* identifying the location of the interac-  
 870 tions. In most cases, it is possible to resolve the different vertices that each  
 871 proton-proton collision makes, and so pile-up jets can be identified and  
 872 rejected.

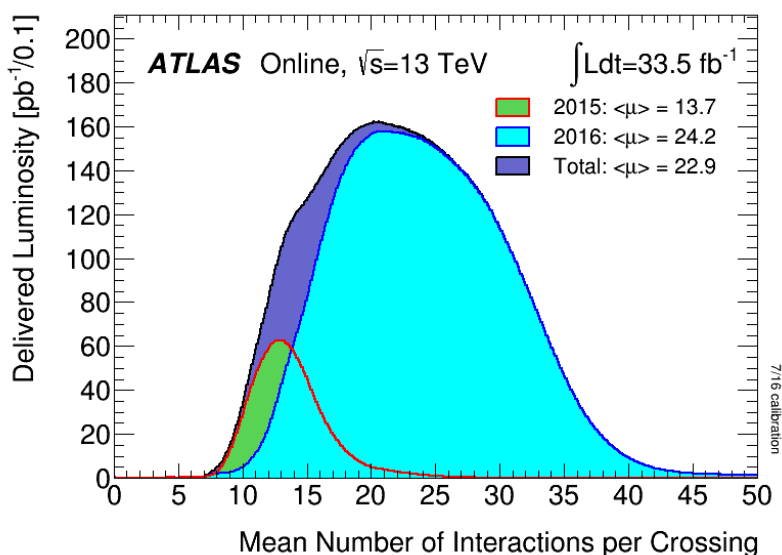


Figure 25: Average number of interactions per crossing shown for 2015 and 2016 separately, as well as the sum of the two years.



873

## 874 THE ATLAS DETECTOR

875 The A Toroidal LHC Apparatus ([ATLAS](#)) detector circumscribes the [LHC](#)'s  
 876 beam pipe, enclosing the collision point with a series of particle detecting  
 877 layers, aimed at making as many measurements of the particles leaving  
 878 the collision point as possible. Its goal is to get a precise measurement of  
 879 all the stable or semi-stable particles flying from proton-proton collisions  
 880 at its center, allowing analyzers to fully reconstruct the kinematics of the  
 881 underlying processes.

882 The [ATLAS](#) detector is the largest detector of its kind, measuring 44 m  
 883 in length and 25 m in height, as seen in [Figure 26](#). The size is mainly de-  
 884 termined by the constraints of the Muon Spectrometer ([MS](#)), discussed in  
 885 [Section 4.4](#), which is the largest and outermost subsystem. The [MS](#) is sub-  
 886 merged in a spatially varying magnetic field provided by three toroidal  
 887 magnets, while the Inner Detector ([ID](#)) ([Section 4.2](#)) is encased by a su-  
 888 perconducting solenoid, which provides a uniform 2 T field throughout  
 889 its volume [[38](#)]. A calorimeter system is located between the [MS](#) and [ID](#),  
 890 with components to measure the energy of electromagnetic and hadronic  
 891 systems.

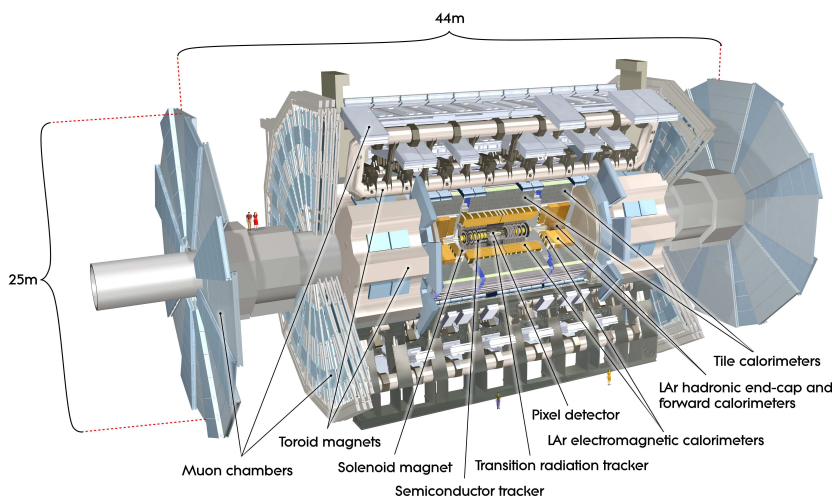


Figure 26: Diagram of the [ATLAS](#) detector, with subsystems and magnets identified.

892 4.1 COORDINATE SYSTEM USED IN THE [atlas!](#) ([atlas!](#)) DETECTOR

893 The [ATLAS](#) detector is centered around the  $pp$  collision point, and is built  
 894 radially out from the beam pipe, maintaining as much rotational symme-  
 895 try around the beam pipe as possible. It is also symmetric in the forward-

backward directions. A coordinate system using the collision point as the origin is used, with the beam line defining the  $z$ -axis in the counter-clockwise direction. The positive  $x$  direction is defined as pointing to the center of the LHC ring, while the positive  $y$  direction points upwards. For ease of reference, the side of the detector in the positive- $z$  direction is referred to as the A side, and the other side is referred to as the C side.

Because of the cylindrical design of the detector, angular coordinates are often used. The azimuthal angle  $\phi$  defines the angle around the beam pipe and the polar angle  $\theta$  defines the angle from the beam axis ( $z$ ). However, a transformation of the polar angle called pseudorapidity ( $\eta$ ) is used more often, and is defined as

$$\eta = -\ln[\tan \frac{\theta}{2}]. \quad (29)$$

$\eta$  is used because the particle distribution from LHC collisions is roughly uniform in this variable. Building on this definition, angular distance between objects is typically defined as

$$\Delta R = \sqrt{\Delta\eta^2 + \Delta\phi^2}. \quad (30)$$

Often variables are defined purely in the transverse plane, which is indicated by a subscripted  $T$ , as in  $p_T$ , which gives an object's transverse momentum.

#### 4.2 THE INNER DETECTOR

The Inner Detector (ID) is used for the measurement of tracks, estimates of the paths charged particles take as they travel through the detector. Collisions in the detector produce about 1000 particles, so identifying and differentiating all the tracks resulting from a collision is challenging.

The ID consists of three separate subdetectors, each of which has multiple layers capable of producing an electrical signal, called a *hit*, when a charged particle travels through its active material. ATLAS tracking software considers all these hits and forms tracks, with the goal of minimizing fake tracks due to random noise and maximizing the efficiency of identifying a real particle. Some details of this procedure are discussed in Chapter 5. The full ID can be seen in Figure 27, while a schematic in Figure 28 shows more detail on the placement of each layer.

##### 4.2.1 The Pixel Detector

The pixel detector lies closest to the beam pipe of the LHC, and has four layers comprising 92 million pixels. There are three standard layers, referred to as Layers 0-2 (L0, L1, L2), and an additional layer added for the 2015 data-taking, called the IBL.

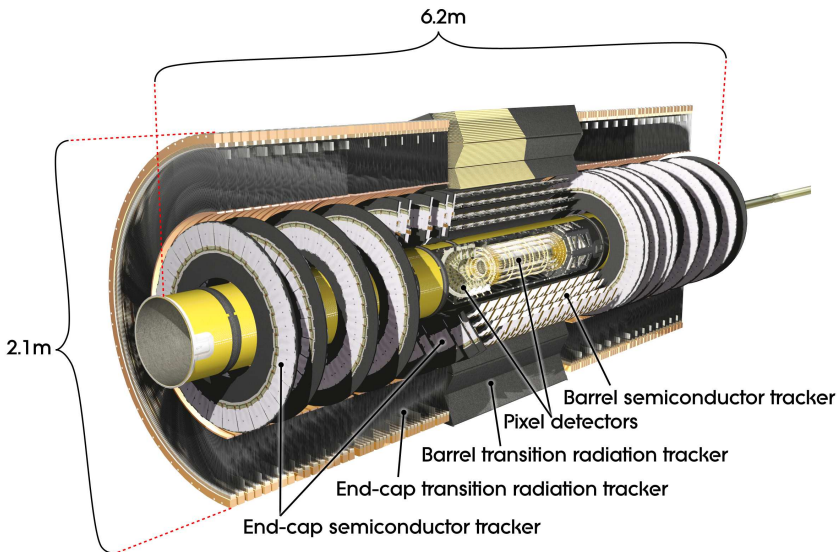


Figure 27: Diagram of the [ATLAS](#) Inner Detector, containing the Pixel, SCT, and TRT subsystems.

#### [931](#) 4.2.1.1 *The Original Pixel Detector*

[932](#) The Pixel Detector consists of high-precision silicon chip pixel modules,  
[933](#) with 1744 in total, and each module is made up of 16 sensors each with  
[934](#) its own read-out system. Each sensor is identical, containing 47232 pixels,  
[935](#) which are typically each  $50 \times 400 \mu\text{m}^2$ , though pixels at the edges of the  
[936](#) sensors are slightly longer, at  $50 \times 600 \mu\text{m}^2$ .

[937](#) As shown in [Figure 28](#), the central  $\eta$  region (barrel) is covered by three  
[938](#) concentric cylindrical layers of sensors with radii of 50.5 mm, 88.5 mm,  
[939](#) and 122.5 mm. In the higher  $\eta$  region (endcap) is covered by a series of  
[940](#) three disks positioned in the  $x - y$  plane. Together, they give complete  
[941](#) coverage out to  $|\eta| = 2.5$ , and a particle coming from the collision point  
[942](#) will typically produce hits in three layers.

[943](#) The sensors are n-type silicon wafers with a voltage applied, and a passing  
[944](#) charged particle produces thousands of electron-hole pairs inside the  
[945](#) material, which drift in the electric field towards the mounted read-out  
[946](#) system. A hit occurs when the resulting current becomes large enough to  
[947](#) pass a threshold designed to suppress noise. A larger total charge deposit  
[948](#) will result in the signal remaining over the threshold for a longer period  
[949](#) of time. This Time Over Threshold (ToT) is recorded along with the initial  
[950](#) timing of the hit. This measurement is spatially accurate in the barrel  
[951](#) (endcap) to  $10 \mu\text{m}$  in the  $R - \phi$  direction and  $115 \mu\text{m}$  in the  $z (R)$  direction.

#### [952](#) 4.2.1.2 *Addition of the IBL*

[953](#) In 2014, the [IBL](#) was added to the Pixel Detector. This layer is placed directly  
[954](#) on top of the beam pipe, inside barrel Lo, providing a measurement  
[955](#) of particles only 3.3 cm away from the interaction point. The [IBL](#) consists of  
[956](#) 14 overlapping staves, each containing 16 modules, the geometry of which

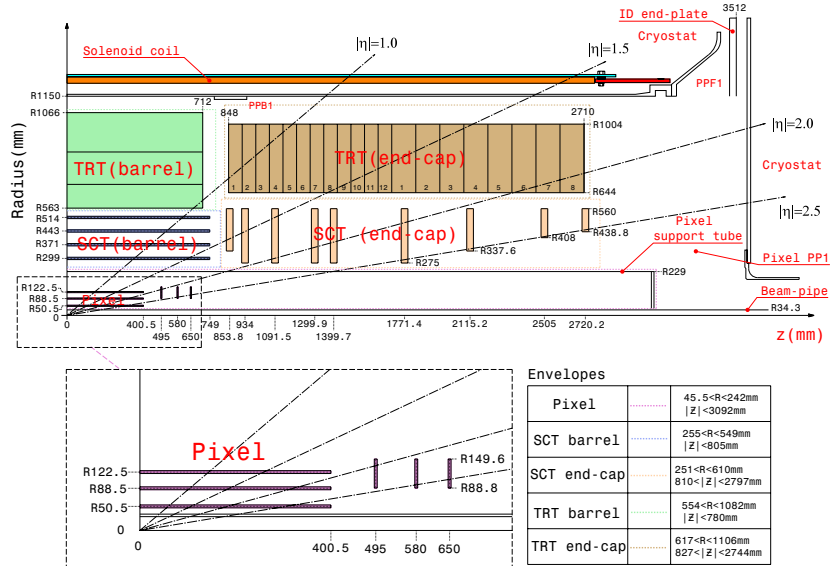


Figure 28: Diagram of one-quarter of the [ATLAS](#) Inner Detector in the  $R - z$  plane, with lines drawn to indicate various  $\eta$  locations.

957 can be seen in [Figure 29](#). These modules contain pixels measuring  $50 \times 250$   
958  $\mu\text{m}^2$ , and allow for particle detection in 90% their area, as compared to the  
959 70% possible with the original pixel modules.

960 The [IBL](#)'s addition provides greater precision for all track measurements,  
961 but it is especially useful for the detection of  $B$  mesons, discussed in [Section 2.1.1.2](#), whose lifetimes of about 1.5 ps allow them to travel as much  
962 as a few mm before decaying. These decays lead to secondary vertices in  
963 [ATLAS](#) events. The location of the [IBL](#) gives a measurement closer to these  
964 secondary vertices, increasing the probability that these vertices can be  
965 resolved.

#### 967 4.2.2 The Silicon Microstrip Tracker

968 The [SCT](#) employs a similar technology to the Pixel Detector, with 15912 sen-  
969 sors and 6.3 million readout channels. Its main difference from the Pixel  
970 Detector is in the readout, which is performed by a series of 12 cm long  
971 strips with a width of 80  $\mu\text{m}$ . These layers are paired, placed on top of one  
972 another at a small (40 mrad) angle to allow for position determination in  
973 the  $\phi$  and  $z$  directions. Together, these pairs of layers give four spatial mea-  
974 surements for each particle passing through the [SCT](#). In the barrel, these  
975 strips run parallel to the beam pipe, while in the endcap, they are arranged  
976 radially. These strips provide a hit resolution in the barrel (endcap) of 17  
977  $\mu\text{m}$  in the  $R - \phi$  direction and 580  $\mu\text{m}$  in the  $z$  ( $R$ ) direction.

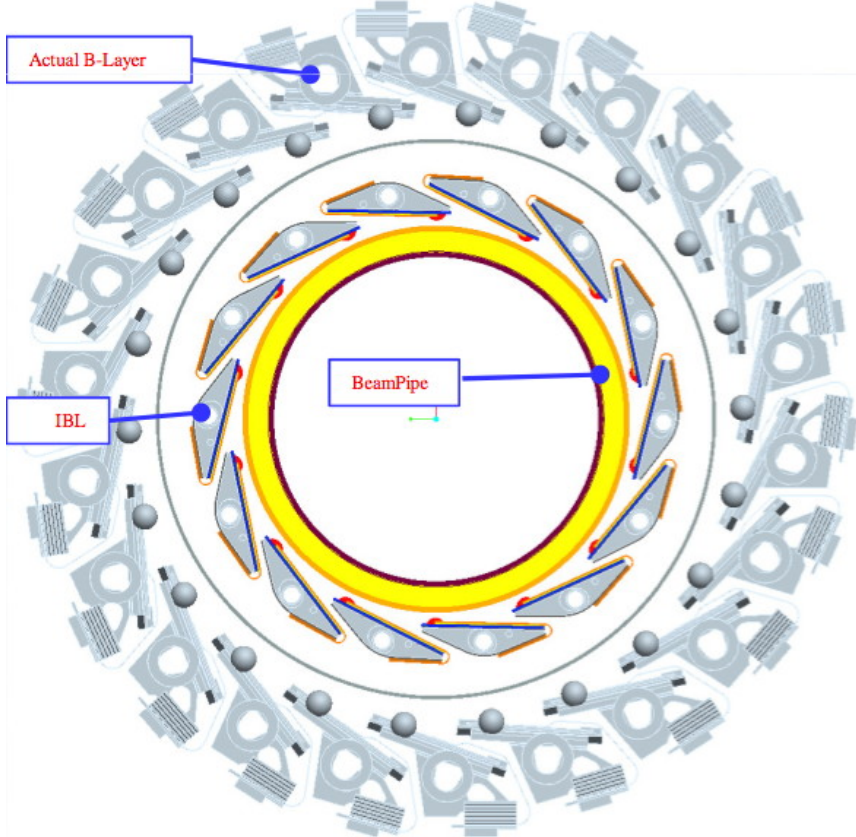


Figure 29: Diagram in the  $x - y$  plane of the IBL and the innermost layer of the pixel detector, Lo [42].

#### 4.2.3 The Transition Radiation Tracker

The Transition Radiation Tracker (TRT) uses 4 mm diameter gas-filled tubes, each with a high voltage wire suspended along the center of the tube. The tubes run the length of the barrel, with a separate wire in the positive and negative  $z$  direction. In the endcap, the tubes are arranged radially. In total, there are about 351,000 readout channels in the TRT. This detector makes measurements only in the  $R - \phi$  direction, where the resolution of each measurement is  $130 \mu\text{m}$ , and coverage extends to  $|\eta| = 2.0$ . Each particle typically creates about 36 hits as it passes through the TRT barrel.

Particles passing through the gas mixture of the TRT ionize the gas, producing electrons which drift towards the wire due to a potential difference applied between it and the tube. In addition, particles passing through the TRT produce radiation as they transition between materials, with larger amounts of radiation for lighter particles. This radiation produces high-threshold signals in the TRT can be used to differentiate electrons from other heavier charged particles, such as pions.

## 994 4.3 THE CALORIMETERS

995 Unlike the tracking detectors, which aim to take measurements of a parti-  
 996 cle with minimal alterations of its trajectory, the calorimeters measure the  
 997 energy of objects by stopping them entirely. Calorimeters contain alternat-  
 998 ing layers of absorber, a material that causes incoming particles to shower  
 999 into lower-energy decay products, and an active material, which detects  
 1000 passing particles, allowing for the reconstruction of these showers.

1001 The [ATLAS](#) calorimeters, which can be seen in [Figure 30](#), provide cover-  
 1002 age out to  $|\eta| < 4.9$ . High granularity electromagnetic measurements are  
 1003 made within  $|\eta| < 2.5$ . In this range, high- $p_T$  electrons have nearly straight  
 1004 tracks, making momentum measurement through track curvature difficult,  
 1005 leaving the calorimeter as the primary energy measurement. The hadronic  
 1006 calorimeters, as well as the higher  $|\eta|$  electromagnetic calorimeters, have a  
 1007 coarser granularity.

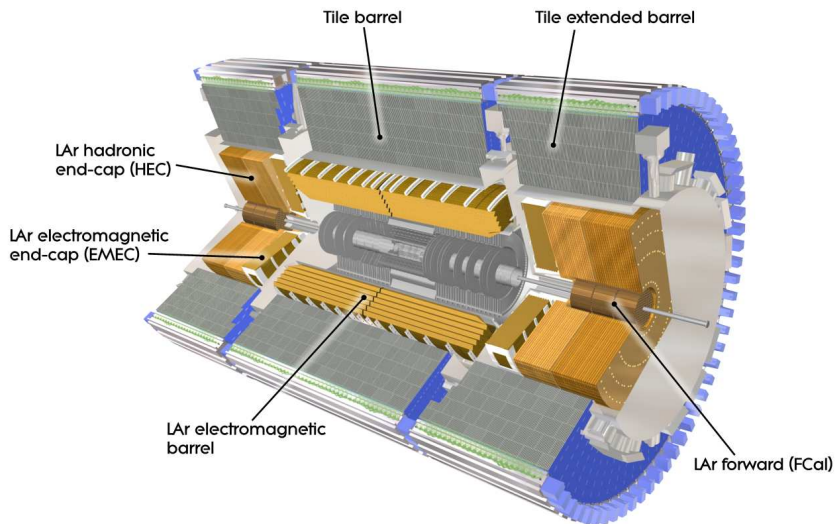


Figure 30: The calorimeter system of the [ATLAS](#) detector.

1008 Besides measuring the energy of passing particles, another task of the  
 1009 calorimeter system is to limit punch-through to the [MS](#), described in [Sec-](#)  
 1010 [tion 4.4](#). All other particles must be fully stopped by the calorimeters to  
 1011 allow for clean signals from muons, and to measure the total energy of the  
 1012 particle. This requirement sets a minimum number of interaction lengths  
 1013 for each of the calorimeters.

1014 **THE LAR ELECTROMAGNETIC CALORIMETER** uses liquid argon as its  
 1015 active detector medium alternating with layers of lead acting as the ab-  
 1016 sorber. Signals are read out with capacitively coupled copper plates. The  
 1017 layers are shaped like accordions, which allows for complete coverage with  
 1018 multiple layers of active material, three in central  $\eta$  ( $0 < |\eta| < 2.5$ ) and two  
 1019 at higher  $\eta$  ( $2.5 < |\eta| < 3.2$ ). [Figure 31](#) shows the layout of a central  $\eta$  mod-  
 1020 ule, including this accordion-like layering. At  $|\eta| < 1.8$ , an instrumented  
 1021 liquid argon presampler provides a measurement of energy lost prior to

1022 reaching the calorimeters. The total energy resolution for this detector is  
 1023 about  $10\%/\sqrt{E}$ , with an additional constant term of 0.2%.

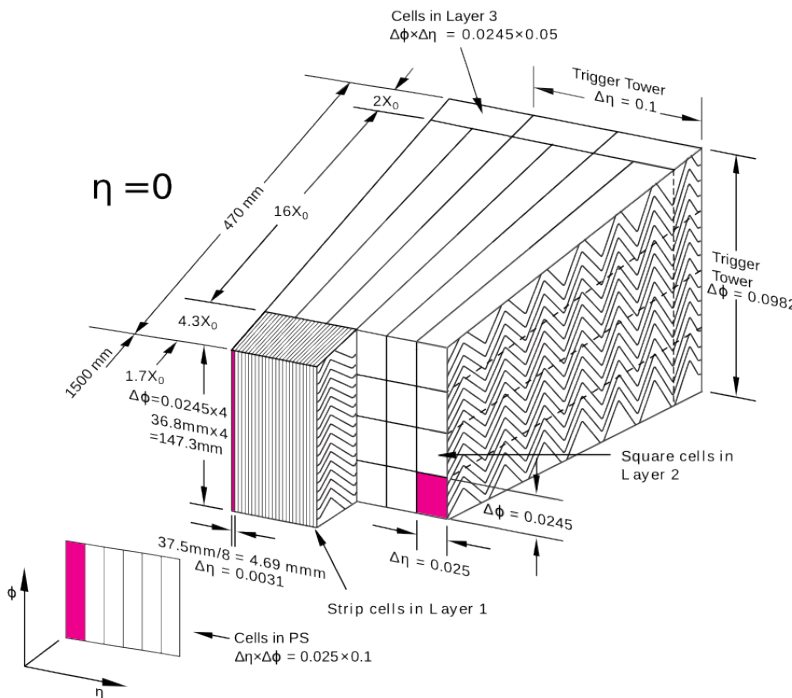


Figure 31: Layout of the LAr calorimeter module at central  $\eta$  [38].

1024 **THE TILE CALORIMETER** is a hadronic calorimeter which surrounds  
 1025 the LAr Calorimeter. It uses layers of steel as its absorber with scintillating  
 1026 tiles as the active material between them, which are read out by photomul-  
 1027 tiplier tubes. The Tile Calorimeter covers  $|\eta| < 1.7$  with a typical energy  
 1028 resolution of about  $50\%/\sqrt{E}$  with a constant term of 5%.

1029 **THE LAR HADRONIC ENDCAP CALORIMETER** covers the hadronic calorime-  
 1030 try for higher  $\eta$ . It uses liquid argon active material and copper plate  
 1031 absorbers, resulting in an energy resolution of approximately  $70\%/\sqrt{E}$   
 1032 with a constant term of 5%. This calorimeter covers  $1.5 < |\eta| < 3.2$ , over-  
 1033 lapping with the hadronic calorimeters in either direction of its  $\eta$  range.

1034 **THE FCAL** or forward calorimeter provides electromagnetic and hadronic  
 1035 coverage at very high  $\eta$  ( $3.1 < |\eta| < 4.9$ ). This calorimeter also uses liquid  
 1036 argon as its active material, and uses copper-tungsten as the absorber. Its  
 1037 energy resolution is about  $70\%/\sqrt{E}$  with a constant term of 3%.

#### 1038 4.4 THE MUON SPECTROMETER

1039 The Muon Spectrometer (MS) measures charged particles that penetrate the  
 1040 calorimeter system. Because the calorimeters are designed to completely  
 1041 absorb electrons, photons, and hadrons, the MS mainly detects muons,

which pass through the calorimeter with very little loss of energy. The goal of the MS is to give a high-precision measurement of these muons, and also to be able to quickly identify events with muons for the sake of triggering, discussed in [Section 4.6](#). The layout of the MS can be seen in Figures 32 and 33. Muons can be measured for all  $|\eta| < 2.7$ , and they can be triggered on for  $|\eta| < 2.4$ . The entire system is about 24 m tall and 40 m long.

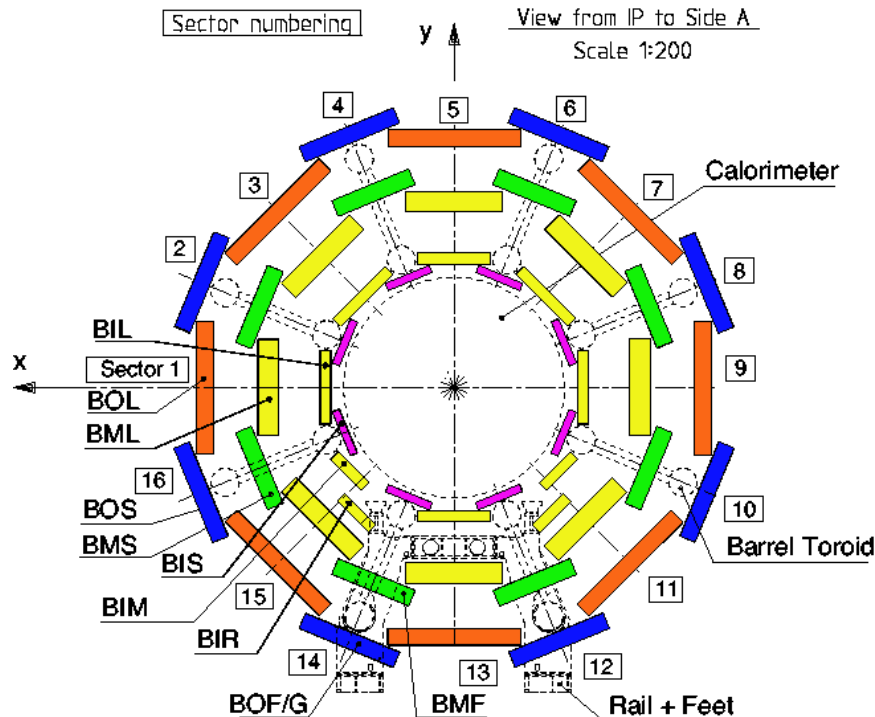


Figure 32: An  $x$ - $y$  view of the MS. The three barrel layers are visible, as well as the overlapping, differently sized chambers. The outer layer of the MS is about 20m in diameter.

To achieve these goals, the MS has several subsystems. The system responsible for precision measurement is called the Monitored Drift Tubes (MDTs). This subdetector consists of chambers of three to eight layers of tubes, with three layers of chambers covering both the barrel and endcap regions. In the barrel, these chambers are arranged in layers concentric cylinders with small overlaps between adjacent chambers. The chambers are oriented such that the drift tubes are parallel to the beam line. In the endcap, the chambers form disks with drift tubes approximately aligned in the  $R$  direction.

The tubes each contain an Ar/CO<sub>2</sub> gas mixture and a single high voltage wire which runs at its center along its length. Charged particles excite the gas as they pass through it, producing electrons which drift towards the high voltage wire. The resulting electric signal is read out, and the magnitude and timing of the signals are both used to differentiate particle traces from noise.

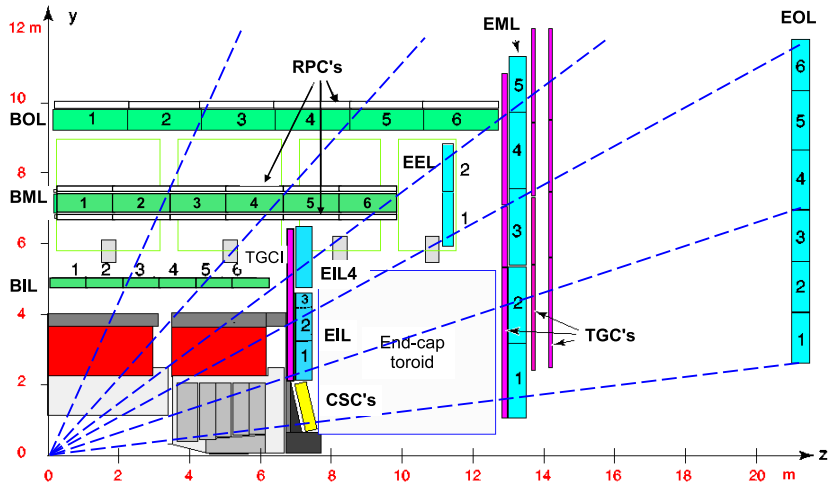


Figure 33: An  $r$ - $z$  view of the MS. The three layers of the barrel and endcap MS are visible.

Though very effective at giving a precise measurement, the MDTs have two shortcomings. The first is that the measurement is only precise in the direction perpendicular to the tubes; in the direction parallel to them, the resolution is not much better than the length of the drift tube, which are typically several meters long. The resolution in the perpendicular direction is about  $35 \mu\text{m}$  with the combined measurement of all the tubes in a chamber. The second major shortcoming is that the MDTs are slow, with a maximum drift time of about 700 ns.

The slow drift time means that muons from sequential collisions can appear in the same event, and that the signals from the MDTs are received too late to be used for triggering. To solve the former problem, another detector called the Cathode-Strip Chambers (CSCs) is used in high-rate regions of the MS. This detector consists of multi-wire proportional chambers which have cathode strips on either side of the anode in orthogonal directions, providing a  $40 \mu\text{m}$  resolution in one direction and 5mm resolution in the other. Their drift times are much shorter than those of the MDTs, at about 40 ns. They are placed in the forward region of the detector ( $2 < |\eta| < 2.7$ ) where the incident particle rates are highest.

To achieve responses fast enough to be used for triggering, Resistive Plate Chambers (RPCs) and Thin Gap Chambers (TGCs) are used. These chambers both take less than 25 ns to produce a signal. The RPCs are used in the barrel and are made up of two high-resistance plastic plates with a gas mixture under an electric field between them. Passing particles ionize this gas, and the resulting signal is read out via metallic strips mounted to the plastic plates. The TGCs used in the endcap are a form of multi-wire proportional chambers, like the CSCs. Unlike the CSCs, the cathode is placed extremely close to the wires, speeding up its operation.

The massive MS is subject to deformations due to gravity and the magnetic field. To achieve a high precision alignment, these deformations are

1093 constantly monitored in each **MDT** chamber with a set of four optical align-  
 1094 ment rays, which give alignment information at the precision of  $<30\ \mu\text{m}$ .  
 1095 In addition, a sag-adjustment system can use this information to re-align  
 1096 any wires that droop under gravity's pull. Lastly, the **MS** can be aligned  
 1097 using the tracks made from hits it measures, discussed more in [Section 6.3](#).

1098 4.5 THE MAGNET SYSTEM

1099 The **ATLAS** magnet system consists of four superconducting magnets: an  
 1100 inner solenoid, a barrel toroid, and two endcap toroids. Collectively, they  
 1101 are 22m in diameter and 26m long, and their basic layout can be seen in  
 1102 [Figure 34](#).

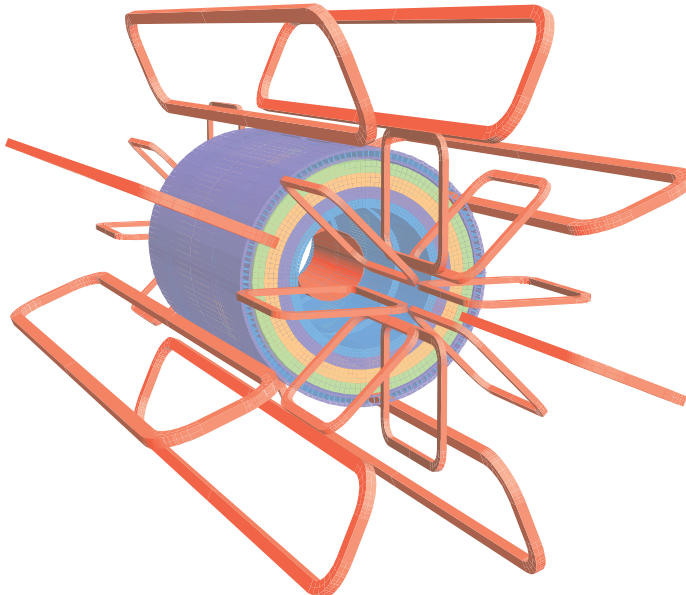


Figure 34: The magnet system of the **ATLAS** detector. The inner cylinder shows the solenoid which gives a uniform magnetic field in the **ID**. Outside of that are the barrel and endcap toroids, which provide a non-uniform magnetic field for the **MS**.

1103 The solenoid is inside the calorimeter volume and provides a uniform  
 1104 2T magnetic field for particles traveling through the **ID**. This axial field  
 1105 causes the trajectories of charged particles to bend in the  $x - y$  plane, and  
 1106 measurements of the curvature of these trajectories give the most accurate  
 1107  $p_{\text{T}}$  measurement for many particles according to the equation

$$p_{\text{T}} = qB\rho \quad (31)$$

1108 where  $q$  is the charge of the particle,  $B$  is the magnetic field in the  $z$   
 1109 direction, and  $\rho$  is the radius of curvature.

1110 Because the solenoid is placed between the tracking system and the  
 1111 calorimeter, it is important that it interfere minimally with particles in  
 1112 order to allow the calorimeter to measure their full energies. The solenoid

is placed inside the same vacuum chamber as the LAr calorimeter and is made of Al-stabilized NbTi superconductor with aluminum casing, giving it a total thickness of about 0.66 radiation lengths.

The barrel toroid is outside the calorimeters and provides the magnetic field for the barrel [MS](#), which varies from 0.2–2.5T. The endcap toroids have a magnetic field range of 0.2–3.5T. All three toroid magnets are made with Al-stabilized Nb/Ti/Cu superconducting coils supported by Al-alloy struts.

The magnets are cooled with liquid helium, and take up to a month to be brought down to operating temperatures, about 4.5 K. All magnets have cold masses surrounding them to absorb heat in the event of a quench.

The  $B$ -field resulting from this magnet system can be seen in [Figure 35](#). The plot on top demonstrates the relatively constant field rate within the barrel which drops steeply at  $|z|=2$ . The bottom plot shows the field integral in the [MDTs](#) as a function of  $|\eta|$ , demonstrating the good coverage out to  $|\eta|<2.6$  excluding a transition region between the barrel and endcap, where the field changes rapidly, making precise  $p_T$  construction difficult.

## 4.6 THE TRIGGER SYSTEM AND DATA ACQUISITION

The [LHC](#) provides proton bunch crossings every 25 ns, and each of these events contains about one MB of data, corresponding to 40 TB/s<sup>1</sup>, a completely unmanageable amount of data. In addition to this concern, many of [ATLAS](#)'s subdetectors like the Pixel Detector, the LAr Calorimeter, and [MDTs](#) take much longer than 25 ns to read out, making keeping up with the bunch crossing rate impossible. To reduce the total data read out and allow for selective reading out of the slower detectors' buffers, a triggering system is used.

The trigger system uses fast detectors to get a coarse picture of an event's topology, which is then compared to a trigger menu, which lists the types of events that are interesting enough to keep. Overall, the trigger system reduces the 40 million events a second to about 1000 to be fully read out from the [ATLAS](#) detector.

This filtering of events is done in two steps: the [L<sub>1</sub>](#) trigger is implemented in hardware and reduces the initial 40MHz to 100kHz, while the [HLT](#) is implemented in software, further reducing the rate to 1kHz [[43](#)]. The [L<sub>1</sub>](#) trigger uses coarse granularity information from the fast read-out subdetectors: the calorimeters, the [RPCs](#) and [TGCs](#).

The coarse grained calorimeter information used for the [L<sub>1</sub>](#) trigger decision is referred to as L<sub>1</sub> Calorimeter Trigger ([L<sub>1</sub>Calo](#)) and uses information from all calorimeter systems. [L<sub>1</sub>Calo](#) is responsible for all triggers excluding muons, meaning it must be capable of identifying a large number of different objects and event topologies, including high- $p_T$  objects,  $E_T^{\text{miss}}$ , and large amounts of hadronic energy. The trigger can also identify isolated

---

<sup>1</sup> This number is actually an overestimate, as not all bunches are filled due to the gaps produced by the [LHC](#)'s injector complex, discussed in [Section 3.1](#).

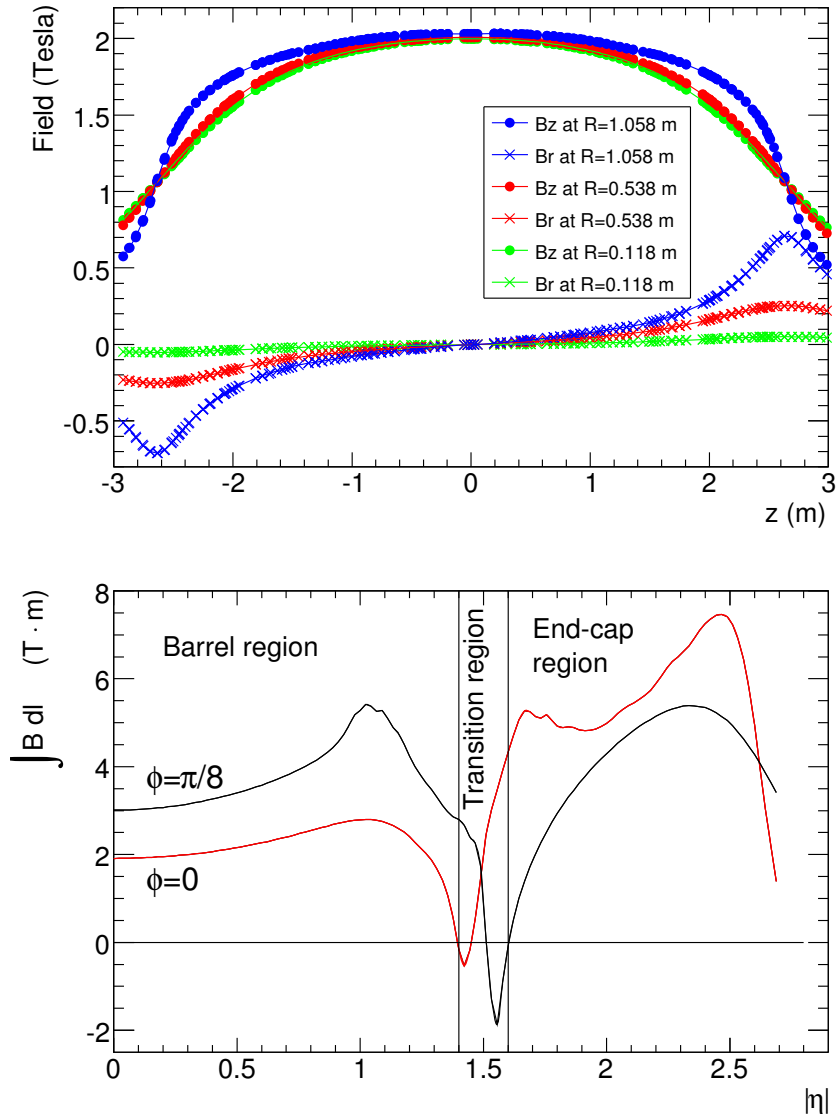


Figure 35: Plots of the magnetic field within the [ATLAS](#) detector. Top is the field (broken into its  $R$  and  $z$  components) as a function of  $z$  for several different values of  $R$ . Bottom is the field integral through the [MDTs](#) as a function of  $|\eta|$  for two different  $\phi$  values.

objects, objects with very few calorimeter deposits from other objects near them.

For muon triggers, the trigger algorithm looks for patterns of hits from the [RPC](#) and [TGC](#) that are consistent with high- $p_T$  muons with origins at the interaction point.

An example of the [L1](#) trigger rates for different types of events can be seen in [Figure 36](#) for one run in July 2016. The common features to all rates are due to [LHC](#) luminosity changes, deadtimes due to detector inefficiency, and adjustment of trigger rates to optimize bandwidth.

All of this information is analyzed by the Central Trigger Processor ([CTP](#)), which uses a trigger menu identifying all types of events to be kept

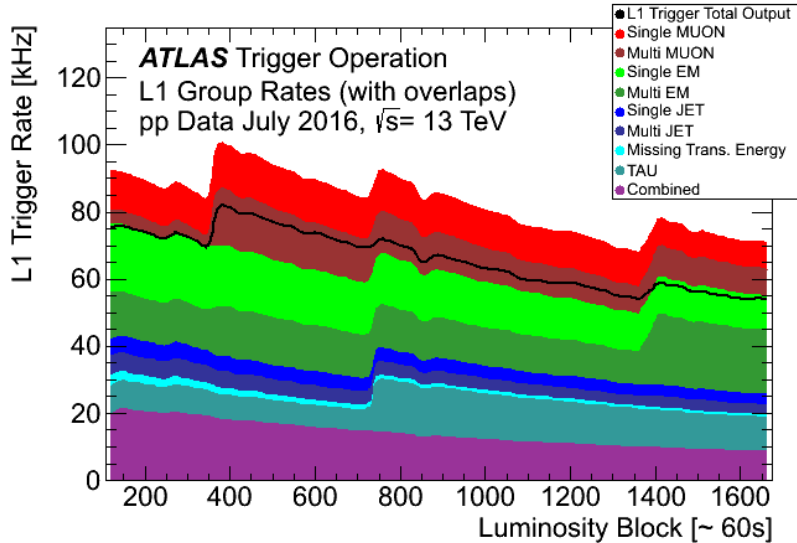


Figure 36:  $L_1$  trigger rates for a run in July 2016 as a function of luminosity block, an approximately 60-second long period of data-taking. The total rate is lower than the combined stack because of overlapping triggers.

to return a trigger decision. Due to the limited size of detector buffers, the event must be processed in about  $2.5 \mu\text{s}$ . This ensures that the information to be read out has not yet been overwritten when the trigger decision is made. This decision is passed to the Trigger Timing and Control (TTC), which communicates with all subdetectors. Upon receiving a  $L_1$  trigger, the subdetectors read out all the information they've stored about the event and place it on their Read Out Boards (ROBs).

The HLT takes the data from particular Region of Interests (RoIs), areas containing interesting objects that caused the  $L_1$  trigger. With a more complete picture of the hits observed by the detector, tracks are formed, and the HLT can use all of this information to determine whether or not the event is still interesting enough to keep. This process has its own trigger menu with dedicated  $L_1$  seeds for each item. HLT triggers typically have slightly higher thresholds than their corresponding  $L_1$  triggers to ensure that events that would pass the HLT requirements are very likely to have passed the  $L_1$  requirements. Figure 37 shows the HLT rates for the same run in July. In addition to the event types seen in Figure 36, the HLT can also identify events with  $b$ -jets, differentiate between electrons and photons, and identify events interesting for B-physics.

Events passing the HLT trigger are written to disk to be analyzed. An example of the total trigger efficiency for single electron triggers is shown in Figure 38.

Events types that occur very frequently, such that it would require too much of the total trigger bandwidth to record all events passing a given threshold, are prescaled. Events passing these triggers are only recorded a fraction of the time, and these prescaling rates are used to weight events

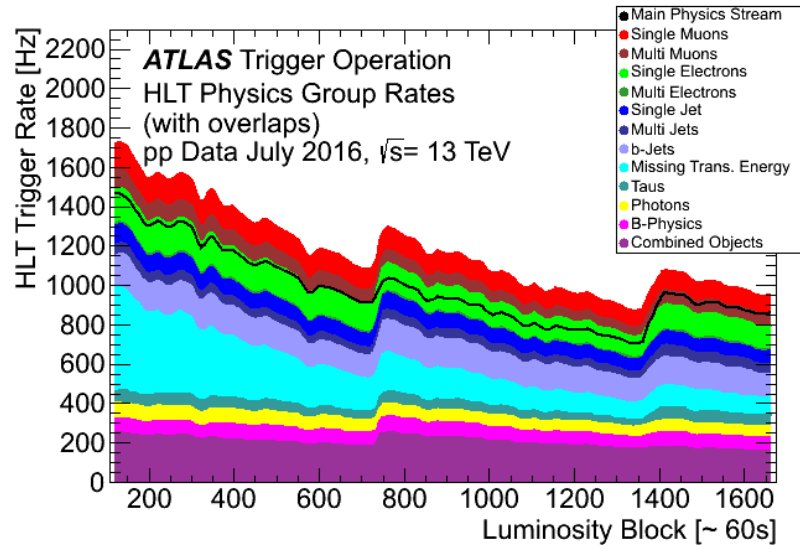


Figure 37: **HLT** trigger rates for for a run in July 2016 as a function of luminosity block, an approximately 60-second long period of data-taking. The total rate is lower than the combined stack because of overlapping triggers.

passing these triggers when they are analyzed. For example, the lowest unprescaled single electron trigger in 2016 data-taking required an electron with  $p_T$  of 60 GeV. A trigger requiring electrons with  $p_T$  of only 10 GeV also exists, but only one in ten events passing this trigger is recorded.

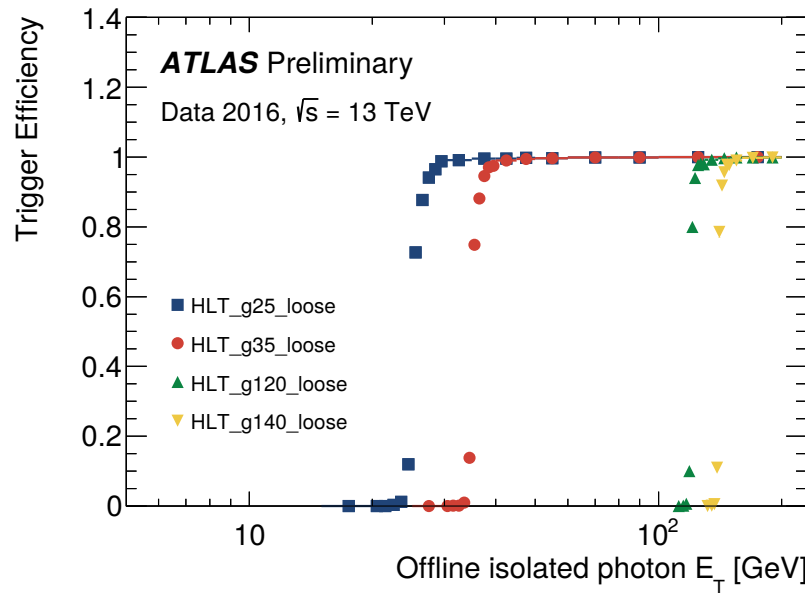


Figure 38: Photon trigger efficiency as a function of  $E_T$  for four different **HLT** triggers with photon  $p_T$  requirements of 25, 35, 120, and 140 GeV [44].

## 1196 4.7 MONTE CARLO EVENT GENERATION

1197 The complex events of the LHC are difficult to model, but modeling them  
1198 is crucial to analyzers' understanding of SM backgrounds and potential  
1199 signals. To simplify the modeling process, particle interactions are broken  
1200 down into very small steps, each with associated probabilities of various  
1201 outcomes. This modeling method is called Monte Carlo simulation (MC),  
1202 and, at the LHC it is broken into several larger steps which are each han-  
1203 dled by different software.

1204 The first step, discussed in [Section 2.1.3](#), is to determine the energies  
1205 of the initial particles in a collision, which are provided by several differ-  
1206 ent PDF sets. These distributions come from experimental measurements,  
1207 though there is some variation between different sets. Three different sets  
1208 are used in this analysis: NNPDF2.3LO [45] and NLO CT10 [46] for back-  
1209 ground and signal processes, and MSTW 2008 [15] for pile-up events, dis-  
1210 cussed more in [Section 3.4](#).

1211 With the initial states of the constituents of the protons described by  
1212 these probabilistic models, the next step is to model the hard scattering  
1213 process resulting from the interaction of two of these particles. This is  
1214 accomplished by a generator, which calculates the cross-sections of the  
1215 Feynman diagrams of a given process. In particular, these generators typi-  
1216 cally produce matrix elements, which describe the probability to go from  
1217 an initial to final state via a hard scattering, including the kinematic prop-  
1218 erties of the final state. The generator uses these matrix elements to assign  
1219 one of these hard scattering final states to each event. These hard scat-  
1220 tering outputs are then passed to the next step, where parton showering,  
1221 hadronization, and final and initial state radiation can occur.

1222 Because these matrix elements must be calculated for each event's spe-  
1223 cific kinematic properties, it can be very computationally intensive, espe-  
1224 cially when the calculations are performed at very high order. To save  
1225 computational time, matrix elements are sometimes calculated at a lower  
1226 order, and later, the total cross-section for a given process can be calculated  
1227 at a higher order and used to scale the overall number of events generated  
1228 for the process. These calculations can also be tuned, varying parameters  
1229 in the generation to create outputs that most closely match experimental  
1230 data.

1231 Examples of generators include MADGRAPH5\_AMC@NLO [47], POWHEG  
1232 Box [48–50], and SHERPA [51]. Each has different strengths and is used  
1233 to describe processes that best match those strengths. POWHEG Box, for  
1234 example, cannot perform its own parton showering, and must be inter-  
1235 faced with another generator, typically PYTHIA [52], in order to describe  
1236 any physics processes beyond the hard scattering, which can cause dis-  
1237 continuities in its predictions for large numbers of partons. However, it  
1238 can calculate matrix elements at NLO, giving it an advantage in calculating  
1239 some complex processes. SHERPA performs its own parton showering, but  
1240 in most cases calculates its matrix elements at LO. The main advantage  
1241 of MADGRAPH5\_AMC@NLO, which must also be interfaced with another

generator (typically PYTHIA) to perform parton showering, is its simple user interface. Instead of designating specific processes to be generated, it allows users to specify a final state to be generated, and all processes capable of producing that state will be included.

Once the final state particles of the hard interaction and showering have been calculated, the pile-up of the LHC (described in Section 3.4) must be accounted for. Events called *minimum bias* are generated to match the overall production of the LHC collisions, with no preselection. These events are overlaid on the original hard scatter to produce a more realistic representation of the many simultaneous interactions observed in the ATLAS detector.

This collection of particles must then be translated into signals in the detector. Their trajectories in the magnetic fields of the detector, their interactions in each layer, and the way these interactions deposit charge in each subdetector are modeled in software called GEANT4 [53]. In this software, every piece of the ATLAS detector is modeled, including the magnetic field and the many different materials. Particles then follow trajectories through the simulated detector and interact with the different materials based on several preprogrammed options for each material. For example a photon traveling through a material could continue along its trajectory, convert into a positron-electron pair, or deposit energy. As it crosses into a new material, a new set of options opens up for interactions. The particle is tracked until all of its energy is lost or it exits the geometry of the simulation.

The model of the detector used for this process is iteratively perfected by comparing data to MC. Figure 39 shows an example of a discrepancy between the simulation and observed data in the number of secondary vertices in a pixel module, which should correspond to the amount of material in the area. Observations of discrepancies like this can be used to correct the materials in the simulation.

Custom ATLAS code converts the energy deposited in active sensors into signals that resemble the expected detector response. These responses are typically very complicated with many parameters, and are frequently iterated on to best match the data. Electronic noise must also be added to correctly approximate the operating conditions of the detector. Additional alterations to this signal translation, including dead sensors and misalignments of the detector, can also be added at this stage.

Once the simulated particles have been converted into detector signals, the same reconstruction software used on data can be used on the MC, converting the detector signals back into particle interpretations. This reconstruction process is described in Chapter 6. The original information about the particles from the generator, referred to as *truth* information, is also kept, and can be compared to the reconstruction output to study its efficacy.

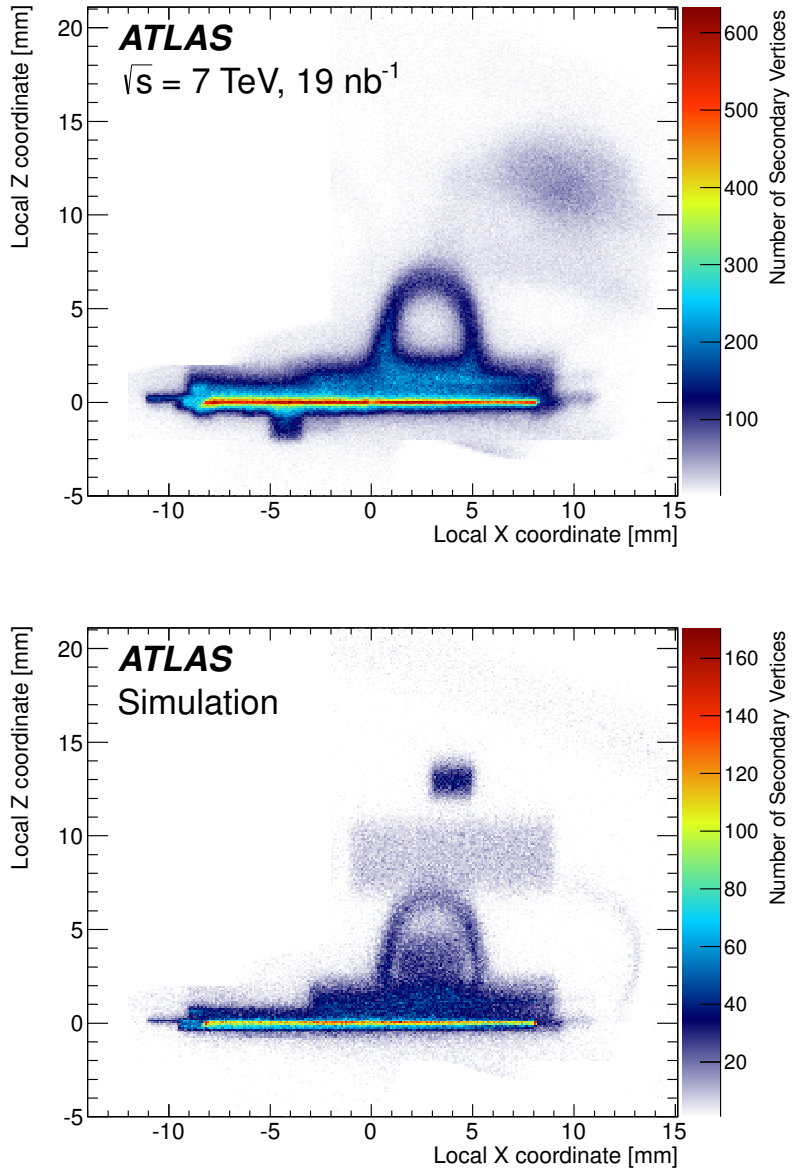


Figure 39: Number of secondary vertices in a module in the first layer of the pixel detector in data (top) and MC (bottom). There are more events in the data than the MC [54].



1286  
 1287 INNER DETECTOR TRACKING AND PIXEL  
 1288 CLUSTERING

---

1289 5.1 OVERVIEW OF TRACKING IN THE ATLAS DETECTOR

1290 Creating tracks from individual hits in the Inner Detector is one of most  
 1291 challenging parts of the reconstruction of [ATLAS](#) events. Each event typi-  
 1292 cally contains thousands of hits in the pixel detector alone, which must  
 1293 be combined into one coherent picture of which particles traversed the  
 1294 detector, and how they moved and lost energy as they traveled. A typi-  
 1295 cal particle deposits charge in several pixels per layer, forming a series of  
 1296 clusters which can be connected together to form a track. This track can  
 1297 in turn be used to measure the charge, momentum, and trajectory of the  
 1298 particle.

1299 An example of this process can be seen in [Figure 40](#), which shows the  
 1300 tracks formed in an event and the corresponding hits in the Pixel Detec-  
 1301 tor and the [SCT](#). In the  $r - z$  view, the multiple vertices formed by sim-  
 1302 taneous interactions are visible. This event has 17 reconstructed vertices,  
 1303 slightly less than the Run 2 average.

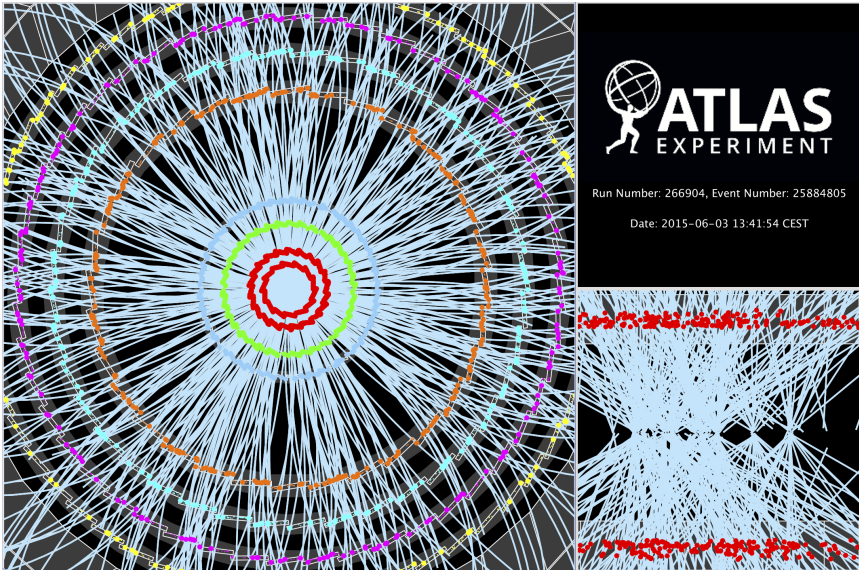


Figure 40: Event display from June 2015, with particle tracks in light blue. The main image displays a view of the  $x - y$  plane of the [ID](#). The [IBL](#) and Lo of the Pixel Detector are shown in red, with the remaining two layers of the Pixel Detector in green and blue. Outside those are the four double layers of the [SCT](#). The smaller image on the right shows an  $r - z$  view, zoomed in to only show hits in the [IBL](#) [55].

1304 In order to used to form tracks, hits from the [ID](#) must first be pre-  
 1305 processed [56]. Nearby Pixel and [SCT](#) hits are turned into clusters, which

1306 serve as the input to the tracking system, rather than individual hits. The  
 1307 details of Pixel clustering are discussed in [Section 5.2](#). The [SCT](#) clusters  
 1308 are translated into space-time points using the two measurements from  
 1309 its paired layers. In the [TRT](#), drift times are used to reconstruct the parti-  
 1310 cle's distance from the center of the tube, forming *drift-circles* that indicate  
 1311 possible particle positions.

1312 Next, seed tracks are formed using the clusters in the Pixel Detector and  
 1313 the first layer of the [SCT](#). The seed tracks are extended to the remainder  
 1314 of the [SCT](#), and are fit. Using the fit quality, any outlier clusters associated  
 1315 with the track are removed.

1316 At this stage, quality cuts are made to remove fake tracks. The track-  
 1317 ing algorithm then identifies *holes*, points where the track passes through  
 1318 an active sensor, but no cluster exists. Tracks with too many holes are re-  
 1319 moved, as are tracks with a high fraction of clusters shared with other  
 1320 tracks.

1321 The remaining tracks are extended to the [TRT](#), where they are matched  
 1322 to drift-circles. The tracks are then re-fit to include all the [ID](#) subdetectors.  
 1323 In the case that this fit is worse than the fit without the [TRT](#), outlier [TRT](#)  
 1324 hits are identified and the track is re-fit without them.

1325 Afterwards, unassociated hits in the [TRT](#) are formed into track segments,  
 1326 which can be extended back to the [SCT](#) and Pixel Detector to form complete  
 1327 tracks. This method is especially useful for identifying tracks that did not  
 1328 originate from the initial hard-scattering interaction.

1329 Lastly, this collection of tracks is used to reconstruct vertices. First, tracks  
 1330 are associated with primary vertices, which must be consistent with the  
 1331 [ATLAS](#) beam spot. Following this, secondary vertices are formed, which  
 1332 can result from long-lived particles or interactions with the detector.

## 1333 5.2 CLUSTERING IN THE PIXEL DETECTOR

1334 The process of going from clusters to a track is relatively simple in an  
 1335 isolated environment in which one particle travels cleanly through all the  
 1336 layers, but can be complicated by multiple close-by particles, which can  
 1337 produce hits that are merged into one cluster. Clusters can also have mis-  
 1338 leading shapes due to a particle's emission of other low-energy particles,  
 1339 called  $\delta$ -rays [57]. In these cases, it can be hard to tell how many particles  
 1340 were involved in creating a cluster, and where exactly each of those parti-  
 1341 cles passed through the layer. A few examples of particle interactions with  
 1342 the pixel sensor can be seen in [Figure 41](#).

1343 Clusters are initially made by a process called Connected Component  
 1344 Analysis ([CCA](#)). In this process, pixels with hits above a charge thresh-  
 1345 old are identified in each layer, and are grouped together if they share any  
 1346 edge or corner. The position of the resulting cluster is defined by local  
 1347  $x$  and  $y$  coordinates, which are defined relative to the module on which  
 1348 the cluster appears. Determining the position of the particle that formed  
 1349 that cluster is less straightforward, and has recently been updated from a  
 1350 charge interpolation method to a method using a Neural Network ([NN](#)).

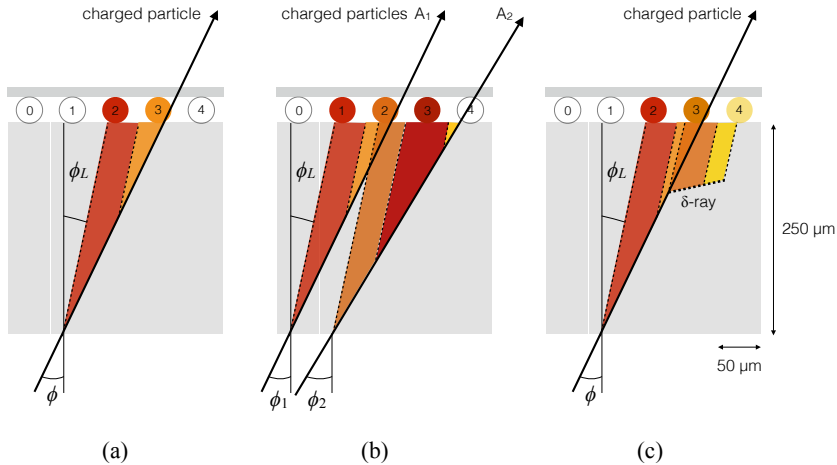


Figure 41: A few possible types of clusters in the Pixel Detector. (a) shows a single particle passing through a layer of the detector, (b) shows two particles passing through the detector, creating a single merged cluster, and (b) shows a single particle emitting a  $\delta$ -ray as it passes through the detector [57].

### 1351 5.2.1 Charge Interpolation Method

1352 A typical cluster contains a few pixel hits spanning in the  $x$  and  $y$  direc-  
 1353 tions, each with its own measurement of charge deposition. In the charge  
 1354 interpolation method, these individual hits are combined to make one esti-  
 1355 mation of the position a single particle which passed through them, using  
 1356 the following equation:

$$x_{cluster} = x_{center} + \Delta_x(\phi, N_{row}) \cdot \left[ \Omega_x - \frac{1}{2} \right] \quad (32)$$

$$y_{cluster} = y_{center} + \Delta_y(\phi, N_{col}) \cdot \left[ \Omega_y - \frac{1}{2} \right] \quad (33)$$

1357 where  $\Omega_{x(y)}$  is defined by

$$\Omega_{x(y)} = \frac{q_N}{q_1 + q_N} \quad (34)$$

1358 and  $q_1$  gives the total charge in the first row (column), and  $q_N$  gives  
 1359 the total charge in the last row (column).  $\Delta_{x(y)}$  is a function derived from  
 1360 either data or MC and produces an output related to the projected length  
 1361 of the particles track on the pixel sensor and is measured as a function of  
 1362  $\phi$ , the incident angle of a particle on the sensor, and  $N_{row(col)}$ , the number  
 1363 of pixels in the cluster in the  $x$  and  $y$  direction.

1364 In a simple case, such as (a) of Figure 41, this method works well. How-  
 1365 ever, in cases like (b), it has no ability distinguish two-particle from one-  
 1366 particle clusters, and assigns a cluster center between the two particles'

locations, despite the intermediate pixel having the lowest charge. Furthermore, because this method doesn't differentiate two-particle clusters, the tracking software can't use that information to determine if multiple tracks may share two-particle clusters. Allowing tracks to share clusters indiscriminately in dense track environments creates fake tracks from the many possible cluster combinations. In cases like (c), the  $\delta$ -ray will bias the measurement of the particle's position in whichever direction it is emitted.

### 1374 5.2.2 Improving Measurement with Neural Networks

1375 To address these problems, a series of NNs was created [57]. The first esti-  
 1376 mates the number of particles in a given cluster, the second estimates their  
 1377 positions within the cluster, and the third assesses the uncertainty of the  
 1378 position measurement. They are referred to, respectively, as the *Number*,  
 1379 *Position*, and *Error NNs*.

1380 These NNs are taken from the AGILEPack library [58], and trained using  
 1381 simulated ATLAS MC. Each NN is given the following inputs:

- 1382 • a  $7 \times 7$  grid of cluster `Tot` information<sup>1</sup>
- 1383 • a 7-element vector containing the  $y$ -size of the pixels in the grid<sup>2</sup>
- 1384 • the layer of the pixel detector that the cluster was observed in
- 1385 • a variable indicating whether the cluster is located in the barrel or  
 1386 endcap
- 1387 •  $\theta$  and  $\phi$  variables projecting the incident angles of the particle on the  
 1388 sensor<sup>3</sup>
- 1389 • the pixel module's  $\eta$  index, a label assigned to each module that  
 1390 differentiates modules based on their  $\eta$  position

1391 Each NN is trained with truth information to make predictions about  
 1392 cluster features. The Number NN predicts the number of particles asso-  
 1393 ciated with the cluster, required to be between 1 and 3. Then, the same  
 1394 inputs are fed into one of three Position NNs, each identified by the num-  
 1395 ber of particles it attempts to locate, according to the prediction from the  
 1396 Number NN. The Position NN outputs a prediction of the  $x$  and  $y$  positions  
 1397 of each particle, and these predictions are used as inputs to the Error NN,  
 1398 in addition to the inputs listed above.

1399 The training of the Error NN is slightly more complicated than the oth-  
 1400 ers, as it makes a prediction of the efficacy of the previous NN. It is trained

---

<sup>1</sup> Clusters spanning more than seven pixels in either direction are rare, but when they occur they are rejected, and the original charge interpolation estimate of a single particle's position is kept.

<sup>2</sup> The pixel detector contains some long pixels at the edges of modules, and this is intended to help the NN identify these cases.

<sup>3</sup> If the NN is applied before tracking is performed, these angles project to the nominal interaction point, and if tracking has already been performed, the angles are taken from the track fit to the cluster.

1401 to predict the difference between the Position **NN**'s outputs and the true  
 1402 positions of the particles. In the training, cases in which the Number **NN** in-  
 1403 correctly assessed the true number of particles in the cluster are excluded.

1404 An example of the output of this process can be seen in [Figure 42](#),  
 1405 where the improved position resolution from the ability to identify a multi-  
 1406 particle cluster is evident.

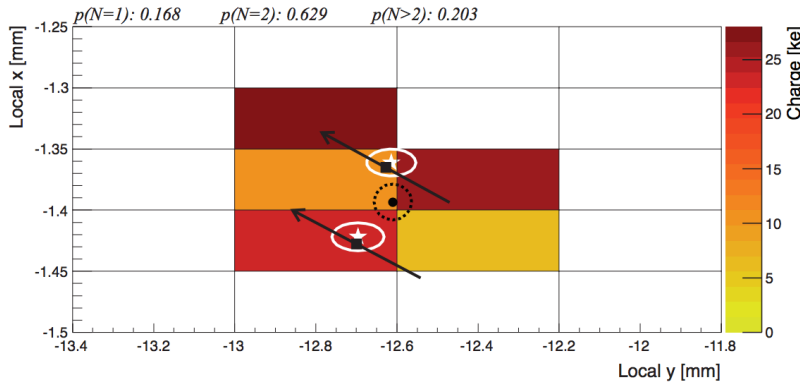


Figure 42: One example of a two-particle cluster and its truth information compared with the output of the **NNs**. The boxes represent pixels, with a color scale indicating charge. At top, the  $p(N = i)$  values give the output of the Number **NN**, the probabilities that the cluster contains 1, 2, and 3 particles. Given the highest probability is for  $N = 2$ , the other **NNs** predict the postion and errors of the two particles (in white). The black arrows and squares represent the truth information from the cluster, and the black dot and dotted line show the position measurement for the un-split cluster [57].

1407 The particle location predictions from the **NNs** are then handed to the  
 1408 tracking software, which now can use these multiple particle position es-  
 1409 timations as independent hits to be fit. As a result, tracks in dense envi-  
 1410 ronments have fewer clusters shared between multiple tracks, and their  
 1411 trajectories are known to a greater degree of precision.

## 1412 5.3 IMPACT OF THE NEURAL NETWORK

1413 The **NN** was first applied to 7 TeV data, where it improved position res-  
 1414 olution for particles in small and large clusters. [Figure 43](#) shows the im-  
 1415 provement from the addition of the **NN** in  $x$  resolution in different cluster  
 1416 sizes. The improvement from charge interpolation clustering is particu-  
 1417 larly evident in the 4-pixel case, where the double peaked structure of the  
 1418 interpolation method has been completely removed with the **NN**.

### 1419 5.3.1 The Neural Network in 13 TeV Data

1420 In Run 2, the tracking algorithm is first run on the **CCA** clusters with posi-  
 1421 tions determined via charge interpolation, where it constructs tracks with  
 1422 loose quality requirements. In this step, the tracking algorithm allows

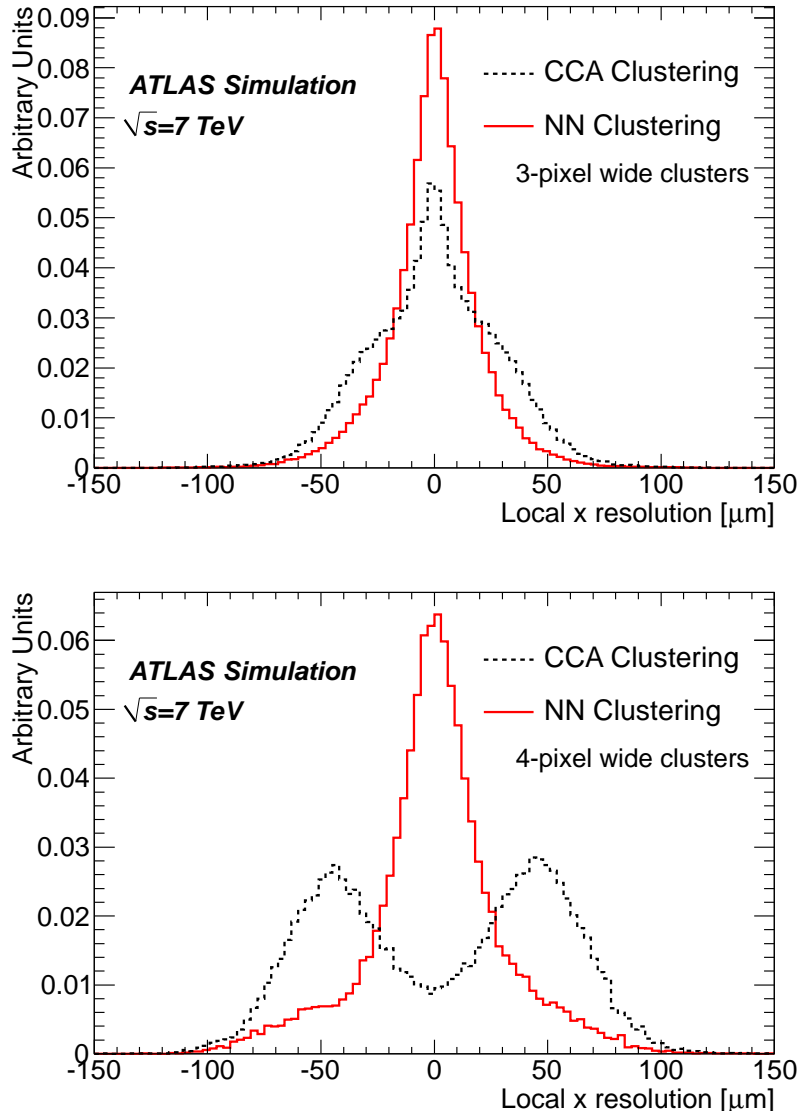


Figure 43:  $x$  resolutions for clusters with 3 (top) and 4 (bottom) pixels in the  $x$  direction in 7 TeV data for **CCA** (using only charge interpolation to determine position) and **NN** clustering taken from **MC** [57].

shared clusters, clusters used in multiple track fits [59]. The **NN** is then used to identify which clusters are likely to have had multiple particles pass through them, and to estimate the positions of those particles. In the case that the cluster is determined to have resulted only from one particle, tracks that share that cluster are penalized. In general, tracks with more than two shared clusters are rejected.

Because the **NN** is trained only with **MC** simulations, any mismodeling of the way charge is deposited in the **ATLAS** detector could cause the **NN** to perform in an unexpected way when applied to data. The potential impact of this mismodeling was investigated with 13 TeV **MC** [60]. The goal of these studies was to determine which variables the **NN**'s predictions were

1434 most sensitive to, and whether it was likely that these variables could be  
1435 mismodeled enough to produce unexpected results in data.

1436 One example of a variable capable of significantly altering the **NN** out-  
1437 puts was the overall charge scale. To study its impact, the **ToT** of all pixels  
1438 in a cluster were scaled up and down, and the resulting outputs of the  
1439 **NN** were compared, as shown in [Figure 44](#). In this case, the likelihood to  
1440 misidentify multi-particle clusters and single-particle clusters depended  
1441 significantly on this scaling. However, this scaling is unlikely to be mis-  
1442 modeled by more than 10%, so very extreme effects from a difference be-  
1443 tween data and **MC** are unlikely. Overall, it was found that variations on  
1444 the cluster charge produced a significant impact on predictions, while all  
1445 other variations, such as incidence angle variation and spatial smearing of  
1446 charge, had a minimal effect.

1447 In addition to studies on the impact of alterations of individual simula-  
1448 tion variables, studies directly comparing the **NN** output in data and **MC**  
1449 were performed. [Figure 45](#) shows a comparison of how often the **NN** identi-  
1450 fies different types of clusters in data and **MC**. Each figure is made using by  
1451 selecting pairs of collimated tracks that share a common cluster on a given  
1452 layer, then calculating the fraction of those clusters that are determined by  
1453 the **NN** to be single or multi-particle clusters. This fraction is plotted as a  
1454 function of the distance between the two tracks in the cluster's layer. Very  
1455 good agreement is seen between the two samples, demonstrating that the  
1456 **MC**-trained **NN** performs similarly on both **MC** and data.

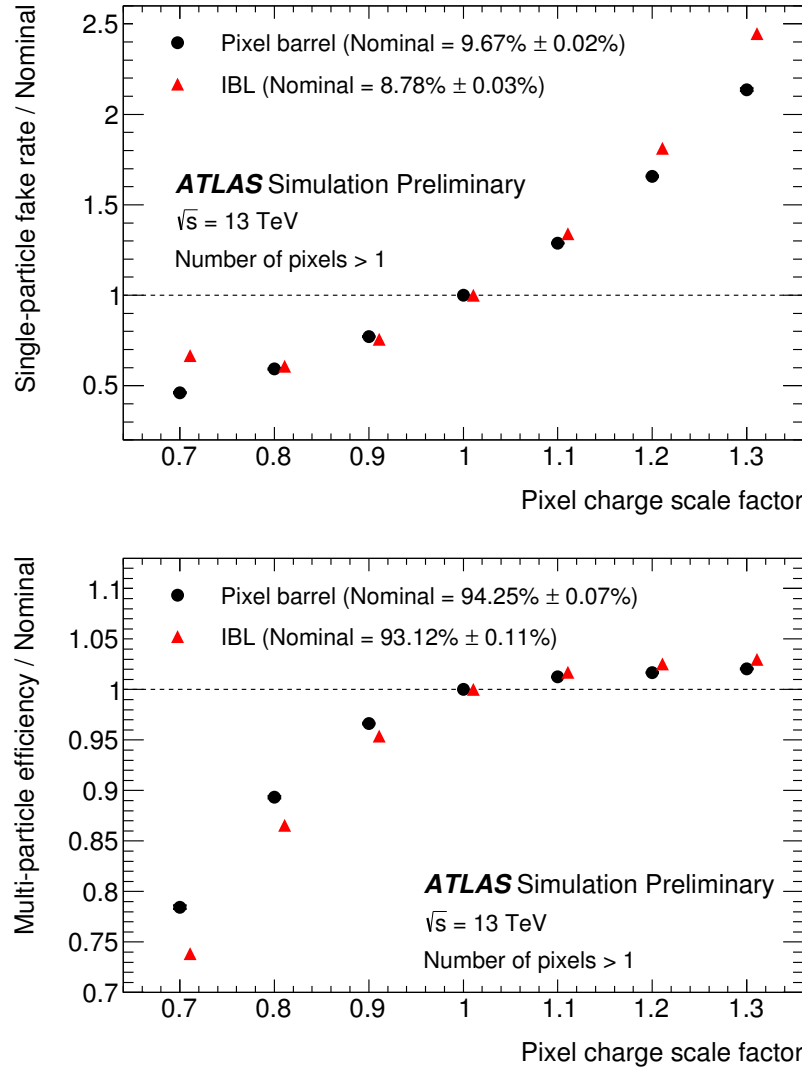


Figure 44: Performance of the pixel neural network used to identify clusters created by multiple charged particles, as a function of constant coherent scaling of the charge in each pixel in the cluster. The top figure shows the rate at which the neural network wrongly identifies clusters with one generated particle as clusters with multiple particles. The bottom figure shows the rate at which the neural network correctly identifies clusters generated by multiple particles as such.

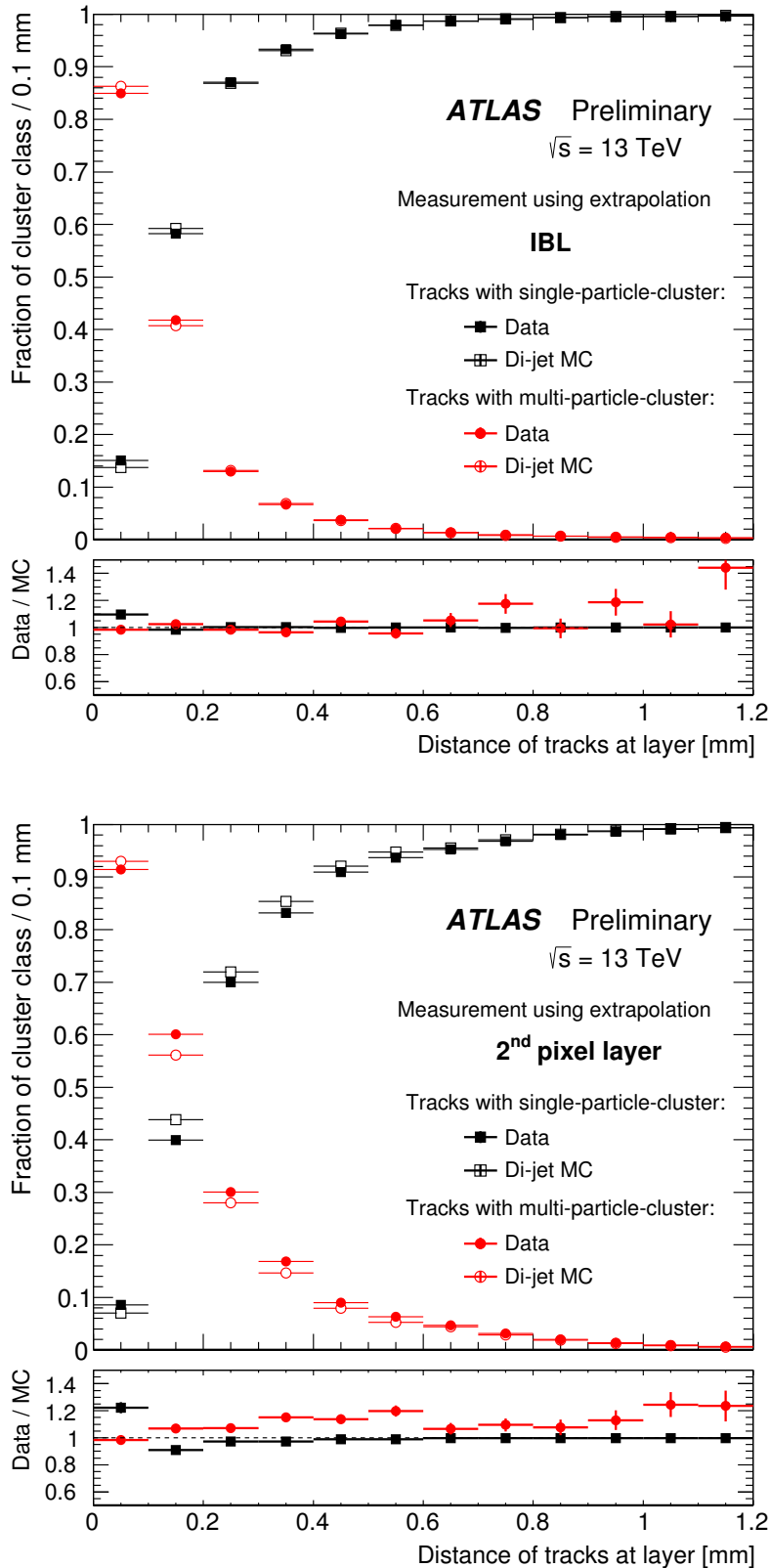


Figure 45: Fraction of cluster classes as a function of the distance between tracks for IBL (top) and 2nd pixel layer (bottom).



1457

1458 OBJECT RECONSTRUCTION IN THE ATLAS DETECTOR

---

1459 Object reconstruction is the computationally intensive process of interpreting  
 1460 the signals from the approximately 100 million read-out channels of  
 1461 the [ATLAS](#) detector into a collection of particles and jets, the objects with  
 1462 which physics analysis can be performed. This process is complicated, and  
 1463 requires dedicated working groups in the [ATLAS](#) experiment that optimize  
 1464 the understanding of each type of object. These groups must all collabo-  
 1465 rate to provide a full picture of the events in the detector. For each object  
 1466 type, candidate objects are reconstructed, and then an identification step  
 1467 is performed, which chooses which candidates will be used at the analysis  
 1468 level, based on a series of quality requirements.

## 1469 6.1 ELECTRONS

1470 Electrons are reconstructed through a combination of [ID](#) and calorimeter  
 1471 measurements. They travel through the tracking system, leaving charge de-  
 1472 posits in each layer, then are absorbed by the electromagnetic calorimeter.  
 1473 These two measurements work in conjunction to deliver high resolution  
 1474 measurements of electron momentum from low- $p_T$ , where track curvature  
 1475 gives the most reliable measure of the electron's energy, to high- $p_T$ , where  
 1476 the tracks are almost perfectly straight, but the calorimeter can still pro-  
 1477 vide a reliable measurement.

1478 In the central region ( $|\eta| < 2.47$ ) of the [ATLAS](#) detector, electron recon-  
 1479 struction begins with the identification of energy deposits in the electro-  
 1480 magnetic calorimeter. The clusters of calorimeter cells are seeded by slid-  
 1481 ing longitudinal windows, which are measured in units of 0.025 in  $\eta$  and  $\phi$ .  
 1482  $3 \times 5$  unit windows are used, which require at least 2.5 GeV in the window  
 1483 to form a seed [61].

1484 These clusters are matched to [ID](#) tracks by extrapolating each track to the  
 1485 middle layer of the calorimeter and identifying nearby clusters. If there are  
 1486 multiple tracks associated with a given cluster, tracks with silicon hits are  
 1487 preferentially chosen, and then the track with the smallest  $\Delta R$  to the center  
 1488 of the cluster is selected. If a matching track is found, it is used to deter-  
 1489 mine the likely direction of bremsstrahlung radiation in the calorimeter,  
 1490 and maximum distance to match a track to a cluster is expanded in the  $\phi$   
 1491 direction to account for this radiation. If no track is found, the cluster is  
 1492 rejected.

1493 The calorimeter clusters are then rebuilt in larger windows,  $3 \times 7$  in the  
 1494 barrel and  $5 \times 5$  in the endcaps. An estimate of the energy is made by sum-  
 1495 ming the measured calorimeter energy with estimates of the energy lost  
 1496 before the electron reached the calorimeter, energy outside of the cluster  
 1497 window, and energy not fully deposited in the calorimeter. These estimates

1498 are made with parametrized functions determined from a combination of  
 1499 MC and measurements of energy loss determined with the presampler.

1500 The  $p_T$  of a central electron is determined through a combination of the  
 1501 calorimeter energy measurement and track measurements of the electron,  
 1502 while its  $\eta$  and  $\phi$  are taken from the track at its vertex.

1503 In the forward region, where no tracking is available, electron energy is  
 1504 determined more roughly. Calorimeter cells are formed into variable-sized  
 1505 clusters in regions of significant energy deposition, and the center of the  
 1506 cluster is used to determine angular coordinates of the electron. However,  
 1507 because these electrons have worse resolution in both their position and  
 1508 energy, they are rejected in this analysis.

1509 These reconstructed electron candidates' quality are then assessed based  
 1510 on an algorithm that uses multivariate analysis to assign a likelihood that  
 1511 a candidate is a true electron based on input from just under twenty differ-  
 1512 ent variables. These include track quality, hadronic leakage, cluster shape,  
 1513 and transition radiation, incorporating information from as many subde-  
 1514 tectors as possible in its determination of the candidate's quality. Each  
 1515 variable is assigned a probability distribution function for true electrons  
 1516 and background processes, and they are collectively used to provide a  
 1517 *likelihood* value which can be cut on.

1518 Three levels of identification, Loose, Medium, and Tight, are defined with  
 1519 different likelihood cuts, with electron candidates passing tighter identifi-  
 1520 cation levels always a subset of looser electrons. Figure 46 gives the effi-  
 1521 ciencies at each of these working points both for true electrons and for  
 1522 hadrons, which can be misidentified as electrons. Tighter working points  
 1523 have worse efficiencies, but lower misidentification rates for hadrons as  
 1524 well as photons.

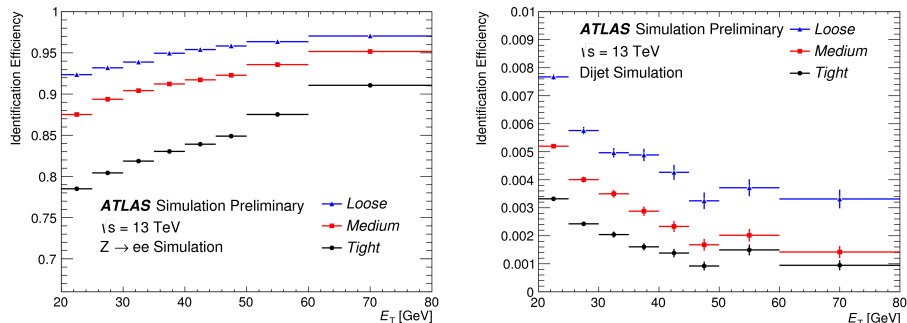


Figure 46: Identification efficiencies from MC samples for Loose, Medium, and Tight working points. Left is the efficiency for identification of true electrons taken from  $Z \rightarrow ee$  MC, and right is the efficiency for misidentification of jets as electrons taken from dijet MC [62].

1525 MC efficiencies can be compared to efficiencies measured in data to ob-  
 1526 tain a correction factor, which applied to MC to better emulate the rates at  
 1527 which electrons are reconstructed and identified in data. Figure 47 shows a  
 1528 comparison of the combined reconstruction and identification efficiencies  
 1529 in data and MC, with the resulting correction factors also displayed as the

ratio. This analysis uses the Medium working point, which has correction factors ranging between 2 and 10%.

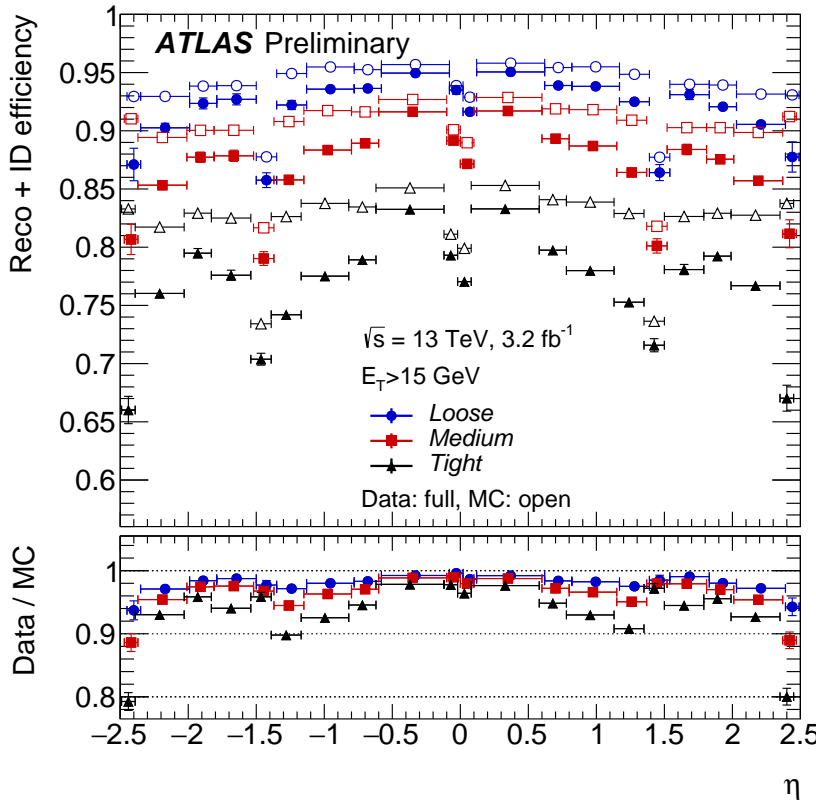


Figure 47: Combined electron reconstruction and identification efficiencies measured as a function of  $\eta$  for data (using the tag-and-probe method on  $Z \rightarrow ee$  events) and  $Z \rightarrow ee$  MC. Distributions include electrons with  $E_T > 15 \text{ GeV}$ . [62].

Requirements are also made on electron *isolation*, which quantifies the amount of energy deposited near the electron according calorimeter and track measurements. Isolation variables are primarily used to reject non-prompt leptons, leptons which aren't produced by the initial hard scattering of the  $pp$  collision. These can be produced by heavy flavor hadron decays and converted photons, as well as misidentified hadrons. Cuts are made on the amount of nearby calorimetric energy and sum of the  $p_T$  of any nearby tracks relative to the electron's energy, forming a series of working points. Working points are created based on their efficiency, including Tight and Loose working points, which operate at 95 and 98% efficiency respectively. The most effective working points target different efficiencies as a function of  $p_T$ , with higher efficiencies possible at high  $p_T$  due to reduced fake backgrounds. There are two such working points, Gradient and GradientLoose. They each have a 99% efficiency for electrons with  $p_T > 60 \text{ GeV}$ , but 90 and 95% efficiencies at 25 GeV. To recover the largest possible fraction of electrons, this analysis uses GradientLoose.

## 1548 6.2 PHOTONS

1549 The reconstruction of photons is performed in parallel to electron recon-  
 1550 struction. Seed clustering is performed, and tracks are matched to these  
 1551 clusters, as in the case of the electron reconstruction described in [Sec-  
 1552 tion 6.1](#).

1553 Photons can be converted to electron-positron pairs in the [ID](#), leaving  
 1554 a pair of tracks, or they can pass through without conversion, leaving no  
 1555 tracks behind. As a consequence, calorimeter clusters resulting from pho-  
 1556 tons can have no tracks associated with them, two tracks, or one track, in  
 1557 the case that one of the conversion tracks is not reconstructed. The recon-  
 1558 struction software attempts to identify all these scenarios and differentiate  
 1559 these clusters from electron and hadron deposits [63].

1560 Two-track clusters are required to consist of two oppositely charged  
 1561 tracks that emerge from a conversion vertex running parallel to one an-  
 1562 other. A likelihood that these tracks are from electrons is determined using  
 1563 the high threshold hits in the [TRT](#), and quality requirements are made on  
 1564 the tracks using this likelihood. For tracks with silicon hits, a loose like-  
 1565 lihood requirement of 10% is made, while tracks without silicon hits are  
 1566 required to have at least 80% likelihood. The tracks are then fit to deter-  
 1567 mine the conversion vertex, and quality cuts are made, such as requiring  
 1568 that conversion vertices within the silicon volume correspond to tracks  
 1569 with silicon hits.

1570 Single track clusters occur most often from conversions in the outermost  
 1571 layers of the [ID](#), and are more difficult to reconstruct. Tracks are typically  
 1572 lost because an electron or positron resulting from the conversion has a  $p_T$   
 1573 too low to be reconstructed, or because the two tracks are so close together  
 1574 that they're identified as a single track. The single track is required to have  
 1575 at least a 95% electron likelihood from [TRT](#) hits, and must not have a hit in  
 1576 the innermost layer of the pixel detector. The conversion vertex is defined  
 1577 as the first hit of the single track.

1578 The tracks associated with these conversion vertices are extrapolated to  
 1579 the calorimeter and matched to cluster, except in the case that there are two  
 1580 tracks that differ substantially in their  $p_T$  measurements, in which case the  
 1581 position of the conversion vertex is used for extrapolation to the calorime-  
 1582 ter, assuming a straight-line trajectory. If multiple vertices are matched to  
 1583 a single cluster, preference is given to vertices with double tracks, silicon  
 1584 hits, and finally to tracks closest to the interaction point.

1585 Any cluster with neither a conversion vertex or a track associated with  
 1586 it is identified as an unconverted photon. Clusters associated with both  
 1587 electrons and photons are assigned to one or the other based on their  
 1588 properties. Clusters are preferentially identified as photons in the case that  
 1589 they are matched to a conversion vertex in which at least one track is  
 1590 associated with both the vertex and the cluster, or if the associated tracks  
 1591 have a  $p_T$  smaller than the cluster's  $p_T$ .  $E/p$ , the ratio of the cluster and  
 1592 track energy measurements, can also be used to differentiate electrons and

1593 photons. Electron candidates are instead reconstructed as photons if they  
 1594 have  $E/p > 10$  or if the track matched to the electron has  $p_T$  below 2 GeV.

1595 Photon energy is determined in a  $3 \times 5$  ( $3 \times 7$ ) window for unconverted  
 1596 (converted) photons in the barrel, where the window is expanded to com-  
 1597 pensate for the increased spread of energy from the conversion products.  
 1598 In the endcap, the  $5 \times 5$  window is used in all cases. Like the electrons,  
 1599 the calibration of the photon's energy accounts for energy loss before the  
 1600 calorimeter, as well as energy deposited outside the cell and beyond the  
 1601 electromagnetic calorimeter.

1602 Photon identification is performed in the range  $|\eta| < 2.37$  using a se-  
 1603 ries of cuts on the shape of the shower in the electromagnetic calorime-  
 1604 ter, as well as the amount of additional energy deposited in the hadronic  
 1605 calorimeter. Photons in the the so called *crack* region of the calorime-  
 1606 ter ( $1.37 < |\eta| < 1.52$ ), where a discontinuity prevents accurate assess-  
 1607 ment of photon energy, are rejected. The photon identification has only  
 1608 one working point, called **Tight**, which has an identification efficiency  
 1609 of 53–64% (47–61%) for unconverted (converted) photons with  $E_T = 10$   
 1610 GeV and 88–92% (96–98%) for photons with  $E_T \geq 100$  GeV [64]. Effici-  
 1611 cies as a function of  $p_T$  measured in the 2016 data and compared to **MC**  
 1612 can be seen in Figure 48.

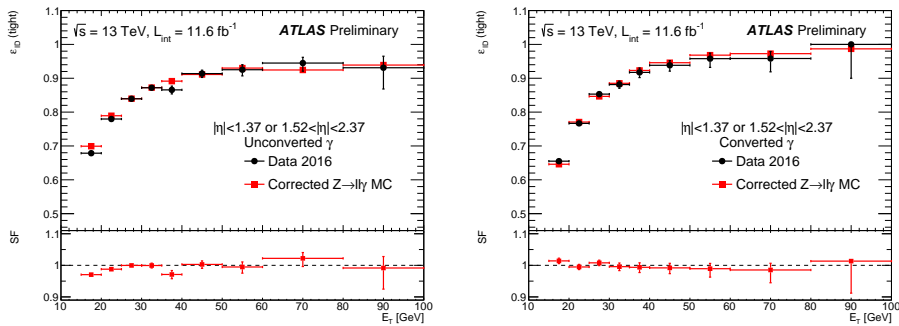


Figure 48: Comparison of Tight identification efficiency measurements from data and  $Z \rightarrow \ell\ell\gamma$  MC for unconverted (left) and converted (right) photons, with an inclusive  $\eta$  selection. The bottom of each figure shows the ratio of data and MC efficiencies. [65].

1613 Photon isolation, like electron isolation, can be determined as the com-  
 1614 bination of nearby calorimeter deposits and tracks. Fixed cuts on the iso-  
 1615 lation as a fraction of photon energy is typically used. A working point  
 1616 called **FixedCutTight** reconstructs the amount of calorimeter energy (ex-  
 1617 cluding that of the photon) in a cone of  $\Delta R = 0.4$  around the photon and  
 1618 the amount of energy from the sum of track  $p_T$  in a cone of  $\Delta R = 0.2$ ,  
 1619 including only tracks associated with the primary vertex. Defined relative  
 1620 to the photon's  $p_T$ , this working point includes photons with calorimetric  
 1621 isolation less than  $0.022 p_T + 2.45$  GeV and track isolation less than  $0.05 p_T$   
 1622 [66].

1623 6.3 MUONS

1624 Muon reconstruction is performed independently in the **ID** and the **MS**,  
 1625 then the two measurements are combined when consistent tracks are found  
 1626 in each system [67]. The **ID** reconstruction is performed using the tracking  
 1627 algorithms described in Section 5.1, and includes tracks with  $|\eta| < 2.5$ .

1628 The **MS** track reconstruction is performed in the  $|\eta| < 2.7$  range and  
 1629 begins with a search in each muon chamber for patterns of hits consistent  
 1630 with a track, called *segments*. The **MDT** chamber hits are fit to a straight line,  
 1631 and nearby **RPC** and **TGC** chambers provide the coordinate orthogonal to  
 1632 the magnetic curvature for these hits. Segments are also built in the **CSC**,  
 1633 where they are required to be loosely consistent with a track originating  
 1634 from the interaction point.

1635 These segments are then fit together, starting from the middle layers  
 1636 of the **MS**, with track quality requirements on the resulting combinations  
 1637 based on the  $\chi^2$  of the fits. Tracks must have at least two segments, ex-  
 1638 cept in the transition region between the barrel and endcap, where a sin-  
 1639 gle segment can qualify as a track. Segments are allowed to be shared  
 1640 between multiple tracks in the initial reconstruction, but after the combi-  
 1641 nation, tracks with shared segments and poor  $\chi^2$  are removed.

1642 These **MS** tracks are then combined with measurements from the **ID** and  
 1643 calorimeters. The best quality muons are combined muons, which have **ID**  
 1644 and **MS** tracks associated to them, the hits of which are re-fit to form a  
 1645 combined track. **MS** hits can be added or removed at this stage based on  
 1646 their consistency with the new track. Lower quality muon candidates are  
 1647 also defined. Extrapolated muons have only **MS** tracks and their trajec-  
 1648 tories are required to be consistent with the interaction point. Calorimeter-  
 1649 tagged muons combine an **ID** track with a calorimeter deposit consistent  
 1650 with a muon, while segment-tagged muons combine an **ID** track with a  
 1651 segment in the **MS**. Muons with shared **ID** tracks are not allowed, with  
 1652 preference given to combined muons, then calorimeter-tagged muons, and  
 1653 lastly segment-tagged muons.

1654 There are four muon identification working points for muons: Loose,  
 1655 Medium, Tight, and High- $p_T$ . These working points all have different effi-  
 1656 ciencies for the identification of muons, balanced against the mis-identification  
 1657 of hadrons. One of the key variables for their discrimination is  $q/p$  signif-  
 1658 icance, which quantifies the consistency between the **ID** and **MS** mea-  
 1659 surements of momentum. The  $\chi^2$  of the combined fit is also an important  
 1660 discriminator.

1661 The Loose, Medium, and Tight selections are inclusive, with all Tight  
 1662 muons passing the Medium requirements, and Medium muons passing the  
 1663 Loose requirements. The Medium working point includes only combined  
 1664 and extrapolated muons, and is the default for most **ATLAS** analyses, in-  
 1665 cluding this one. Extrapolated muons are allowed only outside the **ID**  
 1666 tracking system ( $|\eta| > 2.5$ ) for this working point, but this region is ex-  
 1667 cluded by this analysis because of the decreased efficiency and larger  $p_T$   
 1668 resolution of these muons. As a consequence, this analysis uses only com-

bined muons. For these muons, the Medium working point requires at least three hits in at least two MDT layers (except in the  $\eta < 0.1$  region) and a  $q/p$  significance cut is made to reduce backgrounds. Due to the lack of coverage at low  $\eta$ , there is a drop in efficiency in this region, as shown in Figure 49.

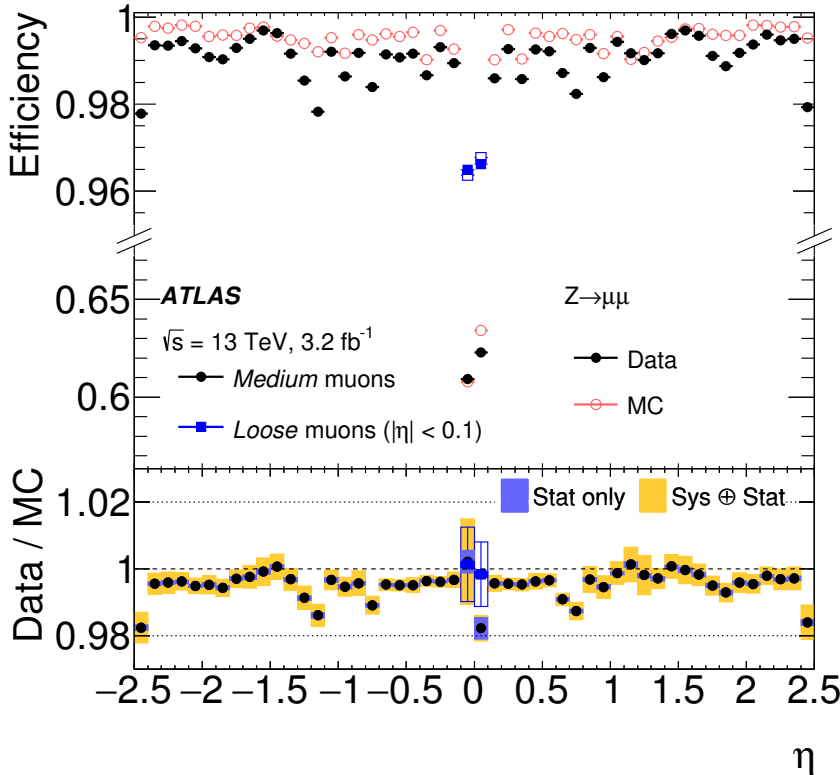


Figure 49: Muon reconstruction efficiency for the Medium and Loose working points measured with  $Z \rightarrow \mu\mu$  events in data and in MC as a function of  $\eta$ . The ratio between the two is shown at the bottom. The Loose working point efficiency is shown only at small  $|\eta|$ , where the loosened requirements cause the largest difference from the Medium working point [67].

The High- $p_T$  working point is designed to minimize the resolution for high- $p_T$  muons, at the cost of lower efficiencies. Muons passing the High- $p_T$  requirements must have at least three MDT hits in three layers, which decreases efficiency but gives greatly improved  $p_T$  resolution. In addition, some regions of the MS with poor alignment are vetoed to cut down on mismeasurement. Compared to the default working point these muons have much lower efficiency: 78% (90%) for High- $p_T$  muons compared to 96% (96%) for Medium in the  $p_T$  range of 4-20 GeV (20-100 GeV). The efficiency as a function of  $\eta$  for this working point can be seen in Figure 50, where the efficiency loss due to the of vetoing of some chambers is especially apparent. Mismodeling of the alignment and the specificity of the momentum resolution cuts cause a large discrepancy between data and MC efficiencies, resulting in scale factors that differ from unity by as much as

1687 10%. This working point was considered for this analysis, where mismeasurement  
 1688 of muons increases SM backgrounds, but ultimately the Medium  
 1689 working point was chosen for its superior efficiency and better modeling  
 1690 in MC.

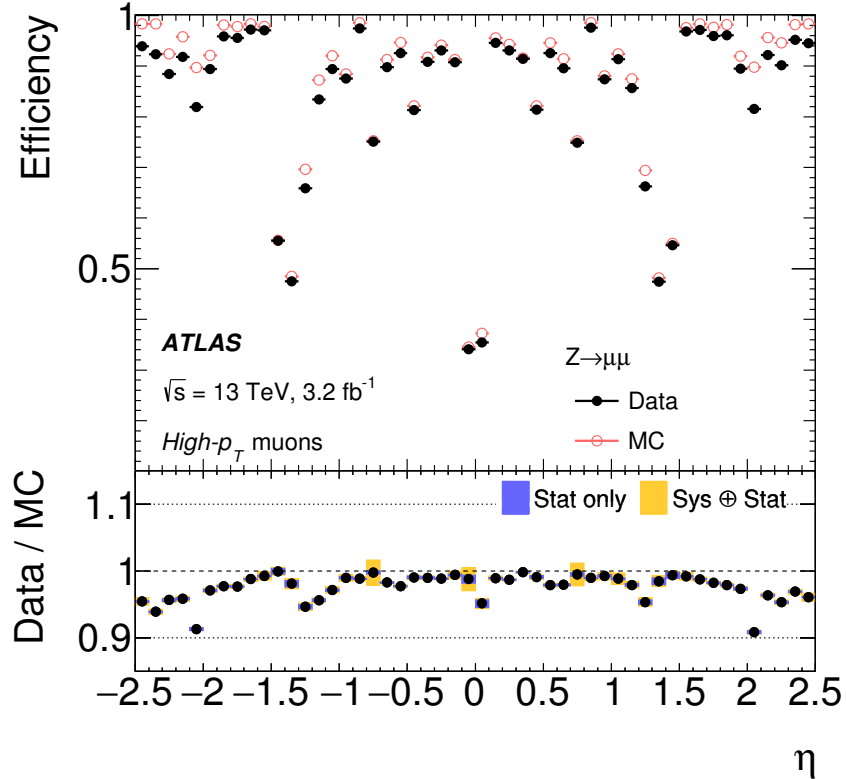


Figure 50: Muon reconstruction efficiency for the High- $p_T$  working point measured with  $Z \rightarrow \mu\mu$  events in data and in MC as a function of  $\eta$ . The ratio between the two is shown at the bottom. [67]

1691 The isolation selection for muons is designed in the same way as the elec-  
 1692 tron isolation, and also called GradientLoose. This working point makes  
 1693 cuts on a combination of nearby calorimeter- and track-based energy mea-  
 1694 surements, with an increasing efficiency as a function of  $p_T$ . The GradientLoose  
 1695 working point is constructed such that muons with  $p_T$  of 25 GeV have an  
 1696 efficiency of 95%, and muons with  $p_T$  of 60 GeV have an efficiency of 99%.

#### 1697 6.4 JETS

1698 Jets are the most complicated objects to reconstruct in the ATLAS detector  
 1699 because each jet is an assembly of many hadronic particles. In contrast to a  
 1700 lepton, whose reconstructed energy can easily be compared to its true en-  
 1701 ergy from simulation, even a jet's true energy is ambiguous, and is depen-  
 1702 dent on the choice of the jet's definition. The standard jet reconstruction  
 1703 algorithm used in the ATLAS experiment is called anti- $k_t$  [68].

This algorithm begins with clusters in the calorimeter defined by topologically connected cells with energy deposits significantly higher than the noise background. There are two collections used most commonly for analysis. One uses cluster energies calibrated for electromagnetic showers ([EM](#)), and another uses clusters calibrated to hadronic showers. The second uses a method called Local Cluster Weighting ([LCW](#)), which first determines the extent to which the cluster is electromagnetic or hadronic based on the energy density and the shower depth, then applies a calibration accordingly for each cluster.

To reconstruct jets, a set of clusters is chosen and the anti- $k_t$  algorithm is then applied. These clusters are grouped together according to the distance measure

$$d_{ij} = \min(k_{ti}^{-2}, k_{tj}^{-2}) \frac{\Delta_{ij}^2}{R^2} \quad (35)$$

where  $R$  is the algorithm's radius parameter, typically set to 0.4,  $\Delta$  gives the angular separation of the two clusters, and  $k_t$  is the transverse momentum associated with the cluster.

The grouping process begins with each cluster as a *pseudo-jet*, with its axis and  $p_T$  is determined as if it were a typical jet. Then, the pair of pseudo-jets with the smallest  $d_{ij}$  are grouped together, forming a new pseudo-jet, and its axis and  $p_T$  are reassessed. This grouping continues until there is a pseudo-jet with  $p_T$  smaller than the  $d_{ij}$  of any pseudo-jet pair, at which point this pseudo-jet becomes a jet, and is removed from the collection. The clustering process continues until all clusters are associated with a jet.

The inverse dependence on the  $k_t$  of the cluster produces jets with energetic cores and softer edges, which matches the expectation from a hadronic shower. In addition it is infrared and collinear safe, with neither soft emission nor collinear particles altering the reconstruction of the jet.

A series of calibrations are then applied to these jets. The first is to correct for additional hadronic energy due to pile-up. [Figure 51](#) demonstrates the impact of pile-up on the energy density of an event. The energy density of each jet is defined as the jet's  $p_T$  divided by the its area, and the overall event's energy density is defined as the median value of this quantity for jets with  $p_T > 20$  GeV. In events with high numbers of primary vertices, the resulting high energy density can affect the amount of stray energy associated with reconstructed jets. To remove the bias on jet energy measurements that results from multiple primary vertices, a correction factor is determined using [MC](#). It is parametrized in terms  $p_T$ ,  $\eta$ , and the number of primary vertices in the event, as well as the average number of interactions per event in the event's luminosity block, which makes correction for out-of-time pile-up possible. Next, jets are corrected to have their origin at the primary vertex instead of the center of the [ATLAS](#) detector. After that, the jets are corrected based on  $\eta$  dependent Jet Energy Scale ([JES](#)) factors derived from data and [MC](#) independently. [Figure 52](#) shows the energy response, the inverse of these factors, for [EM](#) jets. Lastly, an observed bias in the  $\eta$  measurement of jets is accounted for.

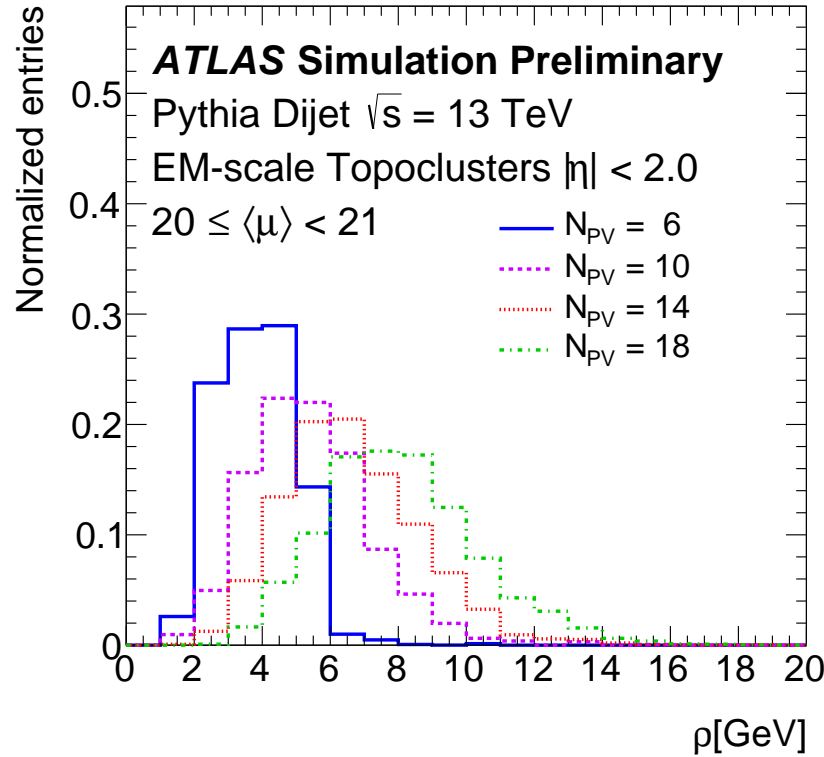


Figure 51: Distribution of event  $p_T$  density,  $\rho$ , taken from MC dijets for different numbers of primary vertices. [69]

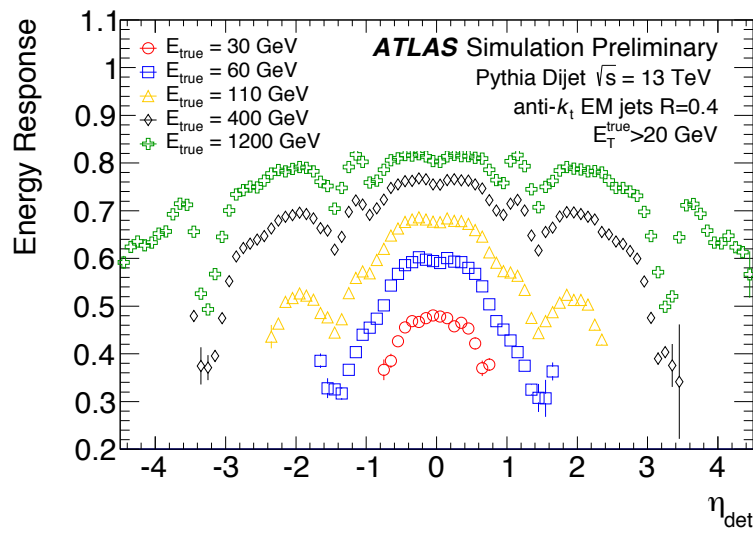


Figure 52: Energy response as a function of energy and  $\eta$  for EM jets in dijet MC. [69]

1746 In addition to correcting for additional energy due to pile-up, it is neces-  
 1747 sary to reject reconstructed jets that come from pile-up vertices. To accom-  
 1748 plish this, a multivariate algorithm called **JVT** was created which builds  
 1749 upon an older method, **JVF** [70].

1750 **JVF** gives the fraction of energy in a jet that comes from the hard-scatter  
 1751 vertex, and is defined as

$$\text{JVF} = \frac{\sum_i p_T^i(PV_0)}{\sum_j p_T^j(PV_0) + \sum_{n \geq 1} \sum_j p_T^j(PV_n)} \quad (36)$$

1752 where  $p_T^i(PV_n)$  gives the  $p_T$  of the  $i$ th track associated with the  $n$ th  
 1753 primary vertex.  $PV_0$  gives the primary vertex associated with the hard-  
 1754 scattering, while the remaining vertices are due to pile-up interactions.  
 1755 Track are associated with a jet according to a processes called *ghost as-*  
 1756 *sociation*, in which they are clustered along with the typical pseudo-jet  
 1757 collection according to the anti- $k_t$  algorithm described above. In the clus-  
 1758 tering process, the tracks energy is ignored so that it doesn't impact the  
 1759 measurement of the final jet.

1760 This fraction decreases with higher pile-up, making the construction of  
 1761 an explicit cut difficult in varying pile-up conditions. **JVT** improved on the  
 1762 method by using a pile-up corrected **JVF**-like variable, defined as

$$\text{corrJVF} = \frac{\sum_i p_T^i(PV_0)}{\sum_j p_T^j(PV_0) + \frac{\sum_{n \geq 1} \sum_j p_T^j(PV_n)}{kn_{PU}}} \quad (37)$$

1763 where  $n_{PU}$  is the number of tracks, which is multiplied by a scaling  
 1764 factor  $i = 0.01$ . This quantity is included in the inputs of the tagger along  
 1765 with other variables measuring the fraction of jet energy that is associated  
 1766 with the hard-scattering vertex. [Figure 53](#) shows the efficiency and fake  
 1767 rate for the two methods, demonstrating **JVT**'s superior stability across  
 1768 events with different numbers of pile-up vertices.

1769 It is possible to differentiate jets resulting from  $b$ -hadron decays from  
 1770 other jets due to the non-negligible lifetimes of the hadrons. Many **BSM**  
 1771 processes preferentially produce  $b$  quarks, as do any processes involving  
 1772 top quarks, so this identification can be useful for any analyses seeking  
 1773 to isolate these instances. Multivariate techniques are used to identify sec-  
 1774 ondary vertices using the **ID** [71]. In **ATLAS**, separate algorithms are used  
 1775 to identify jets with tracks with significantly non-zero impact parameters,  
 1776 tracks that reconstruct a secondary vertex, and tracks that can be identified  
 1777 with a chain of vertices beginning with the primary vertex. This informa-  
 1778 tion is fed into a boosted decision tree, a type of multivariate algorithm,  
 1779 called **MV2c20**, which outputs a discriminant shown in [Figure 54](#). Using  
 1780 this discriminant, a working point is chosen such that  $b$ -jets can be identi-  
 1781 fied with a 70% efficiency, with mis-identification rates at around 12% for  
 1782  $c$ -jets and 0.2% for light-flavor jets.

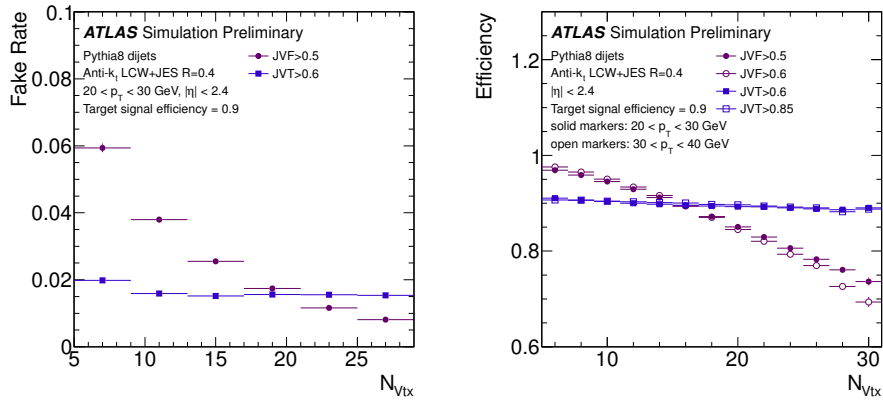


Figure 53: Dijet MC distributions of the number of pile-up jets passing the JVT and JVF cuts (left) and the efficiency for jets from the primary vertex (right) as a function of number of primary vertices in the event [70].

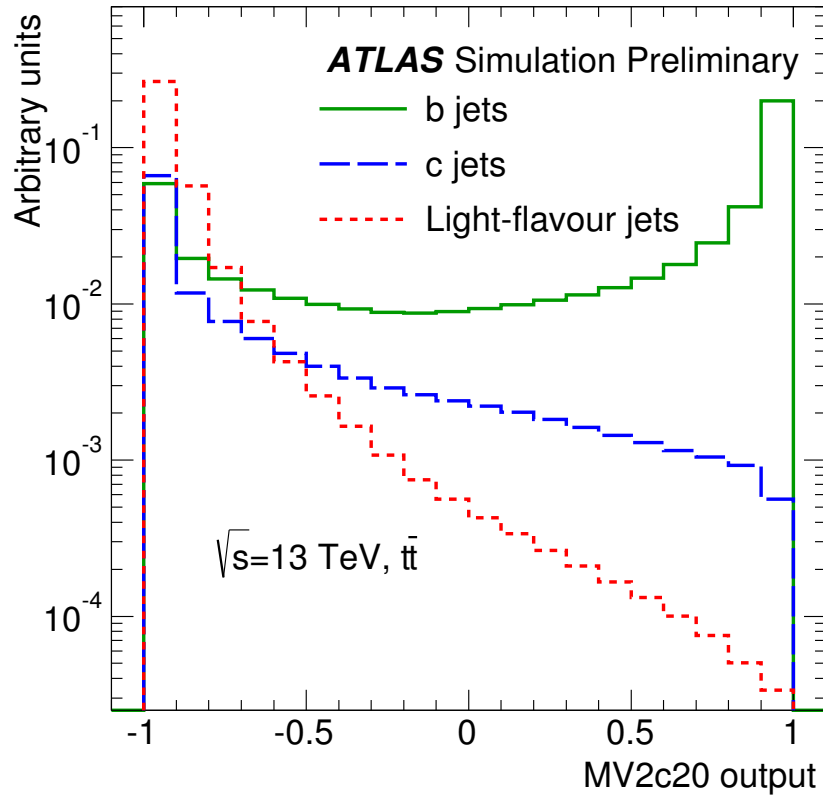


Figure 54: Distribution of MV2c20 output for  $b$ -jets,  $c$ -jets, and light-flavor jets in  $t\bar{t}$  MC [71].

## 1783 6.5 OVERLAP REMOVAL

1784 Because most of these reconstruction methods are run independently, it  
 1785 is common for energy deposits and tracks to be shared between jets and  
 1786 particles of different types. To account for this, a process called Overlap  
 1787 Removal (OR) is used, which iteratively removes overlapping objects. The

process, as well as the calculation of missing transverse momentum described in [Section 6.6](#), is performed on *baseline* objects. These objects have looser selections than the final *signal* objects, and the separate definitions allow analyzers to tune signal objects to best match a [BSM](#) signature, while leaving the [OR](#) process unchanged. The signal and baseline definitions for this analysis are described in [Chapter 8](#).

The first step in the [OR](#) process is to remove reconstructed jets that appear to be due to calorimetric deposits from an electron. To accomplish this, any baseline jet within  $\Delta R = 0.2$  from a baseline electron is removed. A caveat is added due to the frequent production of leptons in the decay of heavy-flavor jets; if the jet is *b*-tagged, the electron will be removed instead. After these electrons and jets have been removed, a new search is done for jets and electrons within  $\Delta R = 0.4$  of one another. In this iteration, the electron is removed, again to reduce backgrounds from heavy-flavor decays.

Next, the muon-jet [OR](#) is applied, which is very similar to that of the electron. Any jet within  $\Delta R = 0.2$  of a muon is removed, unless the jet is *b*-tagged, in which case the muon is removed due to the likelihood that it resulted due to a heavy-flavor decay. The muon-jet [OR](#) then differs from the electron's in that a  $p_T$ -based  $\Delta R$  cut is used in the last step. Muons within  $\Delta R < \min(0.04 + (10 \text{ GeV})/p_T, 0.4)$  of a jet are removed, with the  $p_T$ -dependent cone size designed to reject low- $p_T$  heavy-flavor muons while preserving muons resulting from the decay of high- $p_T$  particles, which are closely aligned with the other products of the decay.

The next step is to remove electrons resulting from muon bremsstrahlung. Any electron within  $\Delta R = 0.1$  of a muon is removed from the event.

Lastly, overlap between photons and both jets and electrons is considered. Baseline photons within  $\Delta R = 0.4$  of an electron are removed, as are jets within  $\Delta R = 0.4$  of a remaining photon.

## 6.6 MISSING TRANSVERSE MOMENTUM

Missing transverse momentum ( $\mathbf{p}_T^{\text{miss}}$ , with magnitude  $E_T^{\text{miss}}$ ), is the negative vector sum of  $p_T$  measured in an event. Because the colliding protons have no initial transverse momentum, the true value of this quantity should be zero unless a particle escapes the detector without being measured, as neutrinos do. In practice, the reconstructed  $E_T^{\text{miss}}$  can also be non-zero due to mismeasurement, or due to gaps in the [ATLAS](#) detector.  $E_T^{\text{miss}}$  reconstruction is perhaps the most complex because it depends on all other object reconstructions performed in the [ATLAS](#) detector.

$E_T^{\text{miss}}$  components are calculated independently for each type of baseline object reconstructed, as well as for a soft term, which comprises the energy observed by the [ATLAS](#) detector but not associated with a baseline object. The soft term can be calculated based either on calorimeter or track measurements [72]. While the Calorimeter Soft Term ([CST](#)) is very sensitive to pile-up, the Track Soft Term ([TST](#)) is much more robust, as it excludes tracks emanating from pile-up vertices. Tracks associated with any recon-

structured object are also removed. Figure 55 shows the dependence of the **TST** resolution on number of primary vertices. Because of this lessened pile-up dependence, the **TST** is used to reconstruct  $E_T^{\text{miss}}$  in this analysis.

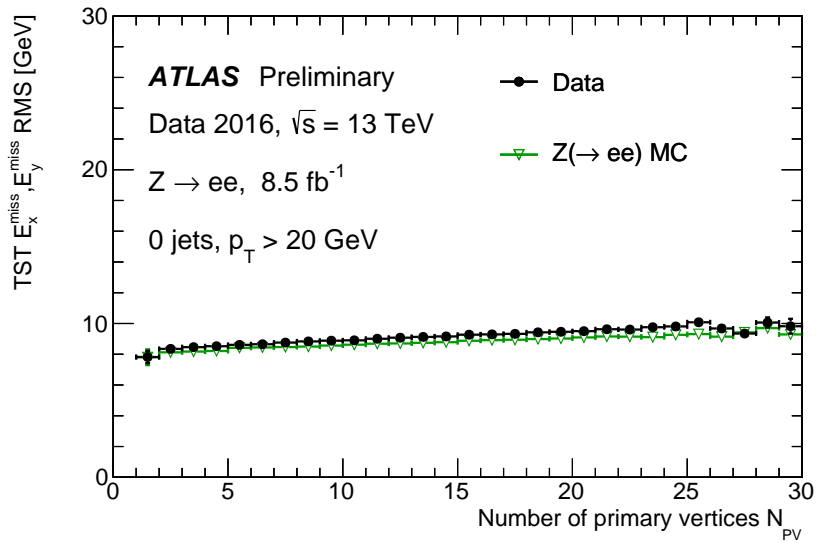


Figure 55: Distributions of the resolution of the  $x$  and  $y$  components of **TST**  $E_T^{\text{miss}}$  in  $Z \rightarrow \mu\mu$  events in data and **MC**.

$Z \rightarrow \mu\mu$  events, which rarely have any true  $E_T^{\text{miss}}$ , can be used to study the contribution of different objects to the total  $E_T^{\text{miss}}$  calculation. Figure 56 shows the the  $E_T^{\text{miss}}$  resulting from muons, jets, and the soft term measured in events with two opposite-sign muons that reconstruct an invariant mass within 25 GeV of the  $Z$  boson mass. Because very little real  $E_T^{\text{miss}}$  exists, these distributions primarily demonstrate how mismeasurement of various objects contributes to the  $E_T^{\text{miss}}$  term. Though the soft term falls off very quickly, rarely producing events with more than 50 GeV of  $E_T^{\text{miss}}$ , both the jet and muon distributions have longer tails, producing more events with higher  $E_T^{\text{miss}}$ . Though these individual terms can cancel in a system where a  $Z$  boson recoils against a jet system, the overall scale of each term indicates the possibility of contributions from mismeasurement; a 30% mismeasurement of the jet or muon term can result in significant  $E_T^{\text{miss}}$ , while a similar mismeasurement of the soft term is unlikely to produce a large impact. The agreement between data and **MC** in these distributions indicates that, at least in the core of the distributions, these  $E_T^{\text{miss}}$  terms are well modeled.

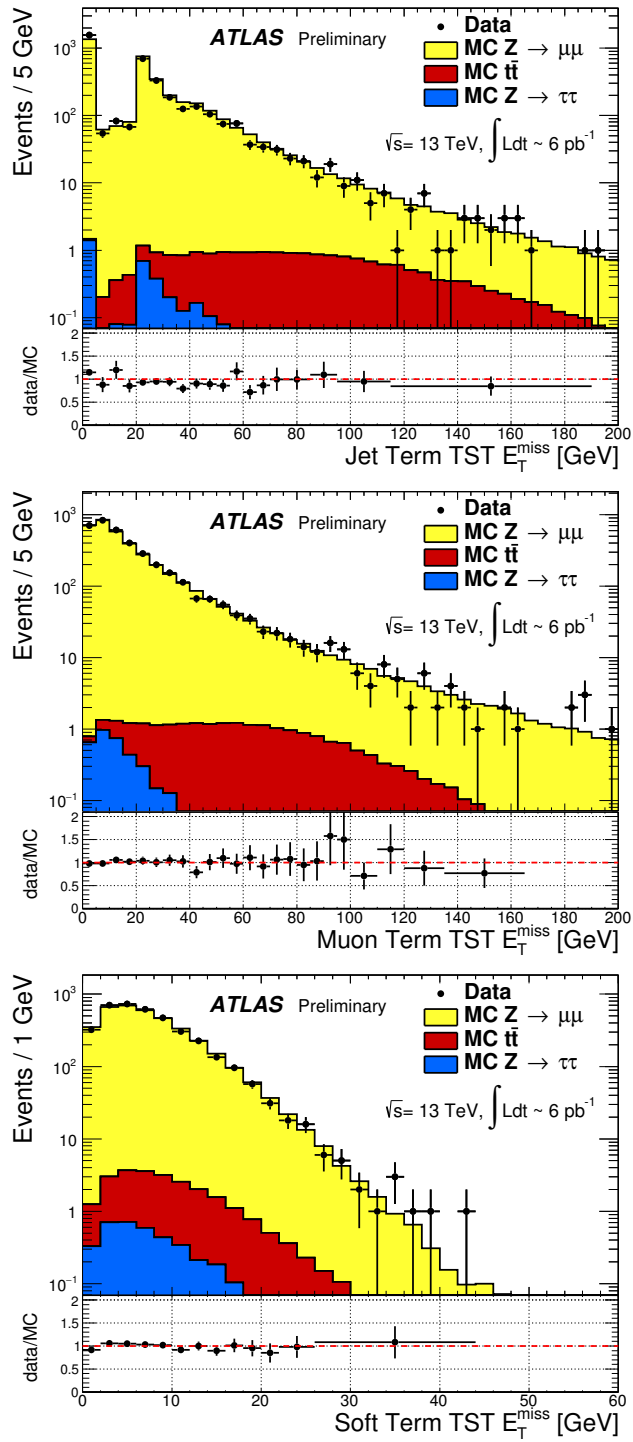


Figure 56: Distributions of the jet term (top left), muon term (top right), and TST (bottom)  $E_T^{\text{miss}}$  in  $Z \rightarrow \mu\mu$  events in data and MC. In the jet term distribution, the feature at zero is due to events with no jets, and the spike at 20 GeV corresponds to the minimum jet  $p_T$  considered for the analysis [73].



1853

## Part IV

1854

### SEARCHING FOR SUPERSYMMETRY

1855

This section describes an analysis of the ATLAS data carried out by the author and her analysis team. The analysis was performed on events from  $pp$  collisions provided by the LHC at  $\sqrt{s}=13$  TeV. It searches for events like those described in [Section 2.2.3](#), which contain a Z boson (decaying to leptons), jets, and missing transverse energy. [Chapter 7](#) describes the SM backgrounds for the analysis. Definitions of the objects used in the analysis is outlined in [Chapter 8](#). [Chapter 9](#) explains the analysis strategy, defining the signal region as well as additional regions used to determine background contributions. Chapters [10](#) and [11](#) describe the methods used to estimate the SM backgrounds and the determination of their uncertainties. The results are presented in [Chapter 12](#), and they are interpreted in [Chapter 13](#).

1856

1857

1858

1859

1860

1861

1862

1863

1864

1865

1866

1867

1868



1869

## 1870 BACKGROUND PROCESSES

1871 This analysis is fundamentally a search for **SUSY** in events with two lep-  
 1872 tons whose invariant mass is consistent with a  $Z$  boson. Additional event  
 1873 selections are made to reduce **SM** processes relative to potential **SUSY** pro-  
 1874 cesses, defined by simplified models discussed in [Section 2.2.3](#). These mod-  
 1875 els include the production of strongly-charged, high-mass particles, which  
 1876 results in events with jets and high  $H_T$ , the scalar sum of the  $p_T$  of all  
 1877 jets and the two leading leptons in the event. These  $R$ -parity conserving  
 1878 **SUSY** models also produce decay chains that terminate with a stable, electri-  
 1879 cally neutral particle, which produces  $E_T^{\text{miss}}$  when it passes through **ATLAS**  
 1880 without detection. All of these features can help isolate these events from  
 1881 backgrounds. To understand what cuts would optimize the sensitivity of  
 1882 the search, it is essential to first understand what these **SM** backgrounds  
 1883 are.

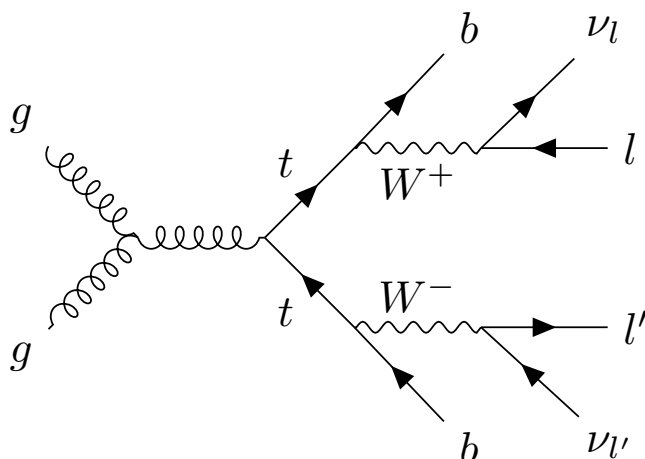


Figure 57: An example Feynman diagram of  $t\bar{t}$  production and decay.

1884 **TOP-ANTITOP ( $t\bar{t}$ )** production is the largest background for this search.  
 1885 [Figure 57](#) shows an example of this process, which results in two jets, lep-  
 1886 tons, and neutrinos, which are seen in the detector as  $E_T^{\text{miss}}$ . Thus,  $t\bar{t}$  events  
 1887 naturally have high  $E_T^{\text{miss}}$  and  $H_T$ , jets, and leptons from two different  $W$   
 1888 boson decays, which may coincidentally form an invariant mass consistent  
 1889 with a  $Z$  boson. These events are very difficult to separate from potential  
 1890 signals, though keeping the mass window small and requiring  $E_T^{\text{miss}}$  and  
 1891  $H_T$  above the typical values for  $t\bar{t}$  events helps reduce this background.

1892 **DIBOSON ( $VV$ )** production is the next leading background. These events  
 1893 can contain real  $Z$  bosons and their dilepton invariant mass will peak on-  
 1894  $Z$  like a signal. In addition, in events like [Figure 58](#), an additional  $W$  boson

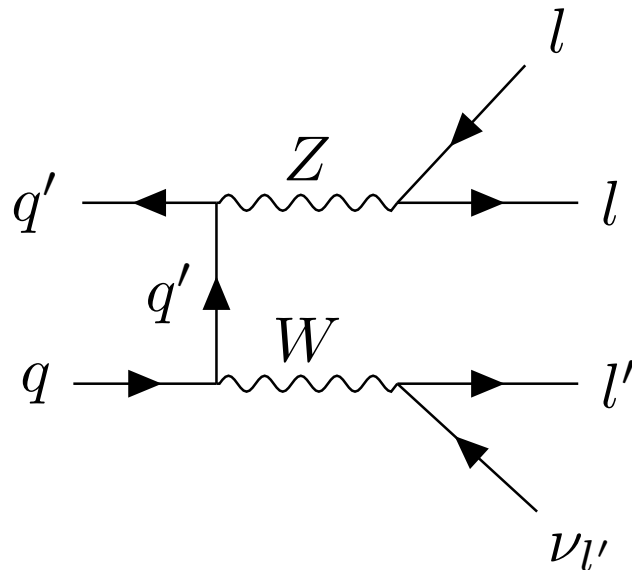


Figure 58: An example Feynman diagram of the production and decay of a  $WZ$  event.

1895 can decay to another lepton and a neutrino, providing  $E_T^{\text{miss}}$ . The pictured  
 1896 process can occur with associated jets due to initial state radiation, but  
 1897 at reduced rates, so adding a jet requirement to the signal region helps  
 1898 reduce these events. If the  $W$  boson in this diagram instead decayed to  
 1899 two jets, there would be no true  $E_T^{\text{miss}}$  from a neutrino, so a  $E_T^{\text{miss}}$  cut in  
 1900 conjunction with a jet cut is very effective in reducing the total diboson  
 1901 background. A veto on a third lepton could also be used to reduce this  
 1902 background, but, depending on the signal model considered, this veto can  
 1903 also decrease signal acceptance, so it is not used in this analysis.

1904  $Z/\gamma^* + \text{JETS}$  processes are very common but, as shown in Figure 59,  
 1905 don't produce any true  $E_T^{\text{miss}}$ . A high  $H_T$  cut helps reduce this background,  
 1906 but this process often occurs with associated jets, producing many events  
 1907 with large amounts of hadronic activity.  $E_T^{\text{miss}}$  is the most powerful vari-  
 1908 able to reduce this background, because though events with mismeasured  
 1909 jets or leptons can fake  $E_T^{\text{miss}}$ , mismeasurements drastic enough to produce  
 1910 hundreds of GeV of  $E_T^{\text{miss}}$  are rare. In addition, events with substantially  
 1911 mismeasured leptons often have dilepton invariant masses that are incon-  
 1912 sistent with a  $Z$  boson, and so a fraction of  $Z/\gamma^* + \text{jets}$  events that do  
 1913 pass the  $E_T^{\text{miss}}$  threshold can be excluded nonetheless.

1914 Other processes can contribute to the Standard Model background at  
 1915 lower rates. Processes similar to  $Z/\gamma^* + \text{jets}$  but with a  $W$  boson instead of  
 1916 a  $Z$  have real  $E_T^{\text{miss}}$  from leptonic  $W$  decays, but only one lepton. However,  
 1917 a fake or non-prompt lepton can cause these events to look very similar to  
 1918 simulated signals. Additionally, there are *rare top* such as  $t\bar{t}$  production in  
 1919 association with  $W$  or  $Z$  bosons that will also be difficult to separate from  
 1920 signal processes.

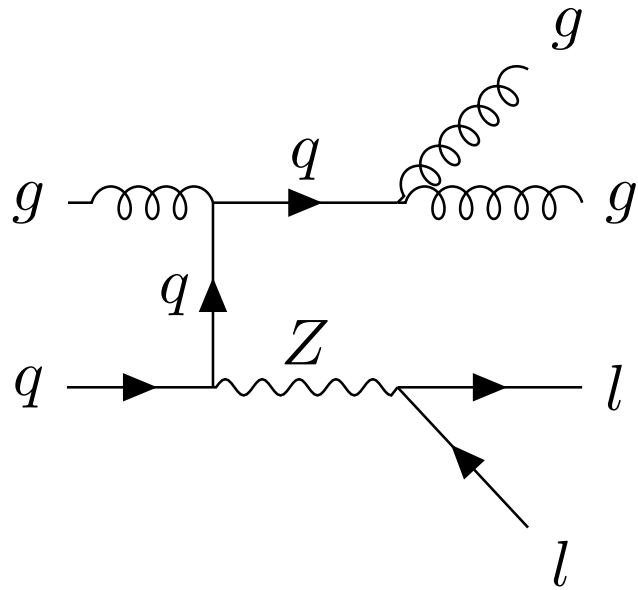


Figure 59: An example Feynman diagram of the production and decay of a  $Z/\gamma^*$  + jets event.

1921 7.1 DATA AND MONTE CARLO SAMPLES

1922 This analysis uses data collected by the ATLAS detector from  $pp$  collisions  
 1923 at a center-of-mass energy of 13 TeV in 2015 and 2016, corresponding to  
 1924 a total luminosity of  $14.7 \text{ fb}^{-1}$ . The data collected use a combination of  
 1925 unprescaled single and dilepton triggers, discussed in greater detail in  
 1926 Section 9.1. These triggers are fully efficient for leptons with a  $p_T$  of at least  
 1927 20 GeV. In addition, photon events are collected for use in a control region  
 1928 using both prescaled and unprescaled triggers, with the lowest trigger  
 1929 threshold at 20 GeV.

1930 MC samples are generated for each background process that appears  
 1931 in the signal and validation regions. Table 2 details the method used to  
 1932 produce each sample, and more information can be found in Section 4.7.  
 1933 These simulated background events, in conjunction with the simulated  
 1934 signal discussed in Section 2.2.3, are used to determine approximate sensi-  
 1935 tivities of the search and optimize signal regions and amount of data used.  
 1936 The background MC also provides a valuable cross-check for many of the  
 1937 data-driven background estimates discussed in Chapter 10, and in some  
 1938 cases, provides the primary estimate of the background.

Table 2: Simulated background event samples used in this analysis with the corresponding matrix element and parton shower generators, cross-section order in  $\alpha_s$  used to normalise the event yield, underlying-event tune and PDF set.

Physics process	Generator	Parton Shower	Cross section	Tune	PDF set
$t\bar{t} + W$ and $t\bar{t} + Z$ [74, 75]	MG5_AMC@NLO	Pythia 8.186	NLO [76, 77]	A14	NNPDF23LO
$t\bar{t} + WW$ [74]	MG5_AMC@NLO	Pythia 8.186	LO [47]	A14	NNPDF23LO
$t\bar{t}$ [78]	POWHEG Box v2 r3026	Pythia 6.428	NNLO+NNLL [79, 80]	PERUGIA2012	NULO CT10
Single-top ( $Wt$ ) [78]	POWHEG Box v2 r2856	Pythia 6.428	Approx. NNLO [81]	PERUGIA2012	NULO CT10
$WW$ , $WZ$ and $ZZ$ [82]	SHERPA 2.1.1	SHERPA 2.1.1	NLO [83, 84]	SHERPA default	NULO CT10
$Z/\gamma^*(\rightarrow \ell\ell) + \text{jets}$ [85]	SHERPA 2.1.1	SHERPA 2.1.1	NNLO [86, 87]	SHERPA default	NULO CT10
$\gamma + \text{jets}$	SHERPA 2.1.1	SHERPA 2.1.1	LO [51]	SHERPA default	NULO CT10
$V(=W, Z)\gamma$ signal	SHERPA 2.1.1	SHERPA 2.1.1	LO [51]	SHERPA default	NULO CT10
	MG5_AMC@NLO	Pythia 8.186	NULO	A14	NNPDF23LO

1939

## 1940 OBJECT IDENTIFICATION AND SELECTION

1941 This section describes the identification and selection of objects in the  
 1942 events of this analysis. Objects are first required to pass *baseline* selections,  
 1943 which are used for Overlap Removal ([OR](#)) and the calculation of  $E_T^{\text{miss}}$ ,  
 1944 then tighter *signal* selection cuts are applied, which define the objects con-  
 1945 sidered in the final analysis of events. Definitions are presented for elec-  
 1946 trons, muons, and jets, which are all required in the Signal Region ([SR](#)) of  
 1947 this analysis, as well as photons, which are used in background estima-  
 1948 tion. This section refers to object definitions, including *quality* selections,  
 1949 described in [Chapter 6](#).

## 1950 8.1 ELECTRONS

1951 Electrons are reconstructed using the algorithm discussed in [Section 6.1](#).  
 1952 All electrons are required to be within  $|\eta| < 2.47$ , to ensure that all tracks  
 1953 are consistently within the tracking capability of the [ID](#) and that associ-  
 1954 ated clusters are within the high-granularity portion of the calorimeter.  
 1955 Baseline leptons are required to have  $p_T > 10$  GeV and pass the [Loose](#)  
 1956 quality standard. Signal leptons are further required to be isolated and of  
 1957 [Medium](#) quality, and must have  $p_T > 25$  GeV. Additional cuts on impact pa-  
 1958 rameter are made for electrons with the goal of identifying only electrons  
 1959 coming from the hard-scatter vertex. These requirements, and all the other  
 1960 requirements made on the electrons can be seen in [Table 3](#).

Cut	Value/description
Baseline Electron	
Acceptance	$p_T > 10$ GeV, $ \eta^{\text{clust}}  < 2.47$
Quality	<a href="#">Loose</a>
Signal Electron	
Acceptance	$p_T > 25$ GeV, $ \eta^{\text{clust}}  < 2.47$
Quality	<a href="#">Medium</a>
Isolation	<a href="#">GradientLoose</a>
Impact parameter	$ z_0 \sin \theta  < 0.5$ mm $ d_0 / \sigma_{d_0}  < 5$

Table 3: Summary of the electron selection criteria.  $z_0$  gives the track's distance from the hard-scatter vertex projected in the  $z$  direction, while  $d_0$  gives the this distance projected onto the  $x - y$  plane.

With these signal requirements, the ATLAS detector is 80% efficient at identifying electrons with a  $p_T$  of 25 GeV, which rises to 90% at  $p_T > 60$  GeV [88].

## 8.2 MUONS

Muons are reconstructed as discussed in Section 6.3. Baseline muons are required to have  $p_T > 10$  GeV and  $|\eta| < 2.5$ , including muons that can be tracked both by the ID and the MS, and must pass a Medium quality cut. Signal muons are additionally required to have  $p_T > 25$  GeV, and to be isolated. As with the electrons, impact parameter cuts are made to ensure that the muon is consistent with coming from a decay from the event’s primary vertex. Additionally, the muon must not be flagged isBadMuon, which reduces the number of events with very inconsistent ID and MS tracks. The full set of requirements can be seen in Table 4.

Cut	Value/description
Baseline Muon	
Acceptance	$p_T > 10$ GeV, $ \eta  < 2.5$
Quality	Medium
Signal Muon	
Acceptance	$p_T > 25$ GeV, $ \eta  < 2.5$
Quality	Medium
Isolation	GradientLoose
Impact parameter	$ z_0 \sin \theta  < 0.5$ mm $ d_0/\sigma_{d_0}  < 3$
isBadMuon	isBadMuon Flag required

Table 4: Summary of the muon selection criteria. The signal selection requirements are applied on top of the baseline selection.

Muons with  $p_T > 25$  GeV are identified with a 95% efficiency, which rises to 99% for muons with  $p_T > 80$  GeV[89]. Including trigger and isolation requirements, these efficiencies drop to about 80% for muons with  $p_T > 25$  GeV and 90% for muons with  $p_T > 200$  GeV. This drop is largely the consequence of incomplete  $\eta$  coverage of the RPCs, discussed in Section 6.3.

## 8.3 JETS

Jets are reconstructed according to Section 6.4, with baseline jets using the anti- $k_t$  algorithm with  $R = 0.4$  using EM clusters. These jets are required to have a minimum  $p_T$  of 20 GeV and  $|\eta| < 2.8$ . For signal jets, this  $p_T$  requirement is increased to 40 GeV and the  $\eta$  cut is tightened to  $|\eta| < 2.5$ .

1985 JVT requirements are enforced on jets with  $p_T < 60$  GeV and  $|\eta| < 2.4$  to  
1986 reduce the number of jets from pile-up. The full set of requirements can  
1987 be seen in [Table 5](#).

Cut	Value/description
Baseline jet	
Collection	AntiKt4EMTopo
Acceptance	$p_T > 20$ GeV , $ \eta  < 2.8$
Signal jet	
Acceptance	$p_T > 30$ GeV , $ \eta  < 2.5$
JVT	$ \text{JVT}  > 0.59$ for jets with $p_T < 60$ GeV and $ \eta  < 2.4$
Signal $b$ -jet	
$b$ -tagger Algorithm	MV2c20
Efficiency	77 %
Acceptance	$p_T > 30$ GeV , $ \eta  < 2.5$
JVT	$ \text{JVT}  > 0.59$ for jets with $p_T < 60$ GeV and $ \eta  < 2.4$

Table 5: Summary of the jet and  $b$ -jet selection criteria. The signal selection requirements are applied on top of the baseline requirements.

1988 Though no  $b$ -jets are required or vetoed in the [SR](#) of this analysis, some  
1989 Control Regions ([CRs](#)) use  $b$ -enhanced and  $b$ -vetoed regions to determine  
1990 the impact of heavy flavor. The specifications for  $b$ -tagging are also de-  
1991 scribed in [Table 5](#).

## 1992 8.4 PHOTONS

1993 Photons are used to estimate the  $Z/\gamma^* + \text{jets}$  background in this analysis,  
1994 and they are reconstructed according to [Section 6.2](#). Baseline and signal  
1995 photons are nearly identical. Each must pass a Tight selection and an  
1996 isolation cut, and have  $p_T > 25$  GeV as well as  $|\eta| < 2.37$ . Signal photons  
1997 with  $1.37 < |\eta| < 1.6$  are rejected due to an discontinuity in the calorimeter  
1998 which results in inferior energy resolutions in this region. The full selection  
1999 requirements can be seen in [Table 6](#).

Cut	Value/description
Baseline Photon	
Acceptance	$p_T > 25 \text{ GeV},  \eta  < 2.37$
Quality	tight
Signal Photon	
Acceptance	$p_T > 25 \text{ GeV},  \eta  < 2.37$ rejecting $1.37 <  \eta  < 1.6$
Quality	tight
Isolation	FixedCutTight

Table 6: Summary of the photon selection criteria.

2000

2001 EVENT SELECTION

---

2002 The goal of this analysis is to identify events resembling [Figure 14](#) in col-  
 2003 lisions in the [ATLAS](#) detector. In order to do this, a Signal Region ([SR](#)) is  
 2004 defined with the goal of maximizing the identification efficiency of signal  
 2005 events while minimizing [SM](#) backgrounds. However, because this analysis  
 2006 re-investigates an excess of events seen in Run 1 with the [ATLAS](#) detec-  
 2007 tor, the signal region was frozen and could not be re-optimized for the  
 2008 new, higher energy data in Run 2. The [SR](#), called SRZ, was predetermined,  
 2009 including events with two opposite-sign, same-flavor leptons that recon-  
 2010 struct a mass,  $m_{\ell\ell}$ , close to that of the Z boson, with the additional require-  
 2011 ment of two jets,  $E_T^{\text{miss}} > 225$  GeV, and  $H_T$  of at least 600 GeV. Additionally,  
 2012 a cut on  $\Delta\phi(\text{jet}_{12}, p_T^{\text{miss}})$  was made in order to reduce the number of events  
 2013 with high  $E_T^{\text{miss}}$  due to mismeasurement of one of the leading two jets.

2014 The freezing of the [SR](#) prevented re-optimization of the cuts for maxi-  
 2015 mum sensitivity to a signal, but the search was still expected to be more  
 2016 sensitive than the previous iteration performed on 8 TeV data. This is be-  
 2017 cause the cross-section for production of this high-mass signal increased  
 2018 dramatically with the increased [LHC](#) energy, while the cross-section for [SM](#)  
 2019 processes increased at lower rates.

2020 Though this [SR](#) was fixed, the methods used to estimate the expected  
 2021 [SM](#) backgrounds were not. A set of Control Regions ([CRs](#)) and Validation  
 2022 Regions ([VRs](#)) were chosen to make these estimations possible. [CRs](#) are re-  
 2023 gions in which the collected data can be used to make an estimate of an  
 2024 expected background in the [SR](#), while [VRs](#) are used to confirm that the  
 2025 background estimate based on the [CR](#) is valid. Both [CRs](#) and [VRs](#) are de-  
 2026 signed to minimize contamination from the [BSM](#) process being searched  
 2027 for. This is desirable because signal contamination in a [CR](#) can lead to an  
 2028 overestimate of the [SM](#) background in the [SR](#), disguising a genuine signal  
 2029 as background. Contamination in a [VR](#), where background estimates are  
 2030 being validated, can make it appear that the [SM](#) background is not well de-  
 2031 scribed by an estimate, causing analyzers to adjust the method to account  
 2032 for the difference, and again, disguising the effect of the same signal in the  
 2033 [SR](#).

2034 The strategy for estimating the [FS](#) backgrounds, for example, depends  
 2035 on a series of [CRs](#) and [VRs](#) depicted in [Figure 6o](#). One estimate, the flavor  
 2036 symmetry method, takes data from CR-FS, a different-flavor region with  
 2037 slightly wider  $m_{\ell\ell}$  bounds than the [SR](#), and uses these events to predict  
 2038 the contribution of flavor symmetric processes to SRZ. An independent  
 2039 method called a sideband fit uses a control region CRT to measure the  
 2040 flavor symmetric events outside of the Z mass window, and uses [MC](#) to  
 2041 extrapolate inside the Z mass window to SRZ. Then, both methods are  
 2042 validated at lower  $E_T^{\text{miss}}$  with an otherwise identical series of regions, with

2043 VRS corresponding to SRZ, VRT corresponding to CRT, and VR-FS corre-  
 2044 sponding to CR-FS.

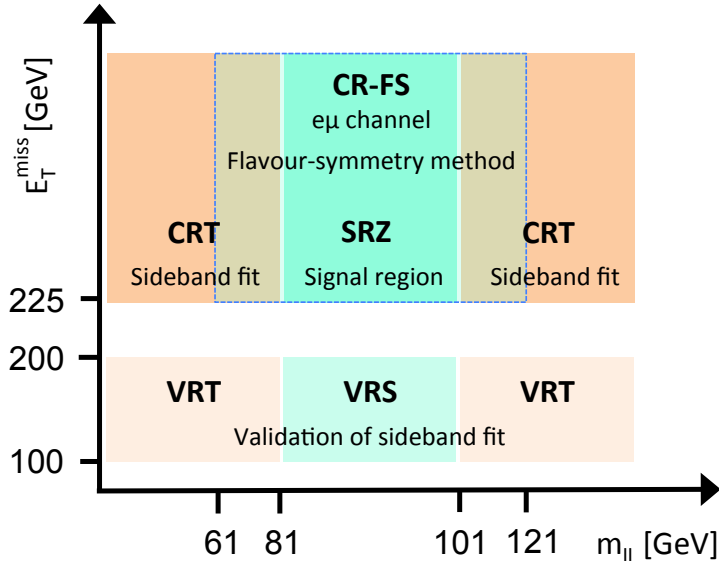


Figure 6o: Schematic diagrams of the control, validation and signal regions for the on-shell Z (top) and edge (bottom) searches. For the on-shell Z search the various regions are shown in the  $m_{\ell\ell} - E_T^{\text{miss}}$  plane, whereas in the case of the edge search the signal and validation regions are depicted in the  $H_T - E_T^{\text{miss}}$  plane.

2045 The background estimation methods, described in [Chapter 10](#), each re-  
 2046 quire their own set of these regions. The full list of regions used in this  
 2047 analysis can be seen in [Table 7](#). In addition to the [FS](#) regions described  
 2048 above, there is one more [CR](#), CR- $\gamma$ , which is a photon region used to pre-  
 2049 dict the number of  $Z/\gamma^* + \text{jets}$  events, a process described in [Section 10.2](#).  
 2050 Additional [VRs](#), VR-ZZ, VR-WZ, and VR-3L, are introduced in order to val-  
 2051 idate the backgrounds taken directly from [MC](#). There are several additional  
 2052 regions used, for example, in the estimation of the fakes and  $Z/\gamma^* + \text{jets}$   
 2053 backgrounds, that are defined in their respective sections.

## 2054 9.1 TRIGGER STRATEGY

2055 In order to collect data for the analysis, triggers must be chosen that pro-  
 2056 vide good efficiency in each of the [SR](#), [VR](#), and [CRs](#). This analysis primarily  
 2057 depends on triggers on leptons, which are required in nearly every region.  
 2058 To simplify the application of trigger scale factors, which correct [MC](#) yields  
 2059 for a given trigger to match the data efficiencies, events are broken down  
 2060 into a series of kinematic ranges, each with a designated trigger. These  
 2061 regions can be seen in [Table 8](#).

2062 In kinematic regions where single lepton triggers are fully efficient, they  
 2063 are preferentially used. In lower- $p_T$  ranges, dilepton triggers are used, tar-

On-shell Z regions	$E_T^{\text{miss}}$ [GeV]	$H_T$ [GeV]	$n_{\text{jets}}$	$m_{\ell\ell}$ [GeV]	SF/DF	$\Delta\phi(\text{jet}_{12}, p_T^{\text{miss}})$	$m_T(\ell_3, E_T^{\text{miss}})$ [GeV ]	$n_{\text{b-jets}}$
Signal region								
SRZ	> 225	> 600	$\geq 2$	$81 < m_{\ell\ell} < 101$	SF	$> 0.4$	—	—
Control regions								
CRZ	<b>&lt; 60</b>	> 600	$\geq 2$	$81 < m_{\ell\ell} < 101$	SF	$> 0.4$	—	—
CR-FS	<b>&gt; 225</b>	> 600	$\geq 2$	<b>61 &lt; <math>m_{\ell\ell} &lt; 121</math></b>	DF	$> 0.4$	—	—
CRT	<b>&gt; 225</b>	> 600	$\geq 2$	<b>&gt; 40, <math>m_{\ell\ell} \notin [81, 101]</math></b>	SF	$> 0.4$	—	—
CR $\gamma$	—	> 600	$\geq 2$	—	$0\ell, 1\gamma$	—	—	—
Validation regions								
VRZ	<b>&lt; 225</b>	> 600	$\geq 2$	$81 < m_{\ell\ell} < 101$	SF	$> 0.4$	—	—
VRT	<b>100–200</b>	> 600	$\geq 2$	<b>&gt; 40, <math>m_{\ell\ell} \notin [81, 101]</math></b>	SF	$> 0.4$	—	—
VRS	<b>100–200</b>	> 600	$\geq 2$	$81 < m_{\ell\ell} < 101$	SF	$> 0.4$	—	—
VR-FS	<b>100–200</b>	> 600	$\geq 2$	<b>61 &lt; <math>m_{\ell\ell} &lt; 121</math></b>	DF	$> 0.4$	—	—
VR-WZ	<b>100–200</b>	—	—	—	$3\ell$	—	$< 100$	0
VR-ZZ	< 100	—	—	—	$4\ell$	—	—	0
VR-3L	<b>60–100</b>	<b>&gt; 200</b>	$\geq 2$	$81 < m_{\ell\ell} < 101$	$3\ell$	$> 0.4$	—	—

Table 7: Overview of all signal, control and validation regions used in the on-shell Z search. More details are given in the text. The flavour combination of the dilepton pair is denoted as either *SF* for same-flavor or *DF* for different flavor. All regions require at least two leptons, unless otherwise indicated. In the case of CR $\gamma$ , VR-WZ, VR-ZZ, and VR-3L the number of leptons, rather than a specific flavor configuration, is indicated. The main requirements that distinguish the control and validation regions from the signal region are indicated in bold. Most of the kinematic quantities used to define these regions are discussed in the text. The quantity  $m_T(\ell_3, E_T^{\text{miss}})$  indicates the transverse mass formed by the  $E_T^{\text{miss}}$  and the lepton which is not assigned to either of the Z-decay leptons.

Lepton $p_T$	Trigger in 2015	Trigger in 2016
Di-electron channel		
$p_T(e_1) > 65 \text{ GeV}$	HLT_e60_lhmedium	HLT_e60_lhmedium_nod0
$p_T(e_1) \leq 65 \text{ GeV}$	HLT_2e17_lhloose	HLT_2e17_lhvloose_nod0
Di-muon channel		
$p_T(\mu_1) > 52.5 \text{ GeV}$	HLT_mu50	HLT_mu50
$p_T(\mu_1) \leq 52.5 \text{ GeV}$	HLT_mu24_mu8noL1	HLT_2mu14_nomucomb
Electron-muon channel		
$p_T(e) > 65 \text{ GeV}$	HLT_e60_lhmedium	HLT_e60_lhmedium_nod0
$p_T(e) \leq 65 \text{ GeV}$ and $p_T(\mu) > 52.5 \text{ GeV}$	HLT_mu50	HLT_mu50
$p_T(e) \leq 65 \text{ GeV}$ and $p_T(\mu) \leq 52.5 \text{ GeV}$ and $p_T(e) < p_T(\mu)$	HLT_e7_lhmedium_mu24	HLT_e7_lhmedium_nod0_mu24
$p_T(e) \leq 65 \text{ GeV}$ and $p_T(\mu) \leq 52.5 \text{ GeV}$ and $p_T(\mu) < p_T(e)$	HLT_e17_lhloose_mu14	HLT_e17_lhloose_nod0_mu14

Table 8: Lepton trigger requirements used for the analysis in different regions of lepton- $p_T$  phase space.

2064 geting either  $ee$ ,  $\mu\mu$ , or  $e\mu$  events. Electron triggers are selected over muon  
 2065 triggers when possible because they have higher trigger efficiencies.

2066 In CR- $\gamma$ , there are no leptons, so an alternate trigger strategy must be  
 2067 used. [Section 10.2.1](#) describes this triggering scheme, which includes a  
 2068 combination of prescaled and unprescaled photon triggers to allow for the  
 2069 collection of low- $p_T$   $\gamma +$  jets events.

## 2070 9.2 SIGNAL EFFICIENCY AND CONTAMINATION

2071 Using the simplified models discussed in [Section 2.2.3](#), the contributions of  
 2072 potential signals in these regions can be studied. In the [SR](#), the goal is to in-  
 2073 clude as much of the potential signal as possible, while excluding as much  
 2074 [SM](#) background as possible. [Figure 61](#) shows the acceptance and efficiency  
 2075 for the simplified models at different mass points. Acceptance is defined  
 2076 as the fraction of signal events that produce signatures that kinematically  
 2077 match the [SR](#), while the efficiency is the fraction of these events expected to  
 2078 be correctly identified by the [ATLAS](#) detector. Acceptance ranges between  
 2079 3–5% for the simplified models considered, while efficiency is typically 70–  
 2080 90%. These studies are performed using [MC](#), with corrections applied to  
 2081 match data efficiencies. These efficiencies are measured as a function of  
 2082  $p_T$  and  $\eta$ , and include separate identification efficiencies for electrons and  
 2083 muons.

2084 Using the same [MC](#), the possibility of signal contamination in the [CRs](#)  
 2085 and [VRs](#) is assessed. Figures [62](#) and [63](#) show the fraction of events in these  
 2086 regions expected to come from signal for different points on the simplified  
 2087 model’s mass grid. Contamination is highest in VRS, at low  $m_{\tilde{g}}$ . However,  
 2088 past analyses have already excluded most models with  $m_{\tilde{g}} < 800 \text{ GeV}$   
 2089 [[1](#)], so this is not a concern. For models with  $m_{\tilde{g}} > 800 \text{ GeV}$ , signal con-

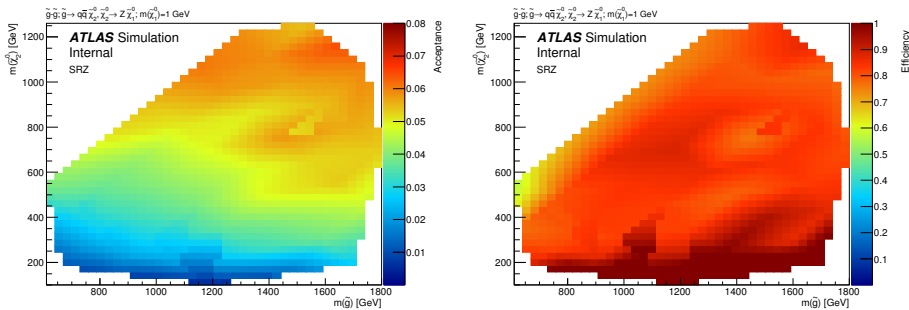


Figure 61: Signal region acceptance (left) and efficiency (right) in SRZ for the simplified model with gluino pair production with  $\tilde{\chi}_2^0$  decays to  $\tilde{\chi}_1^0$  and an on-shell Z boson with 1 GeV neutralino LSP. Acceptance is calculated by applying the signal-region kinematic requirements to truth objects in MC, which do not suffer from identification inefficiencies or measurement resolutions.

tamination in VRS is below 30%, and for models with  $m_{\tilde{g}} > 1$  TeV, the contamination decreases to 10%.

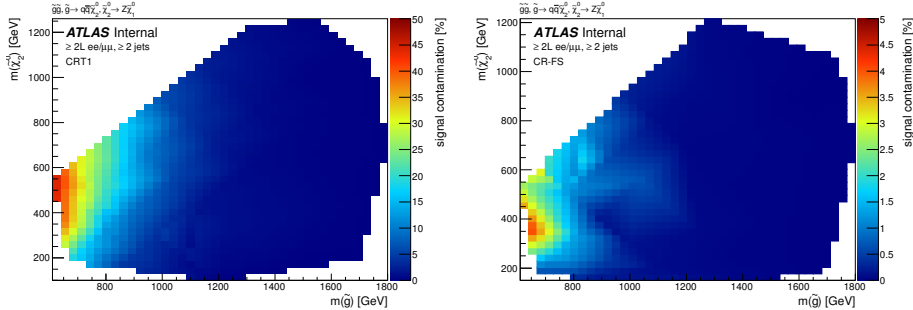


Figure 62: Expected signal contamination in CRT (left) and CR-FS (right) for the signal model with gluino pair production, where the gluinos decay to quarks and a neutralino, with the neutralino subsequently decaying to a Z boson and a 1 GeV neutralino LSP.

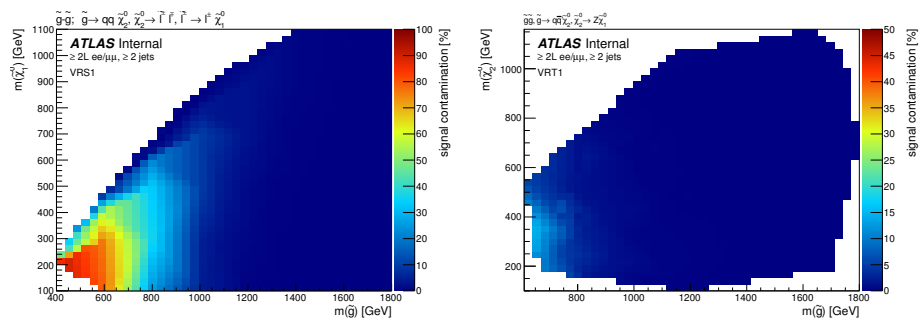


Figure 63: Expected signal contamination in VRS (left) and VRT (right) for the signal model with gluino pair production, where the gluinos decay to quarks and a neutralino, with the neutralino subsequently decaying to a Z boson and a 1 GeV neutralino LSP.

2092

2093 BACKGROUND ESTIMATION

---

2094 This analysis requires two leptons that reconstruct to a  $Z$  mass, at least  
 2095 two jets,  $E_T^{\text{miss}}$ , and  $H_T$ . Any [SM](#) processes that produce this signature will  
 2096 appear as a background to the search. The most important task of the anal-  
 2097 ysis is to identify and estimate these backgrounds, so that any excess of  
 2098 events appearing on top of the standard model background can be iden-  
 2099 tified. The main backgrounds for this analysis are described in [Chapter 7](#).  
 2100 The largest background is from flavor symmetric processes, with smaller  
 2101 contributions coming from diboson processes,  $Z/\gamma^* + \text{jets}$ , rare top pro-  
 2102 cesses, and fake and non-prompt leptons.

## 2103 10.1 FLAVOR SYMMETRIC PROCESSES

2104 Flavor Symmetric ([FS](#)) backgrounds include any processes that produce  
 2105 pairs of leptons with uncorrelated flavor in the final state. In this analysis,  
 2106 the largest contribution comes from  $t\bar{t}$ , with additional events from pro-  
 2107 cesses like  $WW$  and  $Z \rightarrow \tau\tau$ . In these processes, each lepton comes from  
 2108 a decay of different particles. In the case of  $t\bar{t}$ , the two top quarks decay to  
 2109  $W$  bosons, which each produce a lepton in their decays, as shown in [Fig-](#)  
 2110 [ure 57](#). These leptons' flavors are correlated with the flavor of the neutrino  
 2111 that results from the same boson's decay, but not with one another.

2112 10.1.1 *Flavor Symmetry Method*

2113 As a consequence of the independence of the lepton flavors, any [FS](#) process  
 2114 should produce  $ee$ ,  $\mu\mu$ , and  $e\mu$  events in a 1:1:2 ratio. This ratio is taken  
 2115 advantage of in the flavor symmetry method by measuring  $e\mu$  events in  
 2116 data and using them to predict the contribution of these processes in the  
 2117  $ee$  and  $\mu\mu$  channels [1].

2118 To estimate the number of events in SRZ, a control region called CR-FS is  
 2119 used. Both regions are defined in [Table 7](#). CR-FS is very similar to SRZ with  
 2120 two changes: it requires different-flavor leptons instead of the same-flavor  
 2121 leptons required by SRZ, and the  $m_{\ell\ell}$  range it covers has been expanded  
 2122 by a factor of three, now ranging from 61 to 121 GeV. The expansion of the  
 2123  $m_{\ell\ell}$  window is done to increase the number of events in the control region,  
 2124 thus lowering the statistical uncertainty of the prediction <sup>1</sup>.

2125 This control region is expected to be about 95% pure in [FS](#) processes,  
 2126 with most of the remaining events coming from fake or non-prompt lep-

<sup>1</sup> Though this statistical uncertainty is no longer dominant for the analysis, the method was developed for a smaller dataset for which this expansion dramatically decreased the total uncertainty on the background prediction [90]. If the [SR](#) were re-optimized, this would again become an important effect.

tons. The **FS** portion is made up primarily of  $t\bar{t}$  ( $\sim 80\%$ ), with additional contributions from  $Wt$  ( $\sim 10\%$ ),  $WW$  ( $\sim 10\%$ ), and  $< 1\% Z \rightarrow \tau\tau$ .

The 1:1:2 ratio cannot be applied directly to the events measured in CR-FS because the efficiencies for identifying electrons and muons are not identical. Correction factors are applied to account for trigger efficiencies for each channel, selection efficiencies for electrons and muons, the  $m_{\ell\ell}$  expansion, and the purity of the control region. Combining these factors, the estimate for number of events in the  $ee$  and  $\mu\mu$  channels is as follows:

$$N_{ee}^{\text{est}} = \frac{1}{2} \cdot f_{\text{FS}} \cdot f_{Z\text{-mass}} \cdot \sum_{N_{e\mu}^{\text{data}}} k_e(p_T^\mu, \eta^\mu) \cdot \alpha(p_T^{\ell_1}, \eta^{\ell_1}), \quad (38)$$

$$N_{\mu\mu}^{\text{est}} = \frac{1}{2} \cdot f_{\text{FS}} \cdot f_{Z\text{-mass}} \cdot \sum_{N_{e\mu}^{\text{data}}} k_\mu(p_T^e, \eta^e) \cdot \alpha(p_T^{\ell_1}, \eta^{\ell_1}), \quad (39)$$

where  $N_{e\mu}^{\text{data}}$  is the number of data events observed in CR-FS,  $f_{\text{FS}}$  is the fraction of events from **FS** processes in CR-FS,  $f_{Z\text{-mass}}$  is the fraction of events in the widened  $m_{\ell\ell}$  range expected to be in the on-Z range (taken from  $t\bar{t}$  MC),  $k_e(p_T, \eta)$  and  $k_\mu(p_T, \eta)$  are relative selection efficiencies for electrons and muons, calculated in bins of  $p_T$  and  $\eta$  of the lepton to be replaced, and  $\alpha(p_T, \eta)$  accounts for the different trigger efficiencies for events in each channel, binned based on the kinematic properties of the leading lepton. These  $k$  and  $\alpha$  factors are calculated from data in an inclusive on-Z selection ( $81 < m_{\ell\ell}/\text{GeV} < 101$ ,  $\geq 2$  jets), according to:

$$k_e(p_T, \eta) = \sqrt{\frac{N_{ee}^{\text{meas}}}{N_{\mu\mu}^{\text{meas}}}} \quad (40)$$

$$k_\mu(p_T, \eta) = \sqrt{\frac{N_{\mu\mu}^{\text{meas}}}{N_{ee}^{\text{meas}}}} \quad (41)$$

$$\alpha(p_T, \eta) = \frac{\sqrt{\epsilon_{ee}^{\text{trig}}(p_T, \eta) \times \epsilon_{\mu\mu}^{\text{trig}}(p_T, \eta)}}{\epsilon_{e\mu}^{\text{trig}}(p_T, \eta)} \quad (42)$$

where  $\epsilon_{ee/\mu\mu}^{\text{trig}}$  is the trigger efficiency<sup>2</sup> and  $N_{ee/\mu\mu}^{\text{meas}}$  is the number of  $ee/\mu\mu$  events in the inclusive on-Z region described above. Here, the  $k$  factors are related by  $k_e = 1/k_\mu$ . These factors are calculated separately for leading and sub-leading leptons, and the appropriate  $k$  value is selected based on which of the leptons is to be replaced.

In most  $p_T$  and  $\eta$  ranges, the difference between electron and muon selection efficacies is small, so these correction factors are typically within 10% of unity. In the region  $|\eta| < 0.1$  they are up to 50% from unity because of the lack of coverage of the muon spectrometer.  $k_e$  factors measured in

<sup>2</sup> This efficiency is defined by taking all events in the inclusive on-Z selection mentioned above and determining the fraction that passes the relevant trigger requirement defined by [Table 8](#). Because the offline selection made on these events already has some trigger dependence, this calculation of efficiency could be slightly biased. This effect is considered in [Section 11.1.1](#), and the uncertainty applied to the estimate as a result is described.

2153 the 2016 dataset can be seen in [Figure 64](#). In most cases, the only correction  
 2154 factor that differs substantially from is  $f_{Z\text{-mass}}$ , which is typically about  
 2155  $1/3$ .

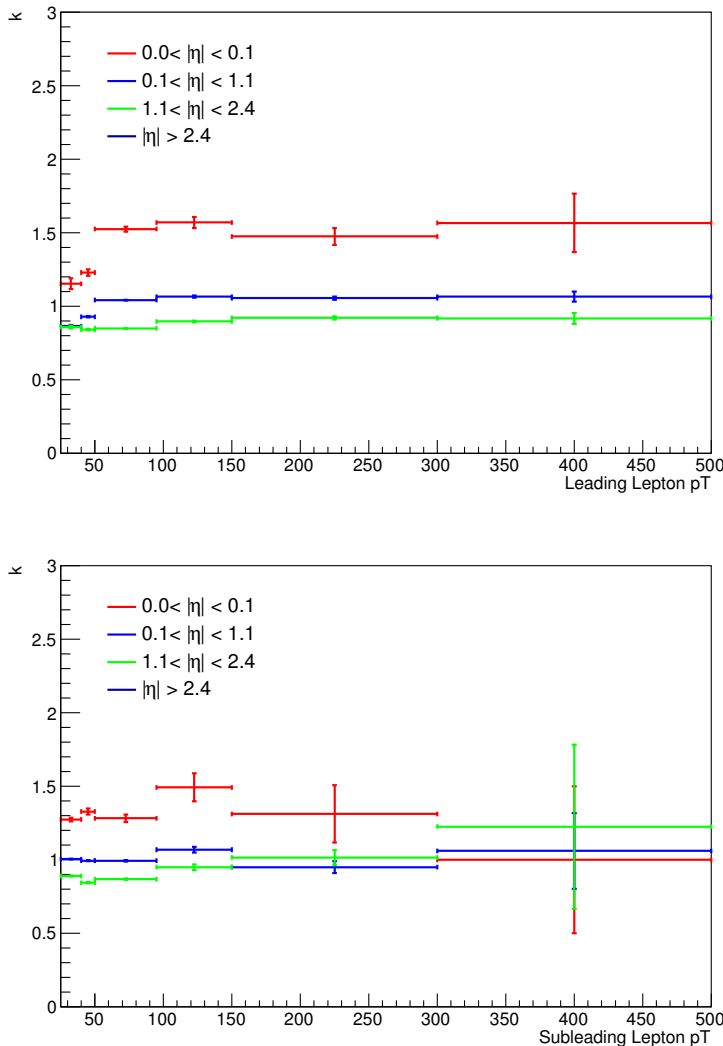


Figure 64: Measurements of  $k_e$ , the ratio of electron to muon events, in bins of  $p_T$  and  $\eta$ . On the top is the measurements indexed by the leading lepton, while the measurements indexed by the subleading lepton are on the bottom. These efficiencies are for the 2016 dataset.

2156 The estimate is corrected for contamination of non-[FS](#) backgrounds in  
 2157 CR-[FS](#). A scaling factor is determined by subtracting these backgrounds  
 2158 from the number of  $e\mu$  events measured in CR-[FS](#), then determining the  
 2159 fraction of the original data events that this pure-[FS](#) number represents.  
 2160 The estimate for the non-[FS](#) backgrounds is taken from [MC](#) for all processes  
 2161 except fakes, which are predicted from data using the matrix method de-  
 2162 scribed in [Section 10.3](#).  $f_{\text{FS}}$  is about 94% in CR-[FS](#).

2163 A prediction is made both for SRZ using the 91 events measured in  
 2164 CR-[FS](#), and the lower- $E_T^{\text{miss}}$  validation region, VRS, with the 277 events in

Region	$ee$ prediction	$\mu\mu$ prediction	combined prediction
SRZ	$16.5 \pm 2.1$	$16.7 \pm 2.0$	$33.2 \pm 3.9$
VRS	$49.7 \pm 4.6$	$49.6 \pm 4.6$	$99.3 \pm 8.5$

Table 9: Yields in signal and validation regions for the flavor symmetric background. Errors include statistical and systematic uncertainties, discussed in [Chapter 11](#).

2165 VR-FS. The background estimation is performed separately for the two  
 2166 data taking periods, 2015 and 2016, because of the changing triggers and  
 2167 conditions. The results are then summed together, as shown in [Table 9](#).  
 2168 The uncertainties in this table are discussed in [Section 11.1.1](#).

2169 [10.1.2 Sideband Fit Method](#)

2170 As a crosscheck to the flavor symmetry method, a [MC](#)-based method is  
 2171 used. This method is called a *sideband fit*, and it begins with a [MC](#) estimate  
 2172 of the signal region across an  $m_{\ell\ell}$  range that includes all values above 40  
 2173 GeV. This region, excluding the on-Z range that makes up the [SR](#), is used  
 2174 as a control region, defined as CRT in [Table 7](#).

2175 The [SM](#) backgrounds are estimated for CRT using [MC](#), except for the  
 2176 fakes background, which is taken from the data-driven method described  
 2177 in [Section 10.3](#). This background prediction is then fit to the measured  
 2178 data yield in CRT with one free parameter,  $\mu$ . This parameter scales the  
 2179 overall normalization of  $t\bar{t}$  [MC](#). All other backgrounds contributing to this  
 2180 control region are constrained by their uncertainties, which are used as  
 2181 nuisance parameters in the fit. Once  $\mu$  has been acquired from this fit, it  
 2182 is applied to the  $t\bar{t}$  [MC](#) yield in the [SR](#). This scaled  $t\bar{t}$  [MC](#) is added to the  
 2183 raw [MC](#) estimates of the other [FS](#) processes to give a final estimate of the  
 2184 [FS](#) background.

2185 The results of the fit can be seen in [Table 10](#), along with the original  
 2186 [MC](#) or data-driven estimates for each background. The bottom half of the  
 2187 table shows the raw [MC](#) estimates, as well as data-driven estimates for the  
 2188 fakes and  $Z/\gamma^* + \text{jets}$  backgrounds. The top half of the table shows values  
 2189 for each of these quantities after the fit. The only significant change after  
 2190 the fit is the  $t\bar{t}$  background, which is scaled with  $\mu = 0.64$ . Normalization  
 2191 factors acquired in CRT, including  $\mu$  and the nuisance parameters for other  
 2192 [MC](#)-driven backgrounds, are applied to SRZ.

2193 To validate the method, it is repeated in VRS using a fit acquired from  
 2194 VRT. These regions are identical to SRZ and CRT, but with  $E_T^{\text{miss}}$  ranging  
 2195 from 100 to 200 GeV. The normalization factors, listed in [Table 11](#), are sig-  
 2196 nificantly different for the two regions. This difference is expected because  
 2197 the  $t\bar{t}$  [MC](#) over-predicts the high- $E_T^{\text{miss}}$  tail. This discrepancy between data  
 2198 and [MC](#) is likely due to a mismodeling of the top quark  $p_T$  distribution,  
 2199 which does not match the spectrum seen in data [91, 92]. [Figure 65](#) shows

channel	$ee/\mu\mu$ CRT	$ee/\mu\mu$ SRZ	$ee/\mu\mu$ SRZ	$ee$ SRZ	$\mu\mu$ SRZ
Observed events	273	60	35	35	25
Fitted bkg events	$272.76 \pm 16.88$	$49.33 \pm 8.04$	$27.09 \pm 4.73$	$22.70 \pm 3.80$	
Fitted flavour symmetry events	$236.96 \pm 21.66$	$28.96 \pm 7.47$	$16.41 \pm 4.33$	$12.55 \pm 3.29$	
Fitted WZ/ZZ events	$4.03 \pm 1.13$	$14.27 \pm 4.45$	$7.81 \pm 2.45$	$6.46 \pm 2.07$	
Fitted SHERPA Z/ $\gamma^*$ + jets events	$1.95 \pm 0.14$	–	–	–	
Data-driven Z/ $\gamma^*$ + jets ( $\gamma$ + jets) events	–	$3.10 \pm 2.25$	$1.02^{+1.25}_{-1.02}$	$2.08 \pm 1.38$	
Fitted rare top events	$4.04 \pm 1.04$	$2.90 \pm 0.76$	$1.39 \pm 0.38$	$1.50 \pm 0.40$	
Data-driven fake lepton events	$25.78 \pm 14.26$	$0.10^{+0.18}_{-0.10}$	$0.46 \pm 0.45$	$0.10 \pm 0.01$	
Expected SM Events	366.71	61.01	33.73	33.73	27.74
MC flavour symmetry events	331.32	40.72	23.09	23.09	17.63
MC WZ/ZZ events	4.02	14.20	7.77	7.77	6.43
MC SHERPA Z/ $\gamma^*$ + jets events	1.94	–	–	–	–
Data-driven Z/ $\gamma^*$ + jets ( $\gamma$ + jets) events	–	3.10	1.02	1.02	2.08
MC rare top events	4.04	2.89	1.39	1.39	1.50
Data-driven fake lepton events	25.39	0.10	0.46	0.46	0.10

Table 10: Background fit results from the sideband fit method. The  $t\bar{t}$  MC’s normalization is taken as a free parameter in the fit to data in CRT, then that normalization factor is applied in SRZ. The results are shown here both divided between the  $ee$  and  $\mu\mu$  channels and summed together. All other backgrounds are taken from MC in CRT, while in SRZ, the Z/ $\gamma^*$  + jets contribution is taken from the  $\gamma$  + jets method. The uncertainties quoted include both statistical and systematic components.

the lepton  $p_T$  distribution in  $t\bar{t}$  events, demonstrating this discrepancy. This sideband fit method corrects for this mismodeling by performing fits in regions very kinematically similar to the signal region.

Fit region	$t\bar{t}$ normalization ( $\mu$ )
CRT	$0.64 \pm 0.18$
VRT	$0.80 \pm 0.09$

Table 11: Summary of the  $t\bar{t}$  normalization factors calculated by the sideband fit to CRT and VRT for the 2015+2016 data.

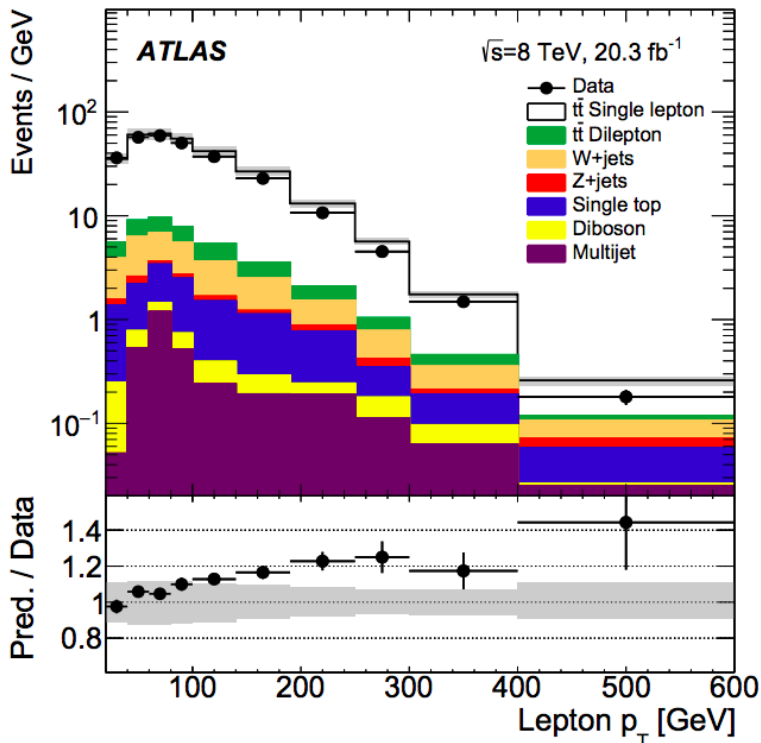


Figure 65: Lepton  $p_T$  distribution in data and MC, demonstrating the overestimate of the high- $p_T$  tail in MC [91].

This method is extremely effective as a crosscheck because it uses a completely independent dataset from the flavor symmetry method, and the two methods have very little overlap in dependence on MC. They produce consistent results in both SRZ and VRS, as shown in Table 12.

## 10.2 $Z/\gamma^* + \text{jets}$ background

The  $Z/\gamma^* + \text{jets}$  background is produced by a process called Drell-Yan in which annihilating quark/anti-quark pairs produce a  $Z$  boson or a virtual photon. These bosons then decay to two leptons, which, in the case of the  $Z$  boson, naturally appear in the  $Z$ -mass window. The boson typically re-

Region	Flavour-symmetry	Sideband fit
SRZ	$33 \pm 4$	$29 \pm 7$
VR-S	$99 \pm 8$	$92 \pm 25$

Table 12: Comparison of [FS](#) background predictions from the nominal method, the flavor symmetry method, and the cross-check, the sideband fit method. Uncertainties include statistical and systematic uncertainties in both cases.

2212 coils off a hadronic system, which can satisfy the jet and  $H_T$  requirement  
 2213 in SRZ. However, this process rarely produces real  $E_T^{\text{miss}}$  (though occasionally  
 2214 neutrinos do appear in hadronic decays of a Z boson), so most events  
 2215 with large amounts of  $E_T^{\text{miss}}$  are the result of mismeasurement. The 200  
 2216 GeV  $E_T^{\text{miss}}$  cut in SRZ includes Z events only from the very high tail of  
 2217 the  $E_T^{\text{miss}}$  distribution, so a small change in the assumptions about jet res-  
 2218 olution or energy scale in [MC](#) can drastically change the prediction. If the  
 2219 prediction of the  $Z/\gamma^* + \text{jets}$  background is too low, this will result in a  
 2220 signal-like peak of data over expected background.

2221 Because of this volatility in the [MC](#) prediction in these high  $E_T^{\text{miss}}$  tails,  
 2222 a data-driven method is used to estimate this background. The method  
 2223 uses  $\gamma + \text{jets}$  events which, like the  $Z/\gamma^* + \text{jets}$  events, contain one boson  
 2224 recoiling against a hadronic system. These  $\gamma + \text{jets}$  events are then cor-  
 2225 rected for the kinematic differences between photons and Z bosons [[33](#),  
 2226 [93](#)]. The sample of  $\gamma + \text{jets}$  events is taken from CR- $\gamma$ , defined in [Table 7](#).  
 2227 This region is similar to the SRZ selection without the  $E_T^{\text{miss}}$  requirement,  
 2228 but it vetoes events with leptons and requires at least one photon. Addi-  
 2229 tionally, the  $\Delta\phi(\text{jet}_{12}, p_T^{\text{miss}})$  cut in SRZ, which is designed to reduce the  
 2230 background from mismeasured jets, is removed for this region because of  
 2231 its unpredictability at very low values of  $E_T^{\text{miss}}$ , when the angle of the  $E_T^{\text{miss}}$   
 2232 is much less meaningful.

2233 Despite their similarities, there are many theoretical differences between  
 2234  $\gamma$  and Z events. The massive Z boson requires more energy to produce  
 2235 than the massless photon, producing a difference in the kinematic distribu-  
 2236 tions for bosons and jets in these events. Another consequence of photon's  
 2237 masslessness is that they must be produced with associated jets; other-  
 2238 wise, the process would violate conservation of energy. As a consequence  
 2239 of these differences, many kinematic variables have different shapes be-  
 2240 tween the two samples. [Figure 66](#) shows a [MC](#) comparison of boson  $p_T$   
 2241 between  $\gamma$  and Z events, demonstrating the shape differences between the  
 2242 two processes.

2243 The most significant experimental difference between Z and  $\gamma$  events is  
 2244 that Z bosons rapidly decay, in the case of this analysis, to two leptons,  
 2245 which are then be observed by the [ATLAS](#) detector. In contrast, the photon  
 2246 is stable, and can be directly detected by [ATLAS](#). This means that the re-  
 2247 constructed Z boson has an energy resolution that's the convolution of the

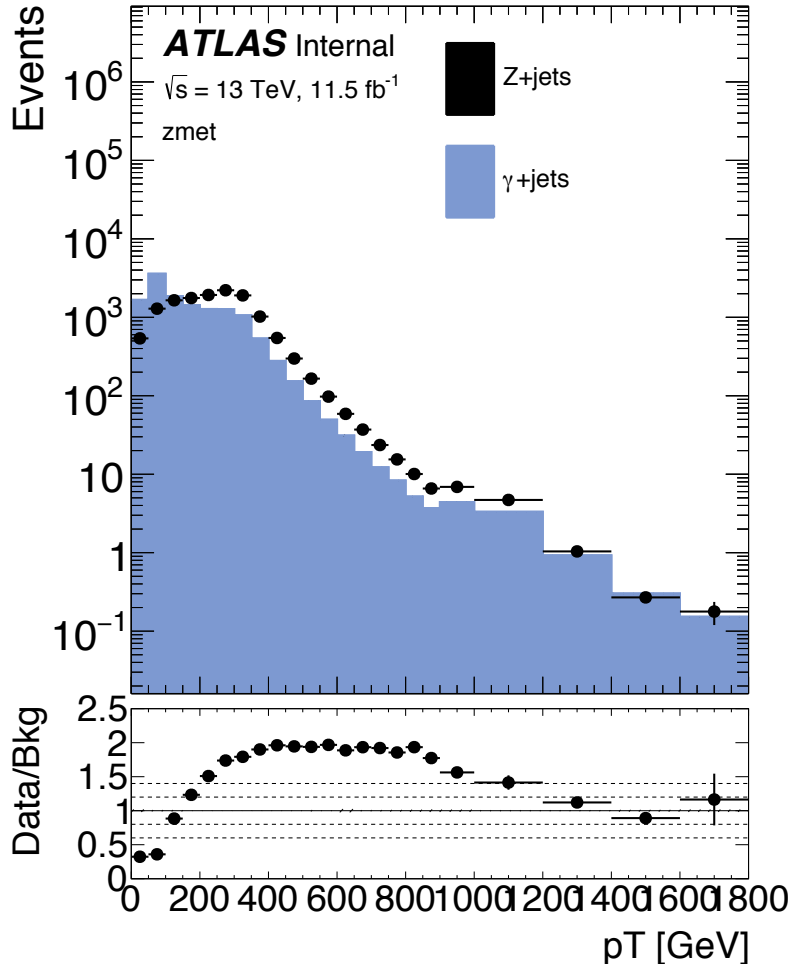


Figure 66: MC comparison of boson  $p_T$  in a selection of photon and  $Z \rightarrow \ell\ell$  events with  $H_T > 600$  GeV. The feature at 1000 GeV is not physical, but a reflection of the change in bin size.

resolutions of either a pair of electrons or a pair of muons, while the photon resolution is the result of only one measurement. Though electron and photon resolutions are similar because both depend on the electromagnetic calorimeter, the difference between the measurement of two objects and one object creates small differences. The muons, whose energy measurements rely on the reconstruction of tracks in the ID and MS, have a very different energy resolution from either electrons or photons.

The goal of this method is to predict the  $E_T^{\text{miss}}$  distribution of the  $Z/\gamma^* +$  jets background using a manipulated  $\gamma +$  jets sample from data. These differences between  $Z$ -jet and  $\gamma$ -jet events can be broken down into two categories: differences which affect the jet energy and measurement, and differences which affect the boson energy and measurement. The differences in the hadronic system are simpler, and mostly consist of different numbers and energies of jets between the two samples, which can be accounted for via reweighting in a variable that's representative of the total

2263 energy scale of the event. The differences in the bosons are more complex,  
 2264 and require the application of smearing functions based on the different  
 2265 observed objects. Together these corrections allow for complete modeling  
 2266 of the  $Z/\gamma^*$  + jets  $E_T^{\text{miss}}$  spectrum with  $\gamma$ +jet events.

2267 10.2.1 *Photon and Z Event Selection*

2268 The baseline photon events come from an inclusive CR with no  $E_T^{\text{miss}}$  cut,  
 2269 a lepton veto, and the requirement of at least one photon, which is called  
 2270 CR- $\gamma$  and defined in Table 7<sup>3</sup>. This selection is very pure in  $\gamma$ +jet events,  
 2271 but some  $V\gamma$  events are also included, which can include real  $E_T^{\text{miss}}$ . These  
 2272 backgrounds are subtracted from the yield in this region according to MC.

2273 The triggering scheme for these  $\gamma$  + jets events is more complicated than  
 2274 in other regions because the lowest unprescaled photon trigger requires a  
 2275 photon  $p_T$  of at least 120 (140) GeV in 2015 (2016) datataking, but the  
 2276 method requires events with much lower  $p_T$  to predict the full  $Z$ -boson  $p_T$   
 2277 spectrum. To accomplish this, the lower- $p_T$  photons are broken down into  
 2278 small  $p_T$  ranges with a different prescaled trigger required in each range,  
 2279 listed in Table 13. The events in each selection are then weighted by the  
 2280 prescale value of the trigger used to reconstruct a smooth  $p_T$  spectrum.

2281 These  $\gamma$  events can then be compared to baseline  $Z \rightarrow \ell\ell$  events with  
 2282 a similar selection. These events have the same dilepton requirements as  
 2283 SRZ, without the  $m_{\ell\ell}$  cut. They also have no  $E_T^{\text{miss}}$  cut, but like the photons,  
 2284 are required to have  $H_T > 600$  GeV as in SRZ.

2285 10.2.2 *Smearing of Photon Events*

2286 While  $Z$ +jet events are measured as a pair of leptons recoiling against a  
 2287 hadronic system,  $\gamma$ +jet events are measured only as one object recoiling  
 2288 against jets. In addition, detector resolution is very different for muons  
 2289 and photons, though electrons and photons are similar. The impact of  
 2290 these differences must be corrected for in  $\gamma$ +jet events in order for them to  
 2291 accurately predict the  $E_T^{\text{miss}}$  distribution of the  $Z$ s. Luckily, in most cases,  
 2292 the resolution of the photon's  $p_T$  is better than that of the  $Z$  boson, so the  
 2293 photon events can be smeared to emulate the  $Z$ s.

2294 To isolate mismeasurement of boson  $p_T$ , this method uses  $E_{T,\parallel}^{\text{miss}}$ , defined  
 2295 as

$$E_{T,\parallel}^{\text{miss}} = E_T^{\text{miss}} \sin\theta \quad (43)$$

2296 where  $\theta$  is the angle between  $p_T^{\text{miss}}$  and the  $p_T$  of the  $Z$  boson. Figure 67  
 2297 shows the  $E_{T,\parallel}^{\text{miss}}$  distribution in MC for the two samples, and demonstrates  
 2298 the discrepancies between them. The core of the photon distribution is sim-  
 2299 ilar to the  $Z \rightarrow ee$  distribution because measurements of both photons and

---

3 This region includes an  $H_T$  cut, which requires the translation of photon  $p_T$  into an equivalent di-lepton  $p_T$  scalar sum. This process is described in Section 10.2.4.

$p_T$ Range [GeV]	Trigger Name
2015 Data-Taking	
$37 < p_T < 45$	HLT_g35_loose_L1EM15
$45 < p_T < 50$	HLT_g40_loose_L1EM15
$50 < p_T < 55$	HLT_g45_loose_L1EM15
$55 < p_T < 125$	HLT_g50_loose_L1EM15
$p_T > 125$	HLT_g120_loose_L1EM15
2016 Data-Taking	
$25 < p_T < 30$	HLT_g20_loose_L1EM12
$30 < p_T < 40$	HLT_g25_loose_L1EM12
$40 < p_T < 45$	HLT_g35_loose_L1EM12
$45 < p_T < 50$	HLT_g40_loose_L1EM12
$50 < p_T < 55$	HLT_g45_loose_L1EM12
$55 < p_T < 65$	HLT_g50_loose_L1EM12
$65 < p_T < 75$	HLT_g60_loose_L1EM12
$75 < p_T < 85$	HLT_g70_loose_L1EM12
$85 < p_T < 105$	HLT_g80_loose_L1EM12
$105 < p_T < 145$	HLT_g100_loose_L1EM12
$p_T > 145$	HLT_g140_loose_L1EM12

Table 13: List of triggers used to collect photon events in 2015 and 2016 data-taking.

2300 electrons are primarily taken from the electromagnetic calorimeter and  
 2301 have the same resolution. For muons, which rely on tracks to determine  
 2302  $p_T$ , the resolution becomes larger at high  $p_T$  values where the tracks are  
 2303 nearly straight. For a muon with a  $p_T$  of 200 GeV, this the resolution is  
 2304 about 5%, while a photon or electron with the same  $p_T$  has a resolution  
 2305 of 1-2% [[Aad:2014zya](#), [Aad:2014nim](#)]. As a consequence, the resolution  
 2306 distributions for photon and  $Z \rightarrow \mu\mu$  events are very different.

2307 A function to smear photon events is derived from the deconvolution  
 2308 of the photon and lepton response functions, taken from 1-jet CRs with  
 2309 no  $H_T$  cut, which are otherwise identical to the baseline  $Z$  and  $\gamma$  selec-  
 2310 tions. In these regions, events are binned in boson  $p_T$ , and in each bin, a  
 2311  $E_{T,\parallel}^{\text{miss}}$  distribution is made. The smearing function is defined for each bin  
 2312 as the deconvolution of the  $Z/\gamma^* + \text{jets}$  and  $\gamma + \text{jets}$   $E_{T,\parallel}^{\text{miss}}$  distributions.

2313 Next, for each photon event, the smearing function matching the event's  
 2314 photon  $p_T$  is sampled, yielding a smearing factor  $\Delta p_T$ . The photon's  $p_T$  is  
 2315 then adjusted according to

$$p_T^{\gamma'} = p_T^{\gamma} + \Delta p_T \quad (44)$$

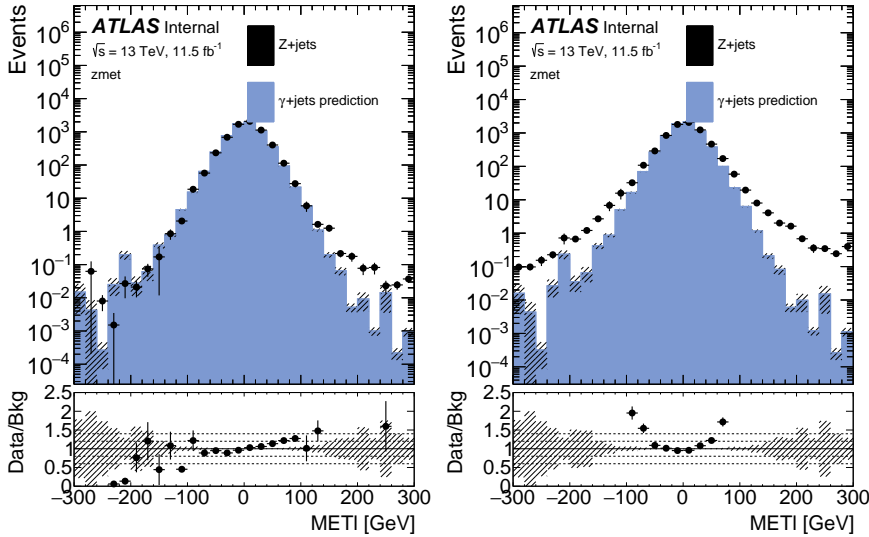


Figure 67:  $E_{T,\parallel}^{\text{miss}}$  distributions in MC for  $Z+\text{jets}$  in the  $ee$  (left) and  $\mu\mu$  (right) channels compared to the  $\gamma + \text{jets}$  prediction in an inclusive region with  $H_T > 600 \text{ GeV}$ .

and the corresponding change in  $E_T^{\text{miss}}$  is made,

$$E_{T,\parallel}^{\text{miss}'} = E_{T,\parallel}^{\text{miss}} - \Delta p_T. \quad (45)$$

The nominal smearing function is taken from MC in order to remove contamination from other backgrounds, and the resulting  $E_{T,\parallel}^{\text{miss}}$  distributions can be seen in Figure 68. Though there is a small amount of oversmearing in the negative tail, the improvement in agreement between the distributions, especially in their cores, is clear.

### 10.2.3 $p_T$ Reweighting of Photon Events

Next, the photon events are reweighted to match the boson  $p_T$  spectrum of the  $Z$  events. This is accomplished by making histograms of boson  $p_T$  for  $\gamma$  and  $Z$  events with binning identical to the  $p_T$  bins used in Section 10.2.2. Photons are binned based on their smeared  $p_T$  determined in the previous step. A reweighting factor  $f(p_T)$  is then calculated in each bin, according to

$$f_{\text{MC}}(x) = \frac{N_{Z/\gamma^*+\text{jets}}(x)}{N_{\gamma+\text{jets}}(x)} \quad (46)$$

in MC, and in data according to

$$f_{\text{data}}(x) = \frac{N_{\text{data}}(x) - N_{t\bar{t}}(x) - N_{\text{VV}}(x)}{N_{\gamma+\text{jets data}}(x)} \quad (47)$$

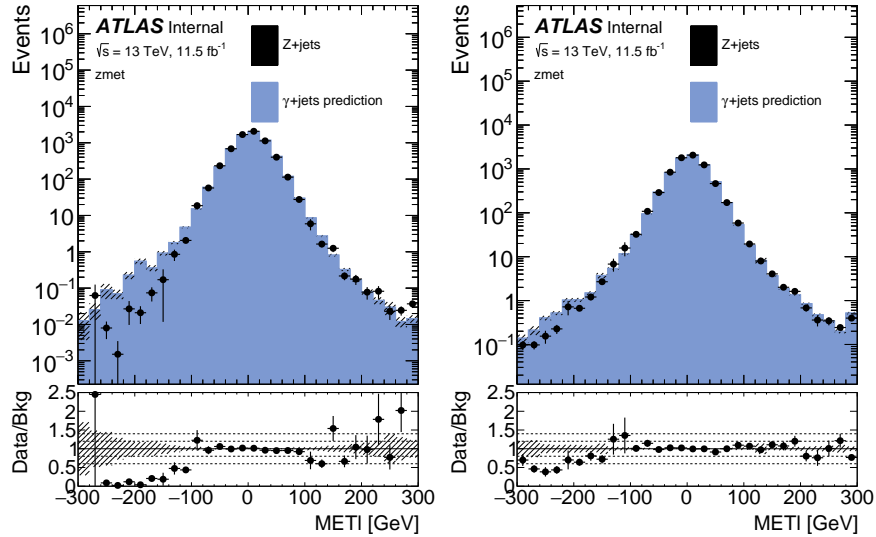


Figure 68:  $E_{T,\parallel}^{\text{miss}}$  distributions in MC for Z+jets ee (left) and  $\mu\mu$  (right) channels compared to  $\gamma + \text{jets}$  in an inclusive region with  $H_T > 600$  GeV after the smearing procedure has been performed. The events in these distributions have also been  $p_T$  reweighted, as described in Section 10.2.3.

where the contamination from other backgrounds is taken from MC and subtracted from the Z selection. The resulting reweighting factors can be seen in Figure 69 and are calculated independently for ee and  $\mu\mu$  events.

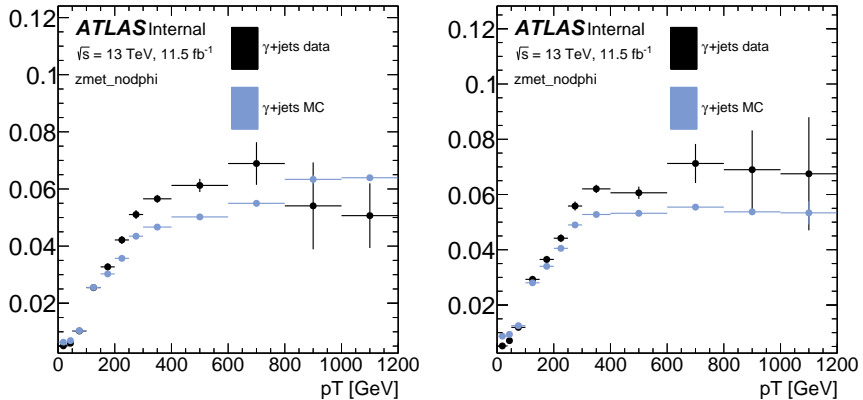


Figure 69: Photon reweighting factors for the ee (left) and  $\mu\mu$  (right) channels derived from data and MC.

This reweighting, though it is performed on the boson  $p_T$ , primarily serves to produce more similar jet distributions between the  $\gamma$  and Z samples. Because, excluding  $E_T^{\text{miss}}$  contributions, the boson  $p_T$  must match the energy of the jet system off which it recoils, these two variables are closely tied. Once the two samples have similar amounts of hadronic energy, the  $E_T^{\text{miss}}$  contribution from mismeasurement of jet energy should also be similar.

Together, the boson smearing and  $p_T$  reweighting produce a  $E_T^{\text{miss}}$  spectrum in the modified photon events that closely match that of the Z events.

2342 Figures 70 and 71 show the comparison of the  $E_T^{\text{miss}}$  distributions be-  
 2343 fore any alteration, with only  $p_T$  reweighting, and after the smearing and  
 2344 reweighting, demonstrating the impact of each step. Once the  $E_T^{\text{miss}}$  distri-  
 2345 bution is well described, the  $\Delta\phi(\text{jet}_{12}, p_T^{\text{miss}})$  can be applied.

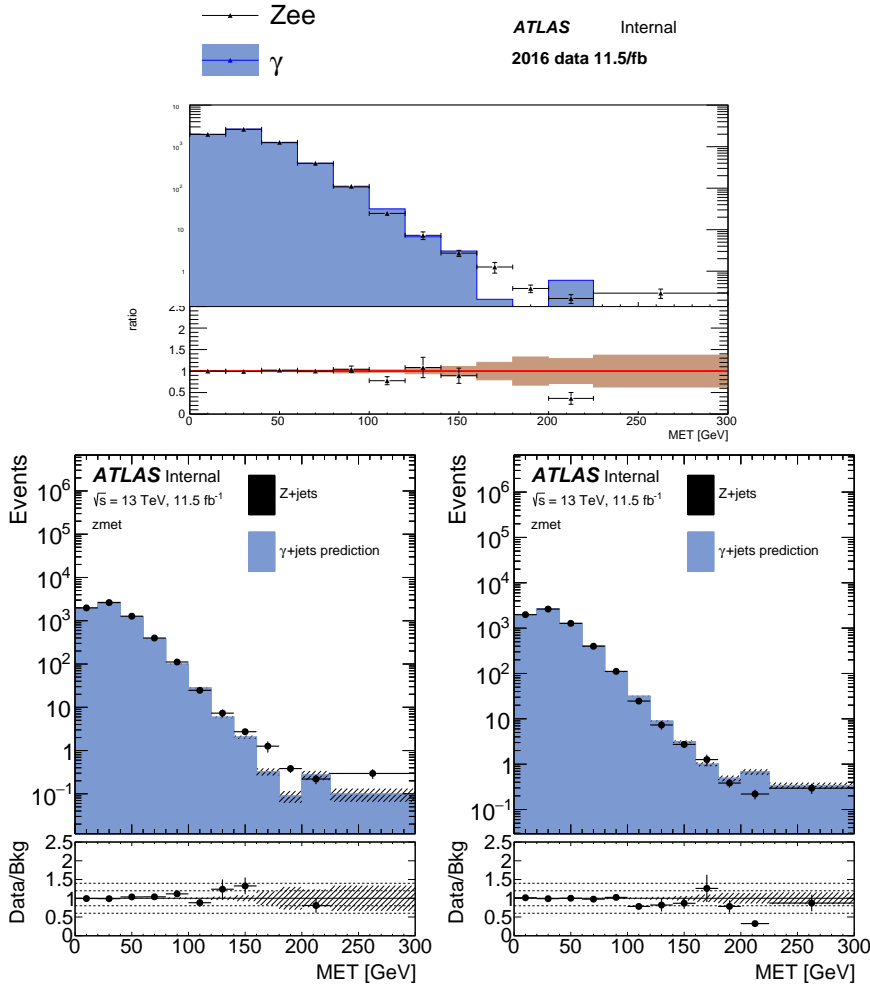


Figure 70:  $E_T^{\text{miss}}$  distribution comparing MC distributions of photon and  $Z$  events before any smearing is applied (top), with only  $p_T$  reweighting applied (bottom left), and after  $p_T$  reweighting and smearing have both been applied (bottom right) in the  $ee$  channel of 2016 data.

#### 2346 10.2.4 Determining $H_T$ and $m_{\ell\ell}$

2347 One complication thus far ignored is that CR- $\gamma$  has no leptons, but some  
 2348 quantities that define the SR require them, namely  $H_T$  (which includes  
 2349 the  $p_T$  of the two leading leptons) and  $m_{\ell\ell}$ . Both of these variables are  
 2350 determined by creating histograms binned in the boson  $p_T$  and sampling.

2351 In the case of  $H_T$ , distributions of the scalar sum of the  $p_T$  of the leading  
 2352 leptons are made for each  $Z$   $p_T$  bin. A sampled value from the distribu-  
 2353 tion is then added to the  $H_T$  of the jets in a photon event to produce the  
 2354 final estimate. This sampling is done before any reweighting is performed

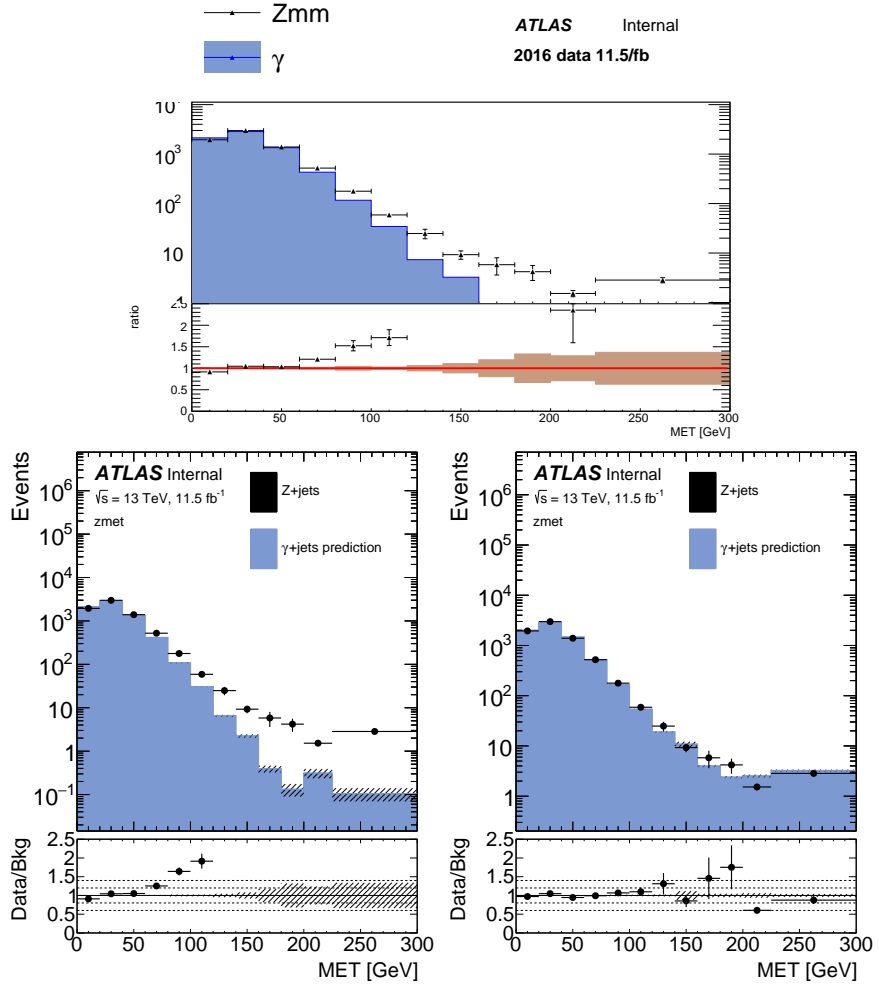


Figure 71:  $E_T^{\text{miss}}$  distribution comparing MC distributions of photon and Z events before any smearing is applied (top), with only  $p_T$  reweighting applied (bottom left), and after  $p_T$  reweighting and smearing have both been applied (bottom right) in the  $\mu\mu$  channel of 2016 data.

because the  $H_T$  is needed to make the preselection for the reweighting process. However, the smearing is performed inclusively in  $H_T$ , so this procedure can be performed using the smeared photon  $p_T$  to choose the distribution to sample.

The  $m_{\ell\ell}$  determination is done after both the smearing and reweighting, and is tied closely to the smearing step. Mismeasurements in lepton  $p_T$  can create  $E_T^{\text{miss}}$  in a  $Z/\gamma^* + \text{jets}$  event, but the same event is likely to migrate off the  $Z m_{\ell\ell}$  window due to the mismeasured lepton. Thus it is very important that the two effects be carefully correlated in the manipulated photon events. To achieve this, MC Z events from the 1-jet CR described in Section 10.2.2 are used to make two-dimensional distributions of  $m_{\ell\ell}$  as a function of the difference between reconstructed and true Z  $p_T$  for the  $ee$  and  $\mu\mu$  channels. A photon event then uses the  $\Delta p_T$  assigned to it dur-

ing the smearing process to index the distribution, and an  $m_{\ell\ell}$  value is sampled from the corresponding bin<sup>4</sup>

To test the soundness of this procedure, it is repeated purely in MC, and the results of the MC prediction and the data prediction are compared to the  $m_{\ell\ell}$  distribution in  $Z/\gamma^* + \text{jets}$  MC in Figure 72. After the  $m_{\ell\ell}$  distribution has been emulated, a cut requiring that the photon events be “on the Z mass peak” can be required.

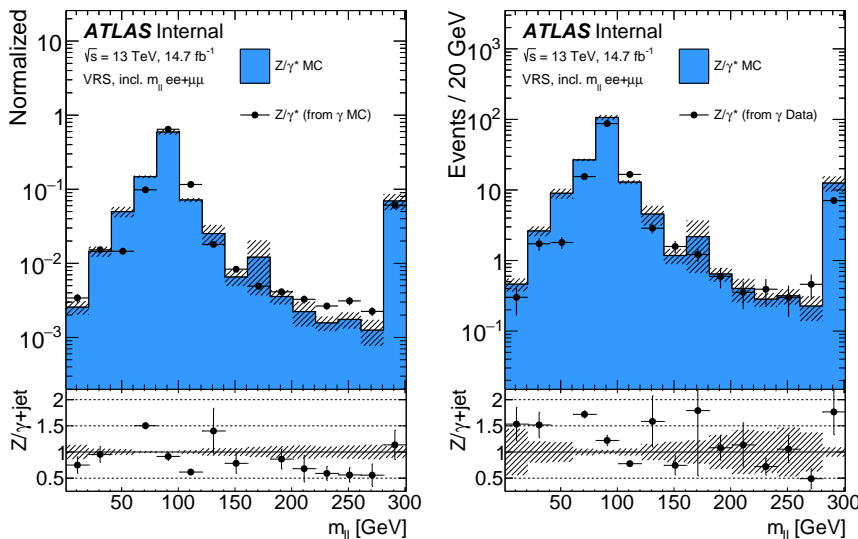


Figure 72:  $Z/\gamma^* + \text{jets}$  MC  $m_{\ell\ell}$  distribution compared to the prediction from  $\gamma + \text{jets}$  method performed on MC (left) and the prediction from  $\gamma + \text{jets}$  method performed on data (right).

### 10.2.5 Subtraction of $V\gamma$ Events

At high  $E_T^{\text{miss}}$ , where the signal region lies, contamination of CR- $\gamma$  with  $V\gamma$  events becomes significant, as shown in Figure 73. These events must be subtracted from the  $\gamma + \text{jets}$  prediction because, once the photons are corrected to approximate Zs, they essentially provide a (not very accurate) prediction of diboson events, which are already accounted for in another background estimate.

This subtraction accomplished by performing the  $\gamma + \text{jets}$  method on  $V\gamma$  MC to approximate these backgrounds’ contribution to the final  $E_T^{\text{miss}}$  distribution. This contribution is then subtracted from the  $\gamma + \text{jets}$  prediction, the impact of which can be seen in Figure 74. As expected, the impact is greatest at high  $E_T^{\text{miss}}$  where these backgrounds are most significant.

<sup>4</sup> Ideally this  $\Delta p_T$  would also include the difference between the true and reconstructed  $p_T$  of the photon events, but this information is of course not accessible in data. Luckily, in the events in the final SR this value is typically negligible compared to the  $\Delta p_T$  from smearing, so the impact is small.

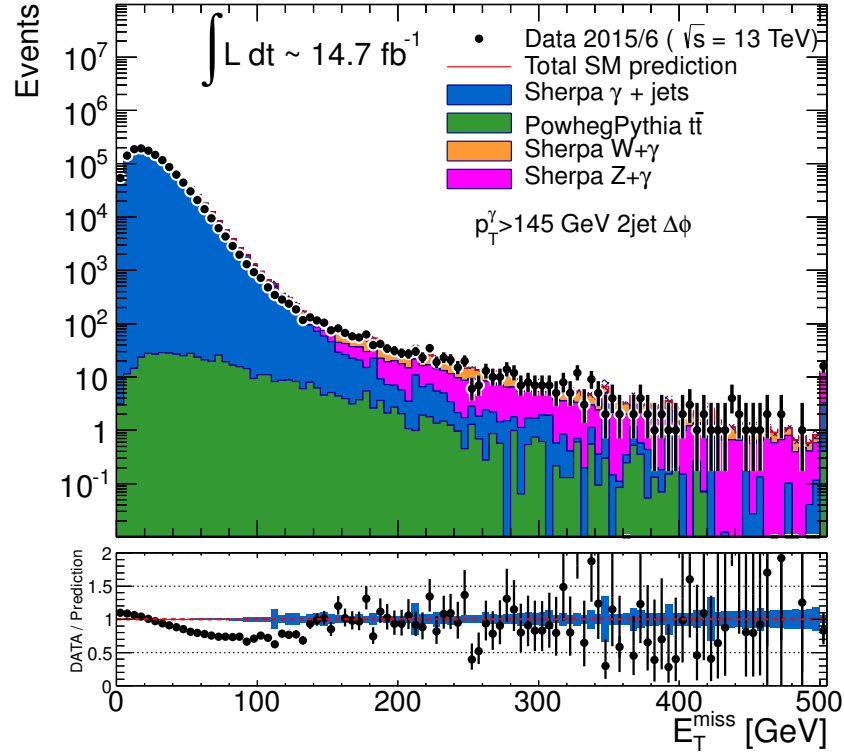


Figure 73: Comparison of data and MC in CR- $\gamma$  without any  $H_T$  cut, including the contributions from various  $V\gamma$  processes.

#### 2387 10.2.6 Validation in Data

2388 The  $\gamma + \text{jets}$  method is validated in a region called VRZ, defined in  
 2389 [Table 7](#), which is similar to SRZ, but with an inverted  $E_T^{\text{miss}}$  cut. [Figure 75](#)  
 2390 shows the low- $E_T^{\text{miss}}$  portion of this VR where the  $Z/\gamma^* + \text{jets}$  background  
 2391 is dominant. Here, the three data-driven background estimates, as well  
 2392 as the remaining MC backgrounds are stacked and compared to the data  
 2393 yield in this region, demonstrating excellent agreement across a wide  $E_T^{\text{miss}}$   
 2394 range.

2395 An additional check can be made in VRZ by removing the  $\Delta\phi(\text{jet}_{12}, p_T^{\text{miss}})$   
 2396 intended to suppress the  $Z/\gamma^* + \text{jets}$  background from jet mismeasurement.  
 2397 [Figure 76](#) shows the distribution of this variable in VRZ, and demonstrates  
 2398 that, even at low values where the  $Z/\gamma^* + \text{jets}$  background is dominant,  
 2399 the  $\gamma + \text{jets}$  method models it accurately.

#### 2400 10.3 FAKE AND NON-PROMPT LEPTONS

2401 The *fakes* background consists of processes that produce only one lepton,  
 2402 but whose events are otherwise kinematically similar to the [SR](#). These pro-  
 2403 cesses include semileptonic  $t\bar{t}$ ,  $W+\text{jets}$ , and single top processes. Though  
 2404 these processes typically only produce one lepton, they can be recon-  
 2405 structed with two leptons due to a hadron being misidentified as a lepton

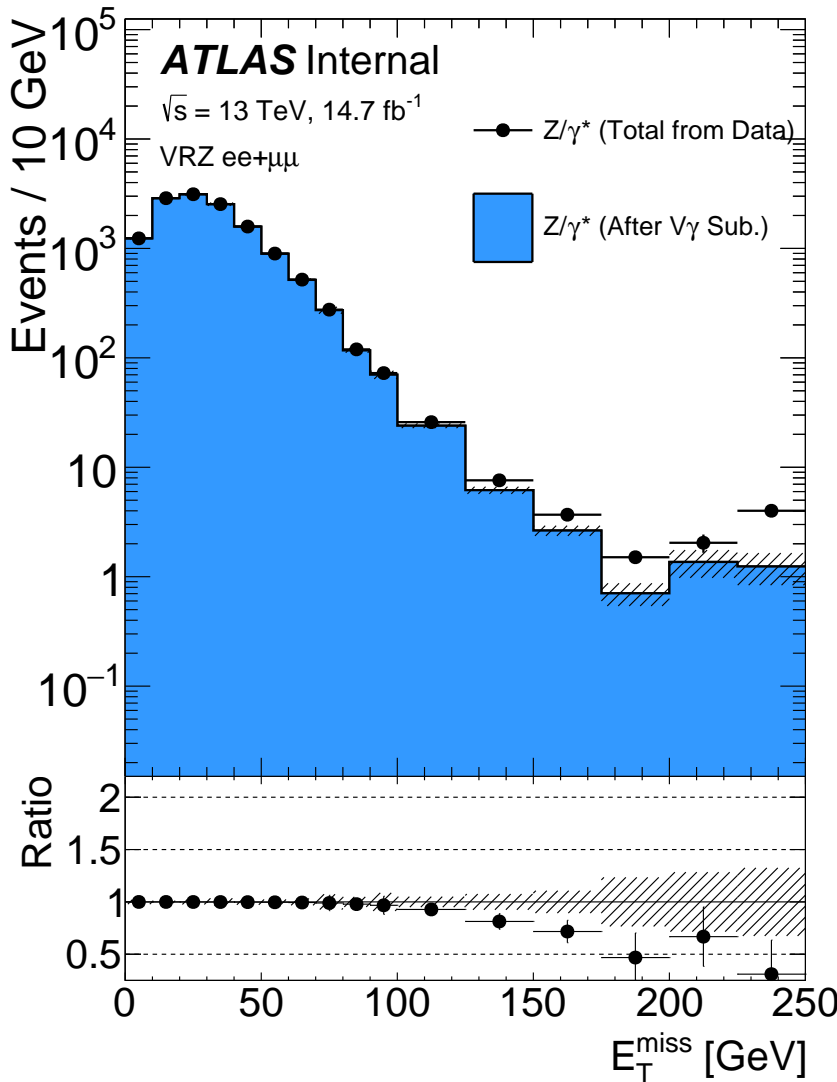


Figure 74: Total  $\gamma + \text{jets}$  data prediction in SRZ (excluding the  $E_T^{\text{miss}}$  cut) and the prediction after the  $V\gamma$  subtraction.

or due to a real non-prompt lepton resulting from photon conversions or  $B$ -hadron decays. As with the  $Z/\gamma^* + \text{jets}$  background, it is very difficult to predict with MC because the flaws in reconstruction are typically less well described by the models used in MC production than the successes. Nonetheless, a rough estimate can be made of this background by using MC, which indicates that the number of fake events in SRZ is consistent with zero.

Despite the small predicted contribution in the SR, a data-driven method called the *matrix method* is employed to estimate these fake events [94]. This method is also used to estimate the fakes contribution to other control and validation regions where their impact is more significant.

In the matrix method, the quality requirements for signal leptons are loosened to give a selection of baseline leptons (see Table 3 and Table 4), which consist of a higher fraction of fake leptons. In each CR, VR, or SR, the

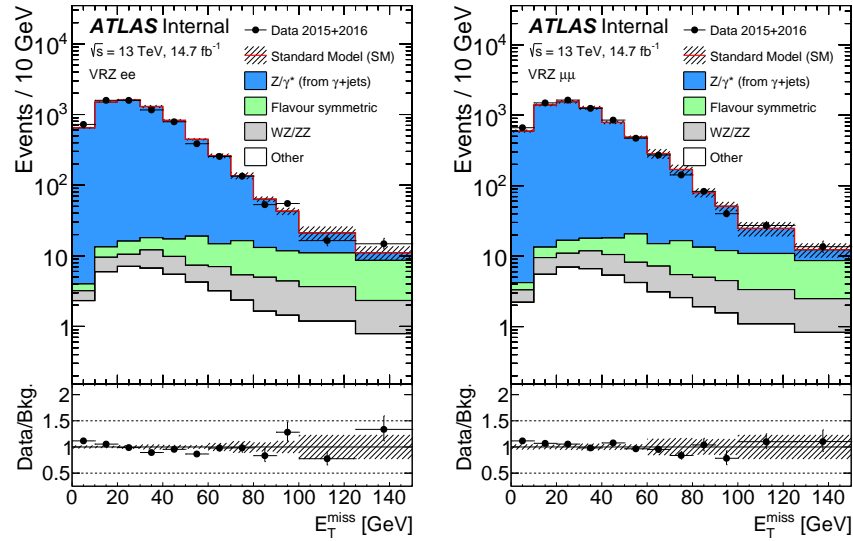


Figure 75:  $E_T^{\text{miss}}$  distribution in VRZ  $ee$  (left) and  $\mu\mu$  (right) with total data yield compared to the sum of the prediction from the  $\gamma + \text{jets}$  method, the prediction from the flavor symmetry method, the prediction from the fake background estimation (included under “other”), and the remaining backgrounds taken from MC.

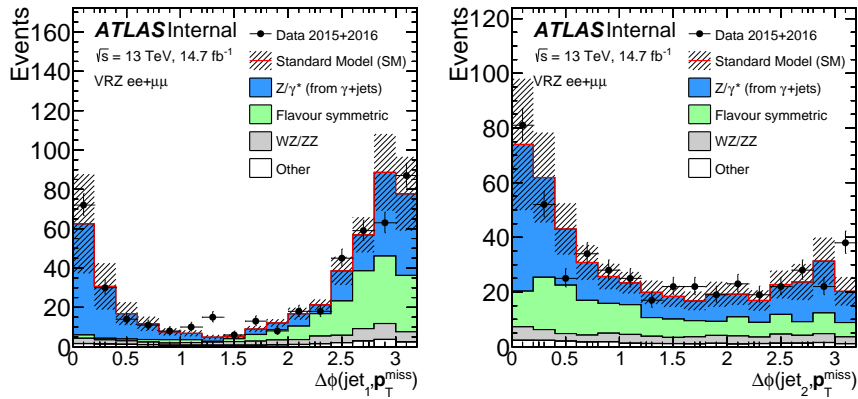


Figure 76:  $\Delta\phi(\text{jet}, p_T^{\text{miss}})$  distribution in for the leading jet (left) and the subleading jet (right). The comparison is performed in VRZ with the cut on  $\Delta\phi(\text{jet}_{12}, p_T^{\text{miss}})$  removed. The total data yield is compared to the sum of the prediction from the  $\gamma + \text{jets}$  method, the prediction from the flavor symmetry method, the prediction from the fake background estimation (included under “other”), and the remaining backgrounds taken from MC.

remaining kinematic selections are made on the baseline leptons, and the number of leptons in the region which pass the signal lepton requirements ( $N_{\text{pass}}$ ) and the number which fail ( $N_{\text{fail}}$ ) are measured. For a 1-lepton

selection, these quantities can be used to predict the number of fake events that pass the selection according to:

$$\frac{N_{\text{fake}}}{N_{\text{pass}}} = \frac{N_{\text{fail}} - (1/\epsilon^{\text{real}} - 1) \times N_{\text{pass}}}{1/\epsilon^{\text{fake}} - 1/\epsilon^{\text{real}}}. \quad (48)$$

The efficiencies  $\epsilon^{\text{real}}$  and  $\epsilon^{\text{fake}}$  give the relative identification efficiency from baseline to signal for genuine, prompt leptons and fake and non-prompt leptons, respectively. For a 2-lepton selection, the principle is the same, but the equation is more complicated, requiring a four-by-four matrix to account for possible combinations of real and fake leptons.

To calculate  $\epsilon^{\text{real}}$ , the tag-and-probe method is performed a selection of  $Z \rightarrow \ell\ell$  data events, CR-real, described in [Table 14](#). In this method, one *tag* lepton passing a signal selection is required, as is another *probe* lepton passing a baseline requirement. Distributions in  $m_{\ell\ell}$  for events with a tag and a passing probe and events with a tag and a failing probe are produced and fit, and the efficiency is computed using the ratio acquired from the fit. A comparison of data and [MC](#) in CR-real can be seen in [Figure 77](#).

Fakes regions	$E_T^{\text{miss}}$ [GeV]	$H_T$ [GeV]	$n_{\text{jets}}$	$m_{\ell\ell}$ [GeV]	SF/DF	OS/SS	$n_{\ell}$
CR-real	–	> 200	$\geq 2$	<b>81–101</b>	$2\ell$ SF	OS	2
CR-fake	< 125	–	–	> 12	$2\ell$ SF/DF	SS	$\geq 2$

[Table 14](#): Control regions used to measure efficiencies of real and fake leptons.

The flavour combination of the dilepton pair is denoted as either “SF” for same-flavour or “DF” for different flavour. The charge combination of the leading lepton pairs are given as “SS” for same-sign or “OS” for opposite-sign.

The fake efficiency,  $\epsilon^{\text{fake}}$ , is determined using the tag-and-probe method in CR-fake, also described in [Table 14](#). This region is different from all other regions considered in this analysis because it requires same-sign leptons. Very few processes genuinely produce two same-sign leptons, so this region is enhanced in fake leptons. An upper limit on  $E_T^{\text{miss}}$  is placed on CR-fake to limit the possible contamination from [BSM](#) processes. According to [MC](#), real, prompt leptons make up about 7% (11%) of the baseline electron (muon) sample and about 10% (61%) of the signal electron (muon) sample in this region. These real lepton backgrounds are subtracted from the CR-fake yields when calculating the efficiencies. [Figure 78](#) shows a comparison of data and [MC](#) in this region.

This method is validated in a fakes-rich validation region with a same-sign lepton requirement,  $E_T^{\text{miss}} \geq 50\text{GeV}$ ,  $\geq 2$  jets, and a veto on  $m_{\ell\ell}$  on the  $Z$ -mass peak for same flavor channels. The results of this validation

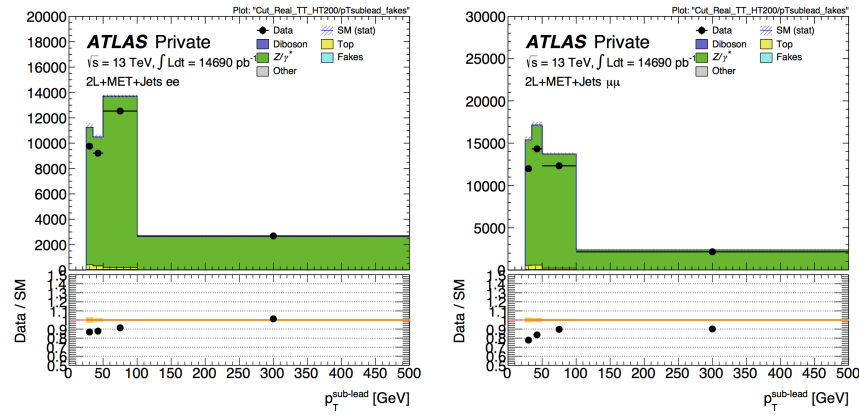


Figure 77: Sub-leading lepton  $p_T$  for  $ee$  (left) and  $\mu\mu$  (right) events in the tight-tight region used to measure the real-lepton efficiency for 2016.

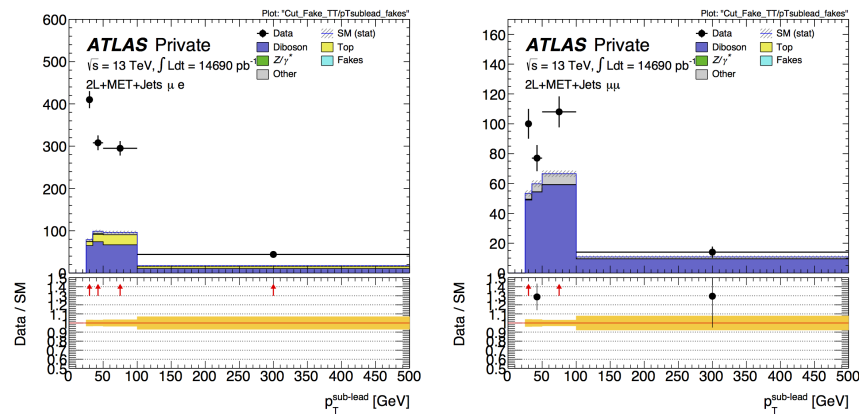


Figure 78: Sub-leading lepton  $p_T$  for  $\mu e$  (left) and  $\mu\mu$  (right) events in the tight-tight region used to measure the fake-lepton efficiency for 2016.

2451 can be seen in Figure 79. With the systematic uncertainties, discussed in  
 2452 Section 11.1.3, the prediction agrees well with the data across a wide range  
 2453 of  $m_{\ell\ell}$  values.

#### 2454 10.4 DIBOSON AND RARE TOP PROCESSES

2455 The remaining backgrounds are diboson processes (excluding WW, which  
 2456 is included in the FS background) and rare top processes. Dibosons events  
 2457 make up about 30% of the events in SRZ, while rare top process contribu-  
 2458 tions are much smaller. Both are taken directly from MC, with validation  
 2459 regions to confirm the accuracy of the prediction. These regions are de-  
 2460 scribed in Table 7, and target different parts of these backgrounds. VR-ZZ  
 2461 is a four-lepton selection designed to select a very pure sample of ZZ  
 2462 events. VR-WZ requires three leptons and makes specific cuts on  $m_T$ , the  
 2463 transverse mass, and  $E_T^{\text{miss}}$  in order to select mostly  $WZ \rightarrow ll\nu\nu$  events.  
 2464 VR-3L is similar to VR-S, but loosens the  $H_T$  and  $E_T^{\text{miss}}$  cuts and requires  
 2465 at least three leptons. This region is designed to target any  $\geq 3$ -lepton  
 2466 process in a region as kinematically close to SRZ as possible while still

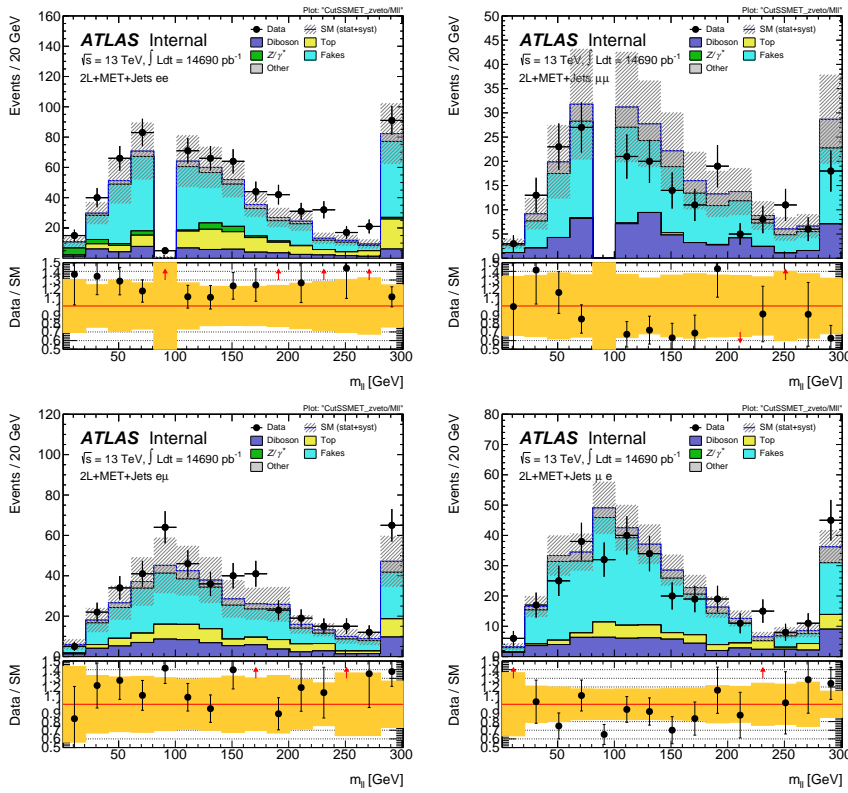


Figure 79: Same sign validation regions in the  $ee$  (top left),  $\mu\mu$  (top right),  $e\mu$  (bottom left) and  $\mu e$  (bottom right) channels combining 2015+2016 data. Uncertainty bands include both statistical and systematic uncertainties.

2467 maintaining enough events to validate. The makeups of these multilepton  
2468 validation regions, as well as VRS, are shown in Table 15.

	VR-S	VR-WZ	VR-ZZ	VR-3L
Observed events	236	698	132	32
Total expected background	$224 \pm 41$	$613 \pm 66$	$139 \pm 25$	$35 \pm 10$
Flavour-symmetric	$99 \pm 8$	-	-	-
WZ/ZZ events	$27 \pm 13$	$573 \pm 66$	$139 \pm 25$	$25 \pm 10$
Rare top events	$11 \pm 3$	$14 \pm 3$	$0.44 \pm 0.11$	$9.1 \pm 2.3$
$Z/\gamma^*$ + jets events	$84 \pm 37$	-	-	-
Fake lepton events	$4 \pm 4$	$26 \pm 6$	-	$0.6 \pm 0.3$

Table 15: Yields in validation regions. In VRS, data-driven background estimates are used for  $Z/\gamma^*$  + jets, fakes, and [FS](#) processes. All other backgrounds are taken from [MC](#), including all backgrounds in the multi-lepton VRS. Uncertainties include statistical and systematic components.

2469 To confirm that the kinematics are well modeled in the diboson vali-  
 2470 dation regions, distributions of boson mass and  $p_T$  are shown in MC and  
 2471 data. Figures 8o and 8i show these distributions for VR-WZ, and Figure 82  
 2472 shows these distributions for VR-ZZ.

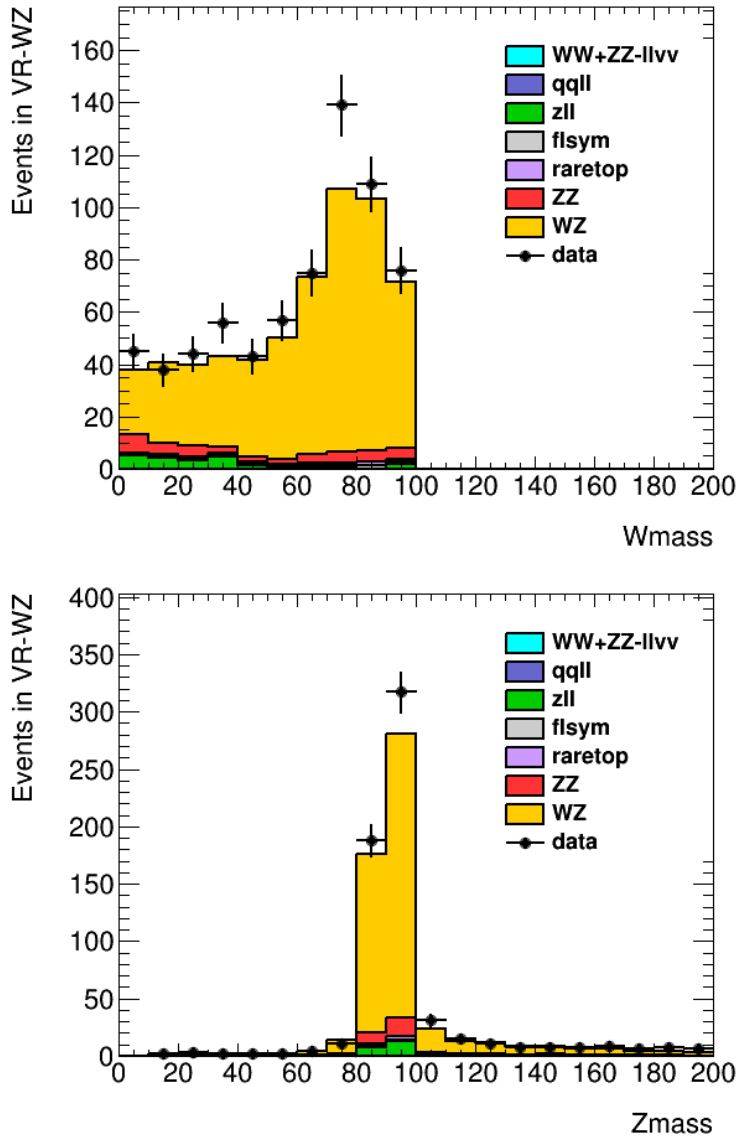


Figure 8o: Distribtuions of data and MC in VR-WZ. Reconstructed transverse mass of the  $W$  (top) and mass of the  $Z$  (bottom).

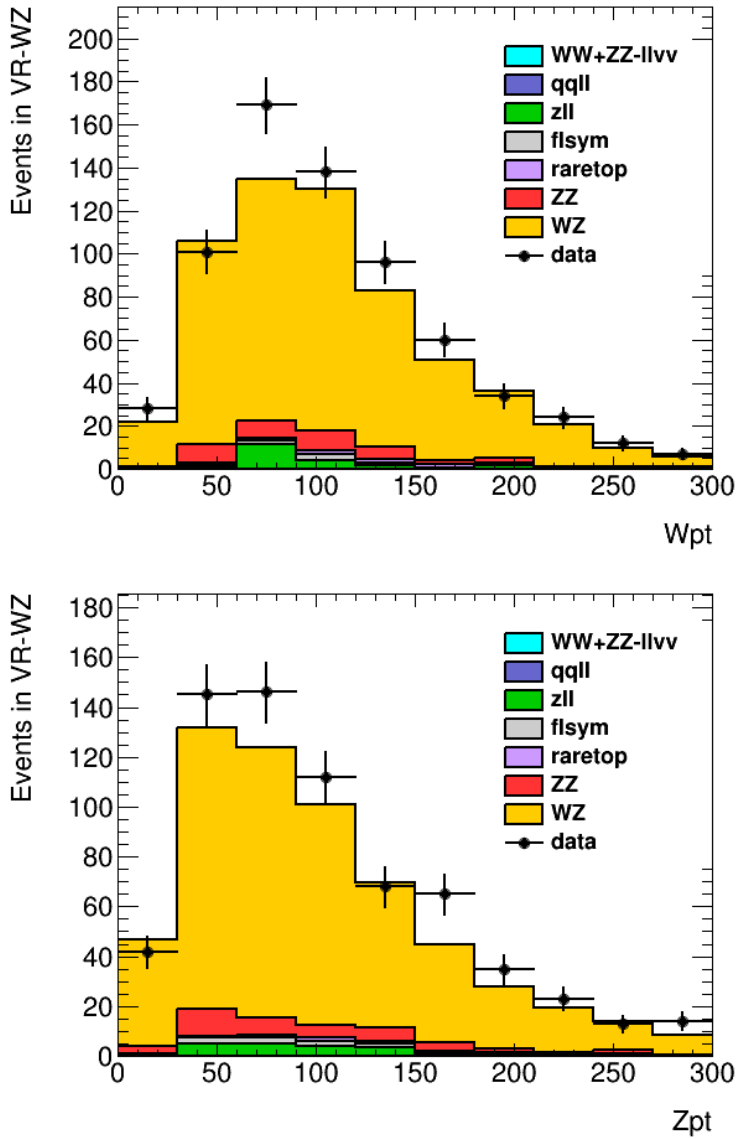


Figure 81: Distribtuions of data and MC in VR-WZ.  $p_T$  of the W (top) and Z (bottom).

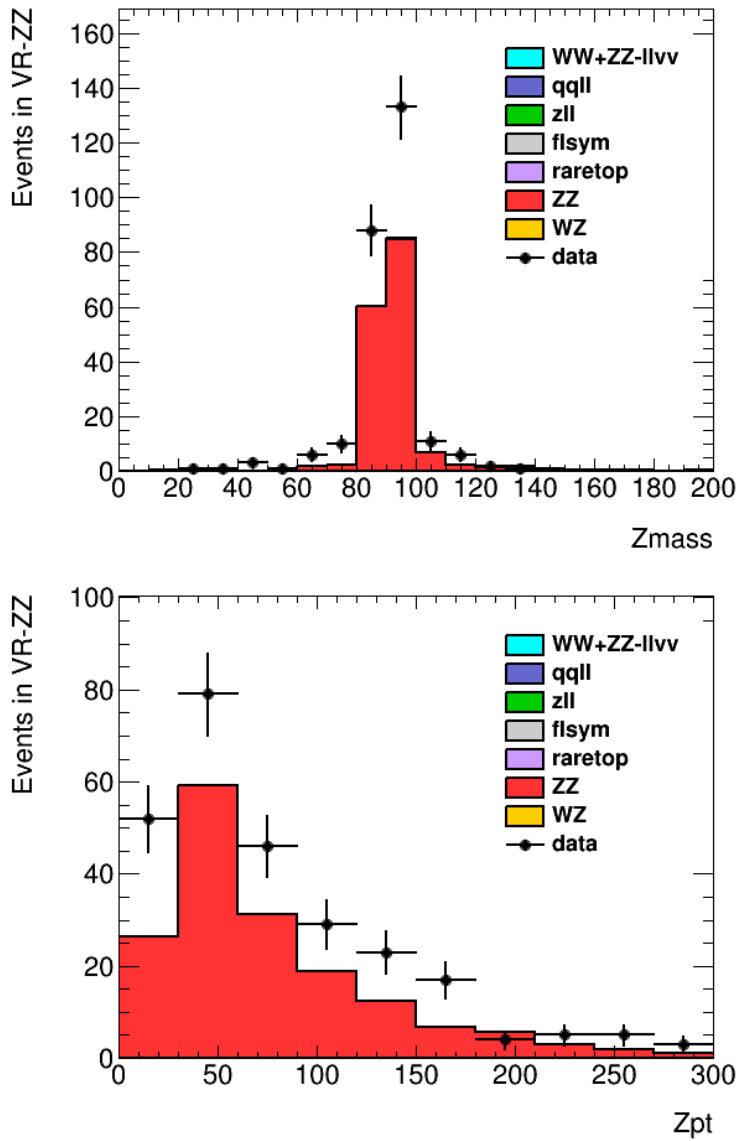


Figure 82: Distributions in VR-WZ. On the top, mass of the Z bosons in the event, and on the bottom,  $p_T$  of the Z bosons.

2473

## 2474 SYSTEMATIC UNCERTAINTIES

## 2475 11.1 UNCERTAINTIES ON DATA-DRIVEN BACKGROUNDS

2476 11.1.1 *Uncertainties on the Flavor Symmetry Method*

2477 The flavor symmetry method is a data driven method that makes its esti-  
 2478 mate primarily on based events populating an [SR-like CR](#) in the different-  
 2479 flavor channel. The statistical uncertainty on these events makes up the  
 2480 dominant uncertainty on the method. To reduce this uncertainty, the  $m_{\ell\ell}$  range  
 2481 on the [CR](#) is expanded, approximately tripling the number of events in [CR-FS](#). The statistical uncertainty is reduced by this expansion, though it is  
 2482 still significantly higher than any of the other systematic uncertainties on  
 2483 this method, as seen in [Table 16](#). Also included in the statistical uncertainty  
 2484 column is the uncertainty on the number of non-[FS](#) events in [CR-FS](#), which  
 2485 is used to scale the prediction to account for contamination in the [CR](#).  
 2486

Reg.	Ch.	Pred.	Uncertainties					
			stat. clos.	MC and $\alpha$	k and $\alpha$	dAOD usage	$m_{\ell\ell}$ shape	total
SRZ	$ee$	16.50	1.82	0.88	0.53	0.12	0.22	2.11
	$\mu\mu$	16.67	1.83	0.79	0.33	0.11	0.23	2.04
	$ee+\mu\mu$	33.16	3.66	1.07	0.86	0.23	0.45	3.94
VRS	$ee$	49.70	3.21	2.34	2.20	0.34	0.75	4.61
	$\mu\mu$	49.60	3.14	2.88	1.40	0.31	0.75	4.56
	$ee+\mu\mu$	99.31	6.34	4.00	3.60	0.65	1.49	8.47

Table 16: Uncertainties in the on-Z signal and validation regions. Nominal predictions are given with statistical uncertainty (including uncertainty from subtracted backgrounds), MC Closure uncertainty, uncertainty on the prediction from varying  $k$  and  $\alpha$  by their statistical uncertainties, comparing the efficiencies from AODs to that of DAOs, and on the  $m_{\ell\ell}$  widening, which includes MC statistics and a data/MC comparison in a loosened region.

2487 The next largest contribution to the uncertainty comes from [MC](#) closure  
 2488 tests, which are used to determine how effective the method is in its predic-  
 2489 tion. If, for example, using weights derived from an inclusive selection at  
 2490 high  $E_T^{\text{miss}}$  lead to a bias, the closure test would indicate that and an appro-  
 2491 priate uncertainty could be placed on the estimate based on the difference  
 2492 between the [MC](#) prediction and the prediction from the flavor symmetry  
 2493 method.

2494 In this test, the entire FS procedure is performed on  $t\bar{t}$  MC, including a  
 2495 recalculation of weighting factors  $\alpha$  and  $k$ . The prediction from  $e\mu$  events  
 2496 in MC is compared to the MC  $ee$  and  $\mu\mu$  events, as seen in Figure 83. The dif-  
 2497 ference between the two predictions is then summed in quadrature with  
 2498 the statistical uncertainty on each prediction to give the total closure un-  
 2499 certainty seen in Table 16. In these closure tests, all predictions agree within  
 2500 the statistical uncertainty, so the largest contributor to the resulting error  
 2501 is MC statistics.

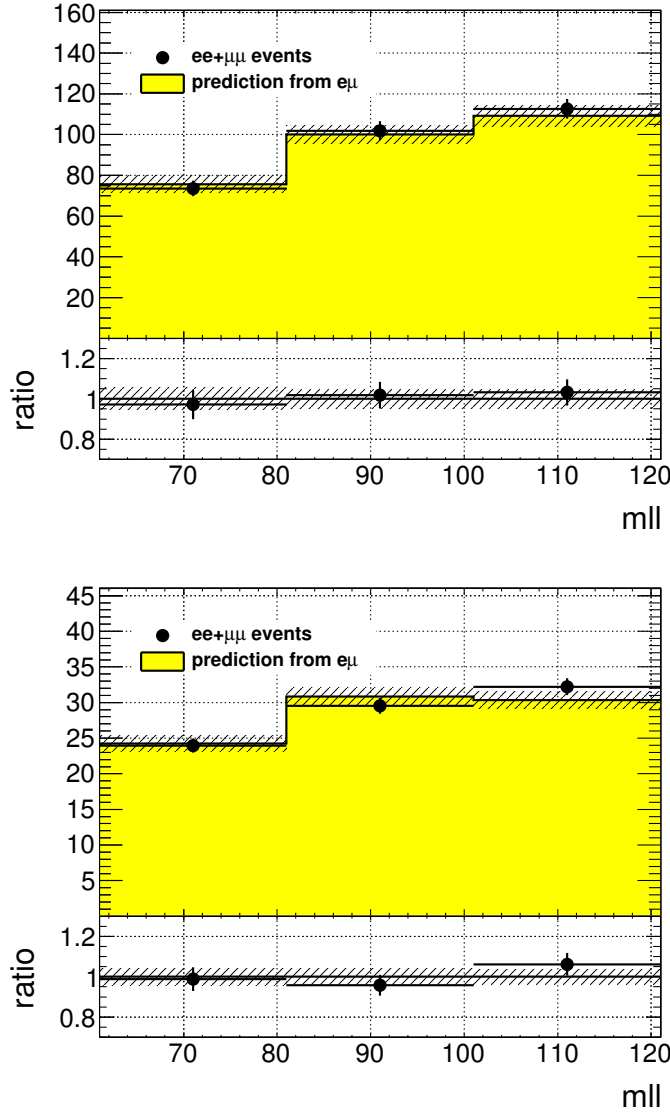


Figure 83: MC closure plots of VRS (top) and SRZ (bottom). The number of events from MC (black points) is compared to the number of events predicted from the flavor symmetry method (yellow histogram). The comparison is performed before the expanded  $m_{ll}$  window is used to predict the on-Z bin, but because the shape is taken from the same MC, the result is identical.

2502 A small uncertainty is added based on the statistical uncertainty on the  
 2503  $k$  and  $\alpha$  factors derived from data. These factors are measured in many dif-  
 2504 ferent bins (see, for example, the different measurements of  $k$  in [Figure 64](#)),  
 2505 and as a consequence, some bins can have very large statistical uncertain-  
 2506 ties. To assess the uncertainty on the total estimate, each measurement  
 2507 of these factors is varied by its uncertainty in order to produce the max-  
 2508 imum and minimum possible prediction. The differences with respect to  
 2509 the nominal prediction are used to create a symmetrized error, which is  
 2510 included in [Table 16](#).

2511 The next uncertainty considers a potential bias in the way the  $\alpha$  factors  
 2512 are calculated. Because they are derived from data, there is already trig-  
 2513 ger dependence in data collection; only events passing a trigger are stored.  
 2514 Additional trigger dependence is created by the data format used for anal-  
 2515 ysis. [ATLAS](#) data and [MC](#) are stored in a format called Analysis Object  
 2516 Data ([AOD](#)), but smaller, slimmer versions of these datasets, called derived  
 2517 AODs ([dAODs](#)) are used for analysis. These [dAODs](#) are designed with spe-  
 2518 cific analyses in mind, filtering on the triggers and objects required by the  
 2519 analyses. As a consequence, in the [dAOD](#) used in this analysis, there are  
 2520 explicit requirements that lepton or  $E_T^{\text{miss}}$  triggers are passed in order for  
 2521 events to be included.

2522 As a consequence, the trigger efficiencies  $\epsilon^{\text{trig}}$  used in [Equation 42](#) to  
 2523 define  $\alpha$  do not consider all possible data events. The  $\epsilon_{\text{trig}}$  factor is  
 2524 calculated for each trigger using events passing the kinematic selection for  
 2525 that trigger, outlined in [Section 9.1](#). The efficiency factor is then measured  
 2526 according to the equation

$$\epsilon^{\text{trig}} = \frac{N_{\text{trig}}}{N_{\text{all}}} \quad (49)$$

2527 where  $N_{\text{trig}}$  is the number of events passing the trigger in the kinematic  
 2528 selection and  $N_{\text{all}}$  is all events in the selection. The latter measurement  
 2529 is the one subject to this bias, as it contains only the events that pass at  
 2530 least one trigger required for inclusion in the [dAOD](#). As a consequence  
 2531 of these missing events, the  $\epsilon^{\text{trig}}$  values will be artificially high. However,  
 2532 because the ratio of trigger efficiencies for the different channels is the  
 2533 only quantity needed for this analysis, the missing events will only bias  
 2534 the prediction if the different channels are differently impacted by the  
 2535 trigger preselection.

2536 Calculating the flavor symmetry method's dependence on these biases  
 2537 requires the use of [MC](#). With a generated [MC](#) sample, there is no trig-  
 2538 ger dependence, so an unskimmed sample can be compared to a typical  
 2539 skimmed [MC dAOD](#) to identify the effect of the skimming. [Figure 84](#) shows  
 2540 a comparison of the  $\alpha$  factors calculated for different bins in  $E_T^{\text{miss}}$  from  
 2541 the nominal source, data, as well as these two [MC](#) sources. A  $E_T^{\text{miss}}$  depen-  
 2542 dence would be the most likely bias between the two [MC](#)-derived  $\alpha$  factors  
 2543 because  $E_T^{\text{miss}}$  triggers are the only triggers besides lepton triggers that will  
 2544 allow an event to be accepted into the [dAOD](#) used by this analysis. Though  
 2545 there is some difference between the data-derived  $\alpha$  and those taken from

2546 MC, it is clear from this plot that there is very little dependence on the  
 2547 choice of an unskimmed or skimmed sample. The calculation of the uncer-  
 2548 tainty is performed by repeating the flavor symmetric method in MC with  
 2549 each of the two  $\alpha$  factors and using the difference between the estimates  
 2550 as a symmetric error.

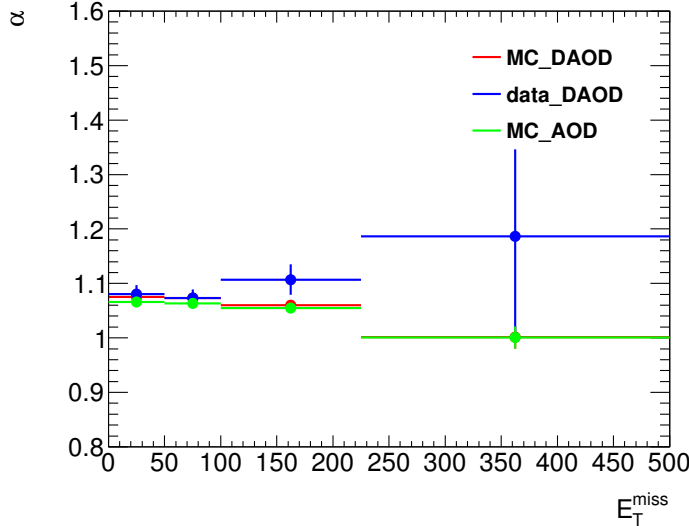


Figure 84:  $\alpha$ , the trigger efficiency ratio, calculated as a function of  $E_T^{\text{miss}}$  from three different sources: data (blue), the usual skimmed  $t\bar{t}$  MC (red), and an unskimmed  $t\bar{t}$  MC (green).

2551 The last uncertainty relates to the main MC dependence of the method -  
 2552 the  $m_{\ell\ell}$  shape of the FS background. A correction factor is taken from MC  
 2553 in order to account for the  $m_{\ell\ell}$  widening, and the accuracy of that factor  
 2554 must be checked. Its shape is compared to that of data in region similar to  
 2555 VR-FS, but with an  $H_T$  cut lowered to 300 GeV to increase statistics. The  
 2556 difference between the fraction of events on the Z-mass peak in data and  
 2557 MC in this region is taken as a systematic uncertainty. To confirm that using  
 2558 this lowered  $H_T$  cut still gives a valid answer, the fractions are compared  
 2559 as a function of  $H_T$  in Figure 85. In these plots, especially in the higher-  
 2560 statistics 2016 plot, it is clear both that the data and MC agree very well  
 2561 and that there is no strong  $H_T$  dependence.

2562 All the uncertainties are calculated independently for the two datasets,  
 2563 then added together. Statistical uncertainties, including the MC closure sta-  
 2564 tistical uncertainties and the  $k$  and  $\alpha$  uncertainties, are added in quadrature  
 2565 between the two years. Uncertainties that are more likely to be correlated,  
 2566 such as the difference between the two estimates in MC closure and the  
 2567 dependence on using a dAOD to calculate trigger efficiencies, are added  
 2568 linearly. The total uncertainty is about 12% of the nominal prediction in  
 2569 SRZ and about 9% in VRS.

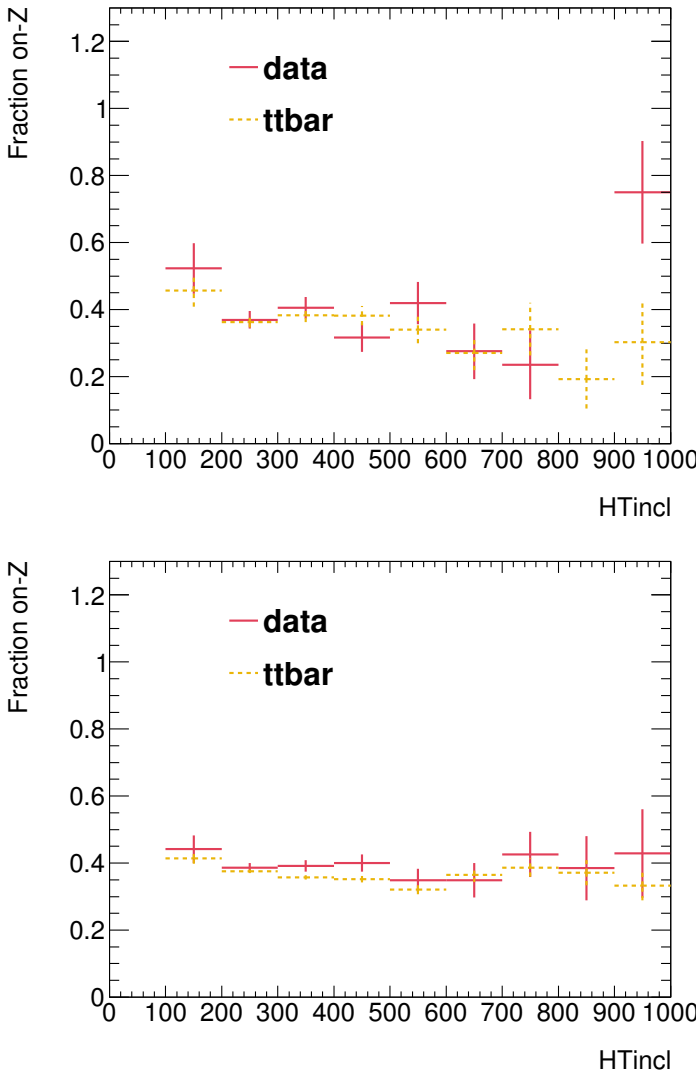


Figure 85: Plots of the fraction of on-Z events with a VR-FS-like selection as a function of  $H_T$ . The top figure shows 2015 data and MC while the bottom figure shows the same for 2016.

2570 11.1.2 *Uncertainties on the  $\gamma +$  jets Method*

2571 One of the largest sources of uncertainty on the  $\gamma +$  jets method is derived  
 2572 by comparing the results from reweighting in different variables. Though  
 2573 boson  $p_T$  is used as the nominal reweighting variable, the differences in  
 2574 the kinematics of  $\gamma$  and  $Z$  events also impact number of jets,  $H_T$ , and  $E_T$   
 2575 (which includes the mass of the boson). The  $\gamma +$  jets method is repeated  
 2576 using each of these variables to reweight, and their  $E_T^{\text{miss}}$  distributions are  
 2577 shown in Figure 86. The maximum difference from the nominal prediction  
 2578 is symmetrized and used as an uncertainty on the method.

2579 Another uncertainty is applied to estimate the validity of using MC in a  
 2580 1-jet CR to determine the smearing functions. Smearing functions are made  
 2581 using data from the same 1-jet region and using MC in a  $\geq 2$ -jet region

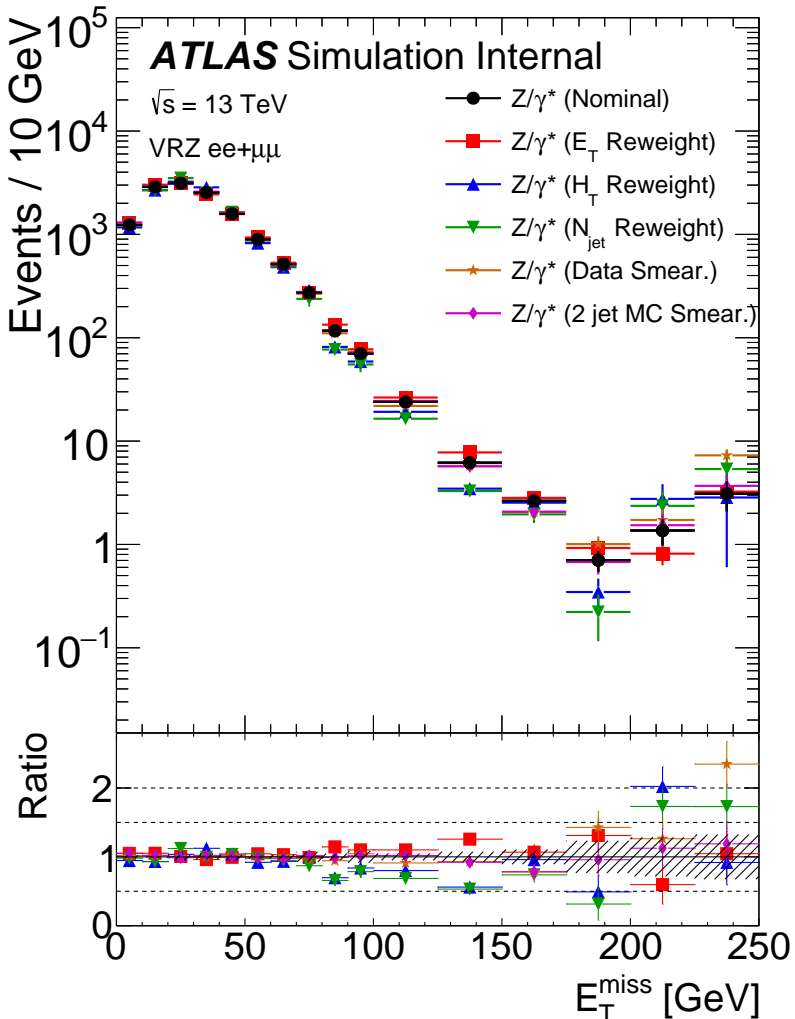


Figure 86:  $E_T^{\text{miss}}$  distributions for  $\gamma + \text{jets}$  predictions using different reweighting variables, as well as distributions with the nominal reweighting but with smearing functions taken from data and from MC in a  $\geq 2$ -jet region.

otherwise identical to the 1-jet CR. These distributions are also shown in Figure 86, and like the alternate reweighting distributions, are used to find a maximum difference from the nominal prediction which is translated into a symmetric error.

As in the flavor symmetric method, the full procedure is carried out on MC in order to test MC closure, including a recalculation of any weights that are typically derived from data. The resulting comparison between  $Z/\gamma^* + \text{jets}$  MC and the  $\gamma + \text{jets}$  method performed on MC can be seen in Figure 87. The final non-closure uncertainty is taken from VRS, where larger numbers of events give a clearer picture of the success of the method than in SRZ. In this region, the statistical uncertainty on the prediction is compared to the non-closure, and the larger of the two is used as the final uncertainty.

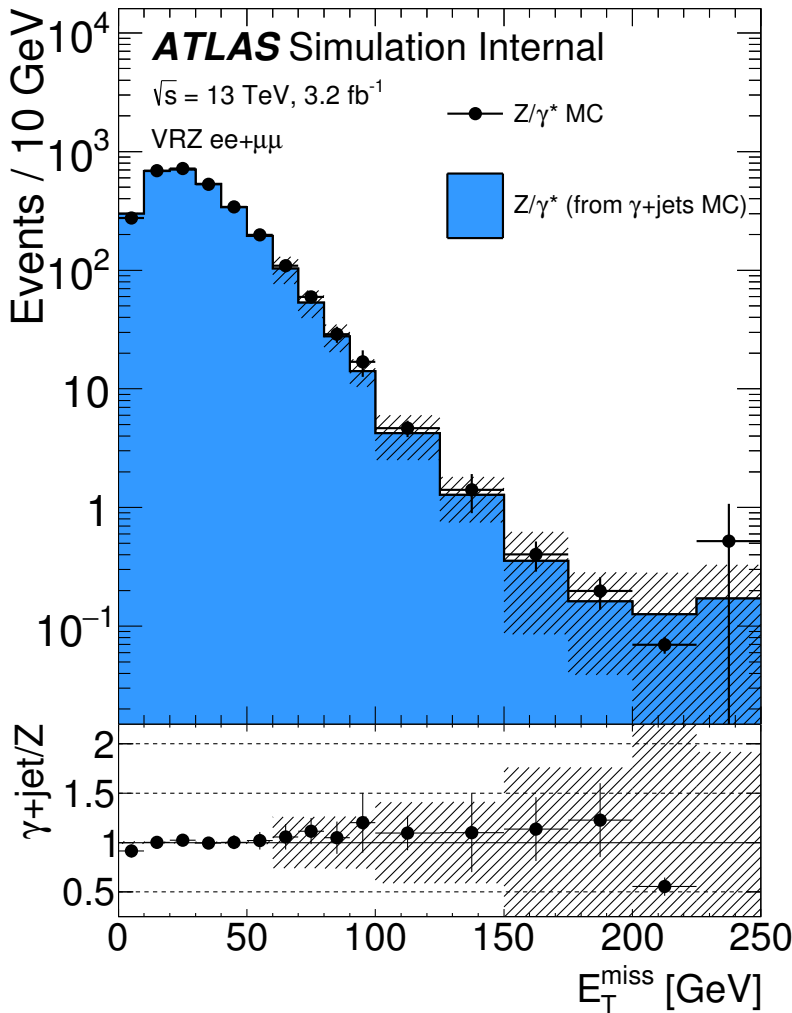


Figure 87: MC closure of the  $\gamma + \text{jets}$  method as a function of  $E_T^{\text{miss}}$  comparing the MC prediction of the Z background with the  $\gamma + \text{jets}$  method performed on  $\gamma + \text{jets}$  MC. The uncertainty band includes both statistical and reweighting uncertainties.

2595 The uncertainty on the  $V\gamma$  contamination in CR- $\gamma$  is also considered.  
 2596 An uncertainty on the MC prediction is made based on comparison of data  
 2597 and MC in a  $W + \text{jets}$  VR, shown in Figure 88. This VR is similar to CR- $\gamma$ , but  
 2598 instead of vetoing events with leptons, requires at least one well-isolated  
 2599 lepton with a  $p_T$  over 25 GeV. At  $E_T^{\text{miss}}$  values over 100 GeV, region is about  
 2600 90% pure in  $W\gamma$  processes. The MC agrees well with data in this region,  
 2601 even at very high  $E_T^{\text{miss}}$ , so an uncertainty of 16% based primarily on sta-  
 2602 tistical uncertainty in this VR is placed on the  $V\gamma$  MC. This uncertainty is  
 2603 propagated to the final result through the subtraction procedure.

2604 An uncertainty on the  $m_{\ell\ell}$  shape is determined using MC closure as well.  
 2605 The comparison of  $m_{\ell\ell}$  shapes in  $Z/\gamma^* + \text{jets}$  MC and the  $\gamma + \text{jets}$  method  
 2606 applied to MC is shown in Figure 72. As with the main MC closure test, the  
 2607 maximum of the statistical uncertainty and the non-closure is taken as the  
 2608 final uncertainty on this background.

2609 One last uncertainty based on the statistical uncertainty on the number  
 2610 of  $\gamma + \text{jets}$  data events used for this method is also included. The full  
 2611 breakdown of uncertainty in SRZ can be seen in [Table 17](#).

Ch.	Pred.	Uncertainties (%)						
		$V\gamma$	MC	$m_{\ell\ell}$	re-	smear	stat.	total
		sub.	clos.	shape	weight			
$ee$	1.02	53.0	21.0	19.0	100.0	65.0	56.0	145.0
$\mu\mu$	2.08	27.0	14.0	23.0	30.0	59.0	40.0	86.0
$ee+\mu\mu$	3.1	36.0	16.0	22.0	43.0	60.0	33.0	92.0

Table 17: Uncertainty breakdown for the  $\gamma + \text{jets}$  method in SRZ. Uncertainties considered are the impact of MC uncertainty on  $V\gamma$  backgrounds, MC closure, uncertainty on  $m_{\ell\ell}$  shape (also determined via MC closure), reweighting uncertainties, smearing uncertainties, and statistical uncertainty on the  $\gamma + \text{jets}$  events used in the method.

### 2612 11.1.3 Uncertainties on the Fakes Background

2613 Systematic uncertainties on the fakes background are derived from a se-  
 2614 ries of variations on the nominal method. Variations include scaling the  
 2615 real and fake efficiencies up and down by their statistical uncertainties,  
 2616 scaling the prompt lepton contamination in CR-fake up and down by 20%,  
 2617 and by requiring and vetoing  $b$ -tagged jets in CR-fake to determine the  
 2618 dependence on heavy flavor. Statistical uncertainties can also be large in  
 2619 regions with small numbers of events in the baseline selection, such  
 2620 as SRZ. In other regions, the  $b$ -tagging dependence provides the largest  
 2621 uncertainty. The full breakdown of uncertainties for the most important  
 2622 regions are listed in [Table 18](#).

## 2623 11.2 THEORETICAL AND EXPERIMENTAL UNCERTAINTIES

2624 Experimental uncertainties cover any detector effect or LHC condition that  
 2625 may not be modeled precisely correctly in MC. For each uncertainty, a stan-  
 2626 dard prescription from the ATLAS experiment is followed. Uncertainties are  
 2627 included on the following parameters:

- 2628 • Luminosity (2.9%) [95, 96]
- 2629 • Jet energy scale [69]
- 2630 • Jet energy resolution [69]
- 2631 • Jet vertex tagging
- 2632 • Heavy flavor tagging
- 2633 •  $E_T^{\text{miss}}$  soft term [72]

Variation	SRZ	CRT	CRFS	VRFS	VRS	VRT
Nominal	$0.10 \pm 1.61$	$25.39 \pm 5.35$	$3.73 \pm 2.19$	$10.53 \pm 3.56$	$3.64 \pm 3.20$	$80.06 \pm 9.80$
EL F Up	0.15	30.23	3.96	10.93	3.56	92.46
EL F Down	0.06	21.80	3.52	10.18	3.54	70.07
EL R Up	0.25	26.17	3.92	11.10	4.13	82.57
EL R Down	-0.07	24.51	3.52	9.92	3.10	77.24
MU F Up	-0.20	32.48	4.77	16.41	5.25	86.48
MU F Down	0.29	20.17	2.91	7.04	2.87	70.12
MU R Up	0.13	25.67	3.78	10.66	3.81	81.18
MU R Down	0.05	25.04	3.67	10.38	3.44	78.72
Total Sys	+0.26 -0.35	+8.64 -6.39	+1.08 -0.87	+5.92 -3.56	+1.70 -0.97	+14.24 -14.42
Total Sys (%)	+261.05 -354.72	+34.01 -25.19	+29.05 -23.23	+56.22 -33.85	+46.57 -26.60	+17.78 -18.02
Real Cont. Up	0.23	20.97	3.06	8.08	3.15	68.79
Real Cont. Down	-0.01	29.67	4.38	12.95	4.16	90.23
b-jet	0.31	40.44	5.28	8.98	5.63	120.50
no b-jet	0.16	23.44	3.08	11.38	3.97	70.55
Total Sys	+0.25 -0.11	+15.65 -4.83	+1.69 -0.93	+2.56 -2.90	+2.09 -0.49	+41.71 -14.74
Total Sys (%)	+260.46 -109.06	+61.66 -19.02	+45.30 -24.85	+24.32 -27.58	+57.31 -13.35	+52.10 -18.42

Table 18: Systematic uncertainties on the fake-lepton background for on-Z regions for 2015+2016 yields. The nominal yield includes statistical uncertainty from the baseline selection in a given region. The following rows indicate the results of varying the real and fake lepton efficiencies up and down by their statistical uncertainty. Real cont. gives an uncertainty on the contamination of real leptons in the fake lepton efficiency.  $b$ -jet and no  $b$ -jet indicate the impact of requiring or vetoing  $b$ -tagged jets in the regions used to measure the fake efficiency.

- 2634     •  $e/\mu$  momentum scale  
 2635     •  $e/\mu$  trigger, reconstruction, and identification efficiencies  
 2636     • Pile-up

2637     These uncertainties are applied to all MC samples used in the analysis.  
 2638     This includes signal models, diboson and rare top samples for the nominal  
 2639     estimate, and all backgrounds taken from MC in the sideband fit.

2640     Theoretical uncertainties include cross-section uncertainties, scale uncer-  
 2641     tainties, and PDF uncertainties. For the diboson samples, the scale uncer-  
 2642     tainties, given in Table 19 are calculated by varying each scale up and  
 2643     down by a factor of two. These are combined with a 6% cross-section un-  
 2644     certainty and a generator uncertainty obtained by comparing PowHEG and  
 2645     SHERPA MC yields in a given region. This generator uncertainty, shown in  
 2646     Table 20, is dominant in most regions. Rare top processes are given a 13%  
 2647     PDF and scale variation uncertainty [47] and a 22% cross section uncer-  
 2648     tainty [75–77].

2649     Signal models have both the central value and uncertainty on cross-  
 2650     sections taken from an envelope of predictions using different scales and  
 2651     PDF sets [97]. The signal processes are calculated at Next-to-Leading-Logarithmic  
 2652     Accuracy (NLO+NLL); they are initially calculated at NLO in the strong  
 2653     coupling constant, with additional terms from next-to-leading-logarithmic  
 2654     resummation of soft gluon emission [98–102].

$VV \rightarrow llvv$ Samples							
	SRZ	VRS	CRT	VRT	VRWZ	VRZZ	VR <sub>3</sub> L
resummation	0.07	0.03	0.01	0.02	0.00	0.00	0.00
renormalization	0.13	0.17	0.16	0.22	0.00	0.00	0.00
factorization	0.01	0.01	0.01	0.03	0.00	0.00	0.00
total	0.15	0.17	0.16	0.22	0.00	0.00	0.00
$WZ \rightarrow lllv$ Samples							
	SRZ	VRS	CRT	VRT	VRWZ	VRZZ	VR <sub>3</sub> L
resummation	0.07	0.05	0.13	0.08	0.02	0.00	0.01
renormalization	0.26	0.20	0.28	0.21	0.07	0.00	0.18
factorization	0.04	0.04	0.02	0.06	0.01	0.00	0.02
total	0.28	0.21	0.31	0.23	0.07	0.00	0.18
$ZZ \rightarrow llll$ Samples							
	SRZ	VRS	CRT	VRT	VRWZ	VRZZ	VR <sub>3</sub> L
resummation	0.27	1.07	0.01	0.01	0.06	0.01	0.53
renormalization	0.28	0.26	0.30	0.60	0.07	0.04	0.14
factorization	0.27	0.25	0.30	0.58	0.13	0.02	0.16
total	0.48	1.13	0.43	0.84	0.16	0.05	0.57

Table 19: Fractional uncertainties of dibosons in signal and validation regions from Sherpa scale variations.

Region	Sherpa Events/fb <sup>-1</sup>	Sherpa Events	Powheg Events/fb <sup>-1</sup>	Powheg Events	% Difference
WZ Samples					
SRZ+VRZ	5.219	76.722	3.286	48.300	37.046
CRT+VRT	1.060	15.583	0.742	10.913	29.970
WW/ZZ Samples					
SRZ+VRZ	1.921	28.244	0.685	10.070	71.424
CRT+VRT	6.281	92.332	3.142	46.188	55.474

Table 20: Comparison of yields in on-Z and off-Z regions in Sherpa and Powheg diboson MC at 14.7 fb<sup>-1</sup>.

## 2655 11.3 IMPACT OF UNCERTAINTIES ON THE SIGNAL REGION

2656 The breakdown of each major uncertainty's contribution to the total un-  
 2657 certainty in SRZ is shown in [Table 21](#). The dominant uncertainty is the  
 2658 diboson generator uncertainty, followed by the statistical uncertainty from  
 2659 the [FS](#) background. Uncertainties smaller than 1% are not shown in the  
 2660 table.

Source	Relative systematic uncertainty [%]
SRZ	
Total systematic uncertainty	17
WZ/ZZ generator uncertainty	13
Flavour symmetry (statistical)	7
WZ/ZZ scale uncertainty	6
$Z/\gamma^* + \text{jets}$ (systematic)	4
Flavour symmetry (systematic)	3
$Z/\gamma^* + \text{jets}$ (statistical)	2
Fake-leptons	1

Table 21: Overview of the dominant sources of systematic uncertainty on the total background estimate in the signal regions. The values shown are relative to the total background estimate, shown in %.

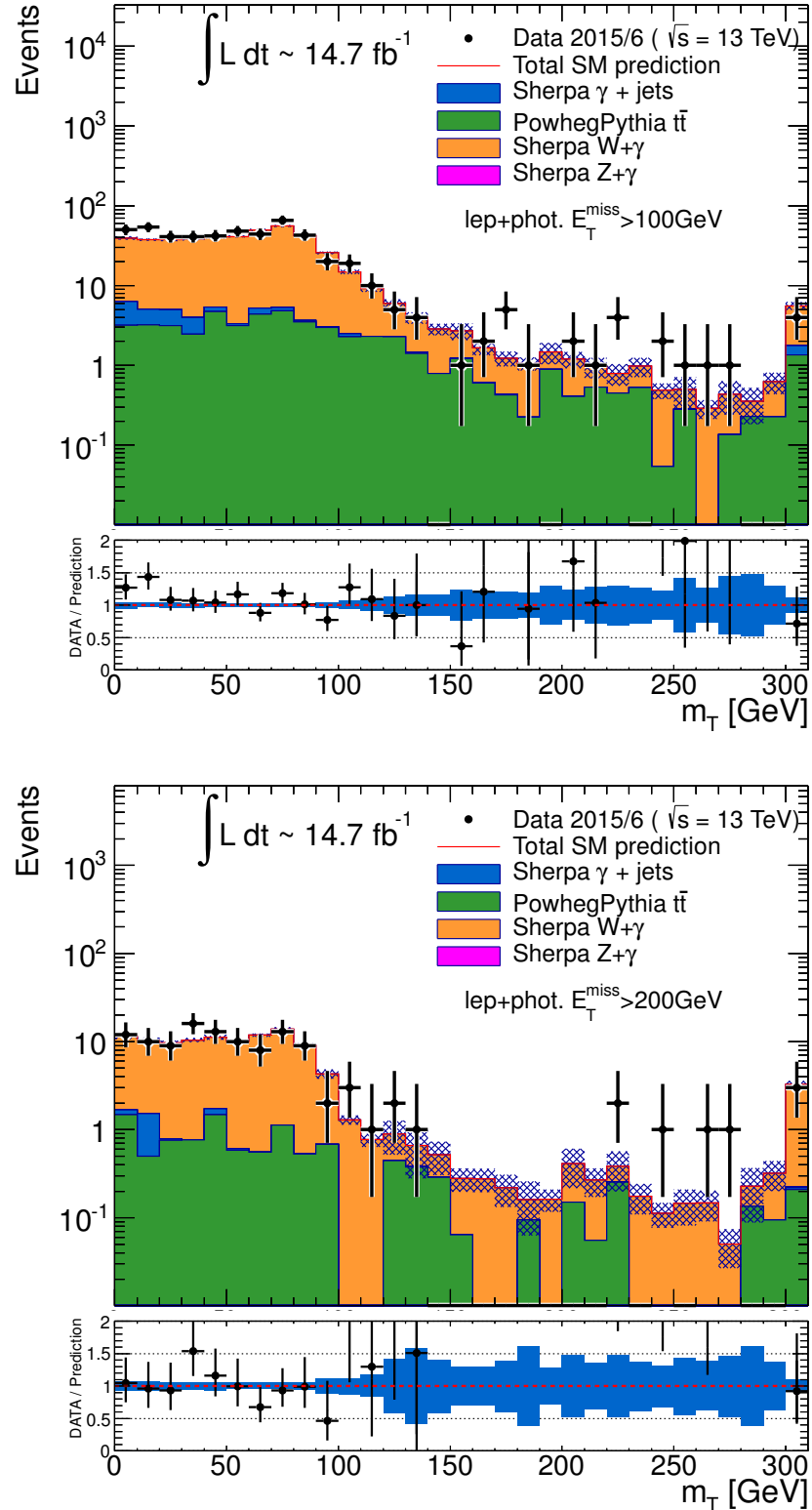


Figure 88: Distributions of  $m_T(\ell, E_T^{\text{miss}})$ , the transverse mass of the lepton and the  $E_T^{\text{miss}}$  in a VR designed to target  $W\gamma$  processes. Top is the distribution with a  $E_T^{\text{miss}}$  cut at 100 GeV, and bottom is the same distribution with a  $E_T^{\text{miss}}$  cut of 200 GeV.

2661

## 2662 RESULTS

2663 The results of the search can be seen in [Table 22](#), which displays the ex-  
 2664 pected and observed numbers of events in SRZ, both divided by channel  
 2665 and inclusively. The predictions and uncertainties for each background are  
 2666 shown, though many of these uncertainties are correlated between back-  
 2667 grounds, so the final uncertainty does not correspond to a simple addition  
 2668 in quadrature of each error. A total of sixty events are observed, with  $53.5 \pm 9.3$   
 2669 events expected. [Figure 89](#) shows the expected and observed results  
 2670 visually for the **SR** as well as three **VRs**, all designed to verify the accuracy  
 2671 of the backgrounds taken from **MC**. Excellent agreement is seen in all cases,  
 2672 with the largest deviation at about  $1\sigma$ .

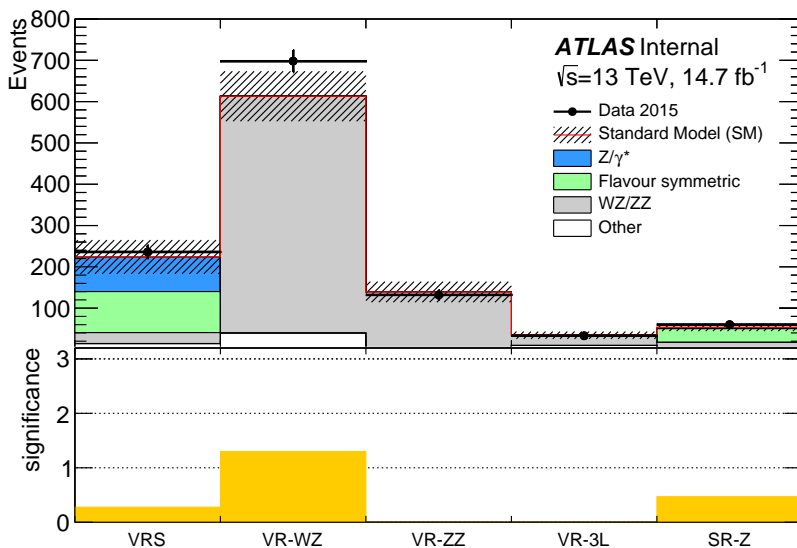


Figure 89: Comparison of background predictions and data yields in four validation regions, as well as the signal region. Definitions of all regions can be found in [Table 7](#), with both rare top and fake backgrounds grouped together under the “other” label. The uncertainty band includes all statistical and systematic uncertainties. Below is a panel of the one-sided statistical significances of the deviations between the predicted and observed quantities for each region.

2673 [Table 22](#) also shows several statistical interpretations of the results. The  
 2674 discovery  $p$ -value for zero signal strength, which gives the probability that  
 2675 the observed events are compatible with a **SM**-only hypothesis, is given as  
 2676  $0.32$ . The significance is listed as  $0.47\sigma$ , which is a reinterpretation of the  $p$ -  
 2677 value into a gaussian significance. This  $p$ -value is one-sided; when the data  
 2678 yield is less than expected the  $p$ -value is set to  $0.5$ , and the significance is  
 2679 set to  $0$ .  $S^{95}$ , the upper limit on the number of signal events that could be

Table 22: Number of events expected and observed in the  $ee$ ,  $\mu\mu$ , and combined channels. Expected predictions include all systematic and statistical uncertainties discussed in Chapter 11. Also shown is the discovery  $p$ -value for zero signal strength ( $p(s = 0)$ ) [103], Gaussian significance, 95% CL observed and expected upper limits on the number of signal events ( $S^{95}$ ), and the corresponding observed upper limit on the visible cross section ( $\langle \epsilon\sigma \rangle_{\text{obs}}^{95}$ ).

	SRZ	SRZ $ee$	SRZ $\mu\mu$
Observed events			
	60	35	25
Total expected background events	$53.5 \pm 9.3$	$27.1 \pm 5.1$	$26.8 \pm 4.4$
Flavour-symmetric ( $t\bar{t}$ , $Wt$ , $WW$ and $Z \rightarrow \tau\tau$ ) events	$33.2 \pm 3.9$	$16.5 \pm 2.1$	$16.7 \pm 2.0$
$Z/\gamma^*$ + jets events	$3.1 \pm 2.8$	$1.0^{+1.3}_{-1.0}$	$2.1 \pm 1.4$
$WZ/ZZ$ events	$14.2 \pm 7.7$	$7.8 \pm 4.3$	$6.4 \pm 3.5$
Rare top events	$2.9 \pm 0.8$	$1.4 \pm 0.4$	$1.5 \pm 0.4$
Fake-lepton events	$0.1^{+0.8}_{-0.1}$	$0.5^{+0.7}_{-0.5}$	$0^{+0.2}_{-0.2}$
<hr/>			
$p(s = 0)$	0.32	0.15	0.5
Significance ( $\sigma$ )	0.47	1.00	0
Observed (Expected) $S^{95}$	$28.2 (24.5^{+8.9}_{-6.7})$	$22.0 (15.8^{+6.5}_{-4.5})$	$12.9 (14.0^{+5.7}_{-3.9})$
$\langle \epsilon\sigma \rangle_{\text{obs}}^{95}$ [fb]	1.9	1.5	0.88

in the SR at a 95% CL, is determined both for the expected and observed number of events. This limit is also reinterpreted based on the integrated luminosity used in the search to produce an upper limit on the visible cross-section of signal events,  $\langle\epsilon\sigma\rangle_{\text{obs}}^{95}$ .

The predictions in SRZ, combined with the MC shapes, are used to produce plots in a broader  $m_{\ell\ell}$  range, seen in Figure 90. These plots are useful demonstrations of efficacy of the background estimation methods, showing the well-modeled  $Z/\gamma^* + \text{jets}$  shape in the same-flavor region, and in the different-flavor region, demonstrating that there are no extreme fluctuations within the region used to predict the flavor symmetric background.

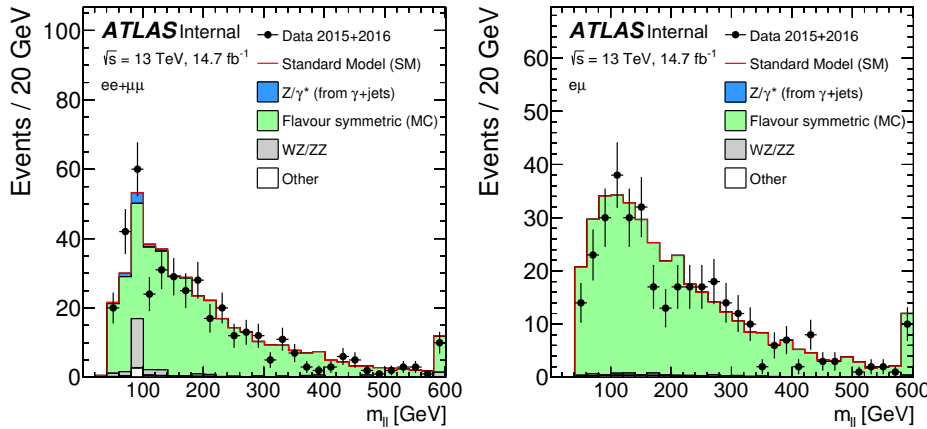


Figure 90: Comparisons as a function of  $m_{\ell\ell}$  of background predictions with observed data in an SRZ-like region, with the  $m_{\ell\ell}$  cut removed. Left is the same-flavor channel, where all background shapes are taken from MC and scaled to their SRZ predictions, except for the  $Z/\gamma^* + \text{jets}$  background, which is taken entirely from the data-driven background. Right is the different-flavor channel, in which the backgrounds are taken directly from MC, except for  $t\bar{t}$ , which is scaled to match the total data yield.

Focusing in on the SR itself, comparisons of background predictions, observed events, and signal models can be made as a function of key variables for the analysis. Figure 91 shows several of these. The first two figures focus on the features of the SR events' leading leptons; they give the mass and  $p_T$  of a hypothetical parent particle reconstructed from the leptons. In the case of events with a real Z boson, these variables simply give that boson's mass at  $p_T$ . The next two figures show distributions in the two most important variables used to differentiate signal from background,  $E_T^{\text{miss}}$  and  $H_T$ . In this analysis, where the frozen SR resulted in cuts on these quantities that are lower than those that would be chosen based on a new optimization, these plots show that, even in more sensitive regions, no large excess above the SM background is seen. The last pair of figures relates to the jets in the event, showing the total number of jets and the total number of  $b$ -jets in the SR events. The  $b$ -jet quantity is not explicitly cut on in the analysis because the fraction of  $b$ -jets produced is extremely model dependent. However, an excess at high  $b$ -jet

2706 multiplicity would suggest a BSM process. In each of these distributions,  
 2707 the observed distributions match the background predictions very well,  
 2708 and no evidence for any of the superimposed signal models is seen.

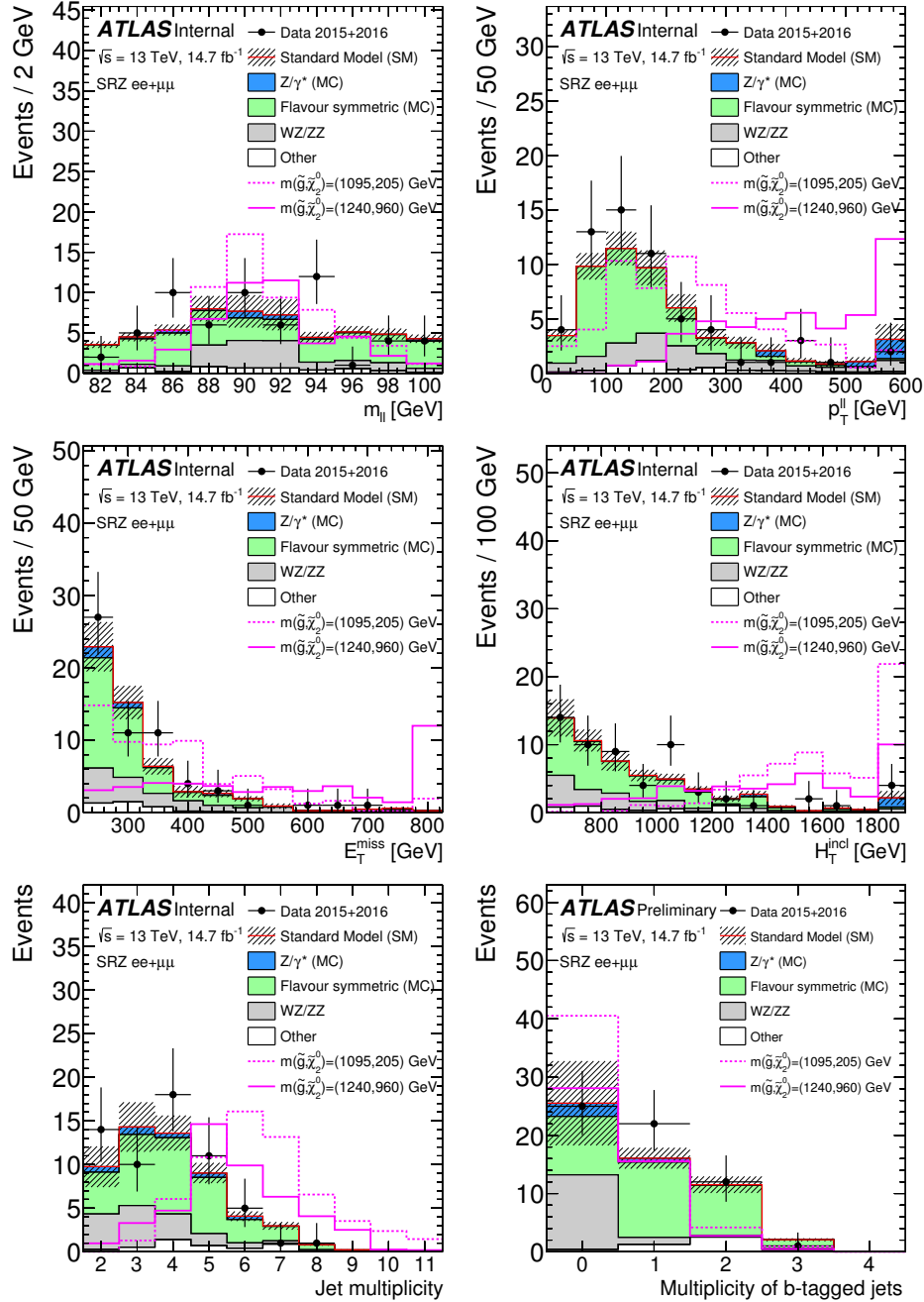


Figure 91: Distributions of observed data, background predictions, and simulated signals are shown in SRZ as a function of  $m_{\ell\ell}$ ,  $p_T^{\ell\ell}$ ,  $E_T^{\text{miss}}$ ,  $H_T$ , number of jets, and number of  $b$ -jets. The two example signals have  $(m(\tilde{g}), m(\tilde{\chi}_2^0)) = (1095, 205)$  GeV. All background shapes are taken from MC, and in the case of flavor symmetric and  $Z/\gamma^* + \text{jets}$  backgrounds, their yields are scaled to match the data-driven predictions. Uncertainties include statistical and systematic components.

2709 Comparisons of the observed and expected yield are also made as a  
2710 function of  $\Delta\phi(\text{jet}_{12}, p_T^{\text{miss}})$ , shown in Figure 92. Here, results are shown  
2711 in a region similar to SRZ with the cut on this variable removed, showing  
2712 the efficacy of the background prediction in a region enhanced in  $Z/\gamma^* +$   
2713 jets events. Again, excellent agreement is seen between the background  
2714 prediction and observed data.

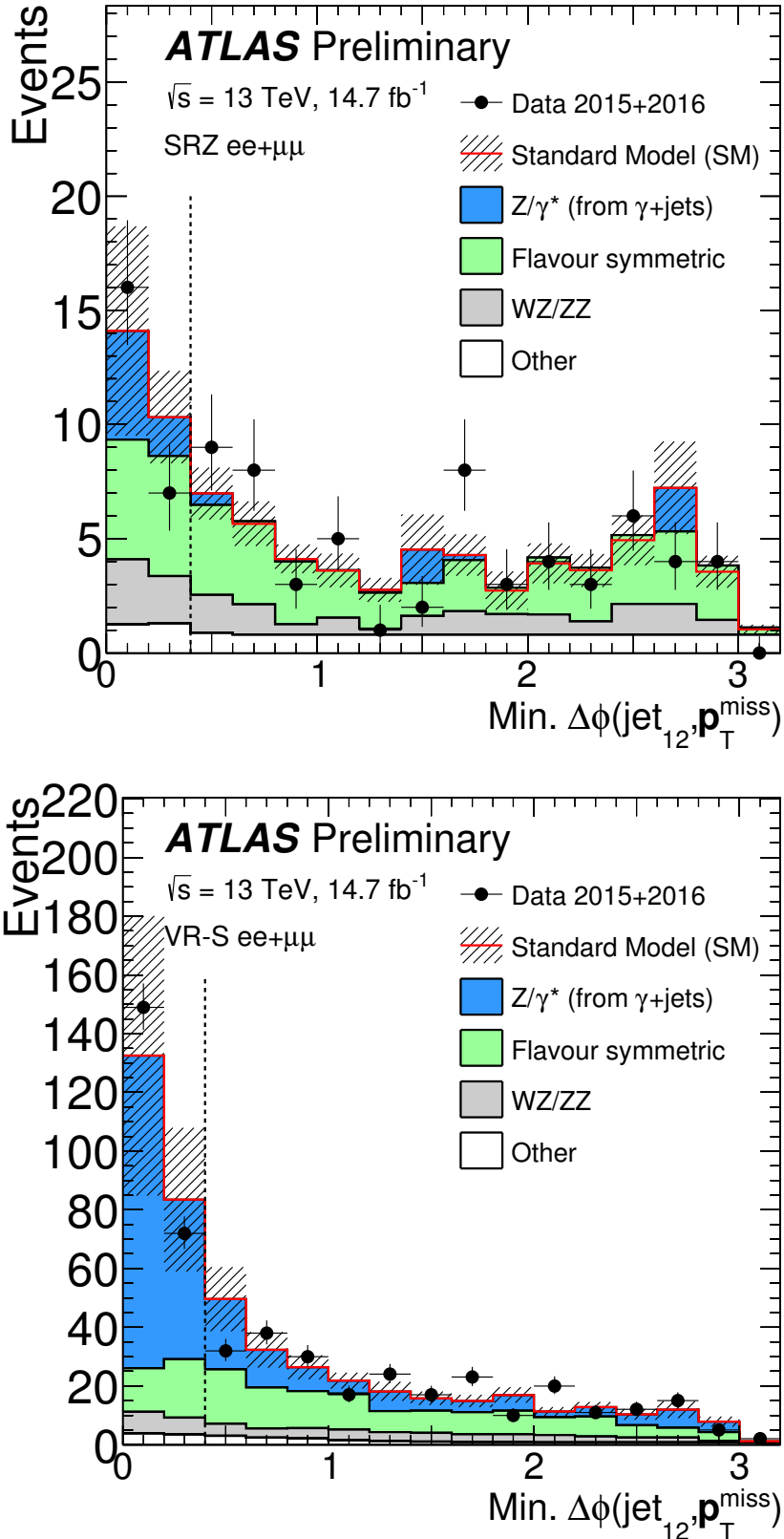


Figure 92: Comparisons as a function of  $\Delta\phi(\text{jet}_{12}, \mathbf{p}_T^{\text{miss}})$  of background predictions with observed data in an SRZ-like (left) and VRS-like (right) region, with the  $\Delta\phi(\text{jet}_{12}, \mathbf{p}_T^{\text{miss}})$  cut removed. All background shapes are taken from MC and scaled to their SRZ predictions, except for the Z/ $\gamma^*$  + jets background, which is taken entirely from the data-driven background.

2715

2716 INTERPRETATIONS

---

2717 Using the simplified models discussed in [Section 2.2.3](#), these results can be  
 2718 interpreted into exclusions of theories based on the masses of the particles  
 2719 involved. Of course, these exclusions include all the assumptions of the  
 2720 models used, so they shouldn't be interpreted to mean that no theory  
 2721 with a given set of particle masses can possibly exist, but they do provide  
 2722 a helpful guideline for targeting future searches and comparing results  
 2723 from different analyses.

2724 Limits are determined using a program called HistFitter [103], designed  
 2725 within the [ATLAS](#) experiment, which builds upon the capabilities of ROOT  
 2726 [104], RooStats [105], and HistFactory [106] to combine the uncertainties  
 2727 of the various background predictions, including their correlations, and  
 2728 produce cross-section limits at 95% CL using the  $CL_S$  prescription [107,  
 2729 108]. In this prescription, a likelihood is constructed based on the expected  
 2730 signal and background contributions to the SR. Nuisance parameters are  
 2731 created based on the statistical and systematic uncertainties for each data-  
 2732 driven background, as well as for each systematic applied to the MC-driven  
 2733 background estimates. The fit uses Gaussian models for nuisance param-  
 2734 eters for all signal and background uncertainties, except for the statistical  
 2735 uncertainty on data- and MC-driven background estimates, which are in-  
 2736 terpreted as Poissonian. Experimental uncertainties are considered fully  
 2737 correlated across the signal and background MC-based estimates.

2738 A fit is performed, leaving a signal strength parameter ( $\mu$ ) free, to max-  
 2739 imize the likelihood, and subsequent fits are preformed to at discrete  $\mu$   
 2740 values to determine the relative likelihood of each value. Using this rela-  
 2741 tive likelihood, the probability of a background-only hypothesis,  $p_b$ , can be  
 2742 determined by setting  $\mu = 0$ , as well as the probability of a signal + back-  
 2743 ground hypothesis  $p_{s+b}$  with any non-zero signal strength, but nominally  
 2744 with  $\mu = 1$ . The confidence limit is constructed as a ratio

$$CL_S = \frac{p_{s+b}}{1 - p_b}. \quad (50)$$

2745 Then, if  $CL_S$  falls below 5%, the signal + background hypothesis can be  
 2746 excluded at 95%. Expected exclusion limits are constructed by assuming  
 2747 the observed data precisely matches the prediction, and  $1\sigma$  uncertainty  
 2748 bands are formed by varying the nuisance parameters away from their fit-  
 2749 ted values to produce a change in the likelihood. The observed limit uses  
 2750 the actual observation of data in the SR to set exclusion limits, so any excess  
 2751 above the expected background will result in worse limits than expected,  
 2752 and any deficit will result in better limits. This exclusion is typically dis-  
 2753 played with error bands that represent a  $1\sigma$  variation in the cross-section  
 2754 of the signal models.

The simplified model discussed in Section 2.2.3, in which pair-produced gluinos decay via a  $\tilde{\chi}_2^0$  to jets, a Z boson, and a  $\tilde{\chi}_1^0$  LSP, is produced in two grids, which differ by their choice of the LSP mass. The first grid assumes a light LSP, fixing its mass to 1 GeV for all mass points, and is shown as a function of  $\tilde{g}$  and  $\tilde{\chi}_2^0$ . The second grid is defined as a function of  $\tilde{g}$  and  $\tilde{\chi}_1^0$ , and its varying LSP mass is defined relative to the  $\tilde{\chi}_2^0$  mass by  $m(\tilde{\chi}_1^0) = m(\tilde{\chi}_2^0) - 100$  GeV. Figure 93 shows the first of these grids, along with exclusions on a similar simplified model, which replaces the gluinos with squarks and uses the same mass scheme. The exclusion contours on the second grid is shown in Figure 94, as a function of  $m(\tilde{g})$  and  $m(\tilde{\chi}_1^0)$ .

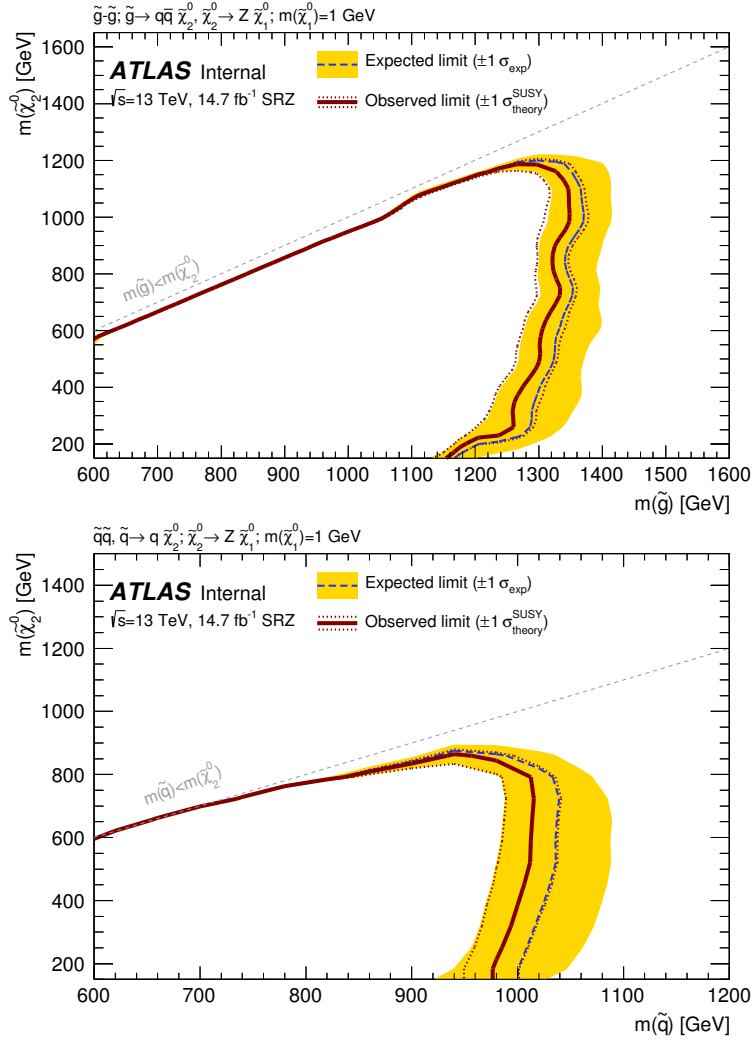


Figure 93: Expected and observed exclusion contours derived from the results in SRZ for the (top)  $\tilde{g}-\tilde{\chi}_2^0$  on-shell grid and (bottom)  $\tilde{q}-\tilde{\chi}_2^0$  on-shell grid. The dashed blue line indicates the expected limits at 95% CL and the yellow band shows the  $1\sigma$  variation of the expected limit as a consequence of the uncertainties in the background prediction and the experimental uncertainties in the signal ( $\pm 1\sigma_{\text{exp}}$ ). The observed limits are shown by the solid red line, with the dotted red lines indicating the variation resulting from changing the signal cross section within its uncertainty ( $\pm 1\sigma_{\text{theory}}^{\text{SUSY}}$ ).

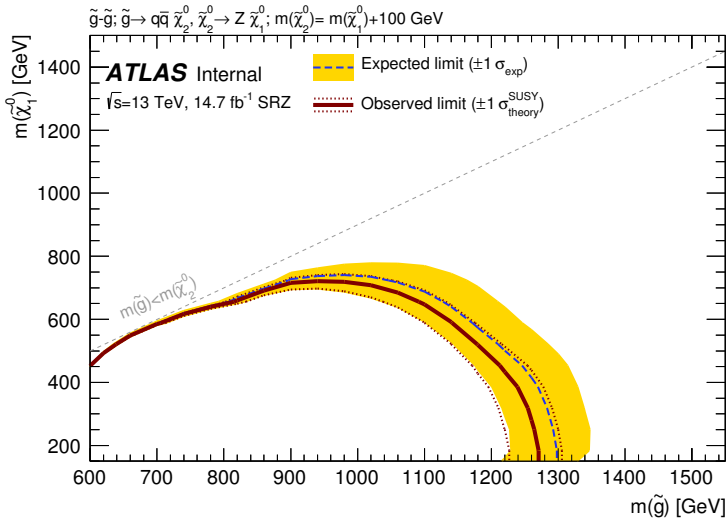


Figure 94: Expected and observed exclusion contours derived from the results in SRZ for the  $\tilde{g}-\tilde{\chi}_1^0$  on-shell grid. The dashed blue line indicates the expected limits at 95% CL and the yellow band shows the  $1\sigma$  variation of the expected limit as a consequence of the uncertainties in the background prediction and the experimental uncertainties in the signal ( $\pm 1\sigma_{\text{exp}}$ ). The observed limits are shown by the solid red line, with the dotted red lines indicating the variation resulting from changing the signal cross section within its uncertainty ( $\pm 1\sigma_{\text{theory}}^{\text{SUSY}}$ ).

2765 In general, the observed exclusions are slightly weaker than the expected  
 2766 exclusions, due to a very small excess of events observed in SRZ. The  
 2767 observed lower limit on  $m(\tilde{g})$  is about 1.3 TeV for models with  $m(\tilde{\chi}_2^0) = 500$   
 2768 GeV for the  $\tilde{g}-\tilde{\chi}_2^0$  grid. These improve significantly on the previous ATLAS  
 2769 exclusion, which used different models for interpretation, but placed a  
 2770 lower limit on  $m(\tilde{g})$  at around 900 GeV for similar  $m(\tilde{\chi}_2^0)$ .



2771

## Part V

2772

### CONCLUSIONS

2773



2774

## 2775 CONCLUSIONS AND OUTLOOK

2776 After a series of moderate excesses observed by the [ATLAS](#) experiment in  
 2777 events with a  $Z$  boson, jets, and  $E_T^{\text{miss}}$ , this analysis performed on 14.7  
 2778  $\text{fb}^{-1}$  of 13 TeV data sees excellent agreement between observations and  
 2779 the background expectation. The resulting exclusion pushes the gluino  
 2780 mass lower limit beyond 1 TeV, putting further constraints on possible  
 2781 [SUSY](#) models. Along with the many other searches for [SUSY](#), this exclusion  
 2782 limits the phase space available for natural [SUSY](#) models. However, [SUSY](#) is  
 2783 adaptable; new theories stretching those bounds are continually proposed  
 2784 as tighter experimental constraints are set, and there are always small gaps  
 2785 in the exclusions where sparticles could hide.

2786 [ATLAS](#)'s dataset for 2016 includes  $36 \text{ fb}^{-1}$ , more than twice the luminosity  
 2787 included in this search. Because no excess was seen in this analysis, the  
 2788 next search in this channel will be able to re-optimize its signal regions for  
 2789 this larger dataset. In fact, because the signal region has been frozen since  
 2790 the 8 TeV search, this analysis's signal region hasn't ever been re-optimized  
 2791 for the increased energy of the [LHC](#)'s collisions. A new signal region that  
 2792 increases  $E_T^{\text{miss}}$  and  $H_T$  requirements will allow for better sensitivity to  
 2793 [SUSY](#) processes.

2794 In addition, the current signal region, in which 60 events were observed  
 2795 with  $14.7 \text{ fb}^{-1}$ , will be populated enough to be subdivided based on event  
 2796 features. The current search is agnostic to the number of  $b$ -jets in the event,  
 2797 for example, but there are now enough events to separate this signal region  
 2798 into complementary  $b$ -tagged and  $b$ -vetoed regions, allowing analyzers to  
 2799 independently target models which produce  $b$ -jets and those that don't,  
 2800 and in the latter case, to dramatically reduce the  $t\bar{t}$  background. Signal  
 2801 regions can also be binned in other model-dependent features, like number  
 2802 of jets, and the  $E_T^{\text{miss}}$  and  $H_T$  requirements can be increased independently,  
 2803 targeting different event topologies.

2804 The [LHC](#) will continue to run through 2018 with a possible increase to  
 2805  $\sqrt{s} = 14 \text{ TeV}$ , and will shut down for upgrades until 2021. Three more  
 2806 years of data-taking at 14 TeV will follow, with approximately twice the  
 2807 current luminosity, referred to as Run 3. After that, the [LHC](#) will shut down  
 2808 again to prepare for the High Luminosity Large Hadron Collider ([HL-LHC](#)),  
 2809 which will begin data-taking in 2026 at a luminosity approximately five  
 2810 times the current rate. This run will result in roughly  $3000 \text{ fb}^{-1}$ , which  
 2811 will allow for dramatically better sensitivity in [SUSY](#) searches. An example  
 2812 can be seen in [Figure 95](#), which shows the potential exclusions on a simple  
 2813 gluino pair-production model with decays via squarks to a [LSP](#), for the  
 2814 approximate luminosities of Run 3 and the [HL-LHC](#).

2815 Searches like this one will surely be repeated with higher and higher  
 2816 luminosities, the analyses increasing both in sensitivity and in complexity.

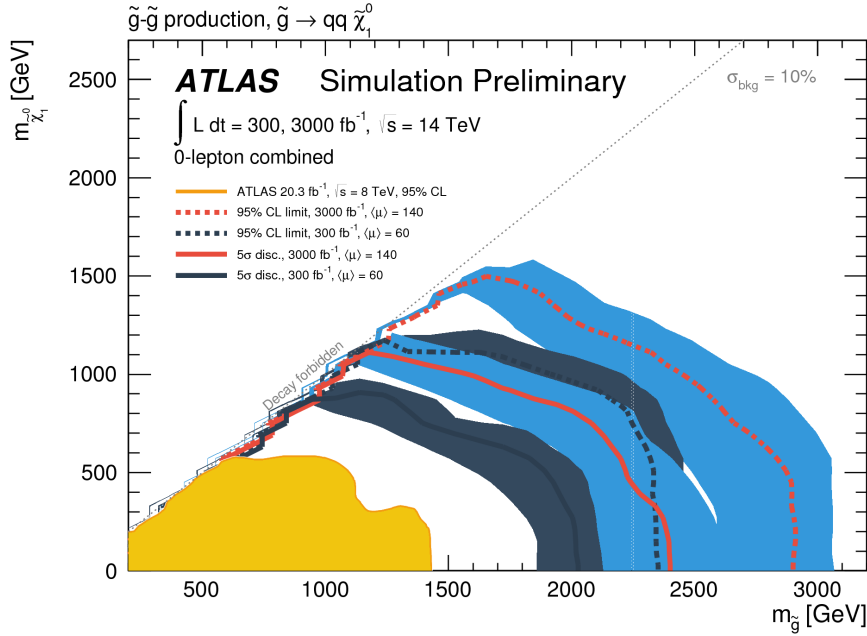


Figure 95: Expected 95% CL exclusion contours (dashed) and 5 $\sigma$  discovery contours (solid) for  $L_{int} = 300^{-1}$  (black) and  $3000^{-1}$  (red) for gluino pair-production, with  $1\sigma$  bands representing the uncertainty on the production cross-section. Superimposed is the observed 8 TeV exclusion for similar models. [109]

2817 Whether or not they uncover any hints of physics beyond the Standard  
 2818 Model remains to be seen.

## BIBLIOGRAPHY

---

- [1] ATLAS Collaboration. “Search for supersymmetry in events containing a same-flavour opposite-sign dilepton pair, jets, and large missing transverse momentum in  $\sqrt{s} = 8$  TeV  $pp$  collisions with the ATLAS detector.” In: *Eur. Phys. J. C* 75 (2015), p. 318. doi: [10.1140/epjc/s10052-015-3518-2](https://doi.org/10.1140/epjc/s10052-015-3518-2). arXiv: [1503.03290 \[hep-ex\]](https://arxiv.org/abs/1503.03290).
- [2] ATLAS Collaboration. *A search for supersymmetry in events containing a leptonically decaying Z boson, jets and missing transverse momentum in  $\sqrt{s} = 13$  TeV  $pp$  collisions with the ATLAS detector.* ATLAS-CONF-2015-082. 2015. URL: <http://cdsweb.cern.ch/record/2114854>.
- [3] C. P. Burgess and G. D. Moore. *The standard model: A primer.* Cambridge University Press, 2006. ISBN: 9780511254857, 9781107404267, 9780521860369.
- [4] S. L. Glashow. “Partial Symmetries of Weak Interactions.” In: *Nucl. Phys.* 22 (1961), pp. 579–588. doi: [10.1016/0029-5582\(61\)90469-2](https://doi.org/10.1016/0029-5582(61)90469-2).
- [5] Abdus Salam. “Renormalizability of Gauge Theories.” In: *Phys. Rev.* 127 (1 1962), pp. 331–334. doi: [10.1103/PhysRev.127.331](https://doi.org/10.1103/PhysRev.127.331). URL: <http://link.aps.org/doi/10.1103/PhysRev.127.331>.
- [6] Steven Weinberg. “A Model of Leptons.” In: *Phys. Rev. Lett.* 19 (21 1967), pp. 1264–1266. doi: [10.1103/PhysRevLett.19.1264](https://doi.org/10.1103/PhysRevLett.19.1264). URL: <http://link.aps.org/doi/10.1103/PhysRevLett.19.1264>.
- [7] D. Galbraith. *The Standard Model of the Standard Model.* 1997. URL: <http://davidgalbraith.org/portfolio/ux-standard-model-of-the-standard-model/>.
- [8] David J Griffiths. *Introduction to elementary particles; 2nd rev. version.* Physics textbook. New York, NY: Wiley, 2008. URL: <https://cds.cern.ch/record/111880>.
- [9] P. Hut and K. A. Olive. “A cosmological upper limit on the mass of heavy neutrinos.” In: *Physics Letters B* 87 (Oct. 1979), pp. 144–146. doi: [10.1016/0370-2693\(79\)90039-X](https://doi.org/10.1016/0370-2693(79)90039-X).
- [10] Huang, Qing-Guo, Wang, Ke, and Wang, Sai. “Constraints on the neutrino mass and mass hierarchy from cosmological observations.” In: *Eur. Phys. J. C* 76.9 (2016), p. 489. doi: [10.1140/epjc/s10052-016-4334-z](https://doi.org/10.1140/epjc/s10052-016-4334-z). URL: <http://dx.doi.org/10.1140/epjc/s10052-016-4334-z>.
- [11] The MEG Collaboration. “Search for the Lepton Flavour Violating Decay  $\mu^+ \rightarrow e^+ \gamma$  with the Full Dataset of the MEG Experiment.” In: (2016). eprint: [arXiv:1605.05081](https://arxiv.org/abs/1605.05081).
- [12] LHCb collaboration. “Observation of  $J/\Psi p$  resonances consistent with pentaquark states in  $\Lambda_b^0 \rightarrow J/\Psi K^- p$  decays.” In: (2015). doi: [10.1103/PhysRevLett.115.072001](https://doi.org/10.1103/PhysRevLett.115.072001). eprint: [arXiv:1507.03414](https://arxiv.org/abs/1507.03414).

- [13] K. A. Olive et al. "Review of Particle Physics." In: *Chin. Phys. C* 38 (2014), p. 090001. doi: [10.1088/1674-1137/38/9/090001](https://doi.org/10.1088/1674-1137/38/9/090001).
- [14] Johan Messchendorp. "Physics with Charmonium – A few recent highlights of BESIII." In: *PoS Bormio2013* (2013), p. 043. arXiv: [1306.6611 \[hep-ex\]](https://arxiv.org/abs/1306.6611).
- [15] A. D. Martin, W. J. Stirling, R. S. Thorne, and G. Watt. "Parton distributions for the LHC." In: (2009). doi: [10.1140/epjc/s10052-009-1072-5](https://doi.org/10.1140/epjc/s10052-009-1072-5). eprint: [arXiv:0901.0002](https://arxiv.org/abs/0901.0002).
- [16] W.J. Stirling. *proton-(anti)proton cross sections*. 2013. URL: <http://www.hep.ph.ic.ac.uk/~wstirlin/plots/plots.html>.
- [17] F. Zwicky. "Die Rotverschiebung von extragalaktischen Nebeln." In: *Helvetica Physica Acta* 6 (1933), 110–127.
- [18] Douglas Clowe, Marusa Bradac, Anthony H. Gonzalez, Maxim Markevitch, Scott W. Randall, Christine Jones, and Dennis Zaritsky. "A direct empirical proof of the existence of dark matter." In: (2006). doi: [10.1086/508162](https://doi.org/10.1086/508162). eprint: [arXiv:astro-ph/0608407](https://arxiv.org/abs/astro-ph/0608407).
- [19] G. Hinshaw et al. "Five-Year Wilkinson Microwave Anisotropy Probe (WMAP) Observations: Data Processing, Sky Maps, and Basic Results." In: (2008). doi: [10.1088/0067-0049/180/2/225](https://doi.org/10.1088/0067-0049/180/2/225). eprint: [arXiv:0803.0732](https://arxiv.org/abs/0803.0732).
- [20] T. S. van Albada, J. N. Bahcall, K. Begeman, and R. Sancisi. "Distribution of dark matter in the spiral galaxy NGC 3198." In: *The Astrophysical Journal* 295 (Aug. 1985), pp. 305–313. doi: [10.1086/163375](https://doi.org/10.1086/163375).
- [21] M. Gell-Mann. *THE EIGHTFOLD WAY: A THEORY OF STRONG INTERACTION SYMMETRY*. 1961. doi: [10.2172/4008239](https://doi.org/10.2172/4008239). URL: <http://www.osti.gov/scitech/servlets/purl/4008239>.
- [22] J. Wess and B. Zumino. "Supergauge transformations in four dimensions." In: *Nuclear Physics B* 70.1 (1974), pp. 39–50. ISSN: 0550-3213. doi: [http://dx.doi.org/10.1016/0550-3213\(74\)90355-1](http://dx.doi.org/10.1016/0550-3213(74)90355-1). URL: <http://www.sciencedirect.com/science/article/pii/0550321374903551>.
- [23] J.-L. Gervais and B. Sakita. "Field theory interpretation of supergauges in dual models." In: *Nuclear Physics B* 34 (1971), pp. 632–639. doi: [10.1016/0550-3213\(71\)90351-8](https://doi.org/10.1016/0550-3213(71)90351-8).
- [24] P. Ramond. "Dual Theory for Free Fermions." In: *Physical Review D* 3 (1971), pp. 2415–2418. doi: [10.1103/PhysRevD.3.2415](https://doi.org/10.1103/PhysRevD.3.2415).
- [25] Stephen P. Martin. "A Supersymmetry primer." In: (1997). [Adv. Ser. Direct. High Energy Phys. 18, 1 (1998)]. doi: [10.1142/9789812839657\\_0001](https://doi.org/10.1142/9789812839657_0001), [10.1142/9789814307505\\_0001](https://doi.org/10.1142/9789814307505_0001). arXiv: [hep-ph/9709356 \[hep-ph\]](https://arxiv.org/abs/hep-ph/9709356).
- [26] Craig J Copi, David N. Schramm, and Michael S. Turner. "Big-Bang Nucleosynthesis and the Baryon Density of the Universe." In: (1994). doi: [10.1126/science.7809624](https://doi.org/10.1126/science.7809624). eprint: [arXiv:astro-ph/9407006](https://arxiv.org/abs/astro-ph/9407006).

- [27] NobelPrize.org. *The Nobel Prize in Physics 2004 - Popular Information*. 2016. URL: [https://www.nobelprize.org/nobel\\_prizes/physics/laureates/2004/popular.html](https://www.nobelprize.org/nobel_prizes/physics/laureates/2004/popular.html).
- [28] ATLAS Collaboration. “Dark matter interpretations of ATLAS searches for the electroweak production of supersymmetric particles in  $\sqrt{s} = 8$  TeV proton-proton collisions.” In: (2016). doi: [10.1007/JHEP09\(2016\)175](https://doi.org/10.1007/JHEP09(2016)175). eprint: [arXiv:1608.00872](https://arxiv.org/abs/1608.00872).
- [29] The ATLAS collaboration. “Further searches for squarks and gluinos in final states with jets and missing transverse momentum at  $\sqrt{s} = 13$  TeV with the ATLAS detector.” In: (2016).
- [30] W. Beenakker, S. Brensing, M. Krämer, A. Kulesza, E. Laenen, L. Motyka, and I. Niessen. “Squark and gluino hadroproduction.” In: (2011). doi: [10.1142/S0217751X11053560](https://doi.org/10.1142/S0217751X11053560). eprint: [arXiv:1105.1110](https://arxiv.org/abs/1105.1110).
- [31] ATLAS Collaboration. *ATLAS SUSY Searches - 95% CL Lower Limits*. “[https://atlas.web.cern.ch/Atlas/GROUPS/PHYSICS/CombinedSummaryPlots/SUSY/ATLAS\\_2016](https://atlas.web.cern.ch/Atlas/GROUPS/PHYSICS/CombinedSummaryPlots/SUSY/ATLAS_2016)”.
- [32] Wim Beenakker, Christoph Borschensky, Michael Krämer, Anna Kulesza, and Eric Laenen. *NNLL-fast: predictions for coloured supersymmetric particle production at the LHC with threshold and Coulomb resummation*. 2016. eprint: [arXiv:1607.07741](https://arxiv.org/abs/1607.07741).
- [33] CMS Collaboration. “Search for physics beyond the standard model in events with a Z boson, jets, and missing transverse energy in  $pp$  collisions at  $\sqrt{s} = 7$  TeV.” In: *Phys. Lett. B* 716 (2012), pp. 260–284. doi: [10.1016/j.physletb.2012.08.026](https://doi.org/10.1016/j.physletb.2012.08.026). arXiv: [1204.3774 \[hep-ex\]](https://arxiv.org/abs/1204.3774).
- [34] CMS Collaboration. “Search for physics beyond the standard model in events with two leptons, jets, and missing transverse momentum in  $pp$  collisions at  $\sqrt{s} = 8$  TeV.” In: *JHEP* 04 (2015), p. 124. doi: [10.1007/JHEP04\(2015\)124](https://doi.org/10.1007/JHEP04(2015)124). arXiv: [1502.06031 \[hep-ex\]](https://arxiv.org/abs/1502.06031).
- [35] *Search for new physics in final states with two opposite-sign same-flavor leptons, jets and missing transverse momentum in pp collisions at sqrt(s)=13 TeV*. Tech. rep. CMS-PAS-SUS-15-011. Geneva: CERN, 2015. URL: <https://cds.cern.ch/record/2114811>.
- [36] Lyndon Evans and Philip Bryant. “LHC Machine.” In: *Journal of Instrumentation* 3.08 (2008), S08001. URL: <http://stacks.iop.org/1748-0221/3/i=08/a=S08001>.
- [37] *LEP design report*. Copies shelved as reports in LEP, PS and SPS libraries. Geneva: CERN, 1984. URL: <https://cds.cern.ch/record/102083>.
- [38] ATLAS Collaboration. “The ATLAS Experiment at the CERN Large Hadron Collider.” In: *JINST* 3 (2008), S08003. doi: [10.1088/1748-0221/3/08/S08003](https://doi.org/10.1088/1748-0221/3/08/S08003).

- [39] The CMS Collaboration. “The CMS experiment at the CERN LHC.” In: *Journal of Instrumentation* 3.08 (2008), S08004. URL: <http://stacks.iop.org/1748-0221/3/i=08/a=S08004>.
- [40] The LHCb Collaboration. “The LHCb Detector at the LHC.” In: *Journal of Instrumentation* 3.08 (2008), S08005. URL: <http://stacks.iop.org/1748-0221/3/i=08/a=S08005>.
- [41] The ALICE Collaboration. “The ALICE experiment at the CERN LHC.” In: *Journal of Instrumentation* 3.08 (2008), S08002. URL: <http://stacks.iop.org/1748-0221/3/i=08/a=S08002>.
- [42] Peter Vankov. “ATLAS Upgrade for the HL-LHC: meeting the challenges of a five-fold increase in collision rate.” In: (2012). DOI: [10.1051/epjconf/20122812069](https://doi.org/10.1051/epjconf/20122812069). eprint: [arXiv:1201.5469](https://arxiv.org/abs/1201.5469).
- [43] ATLAS Collaboration. *2015 start-up trigger menu and initial performance assessment of the ATLAS trigger using Run-2 data*. ATL-DAQ-PUB-2016-001. 2016. URL: <http://cds.cern.ch/record/2136007>.
- [44] ATLAS Collaboration. *Public Egamma Trigger Plots for Collision Data*. “<https://twiki.cern.ch/twiki/bin/view/AtlasPublic/EgammaTriggerPublicResults>”. 2016.
- [45] Richard D. Ball et al. “Parton distributions with LHC data.” In: *Nucl. Phys.* B867 (2013), pp. 244–289. DOI: [10.1016/j.nuclphysb.2012.10.003](https://doi.org/10.1016/j.nuclphysb.2012.10.003). arXiv: [1207.1303 \[hep-ph\]](https://arxiv.org/abs/1207.1303).
- [46] Hung-Liang Lai et al. “New parton distributions for collider physics.” In: *Phys. Rev. D* 82 (2010), p. 074024. DOI: [10.1103/PhysRevD.82.074024](https://doi.org/10.1103/PhysRevD.82.074024). arXiv: [1007.2241 \[hep-ph\]](https://arxiv.org/abs/1007.2241).
- [47] J. Alwall, R. Frederix, S. Frixione, V. Hirschi, F. Maltoni, O. Mattelaer, H. S. Shao, T. Stelzer, P. Torrielli, and M. Zaro. “The automated computation of tree-level and next-to-leading order differential cross sections, and their matching to parton shower simulations.” In: *JHEP* 07 (2014), p. 079. DOI: [10.1007/JHEP07\(2014\)079](https://doi.org/10.1007/JHEP07(2014)079). arXiv: [1405.0301 \[hep-ph\]](https://arxiv.org/abs/1405.0301).
- [48] P. Nason. “A new method for combining NLO QCD with shower Monte Carlo algorithms.” In: *JHEP* 0411 (2004), p. 040. arXiv: [hep-ph/0409146 \[hep-ph\]](https://arxiv.org/abs/hep-ph/0409146).
- [49] S. Frixione, P. Nason, and C. Oleari. “Matching NLO QCD computations with parton shower simulations: the POWHEG method.” In: *JHEP* 0711 (2007), p. 070. arXiv: [0709.2092 \[hep-ph\]](https://arxiv.org/abs/0709.2092).
- [50] S. Alioli, P. Nason, C. Oleari, and E. Re. “A general framework for implementing NLO calculations in shower Monte Carlo programs: the POWHEG BOX.” In: *JHEP* 1006 (2010), p. 043. arXiv: [1002.2581 \[hep-ph\]](https://arxiv.org/abs/1002.2581).
- [51] T. Gleisberg et al. “Event generation with Sherpa 1.1.” In: *JHEP* 0902 (2009), p. 007. arXiv: [0811.4622 \[hep-ph\]](https://arxiv.org/abs/0811.4622).

- [52] T. Sjöstrand, S. Mrenna, and P. Skands. "PYTHIA 6.4 Physics and Manual." In: *JHEP* 0605 (2006), p. 026. DOI: [10.1088/1126-6708/2006/05/026](https://doi.org/10.1088/1126-6708/2006/05/026). arXiv: [hep-ph/0603175 \[hep-ph\]](https://arxiv.org/abs/hep-ph/0603175).
- [53] S. Agostinelli et al. "GEANT4: A simulation toolkit." In: *Nucl. Instrum. Meth. A* 506 (2003), pp. 250–303. DOI: [10.1016/S0168-9002\(03\)01368-8](https://doi.org/10.1016/S0168-9002(03)01368-8).
- [54] Morad Aaboud et al. "A measurement of material in the ATLAS tracker using secondary hadronic interactions in 7 TeV pp collisions." In: (2016). arXiv: [1609.04305 \[hep-ex\]](https://arxiv.org/abs/1609.04305).
- [55] ATLAS Collaboration. "ATLAS event at 13 TeV - First stable beam, 3 June 2015 - run: 266904, evt: 25884805." General Photo. 2015. URL: <https://cds.cern.ch/record/2022202>.
- [56] *The Expected Performance of the ATLAS Inner Detector*. Tech. rep. ATL-PHYS-PUB-2009-002. ATL-COM-PHYS-2008-105. Geneva: CERN, 2008. URL: <http://cds.cern.ch/record/1118445>.
- [57] ATLAS Collaboration. "A neural network clustering algorithm for the ATLAS silicon pixel detector." In: *JINST* 9 (2014), Po9009. DOI: [10.1088/1748-0221/9/09/P09009](https://doi.org/10.1088/1748-0221/9/09/P09009). arXiv: [1406.7690 \[hep-ex\]](https://arxiv.org/abs/1406.7690).
- [58] Luke de Oliveira. *AGILEPack: Algorithms for Generalized Inference, Learning, and Extraction*. 2016. URL: <http://lukedeo.github.io/AGILEPack/>.
- [59] ATLAS Collaboration. *Measurement of performance of the pixel neural network clustering algorithm of the ATLAS experiment at  $\sqrt{s} = 13$  TeV*. ATL-PHYS-PUB-2015-044. 2015. URL: <http://cdsweb.cern.ch/record/2054921>.
- [60] ATLAS Collaboration. *Robustness of the Artificial Neural Network Clustering Algorithm of the ATLAS experiment*. ATL-PHYS-PUB-2015-052. 2015. URL: <http://cdsweb.cern.ch/record/2116350>.
- [61] "Electron performance measurements with the ATLAS detector using the 2010 LHC proton-proton collision data." In: *Eur. Phys. J. C* 72 (2012), p. 1909. DOI: [10.1140/epjc/s10052-012-1909-1](https://doi.org/10.1140/epjc/s10052-012-1909-1). arXiv: [1110.3174 \[hep-ex\]](https://arxiv.org/abs/1110.3174).
- [62] *Electron efficiency measurements with the ATLAS detector using the 2015 LHC proton-proton collision data*. Tech. rep. ATLAS-CONF-2016-024. Geneva: CERN, 2016. URL: <https://cds.cern.ch/record/2157687>.
- [63] ATLAS Collaboration. *Measurement of the photon identification efficiencies with the ATLAS detector using LHC Run-1 data*. 2016. eprint: [arXiv:1606.01813](https://arxiv.org/abs/1606.01813).
- [64] *Photon identification in 2015 ATLAS data*. Tech. rep. ATL-PHYS-PUB-2016-014. Geneva: CERN, 2016. URL: <https://cds.cern.ch/record/2203125>.

- [65] *Photon Identification Efficiencies using 2016 Data with radiative Z boson decays.* Tech. rep. EGAM-2016-003. Geneva: CERN, 2016. URL: <https://atlas.web.cern.ch/Atlas/GROUPS/PHYSICS/PLLOTS/EGAM-2016-003/index.html>.
- [66] *Official Isolation Working Points.* Geneva, 2016. URL: <https://twiki.cern.ch/twiki/bin/view/AtlasProtected/IsolationSelectionTool#Photons>.
- [67] ATLAS Collaboration. “Muon reconstruction performance of the ATLAS detector in proton–proton collision data at  $\sqrt{s}=13$  TeV.” In: (2016). DOI: [10.1140/epjc/s10052-016-4120-y](https://doi.org/10.1140/epjc/s10052-016-4120-y). eprint: arXiv: [1603.05598](https://arxiv.org/abs/1603.05598).
- [68] Matteo Cacciari, Gavin P. Salam, and Gregory Soyez. “The Anti-k(t) jet clustering algorithm.” In: *JHEP* 0804 (2008), p. 063. DOI: [10.1088/1126-6708/2008/04/063](https://doi.org/10.1088/1126-6708/2008/04/063). arXiv: [0802.1189 \[hep-ph\]](https://arxiv.org/abs/0802.1189).
- [69] ATLAS Collaboration. *Jet Calibration and Systematic Uncertainties for Jets Reconstructed in the ATLAS Detector at  $\sqrt{s} = 13$  TeV.* ATL-PHYS-PUB-2015-015. 2015. URL: <http://cds.cern.ch/record/2037613>.
- [70] ATLAS Collaboration. *Tagging and suppression of pileup jets with the ATLAS detector.* ATLAS-CONF-2014-018. 2014. URL: <http://cds.cern.ch/record/1700870>.
- [71] ATLAS Collaboration. *Expected performance of the ATLAS b-tagging in Run-2.* ATL-PHYS-PUB-2015-022. 2015. URL: <http://cdsweb.cern.ch/record/2037697>.
- [72] ATLAS Collaboration. *Expected performance of missing transverse momentum reconstruction for the ATLAS detector at  $\sqrt{s} = 13$  TeV.* ATL-PHYS-PUB-2015-023. 2015. URL: <http://cds.cern.ch/record/2037700>.
- [73] ATLAS Collaboration. *Performance of missing transverse momentum reconstruction for the ATLAS detector in the first proton-proton collisions at  $\sqrt{s} = 13$  TeV.* ATL-PHYS-PUB-2015-027. 2015. URL: <http://cds.cern.ch/record/2037904>.
- [74] ATLAS Collaboration. *Modelling of the  $t\bar{t}H$  and  $t\bar{t}V$  ( $V = W, Z$ ) processes for  $\sqrt{s} = 13$  TeV ATLAS analyses.* ATL-PHYS-PUB-2016-005. 2016. URL: <http://cds.cern.ch/record/2120826>.
- [75] M. V. Garzelli, A. Kardos, C. G. Papadopoulos, and Z. Trocsanyi. “ $t\bar{t}W^{+-}$  and  $t\bar{t}Z$  Hadroproduction at NLO accuracy in QCD with Parton Shower and Hadronization effects.” In: *JHEP* 11 (2012), p. 056. DOI: [10.1007/JHEP11\(2012\)056](https://doi.org/10.1007/JHEP11(2012)056). arXiv: [1208.2665 \[hep-ph\]](https://arxiv.org/abs/1208.2665).
- [76] J. M. Campbell and R. K. Ellis. “ $t\bar{t}W$  production and decay at NLO.” In: *JHEP* 1207 (2012), p. 052. arXiv: [1204.5678 \[hep-ph\]](https://arxiv.org/abs/1204.5678).
- [77] A. Lazopoulos, T. McElmurry, K. Melnikov, and F. Petriello. “Next-to-leading order QCD corrections to  $t\bar{t}Z$  production at the LHC.” In: *Phys. Lett. B* 666 (2008), p. 62. arXiv: [0804.2220 \[hep-ph\]](https://arxiv.org/abs/0804.2220).

- [78] ATLAS Collaboration. *Simulation of top quark production for the ATLAS experiment at  $\sqrt{s} = 13$  TeV*. ATL-PHYS-PUB-2016-004. 2016. URL: <http://cds.cern.ch/record/2120417>.
- [79] M. Czakon, P. Fiedler, and A. Mitov. “Total Top-Quark Pair-Production Cross Section at Hadron Colliders Through  $O(\alpha_s^4)$ .” In: *Phys. Rev. Lett.* 110 (2013), p. 252004. arXiv: [1303.6254 \[hep-ph\]](https://arxiv.org/abs/1303.6254).
- [80] M. Czakon and A. Mitov. “Top++: A Program for the Calculation of the Top-Pair Cross-Section at Hadron Colliders.” In: *Comput. Phys. Commun.* 185 (2014), p. 2930. DOI: [10.1016/j.cpc.2014.06.021](https://doi.org/10.1016/j.cpc.2014.06.021). arXiv: [1112.5675 \[hep-ph\]](https://arxiv.org/abs/1112.5675).
- [81] N. Kidonakis. “Two-loop soft anomalous dimensions for single top quark associated production with a  $W^-$  or  $H^-$ .” In: *Phys. Rev. D* 82 (2010), p. 054018. DOI: [10.1103/PhysRevD.82.054018](https://doi.org/10.1103/PhysRevD.82.054018). arXiv: [1005.4451 \[hep-ph\]](https://arxiv.org/abs/1005.4451).
- [82] ATLAS Collaboration. *Multi-Boson Simulation for 13 TeV ATLAS Analyses*. ATL-PHYS-PUB-2016-002. 2016. URL: <http://cds.cern.ch/record/2119986>.
- [83] J. M. Campbell and R. K. Ellis. “An update on vector boson pair production at hadron colliders.” In: *Phys. Rev. D* 60 (1999), p. 113006. arXiv: [hep-ph/9905386 \[hep-ph\]](https://arxiv.org/abs/hep-ph/9905386).
- [84] J. M. Campbell, R. K. Ellis, and C. Williams. “Vector boson pair production at the LHC.” In: *JHEP* 1107 (2011), p. 018. arXiv: [1105.0020 \[hep-ph\]](https://arxiv.org/abs/1105.0020).
- [85] ATLAS Collaboration. *Monte Carlo Generators for the Production of a W or Z/ $\gamma^*$  Boson in Association with Jets at ATLAS in Run 2*. ATL-PHYS-PUB-2016-003. 2016. URL: <http://cds.cern.ch/record/2120133>.
- [86] S. Catani, L. Cieri, G. Ferrera, D. de Florian, and M. Grazzini. “Vector boson production at hadron colliders: a fully exclusive QCD calculation at NNLO.” In: *Phys. Rev. Lett.* 103 (2009), p. 082001. arXiv: [0903.2120 \[hep-ph\]](https://arxiv.org/abs/0903.2120).
- [87] S. Catani and M. Grazzini. “An NNLO subtraction formalism in hadron collisions and its application to Higgs boson production at the LHC.” In: *Phys. Rev. Lett.* 98 (2007), p. 222002. arXiv: [hep-ph/0703012 \[hep-ph\]](https://arxiv.org/abs/hep-ph/0703012).
- [88] ATLAS Collaboration. *Electron efficiency measurements with the ATLAS detector using the 2012 LHC proton–proton collision data*. ATLAS-CONF-2014-032. 2014. URL: <http://cdsweb.cern.ch/record/1706245>.
- [89] ATLAS Collaboration. “Muon reconstruction performance of the ATLAS detector in proton–proton collision data at  $\sqrt{s} = 13$  TeV.” In: *Eur. Phys. J. C* 76 (2016), p. 292. DOI: [10.1140/epjc/s10052-016-4120-y](https://doi.org/10.1140/epjc/s10052-016-4120-y). arXiv: [1603.05598 \[hep-ex\]](https://arxiv.org/abs/1603.05598).

- [90] ATLAS Collaboration. *Search for supersymmetry in final states with jets, missing transverse momentum and a Z boson at  $\sqrt{s} = 8$  TeV with the ATLAS detector.* ATLAS-CONF-2012-152. 2012. URL: <http://cds.cern.ch/record/1493491>.
- [91] ATLAS Collaboration. “Measurement of the differential cross-section of highly boosted top quarks as a function of their transverse momentum in  $\sqrt{s} = 8$  TeV proton-proton collisions using the ATLAS detector.” In: *Phys. Rev. D* 93.3 (2016), p. 032009. DOI: [10.1103/PhysRevD.93.032009](https://doi.org/10.1103/PhysRevD.93.032009). arXiv: [1510.03818 \[hep-ex\]](https://arxiv.org/abs/1510.03818).
- [92] CMS Collaboration. “Measurement of the integrated and differential t-tbar production cross sections for high-pt top quarks in pp collisions at  $\sqrt{s} = 8$  TeV.” In: *Phys. Rev. D* (2016). Submitted. arXiv: [1605.00116 \[hep-ex\]](https://arxiv.org/abs/1605.00116).
- [93] ATLAS Collaboration. *Search for physics beyond the Standard Model in events with a Z boson and large missing transverse momentum using  $\sqrt{s} = 7$  TeV pp collisions from the LHC with the ATLAS detector.* ATLAS-CONF-2012-046. 2012. URL: <http://cdsweb.cern.ch/record/1448222>.
- [94] ATLAS Collaboration. “Search for squarks and gluinos in events with isolated leptons, jets and missing transverse momentum at  $\sqrt{s} = 8$  TeV with the ATLAS detector.” In: *JHEP* 1504 (2015), p. 116. DOI: [10.1007/JHEP04\(2015\)116](https://doi.org/10.1007/JHEP04(2015)116). arXiv: [1501.03555 \[hep-ex\]](https://arxiv.org/abs/1501.03555).
- [95] ATLAS Collaboration. “Improved luminosity determination in pp collisions at  $\sqrt{s} = 7$  TeV using the ATLAS detector at the LHC.” In: *Eur. Phys. J. C* 73 (2013), p. 2518. DOI: [10.1140/epjc/s10052-013-2518-3](https://doi.org/10.1140/epjc/s10052-013-2518-3). arXiv: [1302.4393 \[hep-ex\]](https://arxiv.org/abs/1302.4393).
- [96] ATLAS Collaboration. “Luminosity determination in pp collisions at  $\sqrt{s} = 8$  TeV using the ATLAS detector at the LHC.” In: *to be submitted to Eur. Phys. J. C* ().
- [97] Michael Kramer et al. *Supersymmetry production cross sections in pp collisions at  $\sqrt{s} = 7$  TeV.* 2012. arXiv: [1206.2892 \[hep-ph\]](https://arxiv.org/abs/1206.2892).
- [98] W. Beenakker, R. Höpker, M. Spira, and P.M. Zerwas. “Squark and gluino production at hadron colliders.” In: *Nucl. Phys. B* 492 (1997), pp. 51–103. DOI: [10.1016/S0550-3213\(97\)00084-9](https://doi.org/10.1016/S0550-3213(97)00084-9). arXiv: [hep-ph/9610490 \[hep-ph\]](https://arxiv.org/abs/hep-ph/9610490).
- [99] A. Kulesza and L. Motyka. “Threshold resummation for squark-antisquark and gluino-pair production at the LHC.” In: *Phys. Rev. Lett.* 102 (2009), p. 111802. DOI: [10.1103/PhysRevLett.102.111802](https://doi.org/10.1103/PhysRevLett.102.111802). arXiv: [0807.2405 \[hep-ph\]](https://arxiv.org/abs/0807.2405).
- [100] A. Kulesza and L. Motyka. “Soft gluon resummation for the production of gluino-gluino and squark-antisquark pairs at the LHC.” In: *Phys. Rev. D* 80 (2009), p. 095004. DOI: [10.1103/PhysRevD.80.095004](https://doi.org/10.1103/PhysRevD.80.095004). arXiv: [0905.4749 \[hep-ph\]](https://arxiv.org/abs/0905.4749).

- [101] W. Beenakker et al. "Soft-gluon resummation for squark and gluino hadroproduction." In: *JHEP* 0912 (2009), p. 041. DOI: [10.1088/1126-6708/2009/12/041](https://doi.org/10.1088/1126-6708/2009/12/041). arXiv: [0909.4418 \[hep-ph\]](https://arxiv.org/abs/0909.4418).
- [102] W. Beenakker et al. "Squark and gluino hadroproduction." In: *Int. J. Mod. Phys. A* 26 (2011), pp. 2637–2664. DOI: [10.1142/S0217751X11053560](https://doi.org/10.1142/S0217751X11053560). arXiv: [1105.1110 \[hep-ph\]](https://arxiv.org/abs/1105.1110).
- [103] M. Baak et al. "HistFitter software framework for statistical data analysis." In: *Eur. Phys. J. C* 75 (2014), p. 153. DOI: [10.1140/epjc/s10052-015-3327-7](https://doi.org/10.1140/epjc/s10052-015-3327-7). arXiv: [1410.1280 \[hep-ex\]](https://arxiv.org/abs/1410.1280).
- [104] Rene Brun and Fons Rademakers. "ROOT — An object oriented data analysis framework." In: *Nuclear Instruments and Methods in Physics Research Section A: Accelerators, Spectrometers, Detectors and Associated Equipment* 389.1 (1997), pp. 81 –86. ISSN: 0168-9002. DOI: [http://dx.doi.org/10.1016/S0168-9002\(97\)00048-X](http://dx.doi.org/10.1016/S0168-9002(97)00048-X). URL: <http://www.sciencedirect.com/science/article/pii/S016890029700048X>.
- [105] Lorenzo Moneta, Kevin Belasco, Kyle Cranmer, Sven Kreiss, Alfonso Lazzaro, Danilo Piparo, Gregory Schott, Wouter Verkerke, and Matthias Wolf. *The RooStats Project*. 2010. eprint: [arXiv:1009.1003](https://arxiv.org/abs/1009.1003).
- [106] Kyle Cranmer, George Lewis, Lorenzo Moneta, Akira Shibata, and Wouter Verkerke. "HistFactory: A tool for creating statistical models for use with RooFit and RooStats." In: (2012).
- [107] Glen Cowan, Kyle Cranmer, Eilam Gross, and Ofer Vitells. "Asymptotic formulae for likelihood-based tests of new physics." In: *Eur. Phys. J. C* 71 (2011), p. 1554. DOI: [10.1140/epjc/s10052-011-1554-0](https://doi.org/10.1140/epjc/s10052-011-1554-0). arXiv: [1007.1727 \[physics.data-an\]](https://arxiv.org/abs/1007.1727).
- [108] A. Read. "Presentation of search results: the CLs technique." In: *Journal of Physics G: Nucl. Part. Phys.* 28 (2002), pp. 2693–2704. DOI: [10.1088/0954-3899/28/10/313](https://doi.org/10.1088/0954-3899/28/10/313).
- [109] *Prospects for a search for direct pair production of top squarks in scenarios with compressed mass spectra at the high luminosity LHC with the ATLAS Detector*. Tech. rep. ATL-PHYS-PUB-2016-022. Geneva: CERN, 2016. URL: <https://cds.cern.ch/record/2220904>.